THE UNIVERSITY *of* EDINBURGH

Optical Studies of Dense Hydrogen at Multi-Megabar Pressures

Ross Howie

A thesis submitted in fulfilment of the requirements
for the degree of Doctor of Philosophy
to the
University of Edinburgh

March 2013

Abstract

Hydrogen, being the simplest and most abundant element in the Universe, is of fundamental importance to condensed matter sciences. Through advances in high pressure experimental technique, hydrogen (and its isotope deuterium) has been contained and studied using *in situ* optical spectroscopy to 315 (275 GPa) at 300 K, pressure and temperature conditions previously thought to be inaccessible. At 200 GPa, hydrogen undergoes a phase transformation, attributed to phase III, previously observed only at low temperatures. This is succeeded at 220 GPa by a reversible transformation to a new phase, IV, characterized by the simultaneous appearance of the second vibrational fundamental mode, new low-frequency phonon excitations, and a dramatic softening and broadening of the first vibrational fundamental mode. To impose constraints on the P-T phase diagram, the temperature stability of phase IV is investigated through a series of low temperature experiments, where the phase IV-III transformation is observed.

Analysis of the Raman spectra suggests that phase IV is a mixture of graphene-like layers, consisting of elongated H_2 dimers experiencing large pairing fluctuations, and unbound H_2 molecules. Isotopic comparisons reveal spectral differences between the phase IV-III transition of hydrogen and deuterium, which strongly indicates the presence of proton tunnelling in phase IV.

Optical transmission spectra of phase IV reveals an overall increase of absorption and a closing band gap reaching 1.8 eV at 315 GPa. No differences between the isotopes were observed in absorption studies, resulting in identical values for the band gap. Extrapolation of the band gap yields 375 GPa as the minimum transition pressure to a metallic state of hydrogen (deuterium).

Declaration

Except where otherwise stated, the research undertaken in this thesis was the unaided work of the author. Where the work was done in collaboration with others, a significant contribution was made by the author.

R. Howie

June 2012

Acknowledgements

I would like to record my thanks to all those who have helped me in the course of this work. In particular, the following:

Prof. E. Gregoryanz for his support, guidance, assistance and encouragement throughout my studies. I would especially like to thank him for captivating my interest in the field of high pressure.

Dr. C.L. Guillaume for his constant support, encouragement, and for always keeping morale high through tough times. Without his unerring patience when coaching, I would not have been anywhere near technically able to conduct the work for this thesis.

Mr. T. Scheler for never failing to help with operating the FIB and for useful discussions in our weekly squash matches.

Ms D.M. Morton and Mr P. Dalladay-Simpson for help and companionship through experiments and at conferences.

To the technical staff at the physics workshop who had to put up with job requests sometimes on a daily basis for the course of the work.

To the Institute of Shock Physics, Imperial College London for financial support.

Finally, to my parents, my sisters and Freyja for their unfailing encouragement and support throughout. I would especially like to thank my mum who has always been there for me and to whom this thesis is dedicated.

Contents

Abstract **i**

Declaration **ii**

Acknowledgements **iii**

Contents **iv**

List of figures **v**

1 Introduction **1**
1.1 Introduction and motivation 1
1.2 Thesis Outline 2

2 A Review of Solid Molecular Hydrogen **5**
2.1 Solid Hydrogen at High Pressure 5
2.2 Pathways to a Metallic State 14

3 A Review of Optical Spectroscopy at High Pressure **20**
3.1 Raman Spectroscopy 20
3.1.1 Theory of Raman Spectroscopy 21
3.1.2 High Pressure Raman Setup 26
3.2 Pressure Calibrants 29

4 Technical Developments **34**
4.1 The Diamond Anvil Cell 34
4.1.1 DAC Preparation 35
4.2 Low Temperature Equipment 40
4.2.1 Cryostat 40
4.2.2 Testing the cryostat: Measurements on dense sodium . . . 41

5 Multi-megabar room temperature compressions of H_2 and D_2 **46**
5.1 Introduction 46
5.2 Phase I-III Transition at Room Temperature 47

5.3 Discovery of phase IV 50
5.3.1 Hydrogen 50
5.3.2 Deuterium 53
5.3.3 Optical Transmission Spectroscopy 57
5.4 Discussion 59
5.4.1 Determining a Structure for Phase IV 59
5.4.2 Evidence for further high pressure phases 66
5.4.3 Use of the H_2 and D_2 vibron as a pressure gauge 70

6 Exploring the stability of phase IV in the *P-T* space 74
6.1 Introduction 74
6.2 Low Temperature Studies 75
6.3 Discussion 81

7 Conclusion 86

Appendix A 88

Bibliography 90

Publications 99

List of Figures

2.1 A) Rotational energy level diagram for free hydrogen (left) and deuterium (right). I is the total nuclear spin and J is the rotational quantum number. The frequencies of the intramolecular rotational excitations are given. B) Raman spectra of D_2 at 0.8 GPa in the fluid state with diagrams of the principal vibrational excitations of solid molecular hydrogen. Diagrams are adapted from [Mao 94]. . 7

2.2 Left panel: Low temperature hydrogen phase diagram for H_2 (black line) and D_2 (red line) adapted from Ref. [Goncharov 11]. Left panel: H_2 vibron frequency vs pressure at 100 K. Phase transitions are separated by dashed lines. Data are taken from Ref. [Mao 94] and Ref. [Loubeyre 02]. 10

2.3 Left: A layer of the C2/c monoclinic structure at 300 GPa as predicted for phase III from Ref. [Pickard 07]. Right: Four layers of the Pbcn structure at 300 GPa with unit cell shown. All atomic positions are taken from Ref. [Pickard 07]. 13

2.4 Phase diagram of hydrogen prior to this work. The melting curve (thick solid line) is a Ketchin fit from Ref. [Gregoryanz 03], and the symbols along it are from Refs. [Datchi 00] (red circles), [Gregoryanz 03] (blue triangles), [Deemyad 08] (orange squares), [Subramanian 11] (purple triangles) and [Eremets 09] (orange diamonds). The solid lines separating the phases I, II, and III are from Ref. [Goncharov 11]. 16

2.5 Pressure evolution of the frequency of the H_2 vibron with pressure. Symbols and lines represent measurements on the LiH part and the hydrogen part of the sample, respectively. Triangles and line (blue) show measurements at 120 K, while diamonds and line (red) represent measurements at room temperature. The inset shows the synthesized LiH sample in hydrogen media at a pressure of 155 GPa. 18

3.1 Energy-level diagram illustrating transitions corresponding to Rayleigh, Raman Stokes, and Raman anti-Stokes scattering 24

3.2 Diagram of the high pressure Raman setup. BP is the band pass filter, M1-M3 are mirrors, P1 is a periscope comprising of two mirrors, S1-S6 are plano-convex spherical lenses, BSC is a 50:50 beam splitter cube, BS is the beam splitter for reflected light, SNF and NF are SuperNotch and notch filters respectively, and WL1-2 are white light sources. 27
3.3 Representative Raman spectra showing the diamond Raman edge on compression of H_2 to 318 GPa (calculated using Ref. [Akahama 10b]). (b) Representative Raman spectra showing the diamond Raman edge upon a cooling cycle of D_2. 32

4.1 Left: Standard diamond anvil cell schematics. Right: Diagram of the modified piston-cylinder diamond anvil cell used in the multi-megabar experiments. 36
4.2 Scanning ion micrographs of a laser drilled gasket hole from directly above (A) and from a 45° angle and scanning ion micrographs of an ion-milled gasket hole from directly above (C) and from a 45° angle (D). 38
4.3 Left: Temperature dependence of the E_{2g} mode at 180 GPa (right) and 190 GPa (left). 42
4.4 Na phase diagram. The lower-pressure region, shown in open circles, is adapted from [Gregoryanz 08] and [Gregoryanz 05]. The solid circle is a measurement in this study. The dot-dashed line shows the extrapolation of the melting curve from 30 GPa with the Simon-Glatzel empirical law. Dashed lines between *tl19* and *hP4* represent hysteresis of the phase transition: the higher pressure phase line represents a phase change on increasing pressure, whilst the lower represents a phase change on decompression. 45

5.1 Representative Raman spectra of H_2 and D_2 at various pressures passing through the phase I to phase III transition. At low pressures, the peak at 2500 cm^{-1} corresponds to the second-order Raman band of diamond, which becomes unresolvable above 100 GPa. The break from 1200 cm^{-1} to 2100 cm^{-1} cuts only the first-order Raman band from diamond 48
5.2 Left: H_2 (black triangles) and D_2 (red diamonds) vibron frequency versus pressure. Right: H_2 (black triangles) and D_2 (red diamonds) vibron FWHH versus pressure. The red and black dashed lines indicate the phase I to phase III transition for D_2 and H_2 respectively. 49
5.3 Top: Representative Raman spectra of H_2 at various pressures passing through the phase III to phase IV transition at 220 GPa. Bottom: Representative Raman spectra of H_2 showing the evolution of phase IV with pressure. 51

5.4 Top left: H_2 vibron mode frequency shift as a function of pressure. Closed triangles and closed circles are the ν_1 and ν_2 vibron modes. The blue dashed line is Raman measurements at low temperature from [Loubeyre 02]. Open diamonds are low temperature infra-red measurements from [Goncharov 98, Hanfland 93]. Top right: H_2 ν_1 (closed triangles) and ν_2 (closed circles) vibron mode FWHH as a function of pressure. Bottom: H_2 lattice modes as a function of pressure. Vertical dashed lines indicate phase transitions. 52
5.5 Representative Raman spectra of D_2 at various pressures. 55
5.6 Top left: D_2 vibron mode frequency shift as a function of pressure. Closed triangles and closed circles are the ν_1 and ν_2 vibron modes. Blue triangles indicate the phase III ν_1 vibron frequencies when phases III and IV coexist. Top right: D_2 ν_1 (closed triangles) and ν_2 (closed circles) vibron mode FWHH as a function of pressure. Bottom: D_2 lattice modes as a function of pressure. Vertical dashed lines indicate phase transitions. 56
5.7 Top: Optical absorption spectra of H_2 in a visible spectral range at 300 K and different pressures. The reference transmission spectrum was measured at 75 GPa. Bottom: H_2 (black squares) and D_2 (red squares) combined band-gap points as a function of the pressure at 300 K. Open triangles are the low temperature data in phase III taken from [Loubeyre 02]. Quadratic [upper (magenta) curve] and cubic [lower (blue) curve] polynomial fits extrapolated to higher pressures are shown as solid lines. Inset: Optical microscopy images of a H_2 sample in transmitted and reflected white light at 275 GPa and 300 GPa. 58
5.8 Top: Top and side views of the *Pbcn* structure at 300 GPa showing bond lengths. The atomic positions are taken from [Pickard 07]. Bottom: Top and side views of the *Pc* structure, where the atomic positions have been taken from [Pickard 12]. Black atoms indicate the top weakly bonded G-layer. The black dashed lines show the next nearest contacts within the layer. 61
5.9 The atomic motions of the (A) low frequency libron Raman mode and (B) soft vibron (ν_1) Raman mode of the *Pbcn* structure as a result of MD simulations taken from [Goncharov 13]. 63
5.10 The frequencies of the observed modes in hydrogen versus the corresponding frequencies of the deuterium modes from 70 to 275 GPa. The blue filled triangles are the ν_1 mode, the red filled circles are the ν_1 modes. The filled squares and stars are the low energy phonon modes. The arrows indicate the change in frequency of the given excitation when pressure is increased. The straight solid line has the slope of $1/\sqrt{2}$ 64

5.11 Comparison of the experimentally observed and theoretically calculated [Pickard 12] Raman intensities and spectral positions of the hydrogen bands at 250 GPa. (A) Experimental raw spectra observed in phase IV (in black); spectra corrected for decreasing sensitivity of the detector are shown above (in red). The broad peaks between 1333 cm^{-1} and 1800 $cm^{-}1$ are due to the first order Raman from diamond. (B) Experimental renormalized spectra plotted as Gaussian distributions for phase IV (vertical black lines); theoretically calculated spectra for Pc. The intensities for renormalized and theoretically calculated spectra are plotted on a logarithmic scale to clearly compare the weaker low frequency modes. 65

5.12 Upper: Illustrations and photomicrographs showing how the sample chamber was observed to partially collapse. Hydrogen vibron frequencies and pressure estimates (calculated using Ref. [Akahama 10b] are indicated at each stage of deformation. Lower: Raman spectra of H_2 (bottom) and D_2 (top) at diamond edge frequencies of 1765 cm^{-1} and 1770 cm^{-1} respectively. The upper spectrum in each isotope shows measurements on the transparent part of the sample. The lower (weaker) spectrum shows measurements on the partially collapsed sample chamber, as illustrated in the photomicrograph inset. The inset shows a photomicrograph in both transmitted and reflected light, whilst the probing laser reflects on the partially collapsed gasket segment of the sample. 68

5.13 Hydrogen and deuterium combined band-gap points (filled squares) as a function of pressure at 300 K. Dotted (black) straight lines are linear fits to the measured data points in phase IV and phase IV'. Quadratic [upper (red) curve] and cubic [lower (blue) curve] polynomial fits extrapolated to higher pressures are shown as solid lines. Inset: Frequency of the ν_1 mode of hydrogen as a function of pressure. Open circles are measured ν_1 vibron frequencies versus pressure. The solid (red) line shows the nearly linear (from 275 to 400 GPa) extrapolation of the ν_1 frequency up to above 375 GPa- the minimal pressure needed to close the optical band gap. Dashed vertical lines indicate the proposed phase transition between phase IV and phase IV'. 71

5.14 H_2 and D_2 vibron frequency versus diamond Raman edge frequency for 10 separate experimental runs. Insets: Vibron frequency versus pressure comparison between this study and [Eremets 11]. Solid symbols represent this study with pressure calibrated using [Akahama 10b] and open symbols are from [Eremets 11]. 72

6.1 Representative Raman spectra of deuterium upon cooling (top) and warming (bottom) showing phase IV-III transformations at 242 GPa. 76
6.2 Representative Raman spectra of deuterium upon cooling (top) and warming (bottom) showing phase IV-III transformations at 247 and 256 GPa. 77
6.3 Top: Frequency discontinuities of the ν_1 modes of H_2 (filled triangles, 262 GPa; filled circles, 242 GPa) and D_2 (open squares, 256 GPa; open diamonds, 247 GPa) across the III-to-IV transformations. Bottom: FWHH of the ν_1 vibrons of H_2 (filled triangles, 262 GPa; filled circles, 242 GPa) and and D_2 (open squares, 256 GPa; open diamonds, 247 GPa) plotted versus temperature. Note the similar values of FWHH for both isotopes in phase III. 78
6.4 Generalized P-T-ν_1 diagrams for (a) D_2 and (b) H_2 showing the difference in the vibron frequency landscapes. 80
6.5 Comparison of the experimentally observed and theoretically calculated [Pickard 12] Raman intensities and spectral positions of the hydrogen bands at 250 GPa. (A) Experimental raw spectra observed in phase III (in black); spectra corrected for decreasing sensitivity of the detector are shown above (in red). The broad peaks between 1333 cm^{-1} and 1800 cm^{-1} are due to the first order Raman from diamond. (B) Experimental renormalized spectra plotted as Gaussian distributions for phase III (vertical black lines); theoretically calculated spectra for Cmca-12 (blue) and C2/c (red). The intensities for renormalized and theoretically calculated spectra are plotted on a logarithmic scale to clearly compare the weaker low frequency modes. 83
6.6 Proposed phase diagram of H_2 (top) and D_2 (bottom). The melting curve (thick solid line) of H_2 is a Ketchin fit from [Gregoryanz 03] and the symbols along it are from [Datchi 00, Gregoryanz 03]. The black diamonds separating the phases I, II and III of H_2 and D_2 are from [Goncharov 11]. The thin red solid lines show the P-T paths taken in this study and the stars along them show phase I to III and III to IV transformations. The dashed lines are proposed boundaries between I-III, III-IV and I-IV phases. The solid purple and orange lines show the theoretically predicted phase III-IV-V transition lines [Pickard 12, Liu 12]. The calculated transition lines between molecular and atomic liquid H_2 are shown with dashed lines and crosses [Tamblyn 10] and triangles [Morales 10]. 85

Chapter 1

Introduction

1.1 Introduction and motivation

As the simplest and most abundant element in the universe, the understanding of hydrogen is vital to multidisciplinary fields in physics. Specifically, the high pressure behaviour of hydrogen is of the utmost importance in the understanding of simple molecules under pressure. How the material behaves under pressure will also have important implications for reaching inertial confinement fusion (ICF) conditions and for planetary modelling, as hydrogen is the primary constituent in Jovian planets.

A long outstanding challenge of condensed matter physics is the production of metallic hydrogen in the experimental laboratory. In 1935, Wigner and Huntington predicted solid molecular hydrogen would to dissociate into an atomic metallic solid at 25 GPa [Wigner 35]. However, this first prediction was still in the early development of quantum mechanics and the predicted transition pressure was outwith experimental capabilities. Now, modern calculations and experiments predict metallization pressures in excess of 300 GPa. In 1968, Ashcroft predicted that atomic metallic hydrogen may be a high temperature superconductor based on a BCS model [Ashcroft 68]. Furthermore, in a later study, a new exotic state of matter was predicted, whereby hydrogen may not be characterized exclusively as a superconductor or superfluid [Babaev 04]. If found to be metastable, metallic hydrogen has been suggested to have revolutionary

applications from lightweight structural materials, to rocket fuel that could provide four times more propellent power than conventional liquid hydrogen rocket fuel [Silvera 10].

The first early efforts to obtain metallic hydrogen used large presses [Kawai 75, Vereshchagin 75], however significant progress was made only when the diamond anvil cell (DAC) was developed to obtain multi-megabar pressures in the late 1980s. As experiments continued to push hydrogen to higher pressures, the predicted metallic transition has yet to be observed, at least not below 1000 K. The DAC has been a vital tool in many important discoveries concerning the phase diagram of hydrogen at high pressures [Mao 94]. Only three solid phases (I, II and III) of solid hydrogen are known and claims of additional solid phases predicted theoretically and observed experimentally remain contraversial.

Metallic hydrogen has only been observed experimentally at high temperatures in the fluid state [Weir 96], alluding to the theory that high temperature may be the simplest pathway to obtaining a metallic form. However, due to technical difficulties, low temperature hydrogen studies have not reached pressures exceeding 300 GPa [Loubeyre 02, Akahama 10a], whilst room temperature experiments have not surpassed pressures of 180 GPa [Baer 07]. The work presented in this thesis has addressed and overcome such technical challenges, opening a window of opportunity to study solid hydrogen at conditions previously thought to be completely inaccessible.

1.2 Thesis Outline

There are 7 chapters in this thesis including this introductory chapter. The outlines for each of the following chapters are presented below.

Chapter 2 serves as an introduction to solid molecular hydrogen and deuterium at high pressure and is divided into two parts: Chapter 2.1 reviews the most important properties and characteristics of solid molecular hydrogen and deuterium and aims to lay the foundation for the work that this thesis builds upon. Chapter 2.2 reviews the experimental approaches that past studies have taken in attempting to reach the elusive metallic state, highlighting the importance of

room temperature studies of hydrogen and deuterium above 180 GPa.

Chapter 3 gives a general background on Raman spectroscopy and details of the Raman spectroscopy setup used in the work presented here. Chapter 3.2 contains a background review of pressure calibrants used in high pressure optical studies.

Chapter 4 gives both general background information and the way in which diamond anvil cell techniques and low temperature methods were developed for the work contributing to this thesis. Chapter 4.1.1 outlines how the diamond anvil cells were prepared, introducing FIB drilled sample chambers for containing hydrogen. Chapter 4.2.1 outlines the developments of the cryostat used in low temperature measurements and Chapter 4.2.2 presents results on dense sodium collected, whilst testing the capabilities of the cryostat.

Chapters 5 presents the first set of experimental results using Raman and visible transmission spectroscopy to investigate dense hydrogen (deuterium) up to 318 (275) GPa at 300 K. This chapter is divided into the results (chapter 5.3) and discussion (chapter 5.4), which are then subdivided. Chapter 5.3 presents the room temperature hydrogen (deuterium) phase I-to-III transition at 190 (185) GPa (chapter 5.3.1). This is succeeded at 220 GPa by a reversible transformation to a new phase, IV. This phase is characterized by the simultaneous appearance of the second vibrational fundamental mode and new low-frequency phonon excitations, and a dramatic softening and broadening of the first vibrational fundamental mode (chapters 5.3.2 - 5.3.3). The optical transmission spectra of phase IV show an overall increase of absorption and a closing band gap, which reaches 1.8 eV at 315 GPa. The extrapolation of the band gap yields 375 GPa as the minimum transition pressure to the metallic state of hydrogen (deuterium) (chapter 5.3.4). Chapter 5.4 opens the discussion in determining a structure for phase IV (chapter 5.4.1). Analysis of the Raman spectra suggests that phase IV is a mixture of graphene-like layers, consisting of elongated dimers and unbound molecules . Furthermore, features of the Raman spectra indicates that the phase IV structure exhibits remarkable fluxional characteristics related to its quantum nature. Evidence for further high pressure phases are discussed and compared with recent theoretical and experimental results (chapter 5.4.2). Finally, the way in which pressure is determined in multi-megabar hydrogen experiments is

questioned and proposes that the frequency of the vibrational mode is the only definitive way to compare studies.

Chapter 6 presents the second set of experimental results, investigating the temperature and pressure stability of the newly discovered phase IV. This chapter is divided into the results (chapter 6.2) and discussion (chapter 6.3). The results present a series of low-temperature experiments, through which the phase III-to-IV transformation is observed, imposing constraints on the P-T phase diagrams. The spectral features of the phase IV-III transition and differences in appearances of the isotopes' Raman spectra strongly indicate the presence of proton tunnelling in phase IV. The implications of phase IV on the P-T phase diagram are discussed and a comparison is made with recent experimental and theoretical results.

Chapter 7 summarizes the main results and also postulates questions to stimulate further investigations.

Chapter 2

A Review of Solid Molecular Hydrogen

2.1 Solid Hydrogen at High Pressure

At low pressures, the anisotropic intermolecular interactions between hydrogen molecules are weak and, as a result, the angular momentum of an individual molecule (J) remains a good quantum number. The molecular wavefunction for any isolated homonuclear diatomic molecule must be symmetric or anti-symmetric under nuclear exchange, having the implication that molecular hydrogen can only occur in two isomeric forms, ortho-hydrogen, with nuclear spin aligned parallel (I = 1, odd J) or para-hydrogen, with nuclear spin anti-parallel (I = 0, even J) [Kranendonk 83]. For hydrogen, the total wavefunction of an isolated molecule, $\psi_{mol} = \psi_{vib}\psi_{rot}\psi_{spin}$, must be anti-symmetric under the exchange of two spin $\frac{1}{2}$ protons. ψ_{vib} is always symmetric and ψ_{spin} is symmetric for the triplet state I=1 and anti-symmetric for the singlet state I=0. Thus, the symmetric total nuclear spin must couple with rotational states which are anti-symmetric under permutation of the nuclei (J=1,3,5...), designating the ortho species. H_2 molecules with anti-symmetric total nuclear spin I=0 can only be coupled with symmetric rotational states (J = 0, 2, 4...), designating the para species. In contrast, D_2 has one extra (spin-$\frac{1}{2}$) neutron per atom. Thus, molecules with I = 0 or I = 2 can only be coupled with even rotational states and molecules with I =

1 only with odd rotational states. This defines ortho-deuterium, corresponding to I = 0, 2 with even J and para-deuterium I = 1 with odd J [Silvera 80].

Fig. 2.1 illustrates the rotational energy level diagram for free hydrogen and deuterium. Due to the large separation of the rotational energy levels, only either the J = 0 (para-hydrogen or ortho-deuterium) or J = 1 (ortho-hydrogen or para-deuterium) states are thermally populated at low temperatures. Pure para-hydrogen molecules freely rotate about their centre of mass, i.e. each has a spherically symmetric wavefunction and have no orientational ordering, whilst ortho-hydrogen aligns even at low temperatures (ortho-hydrogen has figure eight shaped p wavefunctions). At room temperature, 'normal' hydrogen (n-H_2) has an ortho-to-para ratio of 3:1, while 'normal' deuterium (n-D_2) has an ortho-to-para ratio of 1:2 [Silvera 80]. Below pressures of 20 GPa, the ortho-para conversion rate is slow [Silvera 80, Eggert 99] and phase transitions at low temperatures are sensitive to their concentration. For example, it has been found that n-H_2 crystallizes in the hexagonally closed packed (hcp) structure (Phase I) [Hazen 87], whilst molecules in the pure ortho species orient along the body diagonals of a face-centred cubic (FCC) structure with *Pa3* symmetry [Mills 65].

Prior to this thesis, only three firmly established solid phases of n-H_2 and n-D_2 were known: one orientationally disordered phase (I) and two partially or completely ordered phases (II and III) [Mao 94]. The effect of ortho-para distinction on phase transitions is not entirely understood, due to difficulties in performing experiments with pure orth-para composition. Nevertheless, it is currently accepted that ortho-para distinction does not affect the transition to phase III, which is suggested to be classically orientationally ordered [Mazin 97]. From herein, references and measurements of hydrogen reported in this thesis refer to the 'normal' concentration, with the work focussing entirely on transitions above 100 GPa, where the effects of ortho-para distinction are substantially diminished.

The low x-ray scattering efficiency of hydrogen, small sample sizes and limitations due to high pressure apparatus pose challenges to current x-ray diffraction techniques. As such, Raman spectroscopy has been the primary technique for probing the vibrational and electronic excitations in dense solid hydrogen [Mao 94]. The fundamental vibrational excitations of hydrogen,

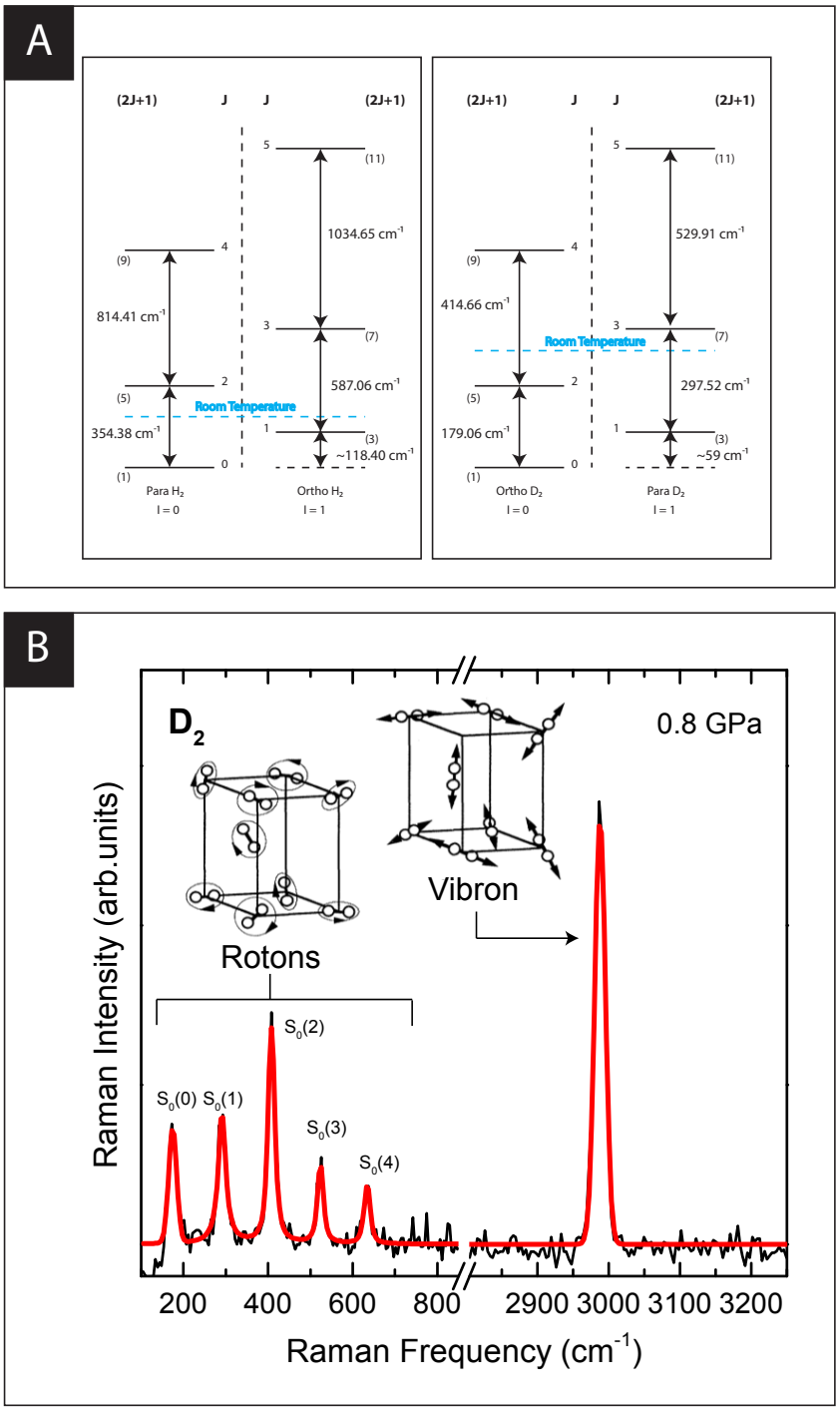

Figure 2.1: A) Rotational energy level diagram for free hydrogen (left) and deuterium (right). I is the total nuclear spin and J is the rotational quantum number. The frequencies of the intramolecular rotational excitations are given. B) Raman spectra of D_2 at 0.8 GPa in the fluid state with diagrams of the principal vibrational excitations of solid molecular hydrogen. Diagrams are adapted from [Mao 94].

illustrated in Fig. 2.1, are intramolecular stretches (vibrons), intramolecular rotations (rotons), lattice vibrations (phonons). The rotational spectrum for the free molecule, which give rise to roton excitations, is given by;

$$E_{rot} = BJ(J+1) \tag{2.1}$$

where B is the rotational constant (59.31 cm^{-1} and 29.91 cm^{-1} for free H_2 and D_2 respectively) and J is the rotational quantum number [Kranendonk 83]. In H_2 (D_2), the $S_0(0)$ roton corresponding to the J=2→0 transition has a Raman frequency of 354.4 cm^{-1} (179.12 cm^{-1}), whilst the $S_0(1)$ roton corresponding to the J=3→1 transition has a Raman frequency of 587.1 cm^{-1} (297.6 cm^{-1}). Rotational transitions and Raman spectra of H_2, are shown in Fig. 2.1. Lattice phonons observable include the Raman active E_2g (TO) mode as well as overtones, which involve combinations of excitations. Although measuring changes in the rotational Raman spectra can provide a great deal of information regarding the molecular rotational and orientational states, such measurements remain experimentally challenging. Thus, it has been changes in the molecular vibron, which are significantly more intense than the rotational Raman spectra, that have been utilized to map out phase boundaries in the majority of studies of hydrogen.

Phase I is observed to be stable up to pressures of 180 GPa at room temperature [Baer 07, Baer 09] and extend to temperatures as high as 1050 K [Eremets 09]. No solid phase is known to exist at temperatures higher than Phase I, with only the transition to a fluid state observed in experiments. Phase I adopts an hexagonally closed packed structure with freely rotating molecules, evidenced by the persistence of rotational transitions (rotons) observed in the Raman spectra. Interestingly, the molecular vibron is observed to harden with pressure up to approximately 38 GPa, after which it begins to soften. This behaviour is indicative that the hydrogen molecules could dissociate with pressure, as this phenomenon is related to partial charge transfer, due to increased coupling of the molecular orbitals through the intermolecular bonds [Mao 94].

At temperatures below 135 K, and in the pressure region of 70-160 GPa [Lorenzana 90, Goncharenko 05], hydrogen enters phase II. The transition to phase II was originally described as one from a spherically symmetric rotational

state of pure para-H_2 or pure ortho-D_2 to a broken symmetry phase, in which the symmetric states deform and the material transforms to an orientationally ordered state [Silvera 81]. It was later shown that mixed ortho-para materials (n-H_2) also transform to phase II at lower pressures, revealing different rotational dynamics and, perhaps, different crystal structures [Silvera 80]. A very large isotope effect is observed for the transition to phase II, which suggests that the transformation is related to the ordering of the quantum rotational degrees of freedom. This is due to the rotational constants, given by:

$$B = \frac{h}{4\pi^2 cI} \tag{2.2}$$

where I is the rotational moment of inertia, which governs the rotational energies, being very different for H_2 and D_2. Raman spectra of phase II reveals a combination of free molecular excitations and the appearance of libron-like vibrations, characteristic of orientationally ordered molecules [Cui 95, Goncharov 98] and changes in the vibron-roton coupled modes (overtones) [Goncharov 96]. Above 140 GPa, the vibron frequency has a rather strong temperature dependence in phase II prior to the transition to phase I, suggesting that the orientational ordering develops gradually with pressure within phase II.

Phases I, II, and III coexist at a triple point at 125 K and 155 GPa (135 K and 165 GPa for D_2), above which a phase line with positive slope separates phases I and III (see Fig. 2.2). Phase III is separated from phase II by an almost vertical phase line from 0 K to 125 K at ∼155 GPa (165 GPa for D_2) [Hemley 88, Goncharov 11]. The transition line between phases II and III occurs at similar pressures for hydrogen and deuterium, indicating that the phase transformation is mainly determined by classical ordering. Phase III was discovered by Raman observations at 77 K, the Raman vibron revealed an astonishing 100 cm^{-1} discontinuity at 155 GPa (see Fig. 2.2) and observations showed a two-phase coexistence in the pressure range of about 20 GPa, which is characteristic of a first-order transition [Hemley 88]. Subsequent infrared absorption (IR) measurements also showed an increase of over two orders of magnitude in the vibron mode activity in phase III [Hemley 88, Lorenzana 89]. In addition to the vibron discontinuity, the II-III transition is characterized by a total alteration of the low-frequency spectra; the roton spectra (or their remnants)

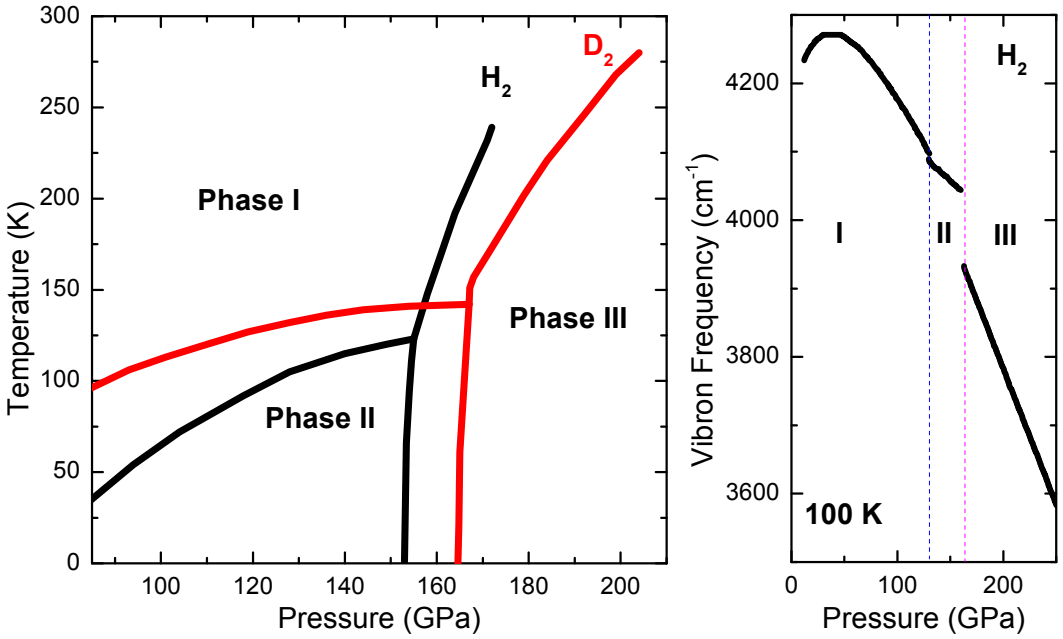

Figure 2.2: Left panel: Low temperature hydrogen phase diagram for H_2 (black line) and D_2 (red line) adapted from Ref. [Goncharov 11]. Left panel: H_2 vibron frequency vs pressure at 100 K. Phase transitions are separated by dashed lines. Data are taken from Ref. [Mao 94] and Ref. [Loubeyre 02].

disappear and a number of new peaks appear at the transition to phase III. These show a very strong pressure dependence, which identifies them as lattice modes (translational and librational), unlike the rotational modes (rotons) in phases I and II, which are very weakly pressure dependent [Goncharov 11]. The frequencies of the Raman modes increase strongly with pressure and the modes become sharper. Features of the Raman and IR spectra of phase III are strongly temperature dependent.

The phase I-III transition exhibits a discontinuity in vibron frequency, which rapidly decreases with increasing temperature, disappearing at 250 K [Goncharov 95]. The disappearance of the discontinuity in the vibron frequency with increasing temperature led to speculation that yet another phase, denoted by I', could exist at higher temperatures, conditions that at the time were deemed inaccessible. The results suggested that phase I' would be of similar structure to phase III, with a critical point at the P-T conditions where the vibron discontinuity vanishes [Goncharov 95]. Further evidence for phase I' was shown in a subsequent study by Baer *et al.*, using coherent anti-Stokes Raman spectroscopy on D_2 [Baer 07, Baer 09]. Comparing the pressure dependence of the Raman shift of the D_2 vibron at temperatures of 77 K and 300 K, they observed a change in the gradient of the vibron frequency versus pressure at 140 GPa. This change was attributed to the phase I-I' transition at 300 K, which was in agreement with a theoretical study by Surh *et. al.* [Surh 97]. However, for both the experimental observations by Goncharov *et. al.* [Goncharov 95], and Baer *et. al.* [Baer 07, Baer 09], the phase I-I' transition line would need to have a negative slope and, therefore, must have a strong temperature dependence, which was not observed by Goncharov *et. al.*,. In a further, more refined study by Goncharov *et. al.*, [Goncharov 11], they concluded that there was not enough evidence in the analysis by Baer *et. al.* to support the existence of phase I'.

The determination of the structure of orientationally ordered hydrogen phases is a very challenging topic. In x-ray diffraction and neutron studies, normally one or two of the strongest reflections originating from the major (100) and (101) peaks of the hcp phase I of hydrogen are observed. X-ray diffraction measurements up to 183 GPa indicate that the centre of each molecule in phases II and III still have an hcp structural basis [Akahama 10c]. This is consistent with neutron scattering measurements of phase II of deuterium, which also observed

basic hexagonal symmetry [Goncharenko 05]. Despite combined Raman, X-ray and neutron diffraction data providing some evidence of partial orientational ordering, the available data still remains insufficient to determine any structure unambiguously. As such, there have been many attempts to identify possible structure candidates for phase II and III through simulations.

Predictions of the molecular orientations of phases II and III are mostly based on fully *ab initio* calculations, which include density functional theory (DFT) and quantum monte carlo (QMC). Such calculations often evaluate the stability of the static structure at zero temperature, neglecting important contributions from zero point motion (ZPM) and thermal effects, which are significant in an element as light as H_2.

The theoretical determination of orientational ordered phases, in particular phase II, remains challenging, as phase II still retains a large amount of orientational disorder. Numerous structures have been proposed for phase II, which include $Cmc2_1$ [Kitamura 00], $P2_1/c$ [Johnson 00, Zhang 07] and $Pca2_1$ [Kohanoff 97, Nagao 99, Stadele 00]. Using the *ab initio* random structure searching (AIRSS) method [Pickard 06], $Pca2_1$ and $P6_3/m$ were identified as "phase II-like" structures [Pickard 09]. The majority of the structures predicted are all similar with orthorhombic primitive cells and lattice sites close to hcp, only differing in molecular orientation. $Pca2_1$ is one of the most comprehensively studied structures as a candidate for phase II. However, as with many of the other candidate structures, there are inconsistencies with experiments; four Raman modes are predicted for $Pca2_1$, whilst Raman experiments observe one single mode.

There have been as many structures predicted for phase III as for phase II. The most promising structure, $C2/c$, was revealed using the AIRSS method, which included estimates of proton zero-point motion. $C2/c$ has 12 atoms per unit cell, with hydrogen molecules centred close to distorted hcp lattice site [Pickard 07]. The structure is qualitatively in agreement with the limited diffraction data and the intense IR activity observed experimentally in phase III. However, as will be discussed later, $C2/c$ is in strong disagreement with the experimental Raman data of phase III presented in this thesis. Another theoretical candidate for phase III, competing in energetic stability with the $C2/c$ structure, is the Pbcn

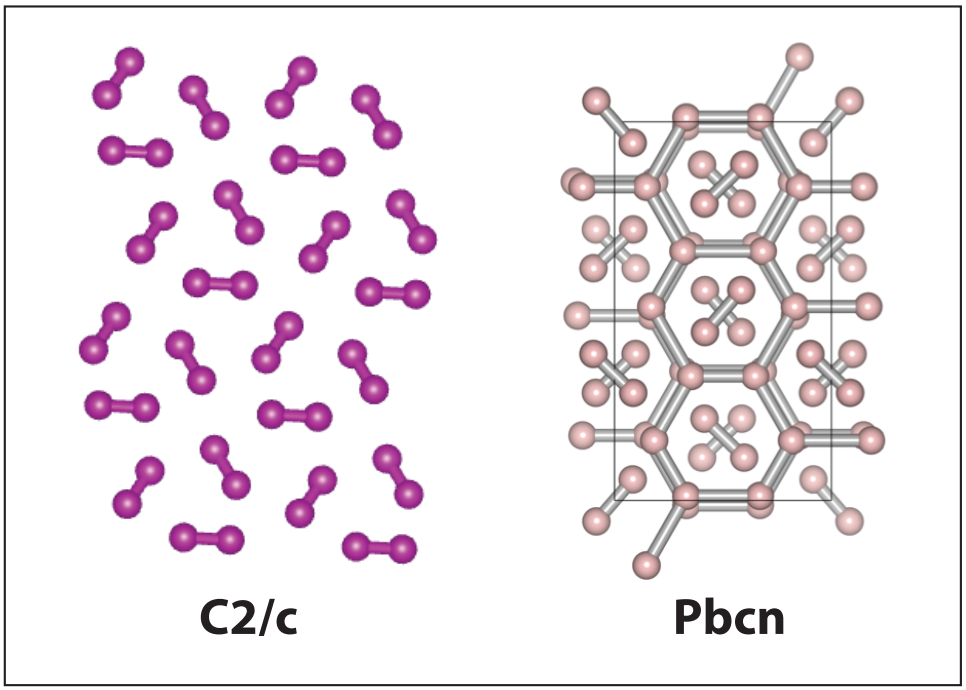

Figure 2.3: Left: A layer of the C2/c monoclinic structure at 300 GPa as predicted for phase III from Ref. [Pickard 07]. Right: Four layers of the Pbcn structure at 300 GPa with unit cell shown. All atomic positions are taken from Ref. [Pickard 07].

structure (see Fig. 2.3). Pbcn has a "mixed" hydrogen structure, comprising of alternate layers of strongly bonded molecules and weakly bonded graphene-like sheets [Pickard 07]. However, *Pbcn* is calculated to be dynamically unstable and predicted Raman modes do not agree with the experimentally observed Raman bands of phase III. Although *Pbcn* cannot be considered viable for phase III, it is of vital importance in the interpretation of the data reported in this thesis. It is interesting that, in spite of a large number of energetically competing structures determined in theoretical calculations, experimental observations show the stability of only one phase III in a very broad pressure-temperature range. The experimentally determined pressure and temperature dependencies of vibron and phonon frequencies suggest that phase III becomes more stable at higher pressures and lower temperatures.

2.2 Pathways to a Metallic State

Arguably, the greatest experimental challenge in high pressure physics still remains reaching and comprehensively measuring the properties of the predicted metallic form of hydrogen. Several claims have been made of reaching such state, with only one shock study providing sufficient evidence that the sample was contained and a conductive fluid phase was reached [Nellis 99, Weir 96]. There are three main experimental approaches that have been explored in attempts to obtain the metallic solid state - cold compression (<300K), high temperature compression(>300 K), and chemical compression.

Cold compression experiments have the advantage that, at low temperatures, anvil failure due to hydrogen diffusion is significantly reduced. Measurements of vibrational and optical properties of hydrogen have been extended to 315 GPa at 100 K [Loubeyre 02, Akahama 10a]. The vibron was still observed at these conditions, signifying the persistence of the H_2 molecule. The important feature of the vibron behaviour with pressure observed at this temperature is the steady decrease of both Raman and IR active vibrons (also observed at room temperature). Using visible transmission spectroscopy, Loubeyre *et. al.* [Loubeyre 02], reported a direct band gap of 2 eV at 315 GPa (100 K) and predicted that a metallic form of H_2 would be observed through direct band gap

closure at 450 GPa. Akahama *et. al.* [Akahama 10a], reported a band gap of 2 eV at a slightly lower pressure of 296 GPa (90 K), indicating that the transition to a metallic state is more likely to occur at 400 GPa. Pressures exceeding 400 GPa still lie outwith the pressure capabilities of current hydrogen DAC experiments, thus alternative pathways to cold compressions must be explored.

While metallic hydrogen has not yet been observed in the low temperature solid, metallization has been achieved in the fluid state [Nellis 99, Weir 96]. Using reverberating shocks to achieve quasi-isentropic compressions, the resistivity of H_2 was observed to decrease continuously by almost 4 orders of magnitude between pressures of 93 and 140 GPa. The resistivity then saturated between 140 GPa and 180 GPa to 500 $\mu\Omega$cm, a typical resistivity value for liquid metals. The observation of a metallic fluid in hydrogen has driven static compression measurements of the melting line using DACs. Although multi-megabar pressures can be achieved in DACs, the temperature range is significantly limited, due to the diffusion of hydrogen into the gasket or diamonds, causing sample loss and anvil embrittlement, inevitably leading to anvil failure. Interestingly, all high temperature studies have focussed on the behaviour of H_2 and there are no studies dedicated to deuterium to provide isotopic comparisons.

The H_2 melting line was first extended to high pressures by Datchi *et. al.* to 526 K and 15 GPa, where it was concluded that it would not be possible to attain higher temperatures, due to sample loss through diffusion of hydrogen [Datchi 00]. By inserting a ceramic disk in the sample chamber, thereby reducing hydrogen diffusion into the gasket, Gregoryanz *et. al.* extended melt line measurements to 800 K at 44 GPa [Gregoryanz 03]. Even with the improvement in hydrogen confinement, experiments could not detect the indistinguishable change in the hydrogen vibron frequency when crossing the melting line at higher pressures. Nevertheless, at elevated temperatures in the fluid, H_2 would still diffuse into the diamonds, causing embrittlement. The most important result from these experiments was the suggestion that the best fit to the melting line is a Kechin curve, implying a maximum on the melting curve. Deemyad *et. al.* later claimed the observation of a maximum in the melting curve using laser heating techniques, however no physical property of hydrogen was reported to prove that hydrogen was actually present in the sample chamber at the P-T conditions claimed [Deemyad 08, Goncharov 09]. More convincing evidence of

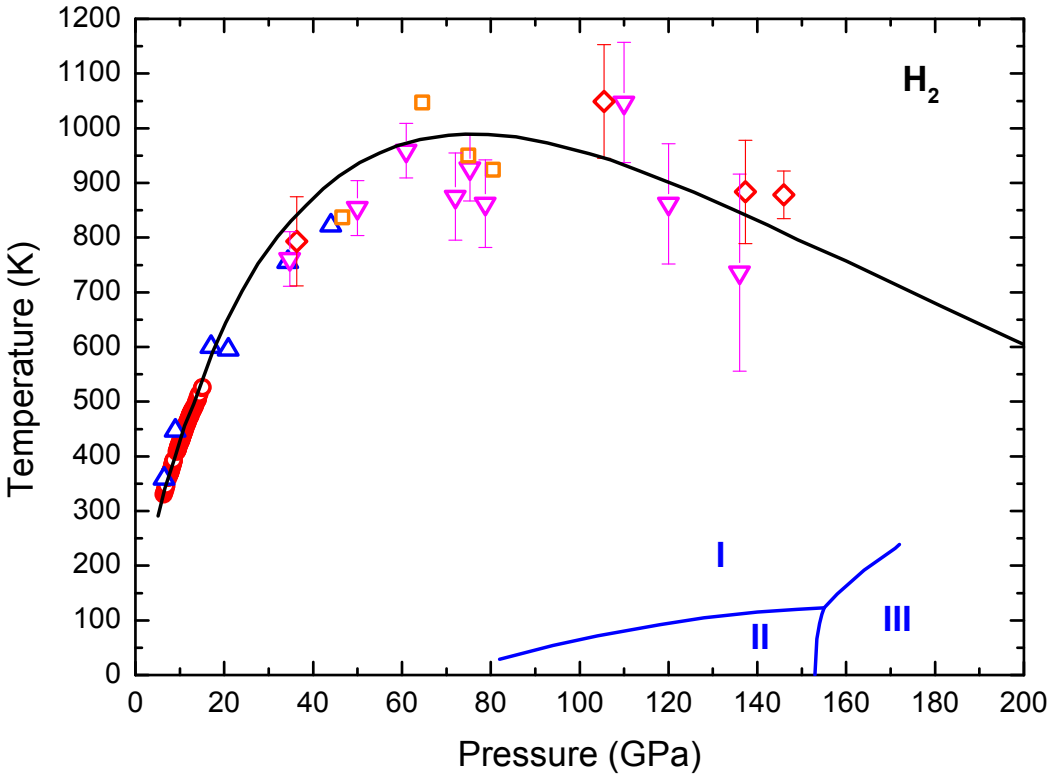

Figure 2.4: Phase diagram of hydrogen prior to this work. The melting curve (thick solid line) is a Ketchin fit from Ref. [Gregoryanz 03], and the symbols along it are from Refs. [Datchi 00] (red circles), [Gregoryanz 03] (blue triangles), [Deemyad 08] (orange squares), [Subramanian 11] (purple triangles) and [Eremets 09] (orange diamonds). The solid lines separating the phases I, II, and III are from Ref. [Goncharov 11].

a maximum was presented in a laser heating study by Eremets *et. al.* and subsequently by Subramanian *et. al.*, however few available data points, large errors in temperature, and difficulties in resolving signal from a sample with a large temperature gradient make it difficult to definitively infer the P-T conditions of the maximum [Eremets 09, Subramanian 11]. Figure 2.4 illustrates all available high pressure melting data on hydrogen.

Nevertheless, all available high temperature data show evidence that the melting temperature of H_2 may decrease with pressure after the maximum. If such behaviour exists, hydrogen may even reach a (possibly metallic) fluid state at room temperature. This accentuates the importance in developing experimental techniques to reach pressures above 180 GPa at room temperatures. In a recent study by Eremets and Troyan, a metallic fluid state of hydrogen was claimed to be observed at room temperature [Eremets 11]. A critical review of this study will be addressed later in Chapter 5.

Recently, there has been much interest in the chemical compression of hydrogen from a fundamental solid state physics perspective. Through theoretical calculations, it has been suggested that *"a little bit of lithium"* could have the profound effect on lowering the metallization pressure of hydrogen through the formation of a poly-hydride [Zurek 09]. Metallic LiH_2, LiH_6 and LiH_8 were predicted to become more stable than the $LiH+H_2$ mixture at pressures above 100 GPa, well within experimental capabilities. Further yet, another theoretical study using *ab-initio* random structure searching [Pickard 11] reported that at a lower pressure of 100 GPa, the lithium-hydrogen compound with much higher hydrogen content (LiH_{16}) is stable against decomposition into LiH_8 and H_2.

A very useful, subtle characteristic of all predicted structures is that they all contain stretched hydrogen molecules. The vibrational intramolecular Raman-active mode, ν_1, is extremely sensitive to any structural changes. It is predicted that LiH_6 will have Raman active optical phonons with the highest mode at frequencies of 2920 cm^{-1} at 100 GPa, which would be a significant deviation from the pure hydrogen vibrational mode (4170 cm^{-1}). In addition, as LiH_6 is predicted to be metallic, it is expected that the sample would become optically opaque in transmitted light, as a result of band-gap closure. However, compressions of a LiH sample embedded in H_2 to pressures as high as 160 GPa did not observe the

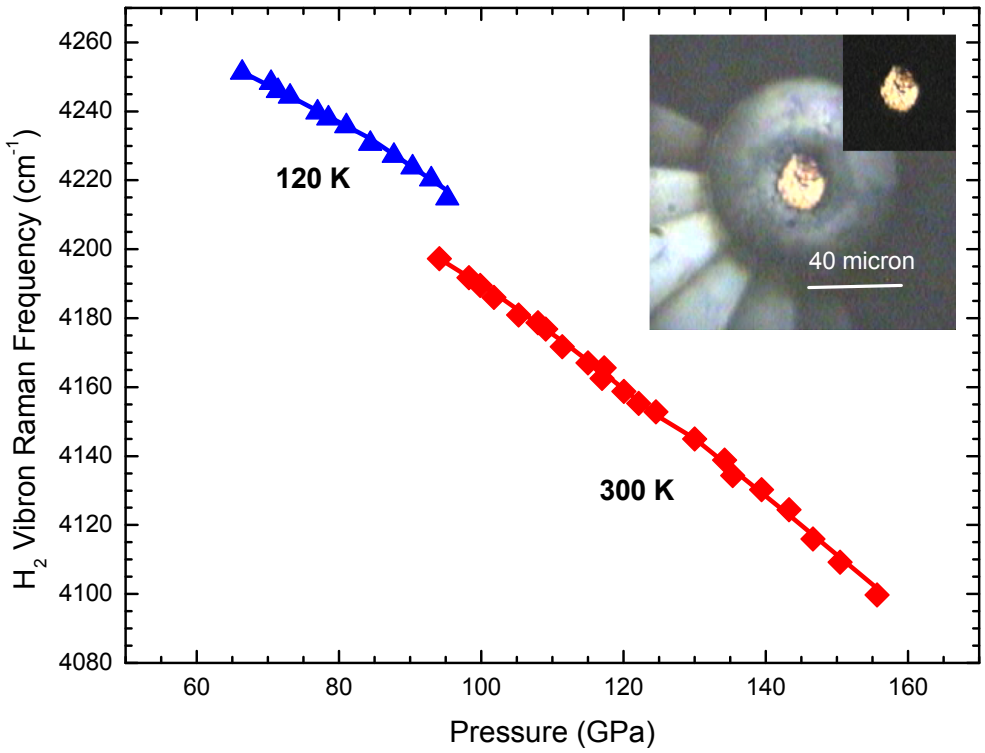

Figure 2.5: Pressure evolution of the frequency of the H_2 vibron with pressure. Symbols and lines represent measurements on the LiH part and the hydrogen part of the sample, respectively. Triangles and line (blue) show measurements at 120 K, while diamonds and line (red) represent measurements at room temperature. The inset shows the synthesized LiH sample in hydrogen media at a pressure of 155 GPa.

predicted formation of LiH_2, LiH_6 and LiH_8 [Zurek 09, Pickard 11, Howie 12b]. Up to pressures of 65 GPa, x-ray diffraction studies showed no structural change. Whilst using Raman spectroscopy up to the maximum pressure reached (160 GPa), only the ν_1 vibron of H_2 was observed in the Raman spectra and its frequency corresponded very well to the known value of pure H_2 at such conditions (see Fig. 2.5). No additional Raman lines or change of colour were detected that would be indicative of the predicted LiH_x compound [Howie 12b].

As such it remains that static studies of hydrogen in the high temperature regime are likely the most accessible pathways to obtaining a metallic solid state.

Chapter 3

A Review of Optical Spectroscopy at High Pressure

3.1 Raman Spectroscopy

The beginning of the 20^{th} century was characterized in physics by the development of the theory of quantum mechanics, which proved consequential in the understanding of the theory of light scattering. A theoretical study by Smekal postulated that the scattering of light by a system with two quantized energy levels contains not only photons with the incident-photon frequency, but also some with altered frequency [Smekal 23]. The actual experimental discovery of Raman scattering was made by two independent groups at the same time. Landsberg and Mandelstam discovered Raman scattering of light in crystals [Landsberg 58, Mandelstam 47], whilst C.V. Raman and K.S. Krishnan, who, guided in their studies in trying to discover the optical analogy of Compton scattering, observed Raman shifts in liquids [Raman 28a, Raman 28b]. Since then, formidable progress in Raman studies has been made. The invention of the laser and improvement of detection techniques simplified how Raman spectra were obtained and also led to discoveries of unknown effects, such as the resonance Raman effect and stimulated Raman effect. By now, Raman scattering in all three normal phases of matter is very well understood and documented [Anderson 71, Herzberg 60, Freeman 74, Hayes 78, Sherwood 72,

Iqbal 84, Ibach 90, Banwell 94].

Raman spectroscopy is a highly versatile tool used to provide a wealth of data that is both easy to obtain and quick to analyse. The Raman spectra can provide information on the elastic, vibrational, electronic, and magnetic properties of a material, through the analysis of the corresponding elementary excitations. Information on the crystal structure can be attained through the analysis of the Raman spectra of phonons. The Raman activity of phonons is highly dependent on vibrational selection rules, which, consequently, depends on both the symmetry and wave vector. Electronic and magnetic states can also be probed through their coupling to vibrational states and observations of electronic and magnetic excitations in the Raman spectra. As these elementary excitations are altered through the application of pressure, Raman spectroscopy is one of the primary diagnostics in high pressure science, used to measure changes in energy of vibrational excitations, phase transformations, chemical reactivity, and magnetic and electronic transitions.

3.1.1 Theory of Raman Spectroscopy

When a transparent gas, liquid or solid is illuminated with a beam of monochromatic radiation of frequency ν_S, most of the incident radiation is transmitted without change, while a small component is scattered. Spectral analysis of the scattered radiation shows that, in addition to scattering without a frequency change of the incident radiation (Rayleigh scattering), it contains discrete components of shifted frequency. Appearing in the spectrum, there are new additional pairs of spectral lines, positioned at symmetrical frequencies either side of the Rayleigh line, i.e.

$$\nu_S = \nu_0 \pm \nu_M, \tag{3.1}$$

where the frequency ν_M is an internal frequency corresponding to rotational, vibrational or electronic transitions within a molecule. In Raman scattering, the system is not excited for any measurable length of time to a higher energy level, but excited to a purely virtual state. Raman scattering is always accompanied

by Rayleigh scattering, with intensity usually 3-5 orders of magnitude greater. Rayleigh scattering itself is only approximately 10^{-4} 10^{-3} of the intensity of the incident excited radiation, thus Raman scattering is a comparatively weak effect. The components appearing in the scattered radiation spectrum at shifted frequencies are known as Raman lines or Raman bands and are collectively referred to as the Raman spectrum. The Raman lines at greater frequencies with respect to the Rayleigh line ($\nu_0 + \nu_M$) are referred to as anti-Stokes lines, whilst those appearing at lower frequencies ($\nu_0 - \nu_M$), as Stokes lines.

Raman scattering can be explained using two different approaches; a classical model and quantum mechanics. The classical model relates the interaction between light and matter to the polarization of the scattering medium. When an electric field is applied to a molecule, Coulombs Law infers that the electrons and nuclei respond by moving in opposite directions. The applied electric field thus induces a dipole moment in the molecule. This dipole moment, μ_{ind} is proportional to the applied electric field intensity, **E**:

$$\mu_{ind}(t) = \alpha \mathbf{E} \tag{3.2}$$

The proportionality constant, α, is defined as the polarizability constant and is characteristic of the molecules of the scattering medium. The variation of polarizability with respect to direction can be described as a tensor, which is explained in Appendix 1. The intensity of the scattered radiation is proportional to the magnitude squared of the induced oscillating dipole. If one considers the electric field intensity, **E**, of the incident electromagnetic wave varying as:

$$\boldsymbol{E} = \boldsymbol{E_0} cos(\omega_0 t), \tag{3.3}$$

where the induced dipole oscillates with angular frequency ω_0. By substituting (3.3) into (3.2), the equation for the induced dipole moment is obtained:

$$\mu_{ind}(t) = \alpha \boldsymbol{E_0} cos(\omega_0 t) \tag{3.4}$$

Considering a given internal motion within the molecule, modulating the

induced dipole moment, classically this infers that the polarizability has a constant term α_0 and a sinusoidal oscillating term with an amplitude α_1:

$$\alpha = \alpha_0 + \alpha_1 cos(\omega_M t) \tag{3.5}$$

Combining equations (3.4) and (3.5), an expression is derived for the induced dipole moment of the molecule vibrating with angular frequency ω_M, acted upon by an electromagnetic wave of angular frequency ω_0:

$$\mu_{ind}(t) = \alpha_0 \boldsymbol{E_0} cos(\omega_0 t) + \alpha_1 \boldsymbol{E_0} cos(\omega_0 t) cos(\omega_M t) \tag{3.6}$$

Using simple trigonometry, a generalised equation is derived for the induced dipole moment, for which angular frequencies ω_0 and ω_0 have been substituted for frequencies ν_0 and ν_M respectively:

$$\mu_{ind}(t) = \alpha_0 \boldsymbol{E_0} cos(2\pi\nu_0 t) + \frac{1}{2}\alpha_1 \boldsymbol{E_0}[cos(2\pi(\nu_0 - \nu_M)t) - cos(2\pi(\nu_0 + \nu_M)t)] \tag{3.7}$$

From the first term in (3.7), it can be seen that the scattered radiation contains an elastic contribution of ν_0; Rayleigh scattering. The second term indicates that the scattered radiation contains Raman bands with frequencies $\nu_0 \pm \nu_M$, corresponding to Raman Stokes scattering with energy $h(\nu_0 - \nu_M)$, and Raman anti-Stokes scattering with energy $h(\nu_0 + \nu_M)$.

From a quantum mechanical point of view, the Raman effect is an interaction between a molecule and a photon of light, with an energy lower than the energy difference between the first excited and ground states in the molecule (see Fig. 3.1). An incident photon of initial energy, hν_0, interacting with a molecule in the ground state, or an excited vibrational state, may excite the molecule to a higher energy level, or unstable virtual state. The molecule then may return to lower excited states in three possible ways:

- A molecule from the ground state returns to the ground state and the scattered photon inhibits the same energy as the incident photon (Rayleigh scattering).

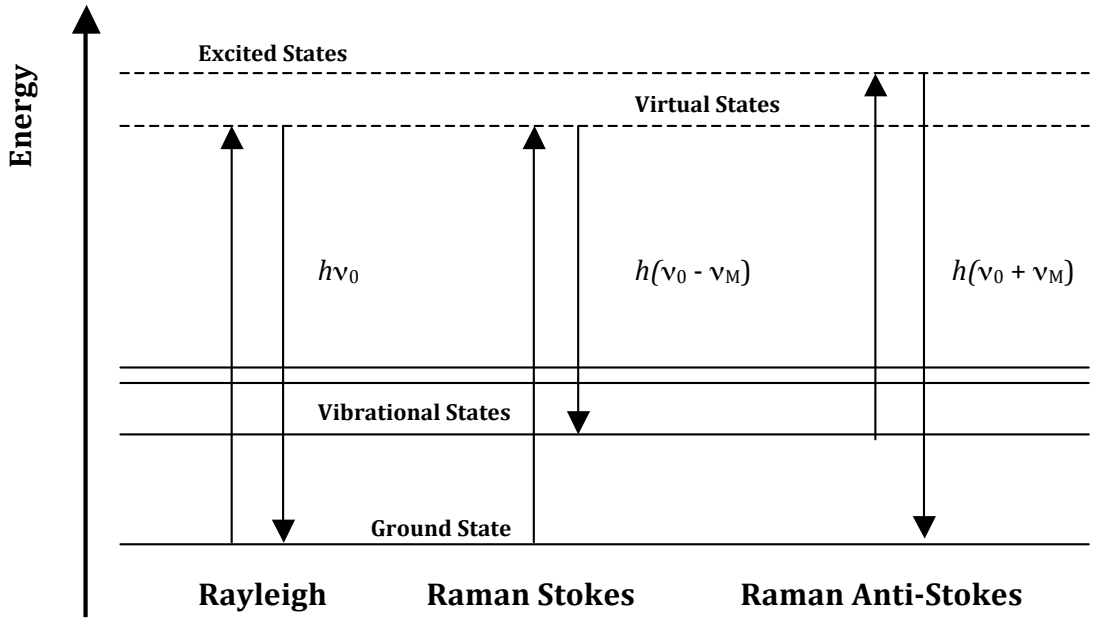

Figure 3.1: Energy-level diagram illustrating transitions corresponding to Rayleigh, Raman Stokes, and Raman anti-Stokes scattering

- A molecule from the ground state returns to an excited vibrational state, higher than the ground state. The energy of the scattered photon is thus equal to the energy of the incident photon, minus the difference in energy between the ground state and excited vibrational state. The energy of the scattered photon is therefore less than the incident photon (Raman Stokes scattering).
- A molecule from a vibrational excited state rises to a higher virtual energy level by interaction with the incident photon and returns to the ground state. The energy of the scattered photon is equal to the sum of the energy of the photon and the difference between the ground state and vibrational excited state. The energy of the scattered photon is therefore greater than incident photon (Raman anti-Stokes scattering).

The most pronounced difference between the classical and quantum models is that the quantum mechanical treatment of Raman scattering explains the difference between the relative intensities of Raman Stokes and Raman anti-Stokes scattering; the intensity ratio being dependent on both temperature and Raman mode frequency. Boltzmann's law infers that the population of molecules lies most prominently in the vibrational ground state. If one introduces a Boltzmann distribution of vibrational populations, it can be shown that the intensity ratio of Raman anti-Stokes to Stokes radiation is given by [Herzberg 60]:

$$\frac{I_{aSt}}{I_{St}} = \frac{(\nu_0 + \nu_M)^4}{(\nu_0 - \nu_M)^4} e^{\frac{-h\nu_M}{k_B T}} \tag{3.8}$$

where ν_0 and ν_M correspond to the frequencies of the incident radiation and the molecular vibration respectively, h is the Planck constant, k_B is the Boltzmann constant and T is the absolute temperature of the sample. Equation (3.8) can be rearranged and expanded giving;

$$ln(\frac{I_{aSt}}{I_{St}}) + \frac{h\nu_M}{k_B T} = ln(\frac{I_{aSt}}{I_{St}})_0 + \frac{h\nu_M}{k_B T_0} \tag{3.9}$$

where T_0 is ambient temperature and $ln(\frac{I_{aSt}}{I_{St}})_0$ is the Raman anti-Stokes to Stokes ratio at such temperature. Rearranging for temperature, T, gives;

$$T = \frac{\frac{h\nu_M}{k_B}}{ln(\frac{I_{aSt}}{I_{St}}) + ln(\frac{I_{aSt}}{I_{St}})_0 + \frac{h\nu_M}{k_B T_0}} \tag{3.10}$$

As the intensity ratio of the Stokes to anti-Stokes scattering is dependent on temperature, Raman spectroscopy can be used as a temperature gauge with systems with high intensity and relatively low frequency Raman excitations. As the intensity of the Raman anti-Stokes scattering increases with increasing temperature, this gauge is particularly suited to high temperature studies.

3.1.2 High Pressure Raman Setup

Raman spectroscopy is a fundamental technique for probing samples at high pressure, and as such, various setups have been reported [Goncharov 03, Goncharov 00].

There are several modifications needed to a typical Raman setup to accommodate the DAC interface. Firstly, in ultra-high pressure experiments, the probing depth must be considered, where samples may reduce to less than 10 μm in diameter, resulting in reduced signal intensity. The diamond windows, typically 2 mm in depth, result in geometric and chromatic aberrations, which can reduce the image quality, the signal-to-noise ratio and the selectivity of depth. Fluorescence in the laser beam originating from the diamond anvils also contribute to a higher background in the Raman spectra, requiring a high level of spatial filtering. These combined contributions require Raman setups to be custom built to address such issues.

All Raman setups follow the principal rule in minimizing the ratio of the input power from the excitation source to the Raman signal received at the spectrometer, whilst maximising the spatial filtering. Each setup has a high number of users, requiring optimum performance and, as a result, needs to be simple to align and easy to optimize. The Raman setup developed for the work contributing to this thesis has 180° backscattering geometry and is illustrated in Fig. 3.2.

Argon-ion lasers of excitation lines 514 nm and and Krypton-ion laser of 647 nm are used. The excitation lasers initially need to be filtered of any wavelengths

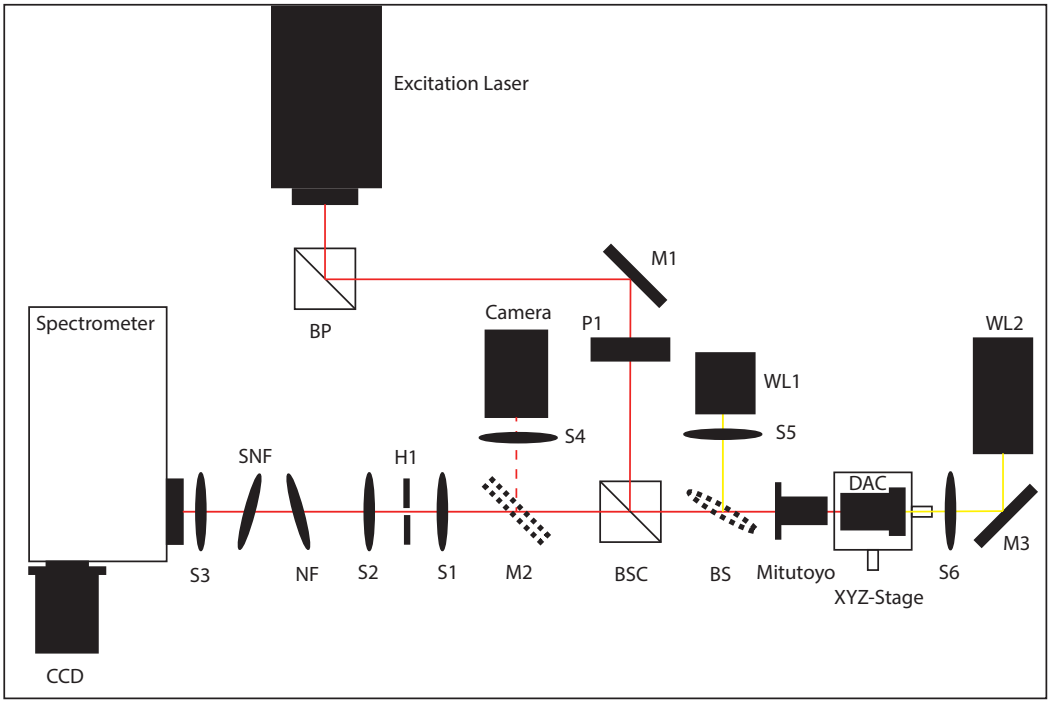

Figure 3.2: Diagram of the high pressure Raman setup. BP is the band pass filter, M1-M3 are mirrors, P1 is a periscope comprising of two mirrors, S1-S6 are plano-convex spherical lenses, BSC is a 50:50 beam splitter cube, BS is the beam splitter for reflected light, SNF and NF are SuperNotch and notch filters respectively, and WL1-2 are white light sources.

emitted outwith the desired excitation line, using a band pass filter (BP). The grating of the band pass filter emits the filtered laser light at 90° relative to the incident light and typically reduces the incident laser power by 2%. High reflectance silver mirrors typically reflect 98% of incident light, however this can dramatically reduce if not cleaned regularly. As such, we used the minimal number of mirrors that are involved in collecting Raman spectra; 1 used to redirect the incident beam (M1) and 2 used as a periscope (P1) to raise the height of the beam. After the periscope, the beam follows a 'T' path; adopting this alignment greatly reduces the time required for realignment. At the intersection of the 'T' is a 50:50 beam splitter cube (BSC), directing the incident beam towards the sample. The beam is then focussed with a Mitutoyo infinity-corrected long working distance objective lens onto the sample. Objective lenses with long working distances are required due to the restricted geometry of the DAC.

The scattered light then follows the same path, passing through the beam splitter cube towards the spectrometer. The beam passes through a spatial filter, comprising of two plano-convex spherical lenses (S1 and S2) of 50 mm focal length and pinhole (H1), with diameter corresponding to the diameter of the excitation laser. The pinhole is placed at the focal point of both lenses, the first lens (S1) focuses the laser onto the pinhole, whilst the second lens (S2) collimates the beam. Both the lenses and pinhole can be adjusted in all x-y-z directions, which is required for optimization of the setup. The use of the pinhole both attenuates undesired elastically scattered laser radiation and makes the depth of focus smaller. By probing a narrower depth of sample, the fluorescence from the diamond is also substantially reduced.

After spatial filtering, the beam passes through both notch (NF) and SuperNotch (SNF) holographic filters, which are used to minimise the Rayleigh scattering from the sample. The notch filters can be adjusted to measure close to the Rayleigh line, however, at the expense of minimising the intensity of the Rayleigh signal. A final lens (S3), with focal length 75 mm, is used to focus the laser light onto the entrance slit of the spectrometer. In all Raman setups, a single grating Acton SpectraPro 2500i spectrograph is used coupled with an 1840 x 1840 Acton CCD.

The sample is imaged using a mirror M2 on a flip mount, directing the image

towards the video camera ccd and focussed with lens S4. WL1 provides a source for reflected light which is focussed using lens S5 and directed to the Mitutoyo objective lens using a second beam splitter (BS). Transmitted light is provided by either a standard LED white light source or a supercontinuum laser (WL2), which is directed towards the sample with mirror M3 and focussed using lens S6. With the removal of the notch filters, the setup allows easily for the acquirement of the sample transmission spectrum.

3.2 Pressure Calibrants

The pressure boundary at which the diamond anvil cell can reach is continuously being pushed to beyond 300 GPa and, as such, it is imperative to have an accurate pressure gauge to probe such conditions. The most common pressure determination method in high pressure physics is the ruby fluorescence technique. When a chip of ruby, Cr^{3+} doped Al_2O_3, is illuminated by focussed laser light, it will fluoresce. This process produces an intense fluorescence doublet, R_1 and R_2, with wavelengths of 692.7 nm and 694.2 nm at ambient pressures respectively. The pressure dependence of Ruby has been calibrated extensively up to 100 GPa. Up to 29 GPa, the R_2 line is approximately linear [Piermarini 75], and follows the relation

$$P = A\delta\lambda \tag{3.11}$$

where P is the pressure in GPa, $\delta\lambda$ is the shift of the R_2 fluorescence line from ambient pressure (694.2 nm), and the constant of proportionality A is given as 0.0274 GPa nm^{-1}. It was subsequently observed by Mao *et. al.* that the shift of R_2 fluorescence line is non-linear at pressures beyond 29 GPa [Mao 78], and the proposed relation is given as;

$$P = 380.8[(\frac{\delta\lambda}{694.2})^5 - 1] \tag{3.12}$$

Ruby fluorescence is also sensitive to the hydrostaticity of the sample. As pressure is increased, the hydrostaticity of the sample reduces, resulting in

broadening of the R_1 and R_2 lines. At pressures higher than 100 GPa, the fluorescence intensity is significantly reduced and the fluorescence lines broaden to the extent that a definitive pressure is undistinguishable.

Above 100 GPa, pressure is often determined from the equation of state (EOS) of noble metal standards, a grain of which is present in the sample. Due to the dimensions of the sample involved at such high pressures, a synchrotron radiation source must be used to measure the compression data of the pressure gauge. In addition, the high pressure chemistry of the sample must be considered using such method, particularly with reactive elements, such as hydrogen.

Due to the low Z number, and consequently low x-ray scattering cross section, studies of H_2 in the megabar regime rely almost solely on optical measurements in determining phase transitions. Samples sizes at such pressures are typically between 1-10 μm, which further restricts the probing method.

In Raman spectroscopy studies, the first-order T_2g Raman mode of diamond is commonly used as a pressure gauge and, in some optical experiments, particularly at multimegabar pressures, the sole means of pressure determination. This method can allow both the probing of the sample and determination of pressure in a single optical measurement. This is of particular advantage when working with samples of hydrogen above pressures of 150 GPa, as it is well known that over exposure of the sample to laser light exacerbates hydrogen diffusion into the diamonds, enhancing the probability of anvil failure [Mao 94].

Diamond was first calibrated as a pressure gauge by Hanfland and Syassen to 30 GPa, where they found that the high-frequency edge of the T_2g Raman band was associated with the stress of the (100) diamond culet face of the diamond and had a linear dependence with pressure [Hanfland 85]. Subsequently, the calibration curve has been studied into the multi-megabar pressure regime and found to no longer follow a linear dependence [Akahama 06, Akahama 10b, Occelli 03]. However, it is apparent through the lack of consistency with results that the determination of pressure using this technique is dependent on many factors. Firstly, the spatial resolution of the Raman setup ultimately affects the probing area and at high pressures the diamonds exhibit large pressure gradients across the culets. It was found, due to the uniaxial strain in the diamond anvils during compression, that the exact frequency shift depended on both the culet

size and sample geometry [Baer 08]. However, more importantly this pressure calibrant is dependent on the sample type. In the work by Akhama *et. al.*, this method has been reportedly calibrated up to pressures of 410 GPa, using the Pt EOS [Akahama 06, Akahama 10b]. The following expression was found to be a "satisfactory" least-squares fit allowing a 3% error in their calculated pressure values;

$$P = A\frac{\delta\omega}{\omega_0}[1 + \frac{1}{2}(B-1)\frac{\delta\omega}{\omega_0}] \tag{3.13}$$

where pressure P is in GPa, ω_0 is the edge frequency at ambient pressures (1333 cm^{-1}, A and B are frequency constants of value 547 GPa and 3.7 GPa respectively. Above 200 GPa, the authors found that a quadratic expression was a better fit to the observed data, particularly at pressures exceeding 300 GPa.

The work by Akahama *et. al.*, remains the highest pressure study calibrating the diamond Raman edge to pressure, and as such, the expression (3.13) was used to calculate pressure above 100 GPa in this thesis. However, the samples used in the study by Akahama *et. al.*, were elemental Sc, Al, Mo, Ni; materials with much lower compressibility than the lighter solid molecular systems (e.g. H_2, N_2, O_2). Due to the large differential between compressibilities of the materials used in the work by Akahama et al., and solid molecular systems, the universality of such pressure calibration is questionable.

Figure 1a shows our Raman spectra of the stressed diamond edge to frequencies up to 1842 cm^{-1} with an H_2 sample, which according to the pressure scale proposed by Akahama et al., [Akahama 10b], would be 318 GPa. At the maximum pressure, the diamond Raman edge is much sharper and more resolvable than that presented in the work by Akahama et al., [Akahama 06, Akahama 10b]. This difference is most likely due partly in probing highly compressible optically transparent samples, compared with the high bulk metals in Refs. [Akahama 06, Akahama 10b]. Fig. 3.3, also shows the diamond Raman edge on cooling, where despite reducing by half in intensity, remains sharp and well defined.

In the low temperature study of H_2 by Loubeyre et al., [Loubeyre 02], a Raman spectrum of diamond is presented, where the phonon frequency of 1783 cm^{-1}

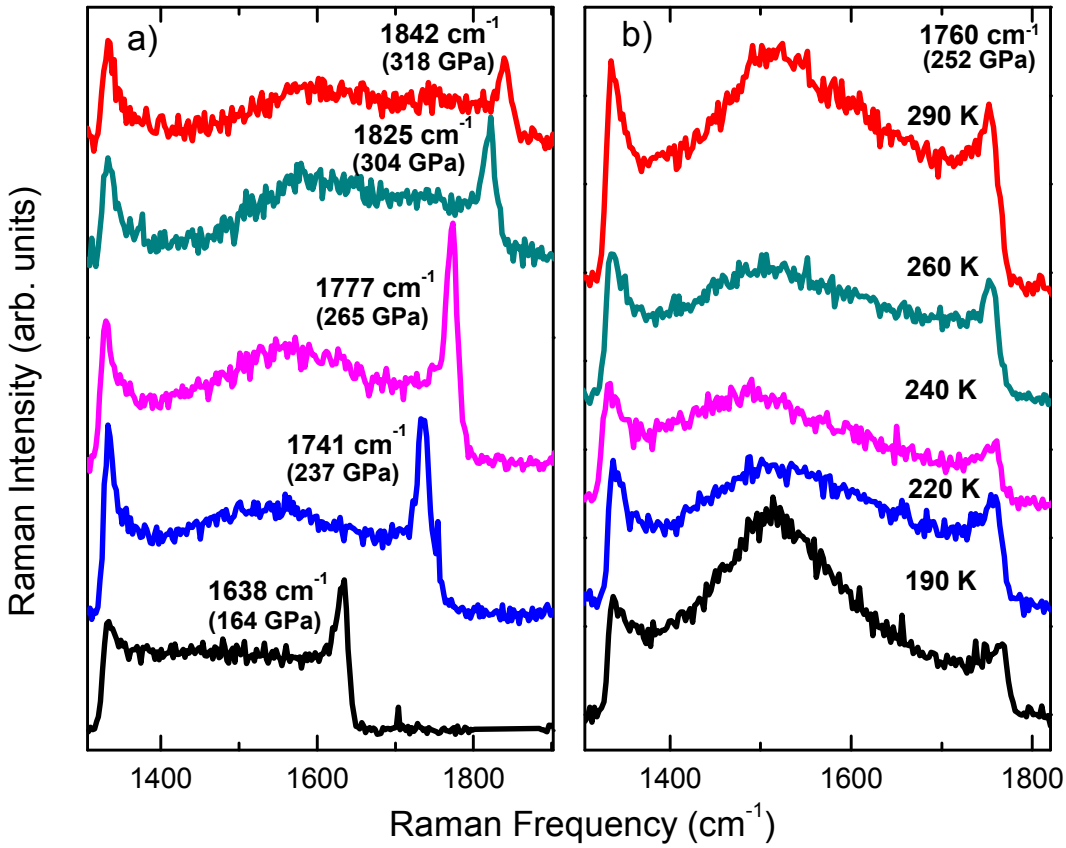

Figure 3.3: Representative Raman spectra showing the diamond Raman edge on compression of H_2 to 318 GPa (calculated using Ref. [Akahama 10b]). (b) Representative Raman spectra showing the diamond Raman edge upon a cooling cycle of D_2.

is used "as the ultra-high pressure gauge under a Gruneisen expansion form to second order with the equation of state of diamond", giving pressures of 290 GPa. According to the work by Akahama et al., [Akahama 10b], the pressures claimed using this method are overestimated by at least 20 GPa. This is contrary to their estimated pressure error of 3 GPa, which when converted to diamond edge frequency, using Ref. [Akahama 10b] is approximately 4 cm^{-1}, a third of their reported diamond edge width.

It is apparent that pressure determination through the first-order Raman spectra of diamond anvils used in high pressure cells is both sample and geometry dependent, and thus cannot be used as a definitive pressure gauge. This poses a major problem when comparing conditions at which phase transitions occur in experiments above 100 GPa. How this problem affects the recent studies of hydrogen [Eremets 11, Howie 12a] will be discussed later in Chapter 4.

Chapter 4

Technical Developments

4.1 The Diamond Anvil Cell

Pressure is a vital thermodynamical variable with diamond anvil cells as the primary apparatus to investigate material properties at static high pressure. The DAC design is based on the opposed anvil principle, developed by Percy W. Bridgman in the early 1900's, with the main difference being that the tungsten carbide anvils used in the Bridgman press were replaced by flawless single crystal diamonds. Pressure is simply force divided by area and great pressures can be achieved by applying a large load on anvils with very small tips, so long as the anvil material can withstand the exerted pressure. Static pressures exceeding 100 GPa were first attained by Mao and Bell in 1976, using the Mao-Bell diamond anvil cell and subsequent variations allowed multimegabar conditions to be reached routinely [Mao 76, Bell 84, Jayaraman 83, Xu 86]. The extreme hardness of diamond enables the generation of static pressures exceeding 300 GPa and the transparency to a wide range of electromagnetic radiation, from high energy x-rays to low energy ultraviolet-visible-infrared radiation, allows a range of *in-situ* experimental probes. To apply pressure to a confined sample, a metallic gasket is used, which is typically a high bulk modulus material, such as rhenium or tungsten. The anvils exert pressure on this gasket, in which a circular sample chamber is confined centred on each anvil. As pressure is exerted beyond the yield strength of the gasket material, the ductile flow of the gasket material

exerts pressure on the sample. The ductile flow ceases when the gasket becomes thin enough to reach mechanical equilibrium through a gradient of pressures supporting the sample chamber.

4.1.1 DAC Preparation

A modified Mao-Bell cell has been used in the work contributing to this thesis and is illustrated in Fig. 4.1. It was found that the alignment of diamonds with culets under 30 μm required less time with tight fitting piston-cylinder type diamond anvil cells compared with other DAC designs. Molykote ball bearing grease was used to lubricate the piston, enhancing the fit of the cell. This procedure allowed diamonds to be aligned within 1 micron after a single gasket indentation to 40 GPa. Reducing the number of indentations minimises the risk of fine 'ring' cracks around the diamond culets, which are often observed after numerous indents. This simple improvement meant that a cell could be prepared and loaded within two working days.

In this work both type Ia Boehler-Almax design and type Ia modified brilliant-cut diamonds were used. The geometry of the diamond cut is an important consideration in actually reaching multi-megabar conditions. Culet diameters ranged from 12 μm to 40 μm and the difference in diameter of each pair did not exceed more than 10 μm. In various experiments, single, double and triple bevelled diamonds were used. It was found that only the triple bevelled diamonds consistently reached pressures above 290 GPa. All diamonds were ultra low fluorescence, an important characteristic to maximise the signal-to-noise ratio of the Raman spectra. Diamonds were glued to tungsten carbide seats with Stycast epoxy. The openings of each seat were chosen, considering the geometry of the complete DAC assembly, so that the excitation laser or transmission light would not be cut when focussed on the sample.

To contain such a light and reactive element such as hydrogen at multimegabar conditions, both the selection of the gasket material and the way in which the gasket is prepared is imperative for the success of an experiment. Firstly, the chemistry between the gasket material and H_2 has to be considered. While many metals are known to react readily with hydrogen, most transition metals between

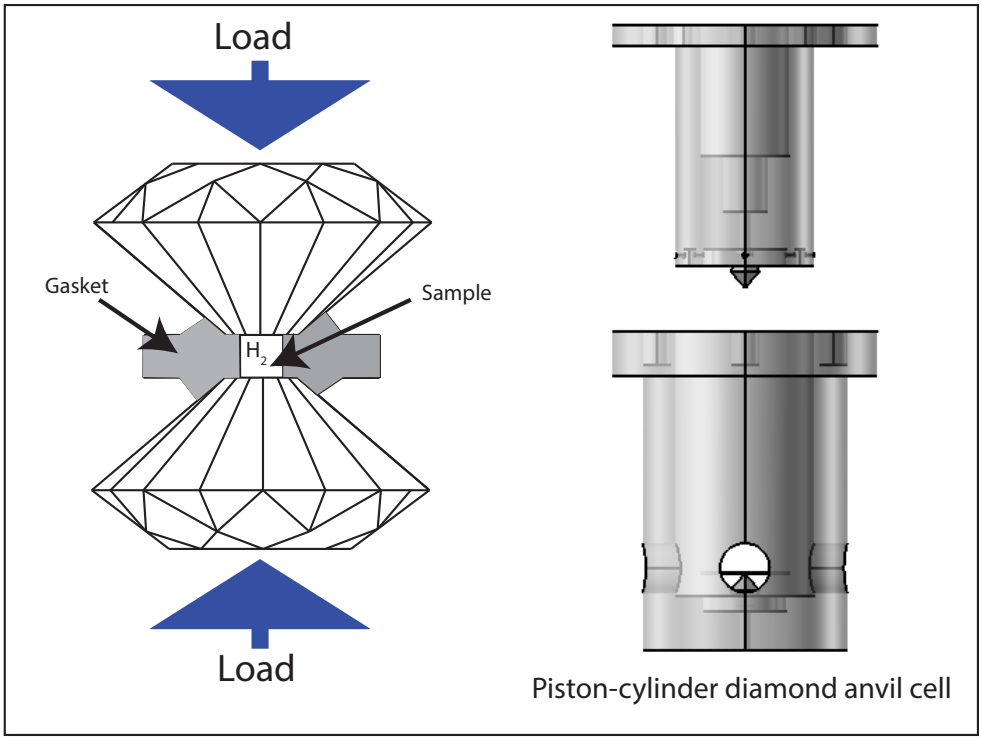

Figure 4.1: Left: Standard diamond anvil cell schematics. Right: Diagram of the modified piston-cylinder diamond anvil cell used in the multi-megabar experiments.

periodic table groups 6 and 11 do not and often both high temperature and high pressure are required for synthesis [Antonov 02]. However, recently there has been much attention on the formation of transition metal hydrides with high pressure alone [Scheler 11b, Scheler 13, Scheler 11a]. Of particular interest is the formation of rhenium hydride and tungsten hydride, since both rhenium and tungsten are used in this study and are common gasket materials. Rhenium hydride is a well studied material and forms from its pure constituents above 5 GPa at room temperature. In a recent study, it was found the the solubility of hydrogen in rhenium hydride increases both with pressure and time approaching the stoichiometric composition of Re_2H. If high temperature is applied, rhenium hydride undergoes a phase transition to the ϵ_2 phase, which has significantly higher hydrogen solubility. This may have an effect on maintaining a sample in high temperature (e.g. 300 K) studies of hydrogen. Due to the formation of rhenium hydride, the bulk properties of the gasket changes, which may affect the maximum pressures that can be reached and the stability of the sample chamber, which will be discussed later. The formation of rhenium hydride was clearly observed around the sample in all experiments where rhenium was used as a gasket. As a precautionary measure, sample spectra were taken on the rhenium gasket, and on the formed rhenium hydride, to ensure the observed spectra of the sample originated from the sample itself.

Although tungsten has a lower bulk modulus than rhenium and its brittleness causes complications in gasket preparation, it does, however, react with hydrogen at much higher pressure (25 GPa), which may reduce sample loss even at higher pressure [Scheler 13]. In an experimental control run using tungsten as the gasket material, the same sample chamber instabilities were observed as those observed in rhenium. Again, the the bulk properties of the gasket material surrounding the sample may change upon the hydrogenation of tungsten and compromise the stability of the sample chamber. Future studies may benefit from using a gasket material that does not form a hydride.

A major improvement to previous experimental techniques was the application of a focussed ion beam (FIB) to drill the sample chamber as opposed to the more common laser drilling or spark erosion techniques. Laser drilling uses an infra-red laser to ablate the surface of the gasket material, causing extensive infra-red damage, which affects a greater ratio of material when working with culets below

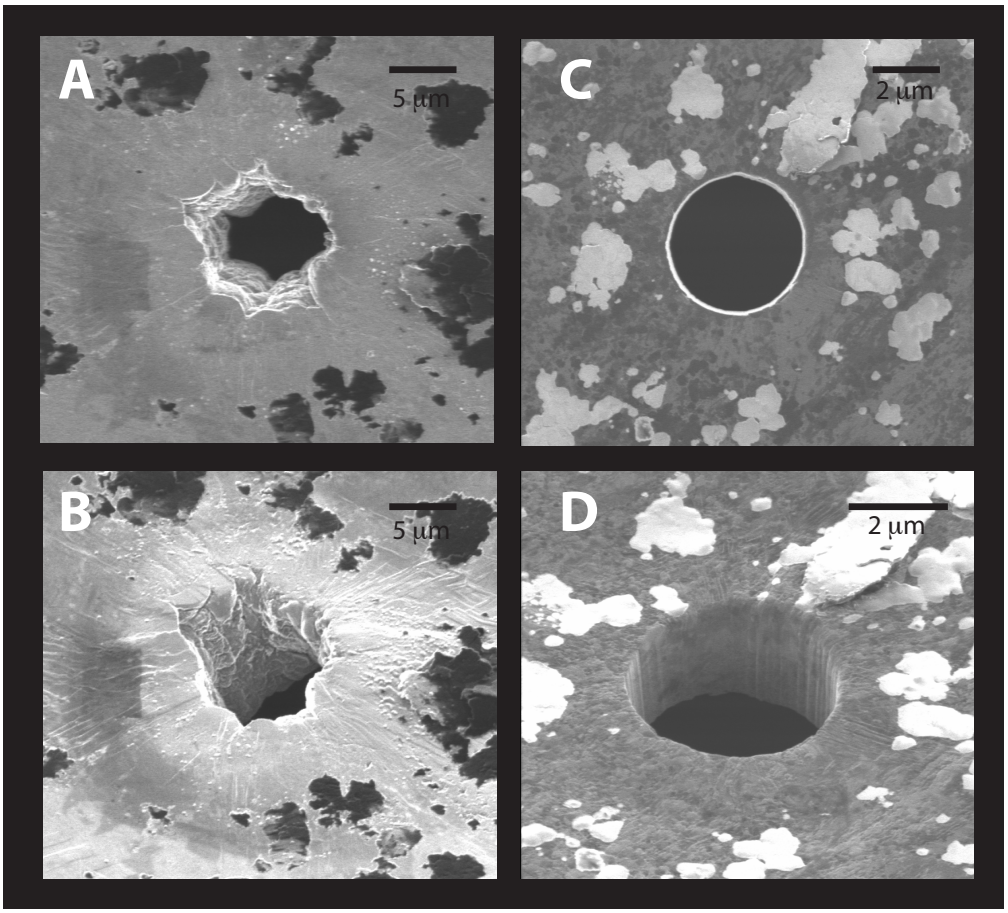

Figure 4.2: Scanning ion micrographs of a laser drilled gasket hole from directly above (A) and from a 45° angle and scanning ion micrographs of an ion-milled gasket hole from directly above (C) and from a 45° angle (D).

20 μm. Although the infra-red damage can be avoided using spark erosion, drilling a sample chamber centred accurately on a micron scale can be problematic. In addition, the size of the sample chamber is limited to either the beam profile in laser drilling or the needle size in spark erosion.

FIB systems work in the same way as scanning electron microscopes (SEM), but use ions from a liquid metal ion source, instead of accelerated electrons. The ions are extracted by field emission from a droplet of supercooled metal in the source and accelerated to 50 keV. FIB systems have many applications, such as imaging over sputtering (which can also be used for milling) and the deposition of metallic films [Reyntjens 01, Volkert 01, Gierak 09]. The use of FIB milling to drill DAC gaskets has been previously reported in [Orloff 00] and was claimed to have helped in reaching high pressure on H_2 [Narayana 98] at 300 K. However, the claims of reaching such pressure with H_2 has been criticised, as no physical property of H_2 was measured. Nevertheless, sample chambers drilled with a FIB system are of superior quality, compared with any other drilling methods. Figure 4.2 shows secondary electron FIB images of gasket holes drilled into rhenium, demonstrating the differences between using laser drilling and FIB milling. All complications ascribed to laser and spark erosion drilling are resolved using FIB milling, whereby holes are drilled cleanly with sub-micron precision. In a study of lithium, the diffusion of lithium into the diamonds at room temperature (a similar process observed with hydrogen) was reduced by using small gasket holes [Guillaume 11]. In this thesis, the smallest possible sample chamber was drilled to minimise the area of contact between the sample and diamond. Such sample chambers could only be drilled with such precision using a FIB system.

The samples were loaded into the DAC using a high pressure gas loading technique. The gas loading setup is a modified design of that reported by Mills *et. al.* [Mills 80]. The DAC is initially open, and placed in a high pressure vessel. 99.9% purity hydrogen (deuterium) is pressurised to 2000 bar in the vessel, using a two stage compressor (the first stage of the compressor feeds the second stage with a gas pressure of 200 bar). Once pressurised, the DAC is closed through a gear system, clamping the sample. Typically, the cell is calibrated to compress the sample to 1 GPa while in the gas loader, to ensure the success of loading. At 1 GPa, $H_2(D_2)$ is in the fluid state and the Raman spectra clearly shows the sharp, well-defined rotons and intense vibron.

4.2 Low Temperature Equipment

4.2.1 Cryostat

A cryostat, based on a modifed Oxford Instruments OptistatCF-V cooling tail, has been developed during the course of this work to allow a variety of DACs to be cooled to low temperatures. Piston cylinder cells have not been loaded into the existing cryostat due to its length prohibiting it to be placed within the cryostat. The original method, for smaller cells, involved securing the cell into a sample holder fixed to the cryostat tail, then lowered into the radiation shield. The sample holder was modified with a detachable thread that allowed a cell, enclosed in a mating threaded cup, to be screwed in via the radiation shield windows. This solution not only allowed the cell to be held in place but also allowed the distance between the window and cell to be varied. This distance is vital in allowing the sample to be both brought into focus and separated from the window adequately to reduce the build up of snow, which distorts the sample image. The existing cryostat radiation shield was not designed initially to use piston-cylinder cells, resulting in a compromise whereby, in bringing the sample into focus, the position of the DAC leads to an increased distance between the sample and point of cooling. This results in an increase in the achievable minimum temperature and an increased cooling/warming time.

To achieve low temperatures, the cryostat must be held under ultra-high vacuum when cooling, using a vacuum pump. When obtaining Raman spectroscopic measurements, it is imperative that the sample is held stationary in order to obtain reliable spectra. As samples are of the scale of 2 μm -10 μm, the slightest vibration can misalign the probing laser from the sample during measurements. To minimise vibrations from the vacuum pump, a braided rubber pvc alloy hose was used to connect the vacuum pump to the cryostat. The hose maintains its dexterity under vacuum and allows the cryostat to be pumped to high vacuum.

The previous design of the cryostat tail incorporates a Rh-Fe thermoresistor at the top of the sample holder, which is the first point of contact between the liquid nitrogen and the sample holder. This point is cooled at a faster rate than the outer body of the DAC, resulting in drastically inaccurate sample temperature measurements. A CLTS temperature sensor has been added to the cryostat,

which is attached close to the back diamond of the DAC each time a sample is to be cooled, enabling accurate temperature measurements. A second heater has been added to allow the sample to be rapidly heated from both above and below the cell.

4.2.2 Testing the cryostat: Measurements on dense sodium

The vibrational Raman spectroscopy of metals at high pressures is not widely used due to several limiting factors. These include the strong background from the sample environment and experimental difficulties associated with the usually weak scattering. Due to the lack of first order Raman activity in the metals of cubic symmetry, such as Na below 100 GPa, Raman spectroscopy cannot provide much information. However, the appearance of complex, low symmetry structures in Na give rise to Raman activity, opening a window of opportunity to study properties such as vibrational dynamics and/or chemical bonding [Marques 11, Ma 09].

Above 100 GPa, Na adopts the *cI16* structure. Group theory analysis predicts 5 Raman active bands of which only an unresolved Raman doublet is observed [Marques 11]. At 118 GPa, there is a significant redistribution of the electronic charges entering the *oP8* phase, resulting in the emergence of a new Raman band with additional high frequency modes [Gregoryanz 08, Marques 11]. At pressures above 127 GPa, Na transforms to the host-guest incommensurate *tI19* phase, which has been shown to exhibit a significant reduction in reflectivity [Lundegaard 09, Lazicki 09]. All 8 Raman active modes in the *tI19* phase originate from the host structure, as the guest structure has only one atom per unit cell therefore will exhibit no Raman activity. At pressures of 178 GPa, Na transforms from the metallic *tI19* structure to to a completely transparent insulating *hP4* structure with one very intense Raman mode at 350 cm^{-1}. Such a dramatic change in the optical properties indicate profound alterations in the electronic structure and bonding. This transition is quite remarkable, as the alkali metals have always been regarded as 'ideal metals'. In addition, analogies were often made between the light alkali metals and the predicted metallic state of hydrogen [Ashcroft 68], however at comparable pressures this may no longer be applicable.

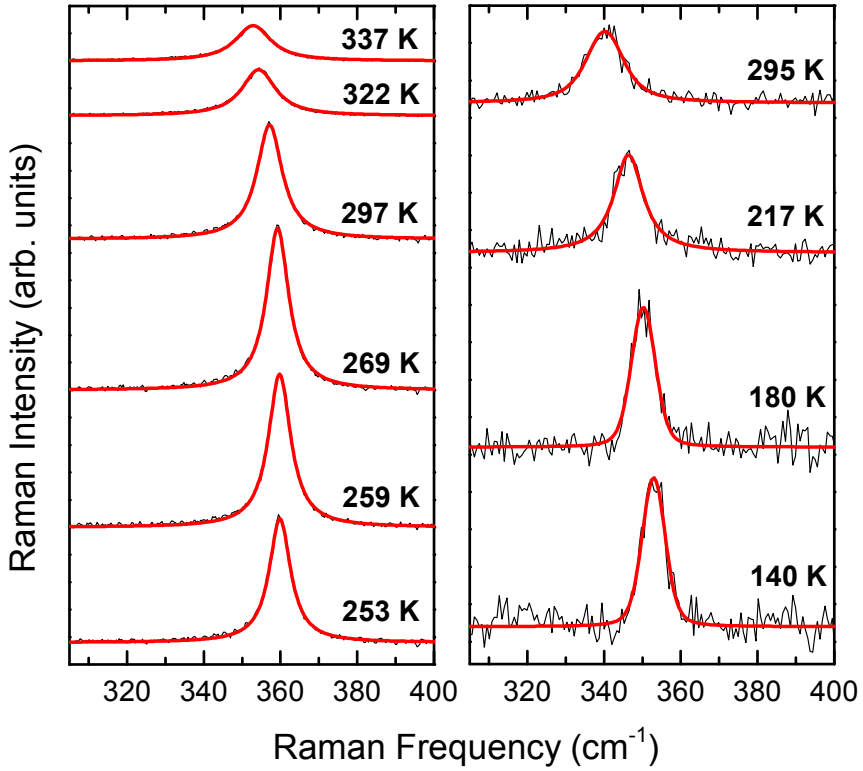

Figure 4.3: Left: Temperature dependence of the E_{2g} mode at 180 GPa (right) and 190 GPa (left).

The *hP4* phase has been shown to be stable up to 218 GPa at room temperature and the single observable Raman mode has been observed to increase in frequency with pressure [Ma 09]. However, the behaviour of the *hP4* Raman mode with temperature is unknown and knowledge of this is vital in the understanding of the stability of the phase in P-T space. Several cooling and heating cycles of dense sodium were performed between 140 to 200 GPa, covering the *tI19* to *hP4* transition. This experiment not only provided an insight into the behaviour of Na-*hP4* phase, but allowed an opportunity to test the capabilities of the cryostat.

At 140 GPa (Na-*tI19*), the sample was heated to a temperature of 550 K and showed no observable melting. This indicates that that the melting temperature must steeply rise with pressure after the melting minima (see Fig. 4.4), reaching values of its maximum in the *bcc* phase (∼1000 K).

At a pressure of 179 GPa, the sample transformed from the *tI19* phase to the *hP4* phase and remained stable to 200 GPa at room temperature, in agreement with the previous study by Ma *et. al.* [Ma 09]. The sample of Na-*hP4* was then cooled to 138 K in 4 pressure intervals on decompression. At 190 GPa, the sample was also heated to 337 K using an external resistance heater. Throughout these temperature cycles, the sample remained optically transparent and the *hP4* Raman mode was sharp and well defined. Fig. 4.3 shows the temperature dependence of the *hP4* Raman mode at 190 GPa and 200 GPa.

The experimentally observed *hP4* Raman mode is of E_{2g} symmetry and correlates with a transverse acoustic phonon. Thus, its frequency shift provides information on the C_{44} elastic constant, which represents the slope of the branch at the centre of the brillouin zone. C_{44} can be estimated from the frequency shift of the E_{2g} mode using the following relation derived from a three body force model for an hexagonal solid with a non-ideal c/a ratio [Upadhyaya 94]:

$$C_{44} = 2\pi^2 M(\frac{\sqrt{3}c}{6a^2})\nu^2, \tag{4.1}$$

where M is the atomic mass, a and c are the measured lattice constants, and ν is the Raman frequency of the E_{2g} mode. The values of C_{44} at 190 GPa, as estimated from the frequency of the E_{2g} mode (120 GPa), and from first principles

calculations (129 GPa) are in very good agreement. One of the shear moduli of an hexagonal media is given by the expression:

$$G=2C_{44}+C_{66} \tag{4.2}$$

The calculations for C_{66} give a value of approximately 40 GPa, showing that the shear modulus of Na-*hP4* is mostly driven by C_{44} [Marques 11]. The measured temperature dependence of the E_{2g} mode at 190 GPa is $\sim$0.2 cm^{-1}/K. This measurement indicates that quite high temperatures are needed to substantially decrease G and thus melt Na-*hP4*. Approximating the point of melting when G$\rightarrow$0, the melting temperatures would reach almost 2000 K at $\sim$190 GPa. The revised phase diagram of Na is illustrated in Fig. 4.4. Previous melting points [Gregoryanz 05] lying below the maximum at 31 GPa have been extrapolated with the Simon-Glatzel law; a relation extensively used for many melting lines [Gregoryanz 03]. Interestingly, the estimates of melting using the temperature dependence of the E_{2g} mode are in some agreement with the extrapolation of the Simon-Glatzel melting line.

On releasing pressure to 175 GPa, a significant reduction in the intensity of the *hP4* Raman mode was observed. After leaving the sample for a period of 24 hours, the *hP4* mode disappeared entirely, replaced by a Raman mode at $\sim$ 160 cm^{-1}, indicating a complete transformation to the *tI19* phase. At this pressure of 175 GPa, the sample was heated to 500 K, showing no transition back to the *hP4* phase. Pressure was increased further to 178 GPa and a cooling cycle performed to 140 K. Although no complete transformation was observed, the Raman mode of the *tI19* phase was observed to drop in intensity as temperature decreased, which could be interpreted as the onset to Na-*hP4*. Nevertheless, these measurements indicate that the Na-*tI19* to Na-*hP4* phase boundary must be vertical or near-vertical (see Fig. 4.4).

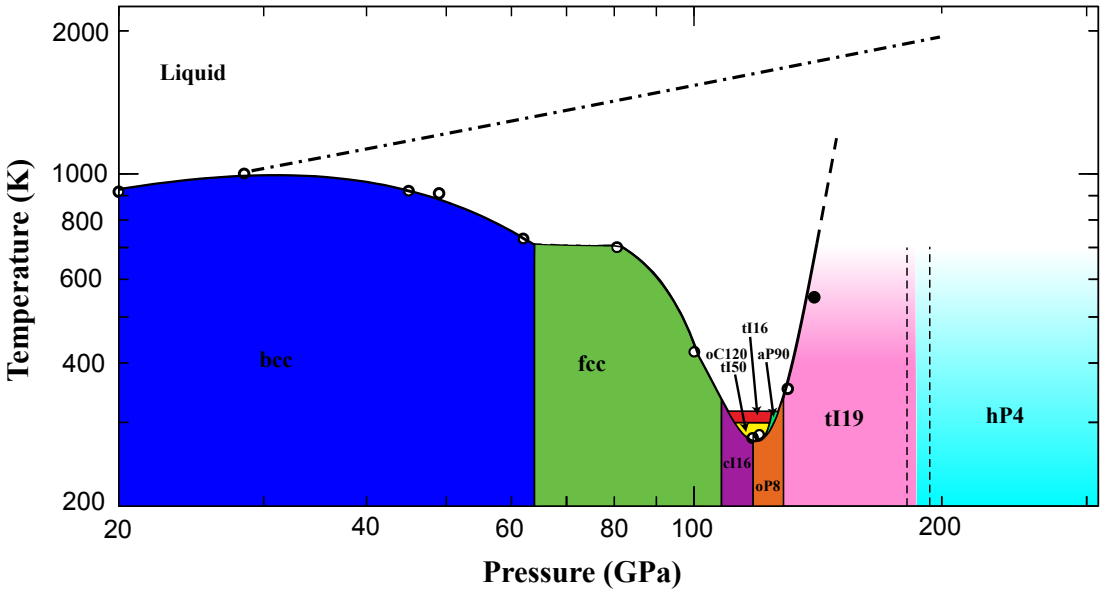

Figure 4.4: Na phase diagram. The lower-pressure region, shown in open circles, is adapted from [Gregoryanz 08] and [Gregoryanz 05]. The solid circle is a measurement in this study. The dot-dashed line shows the extrapolation of the melting curve from 30 GPa with the Simon-Glatzel empirical law. Dashed lines between *tI19* and *hP4* represent hysteresis of the phase transition: the higher pressure phase line represents a phase change on increasing pressure, whilst the lower represents a phase change on decompression.

Chapter 5

Multi-megabar room temperature compressions of H_2 and D_2

5.1 Introduction

By combining all of the experimental improvements discussed in the previous chapters, the first set of experiments compressed H_2 and D_2 at room temperature, reaching pressures of 318 GPa and 275 GPa respectively, conditions previously thought to be inaccessible. Raman spectroscopy was used, both to measure pressure and to determine the bonding characteristics of H_2 (D_2). Both 514 nm Ar^+ and 647 nm Kr^+ ion excitation wavelengths were used for Raman measurements, up to pressures of 200 GPa. Above 200 GPa, only the 647 nm excitation line was used to minimise the pressure-induced background fluorescence from the diamond anvils. Raman spectra were collected with 3s exposure time with a laser power of 40 mW. Visible transmission spectroscopy was measured, using a white light source in the collection region of 400 nm to 900 nm to estimate the direct band-gap of the sample. The pressure of the samples below 90 GPa were initially measured with the frequency of the $H_2(D_2)$ main fundamental vibrational mode (ν_1), that was pre-calibrated to the ruby standard in a separate loading. Above 90 GPa, pressure was measured with the frequency of the stressed diamond

edge and calibrated using the scale reported in [Akahama 10b].

5.2 Phase I-III Transition at Room Temperature

At the solidification point to phase I at 5.5 GPa, the rotons are observed to broaden significantly compared with the liquid state, whilst the ν_1 vibron increases in intensity. On further compression above 100 GPa, the low energy Raman bands below frequencies of 1000 cm^{-1}, which consist of rotons and librons, broaden and decrease in intensity with pressure (see Fig. 5.1). Up to 180 GPa, the ν_1 vibron frequency is observed to shift with pressure, in good agreement with previous studies [Goncharov 11].

Above 190 GPa in H_2 and 185 GPa in D_2, we observe the emergence of a relatively intense broad band at 500 cm^{-1}. This low energy band is similar to a band at 450 cm^{-1} that was observed in phase III of H_2 (H_2-III) at 178 GPa and at a temperature of 18 K [Goncharov 98]. In H_2, the new Raman band is accompanied by the change of slope of ν_1 from -3 cm^{-1}/GPa to -7 cm^{-1}/GPa, whilst for D_2 the slope changes from -2 cm^{-1}/GPa to -5 cm^{-1}/GPa (see Fig. 5.2). The full width at half height (FWHH) also shows an indication of a transition. In H_2, the FWHH increases linearly from 5 cm^{-1} at the solidification point to 45 cm^{-1} at 190 GPa, then abruptly increases to 130 cm^{-1} within a pressure interval of 30 GPa. Similarly in D_2, we observe the FWHH increase linearly, then abruptly increase at the transition but shifted to slightly lower pressures compared with H_2. Both the changes in slope of ν_1 and increased FWHH are in good agreement with previous low temperature measurements (250 K for vibrons and 18 K for librons) of H_2-III [Goncharov 98, Akahama 10a]. No measurements of the D_2-III low frequency Raman bands have been reported at any temperature prior to this study.

By extrapolating the existing low temperature transition lines for H_2 (D_2) [Goncharov 11] to 300 K and 190 GPa(180 GPa), this P-T point would lie on the phase I-III boundary. This is the first solid to solid phase transition to be identified in H_2 (D_2) at room temperature.

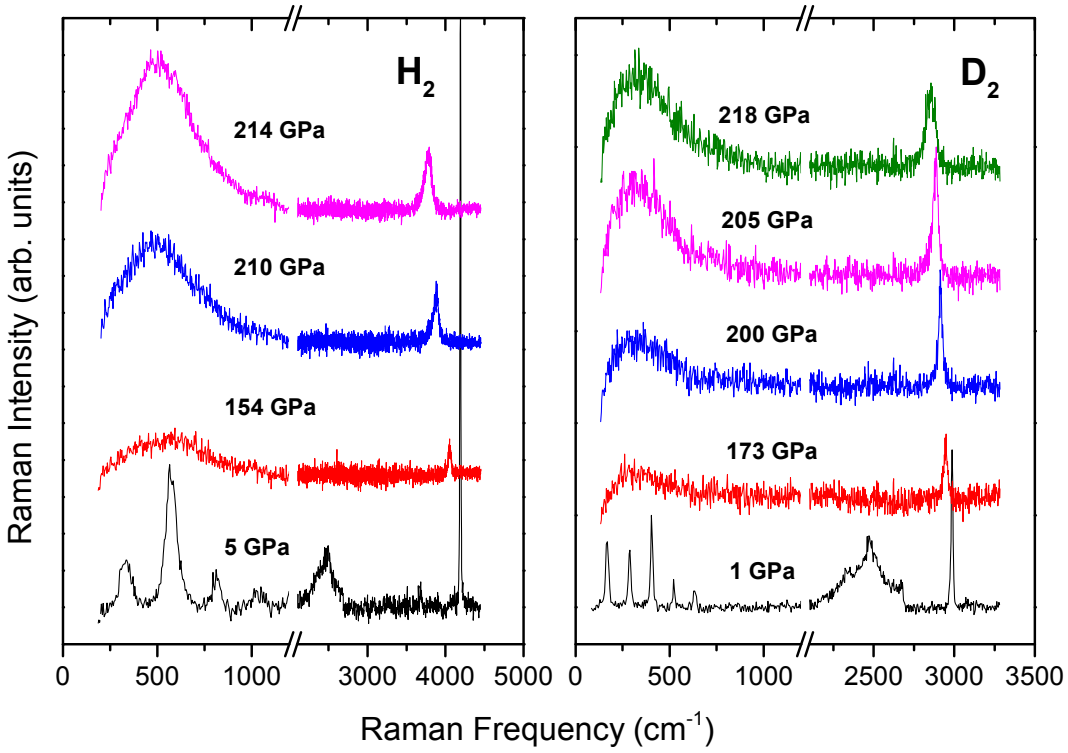

Figure 5.1: Representative Raman spectra of H_2 and D_2 at various pressures passing through the phase I to phase III transition. At low pressures, the peak at 2500 cm^{-1} corresponds to the second-order Raman band of diamond, which becomes unresolvable above 100 GPa. The break from 1200 cm^{-1} to 2100 cm^{-1} cuts only the first-order Raman band from diamond

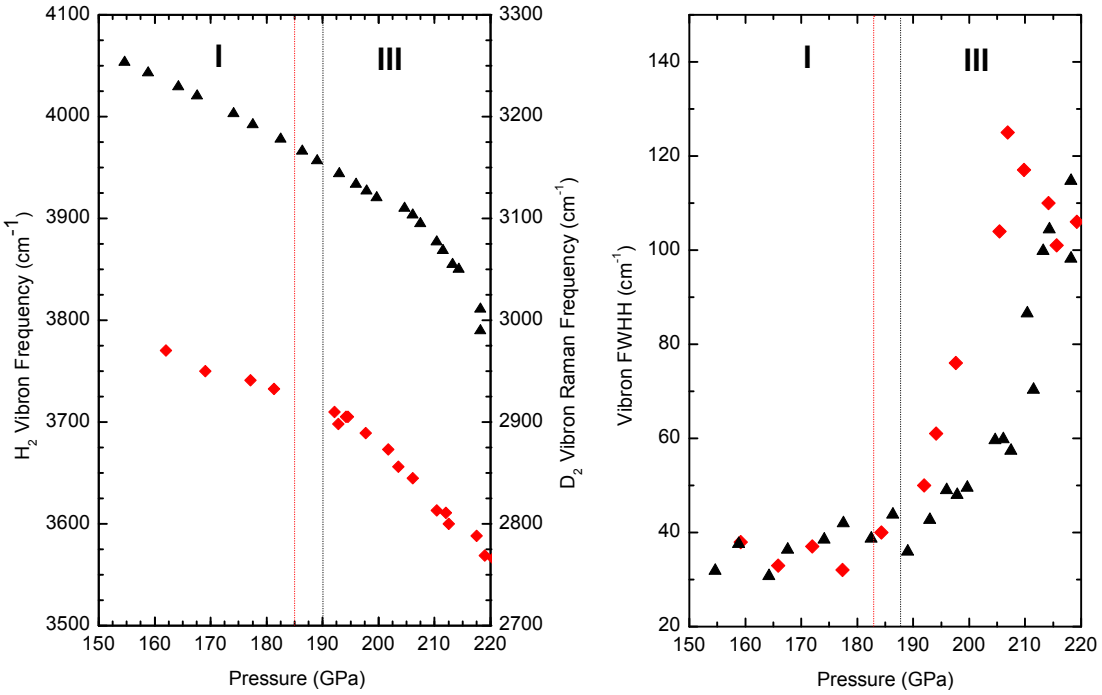

Figure 5.2: Left: H_2 (black triangles) and D_2 (red diamonds) vibron frequency versus pressure. Right: H_2 (black triangles) and D_2 (red diamonds) vibron FWHH versus pressure. The red and black dashed lines indicate the phase I to phase III transition for D_2 and H_2 respectively.

5.3 Discovery of phase IV

5.3.1 Hydrogen

Increasing pressure beyond 220 GPa, a transformation to the new phase IV is observed, evidenced by profound changes in the vibrational spectra and the low energy spectra below 1200 cm^{-1}. At 220 GPa, the low frequency broad band identified as phase III splits into two Raman modes; one mode that is initially weak in intensity at a frequency of 325 $cm^{-}1$, and a broader Raman mode at a frequency of 540 cm^{-1} (see Fig. 5.3). A comparatively weaker Raman mode also emerges at a frequency of 1062 cm^{-1}. At this pressure, the main vibron ν_1 reaches a frequency of 3780 cm^{-1}, whilst a new vibrational mode (from here on in referred to as ν_2) emerges at a frequency of 4150 cm^{-1}.

The ν_1 vibron is observed to soften and broaden very rapidly. The frequency versus pressure gradient changes from -7 to -12.7 cm^{-1}/GPa (see Fig. 5.4), and by 260 GPa, the frequency reduces below the values expected for the vibron in phase III at 77 K [Loubeyre 02]. This would suggest that phase IV has a different molecular bonding character compared to phase III. At 318 GPa, the frequency of the ν_1 vibron is 2750 cm^{-1} which is a 35% reduction compared to the vibron at its maximum frequency of 4260 cm^{-1} at 40 GPa. The intensity of the ν_1 vibron also increases 3-fold from 250 GPa to 318 GPa. There is a discontinuous jump in the FWHH of the ν_1 vibron from 130 cm^{-1} to 204 cm^{-1} at the transition and the FWHH continues to increase with pressure at a rate of 3 cm^{-1}/GPa.

The ν_2 vibron does not soften as rapidly as ν_1, with a frequency versus pressure gradient of -1.2 cm^{-1}/GPa. Whilst the ν_1 vibron is observed to continuously broaden with pressure, the FWHH of the secondary vibron ν_2 lies on the linear extrapolation of the FWHH of phase I (see Fig. 5.4). It is clear that the ν_2 vibron is driven by the normal pressure-induced broadening, unlike the ν_1 vibron; an indication of two very different local atomic environments involved in these modes.

The low frequency Raman band is observed to continuously evolve with pressure, an indication of ongoing changes in the structure of phase IV (see Fig. 5.3 and Fig. 5.4. At 260 GPa, the three low frequency modes are well-defined

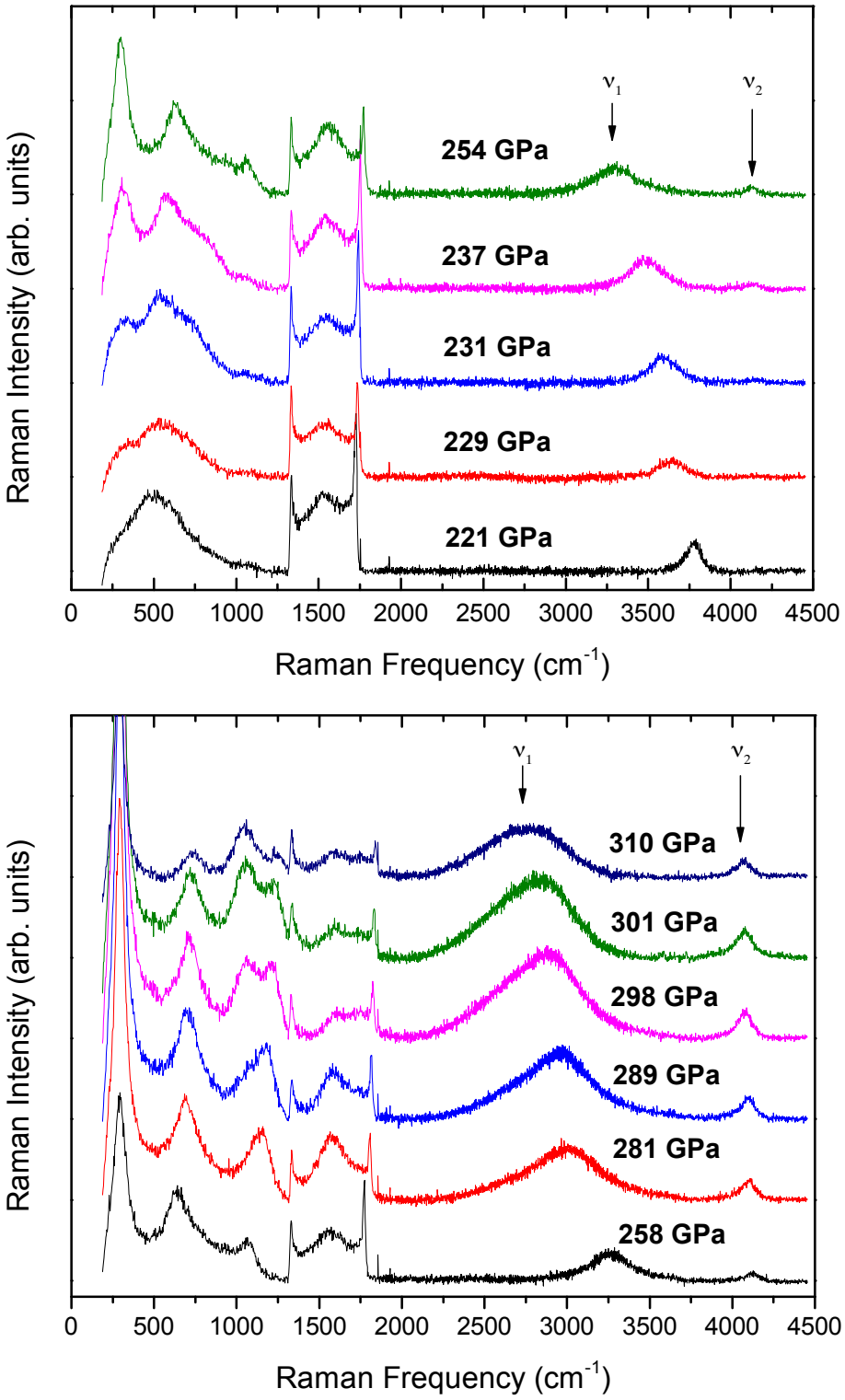

Figure 5.3: Top: Representative Raman spectra of H_2 at various pressures passing through the phase III to phase IV transition at 220 GPa. Bottom: Representative Raman spectra of H_2 showing the evolution of phase IV with pressure.

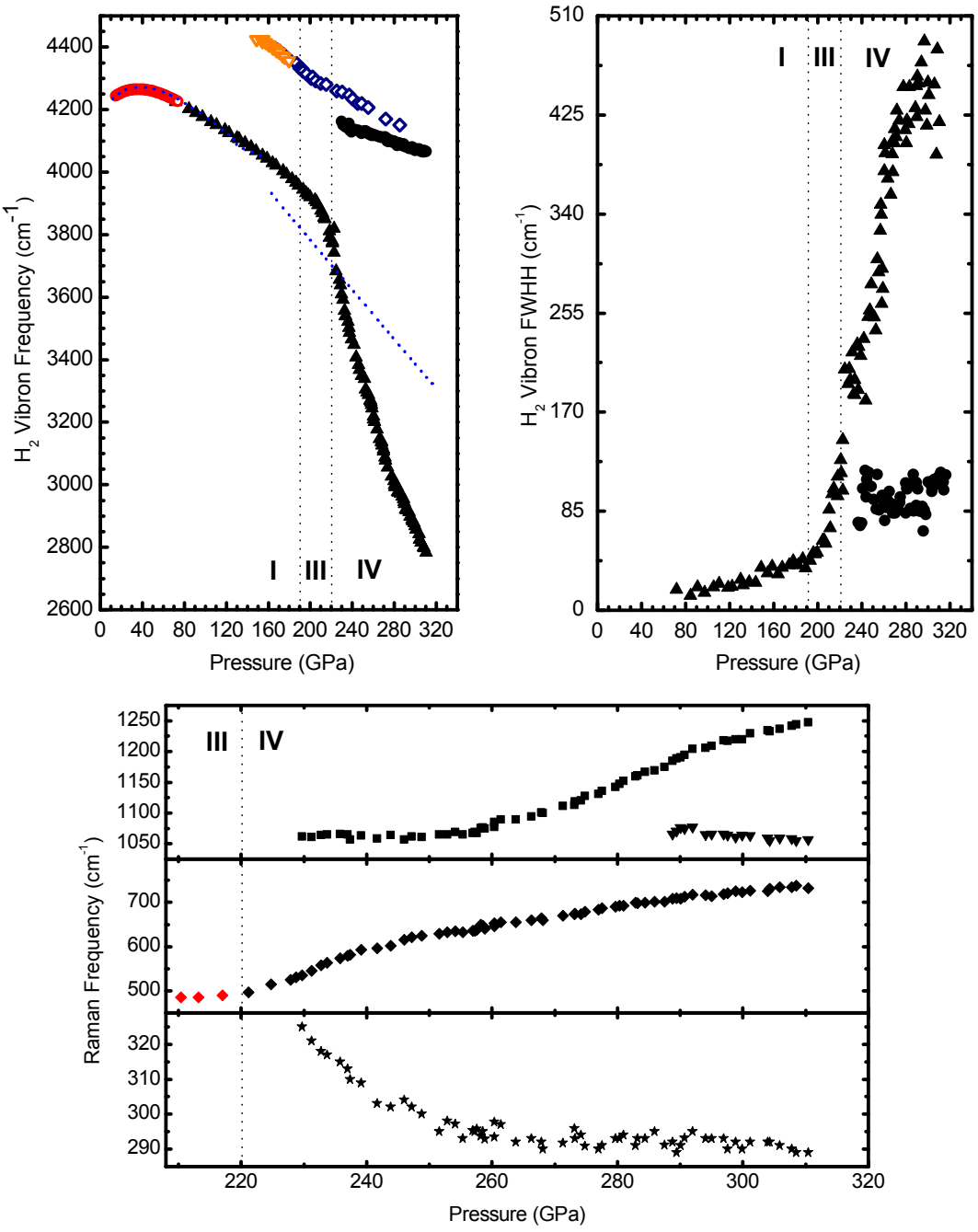

Figure 5.4: Top left: H_2 vibron mode frequency shift as a function of pressure. Closed triangles and closed circles are the ν_1 and ν_2 vibron modes. The blue dashed line is Raman measurements at low temperature from [Loubeyre 02]. Open diamonds are low temperature infra-red measurements from [Goncharov 98, Hanfland 93]. Top right: H_2 ν_1 (closed triangles) and ν_2 (closed circles) vibron mode FWHH as a function of pressure. Bottom: H_2 lattice modes as a function of pressure. Vertical dashed lines indicate phase transitions.

and increase with intensity with pressure. Above 280 GPa, the Raman mode observed at a frequency of 1155 cm^{-1} splits, giving rise to to another band that rapidly increases in intensity with pressure. At the highest pressure reached of 318 GPa, there are four well defined intense Raman modes at frequencies of 289, 732, 1057 and 1247 cm^{-1}. The relative intensity of the lowest frequency mode at 289 cm^{-1} significantly increases with pressure to more than 4-fold higher in intensity than the other 3 modes. Plotting the Raman frequency versus pressure, the modes at 732 and 1247 cm^{-1} are observed to increase with pressure, whilst the frequency of the modes at 289 and 1057 cm^{-1} soften. Such complex behaviour suggests that there could be coupling between the ν_1 vibron and low frequency modes of the same symmetry. Such coupling was observed in the high pressure phases of Ice (Ice-VII and Ice-VIII), whereby softening and gains in intensity were modelled through combinative coupling of deformational, translational and rotational modes [Goncharov 99]. The Raman modes at 289 and 1057 cm^{-1} in H_2 may couple with the ν_1 vibron, as both are observed to soften. Coupling would also explain the rapid gain in intensity of these low frequency modes with pressure.

5.3.2 Deuterium

Deuterium enters phase IV at 230 GPa; 10 GPa higher in pressure than observed in hydrogen. The transition is evidenced by similar changes as were observed in hydrogen (see Fig. 5.5). Two modes initially emerge with Raman frequencies of 265 cm^{-1} and 400 cm^{-1} from the broad phase-III Raman band, with a third emerging at 240 GPa with a frequency of 780 cm^{-1}. These low frequency Raman modes are observed to continuously evolve, and behave similarly with pressure to the corresponding modes of phase-IV hydrogen. The lowest frequency Raman mode softens from 265 cm^{-1} at 230 GPa to 240 cm^{-1} at 270 GPa, whilst the other two modes are observed to harden with pressure (see Fig. 5.6). The mode initially at a frequency of 400 cm^{-1} increases at a rate of 3 cm^{-1}/GPa, whilst the mode at 780 cm^{-1} increases at a rate of 1 cm^{-1}. At the highest pressure reached, all three observable low frequency modes are intense and well defined. The lowest frequency mode is the most intense, with intensity more than 3-fold higher than the other two modes. As with H_2, this rapid gain in intensity may be explained

by coupling with the ν_1 vibron, which is also observed to soften with pressure.

The ν_1 vibron in phase III softens to a frequency of 2760 cm^{-1}, after which co-existence of vibrons from phase III and phase IV are clearly visible up to 250 GPa (see Fig. 5.5). The phase III ν_1 vibron continues to soften at a rate of -5 cm^{-1}/GPa, whilst the phase IV ν_1 vibron softens at a higher rate of -8 cm^{-1}/GPa. It is interesting that the coexistence between phases III and IV was only observed in D_2 and not in H_2. At the transition, there is a discontinuous jump in the FWHH of the ν_1 vibron from 110 cm^{-1} to 150 cm^{-1} and the FWHH continues to increase with pressure at a rate of 3 cm^{-1}/GPa (see Fig. 5.6). Although the ν_1 vibron of D_2 broadens at the same rate as the ν_1 vibron of H_2 in phase IV, the initial FWHH is much greater in H_2 than in D_2, so at any given pressure the FWHH of ν_1 is greater in H_2 than in D_2. Such an increased broadening in H_2 may give reason as to why coexistence of phases III and IV is observed in D_2 and not in H_2: the narrower phase III ν_1 vibron is submerged by the broad phase-IV ν_1 vibron. Another isotopic difference is that the ν_1 vibron of D_2 softens at a slower rate than the ν_1 vibron of H_2. This subtle difference may have important consequences for the expected dissociation at higher pressures.

Above 235 GPa, the secondary vibron ν_2 emerges at a frequency of 3055 cm^{-1} and softens with pressure at a rate of -0.7 m^{-1}/GPa. Whilst the ν_1 vibron is observed to continuously broaden with pressure, the FWHH of the secondary vibron ν_2 lies on the linear extrapolation of the FWHH of phase I (see Fig. 5.6). This again provides evidence of two very different local atomic environments associated with each mode.

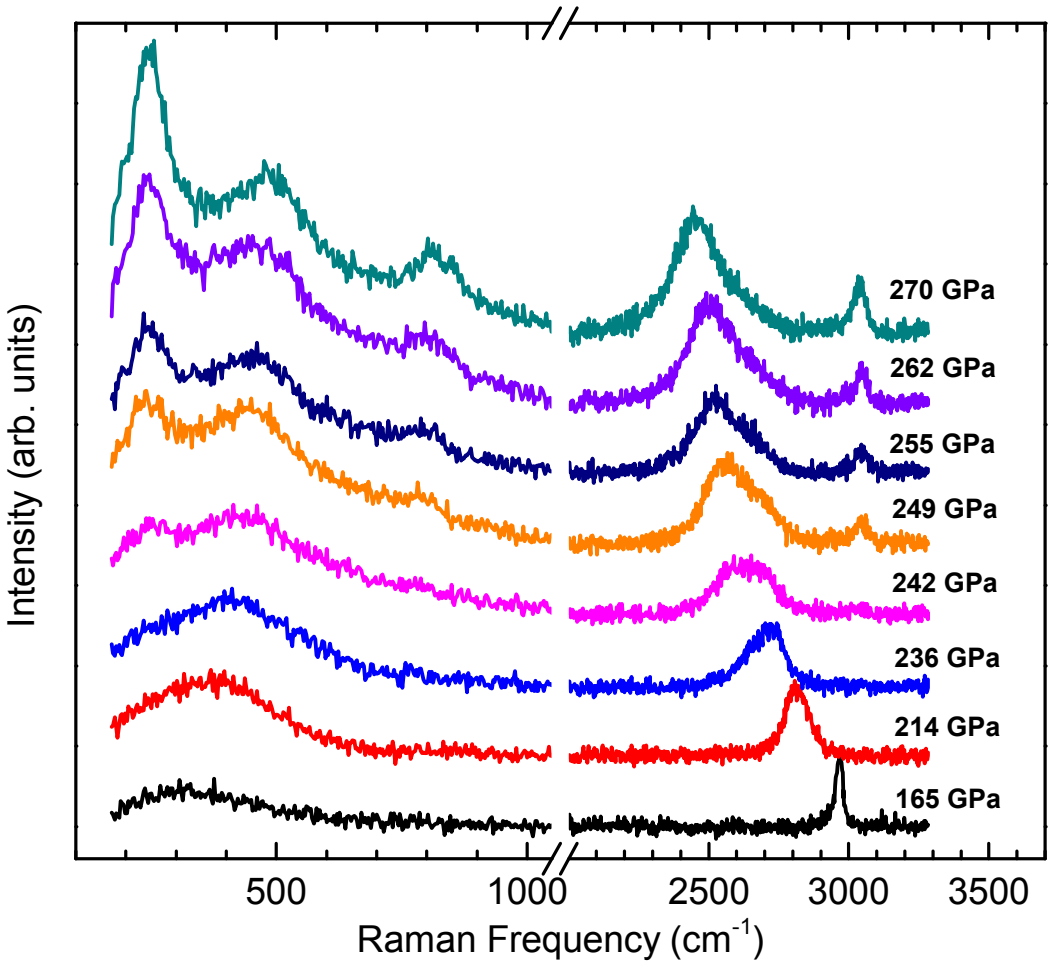

Figure 5.5: Representative Raman spectra of D_2 at various pressures.

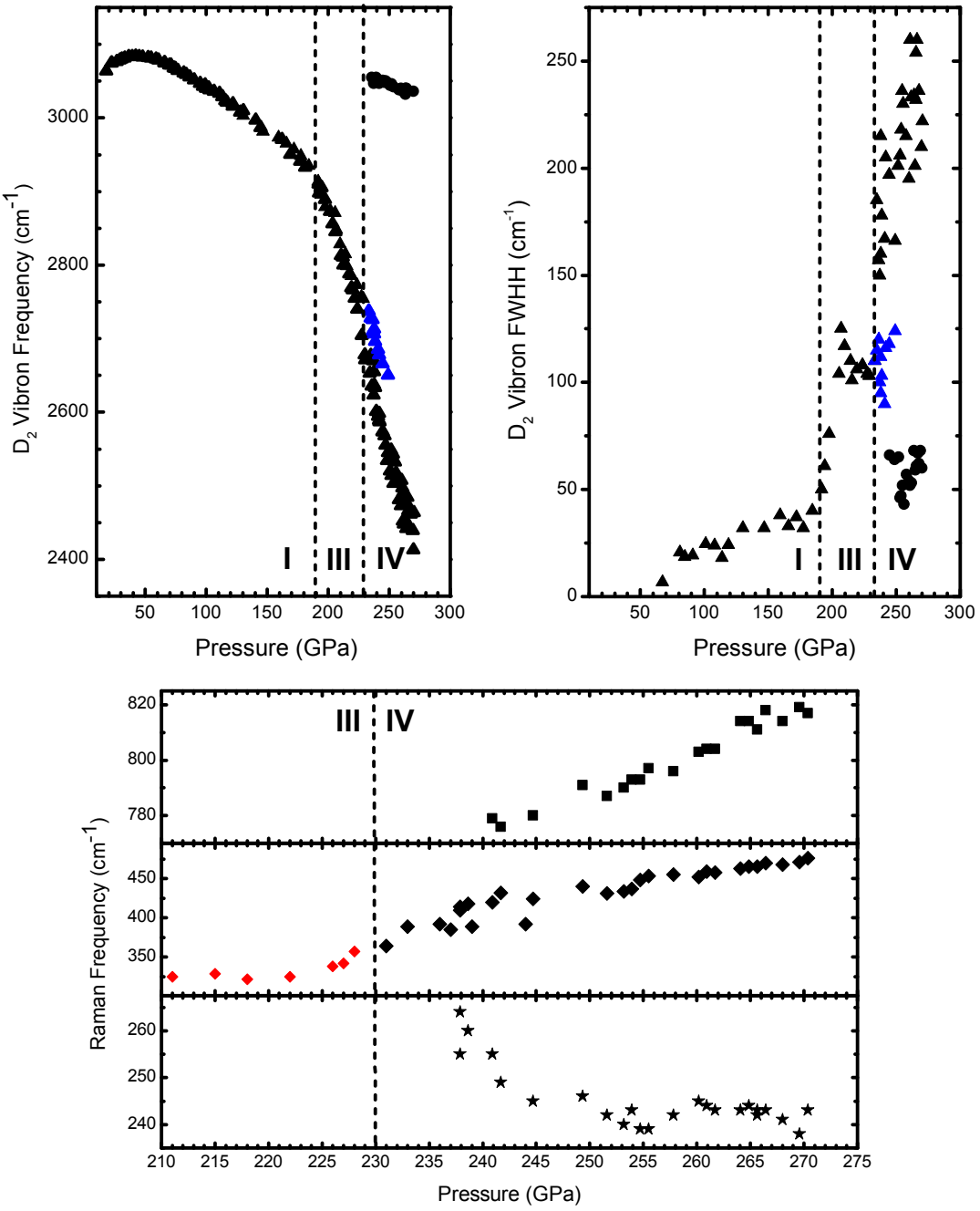

Figure 5.6: Top left: D_2 vibron mode frequency shift as a function of pressure. Closed triangles and closed circles are the ν_1 and ν_2 vibron modes. Blue triangles indicate the phase III ν_1 vibron frequencies when phases III and IV coexist. Top right: D_2 ν_1 (closed triangles) and ν_2 (closed circles) vibron mode FWHH as a function of pressure. Bottom: D_2 lattice modes as a function of pressure. Vertical dashed lines indicate phase transitions.

5.3.3 Optical Transmission Spectroscopy

Measuring the conductivity of hydrogen directly is experimentally challenging, due to the high risk of a reaction between hydrogen and common electrical probes, e.g. platinum, tungsten and gold. Reactions of metallic probes forming hydrides have proved controversial in conductivity measurements of hydrogen rich materials. In 2008, Eremets *et. al.* claimed to have found a new metallic phase of silane (SiH_4) at 50 GPa, and that such phase became superconducting at 100 GPa [Eremets 08]. However in a later study, it was found that silane decomposes into its constituents at pressures above 50 GPa [Hanfland 11], casting doubt on the observed transition. As it turned out, the metallic probes used in the study were platinum, which forms PtH at 27 GPa and has indeed been predicted to become superconducting at conditions claimed for silane [Degtyareva 09, Scheler 11b].

Although not a direct measurement of conductivity, optical transmission spectroscopy provides an *in-situ* method to investigate absorption features that can be used to infer band gap values. In all experimental runs, optical transmission measurements were carried out in the spectral range of 400 - 900 nm, using a white light source. Reference spectra were taken below pressures of 100 GPa in Phase I, after the size of the sample chamber had stabilized. It has been previously suggested that, at multi-megabar pressures, samples may darken due to the stressed diamond culet, giving reduced transmission values. Visually, this effect was not observed in any of the experimental runs and was evidenced by no obvious darkening of the surrounding gasket material (see inset of Fig. 5.7).

At 150 GPa, the band gap of H_2 is estimated at 2.9 eV and appears to decrease linearly with pressure to 2.4 eV at 275 GPa. Both H_2 and D_2 give similar band gap values at any given pressure. Above 275 GPa, a strong band-gap feature appears in the spectra and shifts in red with pressure (see Fig. 5.7). The overall absorption increases with pressure in this regime and the sample becomes visibly darker in appearance. There is also a change in slope of the band-gap versus pressure at 275 GPa, with the band gap dropping to 1.8 eV at 318 GPa. From these estimations, hydrogen could be considered a wide band-gap semiconductor at 318 GPa.

As measurements were conducted in the visible region, only the direct band

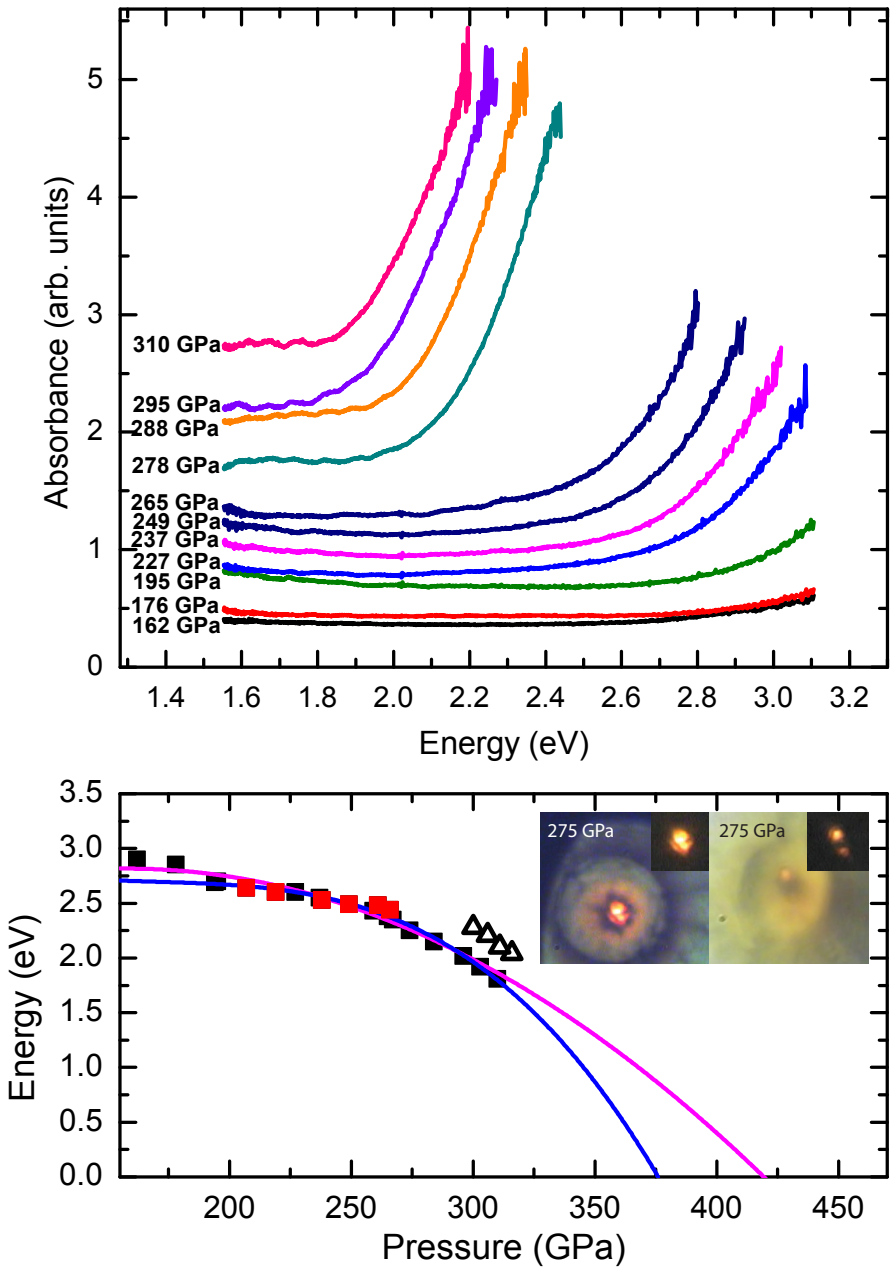

Figure 5.7: Top: Optical absorption spectra of H_2 in a visible spectral range at 300 K and different pressures. The reference transmission spectrum was measured at 75 GPa. Bottom: H_2 (black squares) and D_2 (red squares) combined band-gap points as a function of the pressure at 300 K. Open triangles are the low temperature data in phase III taken from [Loubeyre 02]. Quadratic [upper (magenta) curve] and cubic [lower (blue) curve] polynomial fits extrapolated to higher pressures are shown as solid lines. Inset: Optical microscopy images of a H_2 sample in transmitted and reflected white light at 275 GPa and 300 GPa.

gap could be measured. Absorption could still be occurring at frequencies below the optical range measured, therefore it cannot be ruled out that the samples could still be electrically conducting through an indirect band gap. Although the band-gap shift with pressure is comparable to that for phase III at 75 K (see Fig. 5.7), the overall significant increase in absorption may suggest that, above 275 GPa, hydrogen may become semimetallic.

Using the combined D_2 and H_2 band-gap points different polynomials were used to fit and extrapolate the data (see Fig. 5.7). The pressures at which the band gap is fully closed vary widely, depending on the power of the polynomial but the lowest value is approximately 375 GPa. It is instructive to estimate the frequency of the ν_1 vibron at this pressure, as the ν_1 vibron frequency is an absolute pressure gauge in experiments and should be used for direct result comparison, in both experimental and theoretical studies (see later section). The extrapolation of hydrogen frequency versus pressure is almost linear and yields 2350 $\pm$ 50 cm^1 at 375 GPa. This value is about 55% of the vibron frequency under ambient conditions and is much lower than any frequencies ever reported in experiments.

5.4 Discussion

5.4.1 Determining a Structure for Phase IV

Apart from phase I, the structures of all solid phases of hydrogen are unknown, which makes the definitive interpretation of the observed phenomena of phase IV difficult. Before the discovery of phase IV, it was thought that hydrogen would remain in phase III up until the transition to the metallic state. As such, there have been extensive *ab initio* theoretical calculations of phase III to find potential structure candidates for phase III at pressures in the stability region of phase IV. In a study by Pickard and Needs [Pickard 07], which included contributions of zero-point energy, three structures (*C2/c*, *Cmca-12* and *Pbcn*) were determined as plausible candidates for phase III. The *C2/c* and*Cmca-12* structures all have H_2 molecules with approximately the same bond length (within 1%) and would have a second Raman vibrational mode, due to Brillouin zone doubling with

respect to phase I. This is in some agreement with the experimentally observed infrared [Goncharov 01, Hanfland 93] and ν_2 Raman vibron in phase III. The ν_2 Raman vibron is extremely weak and assigned to a folded mode from the Brillouin zone boundary; the frequency of the Phase III ν_2 vibron is close to that of the strong IR mode, as they both correspond to the vibrational states near the top of the vibrational band. At 175 GPa, both IR and Raman vibrons are relatively close in frequency (4400 cm^{-}1) to that of free molecules in an unbound state. In the following chapter, low temperature Raman data will be used to re-evaluate the appropriateness of these candidates for phase III.

The third proposed structure by Pickard and Needs, *Pbcn*, could explain all the features of the Raman spectra of phase IV [Pickard 07]. This structure is highly unusual; it consists of unbound molecules sandwiched between honeycomb graphene-like (G) layers made of 6-atom rings, yielding both molecular and atomic hydrogen at the same time. Each bond in the G layer has a different size length, ranging from 0.85 to 1.04 $\mathring{A}$ as shown in Fig. 5.8. Density functional theory calculations predict 16 fully-symmetric Raman modes (A_g) for the *Pbcn* structure [Pickard 07]. 6 out of 16 of these predicted Raman modes can be assigned with experimental observations. Using the empirical formula [Herzberg 60];

$$\nu r^3 = const \tag{5.1}$$

where ν is the Raman frequency and r is the bond length, the observed vibron frequencies can be qualitatively assigned to the predicted modes of the *Pbcn* structure. At 300 GPa, the 0.72 $\mathring{A}$ bond, which is very close to the bond length of an unbound molecule, can be assigned to the ν_2 mode (4150 cm^{-1}), while the 0.83 $\mathring{A}$ bond length (bonds within the G-layer) can be assigned to the ν_1 mode (2800 cm^{-1}). Subsequent molecular dynamic (MD) simulations [Goncharov 13] have confirmed this assignment and the atomic motions are illustrated in Fig. 5.9. The 1.04 and 1.03 $\mathring{A}$ calculated bond lengths could correspond to the doublet observed at 1050 and 1200 cm^{-1}. Although 6 Raman modes are calculated in the region of 1500 - 2000 cm^{-1}, this band would most likely be obscured behind the signal from the stressed diamond.

MD simulations have been used to investigate the characteristics of the low

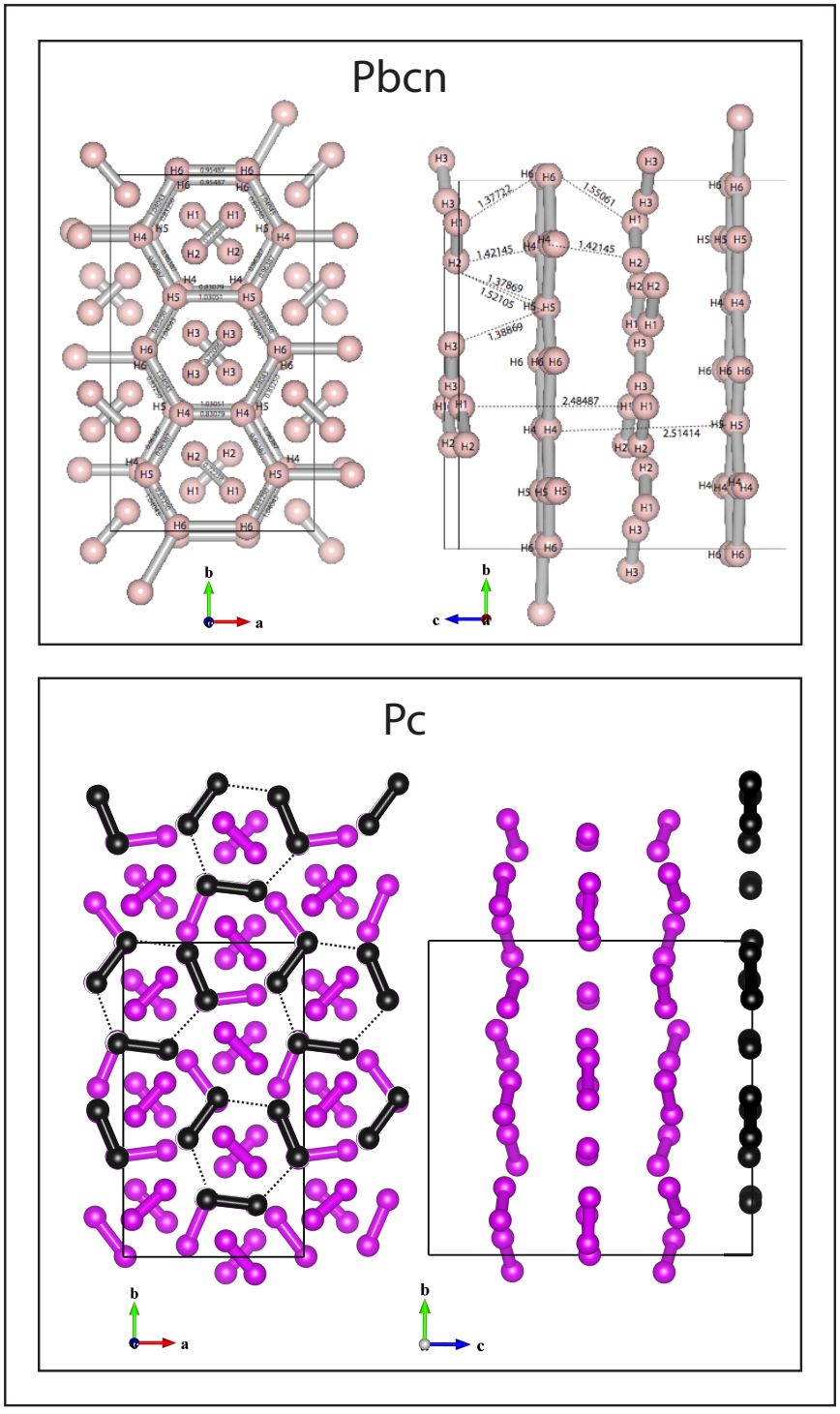

Figure 5.8: Top: Top and side views of the *Pbcn* structure at 300 GPa showing bond lengths. The atomic positions are taken from [Pickard 07]. Bottom: Top and side views of the *Pc* structure, where the atomic positions have been taken from [Pickard 12]. Black atoms indicate the top weakly bonded G-layer. The black dashed lines show the next nearest contacts within the layer.

frequency lattice modes below 1300 cm^{-1} at 240 GPa [Goncharov 13]. Through these simulations, the observed pressure-induced changes in intensity of the low frequency lattice modes are explained through vibrational coupling with the ν_1 mode from the G-layer, which softens with pressure. The mode at 300 cm^{-1} is a unique mode, corresponding to the librational motion of the G-layer hydrogen rings (see Fig. 5.9). Coupling is more obvious between the 300 cm^{-1} lattice mode and the ν_1 vibron, as both are observed to soften and increase with intensity with pressure. The two other low frequency modes (800 and 1050 cm^{-1}) are shown to correspond to molecular translation and rotations in the unbound molecule layer.

The ν_1 vibron mode has a very large isotope effect and pronounced broadening, compared to other phases of hydrogen; an indication of increased anharmonicity of the mode due to hydrogen bond symmetrisation. Such behaviour has been observed in ice-VII, where in the vicinity of the symmetrisation transition, the lattice becomes highly anharmonic, causing both softening and broadening of the O-H stretching mode [Goncharov 99]. Due to the increased anharmonicity, the potential well becomes very shallow, due to the lowering of the barrier between potential wells and can only accommodate two vibrational levels [Goncharov 13]. As the first excited vibrational level is now close to the top of the barrier, proton tunnelling becomes frequent. Because of the larger zero-point energy, tunnelling is more energetically favourable in hydrogen than in deuterium, leading to the enhanced proton tunnelling in the regime approaching symmetrisation as observed in ice [Goncharov 99]. As such, the hydrogen vibron would show larger softening and broadening of the ν_1 mode relative to deuterium, as the lighter hydrogen tunnels more easily. Fig. 5.10 plots the frequencies of the observed modes in hydrogen versus the corresponding frequencies of deuterium modes and there is a clear divergence of the ν_1 vibron mode from the expected $1/\sqrt{2}$ behaviour. Such behaviour is exemplary of the strong quantum characteristics of phase IV.

In subsequent DFT studies, it was shown that the *Pbcn* structure is dynamically unstable, as the lowest frequency libron mode has an imaginary frequency [Pickard 12]. However, three more dynamically stable *Pbcn*-like structures with 6 member rings have been proposed: P_c-48 (which still has imaginary phonons), P_c-96 [Pickard 12] and C_c [Liu 12] (both dynamically stable) symmetries (see Fig. 5.8). These studies calculated that the structures would became stable above 220

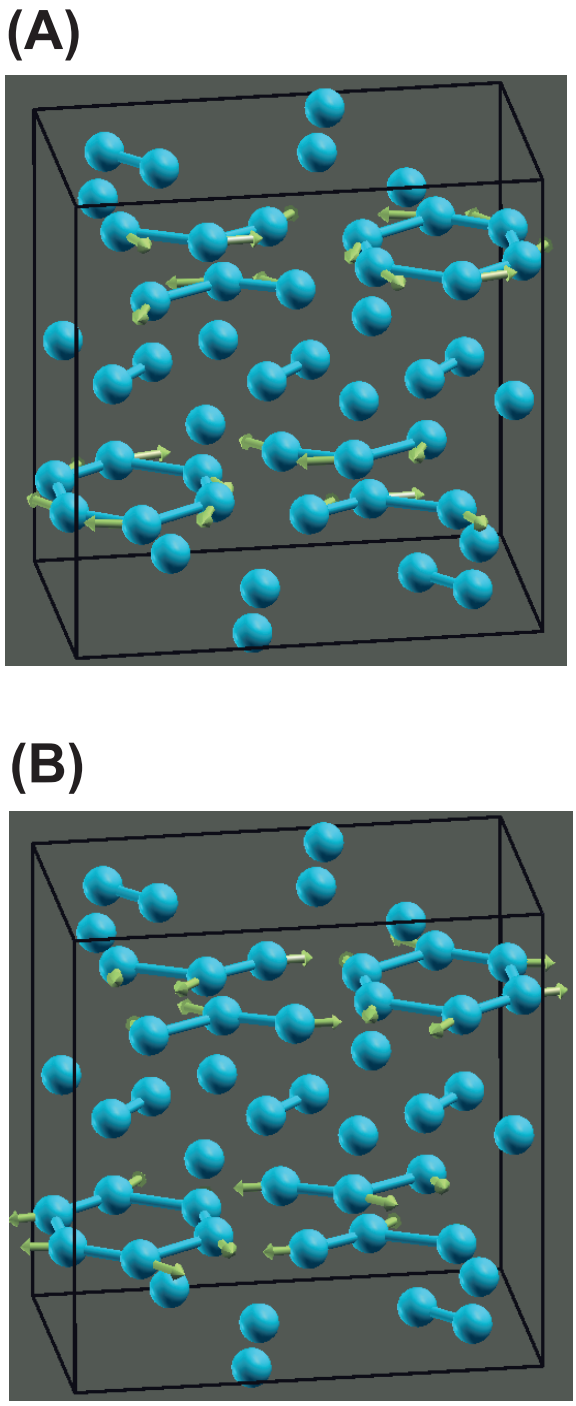

Figure 5.9: The atomic motions of the (A) low frequency libron Raman mode and (B) soft vibron (ν_1) Raman mode of the *Pbcn* structure as a result of MD simulations taken from [Goncharov 13].

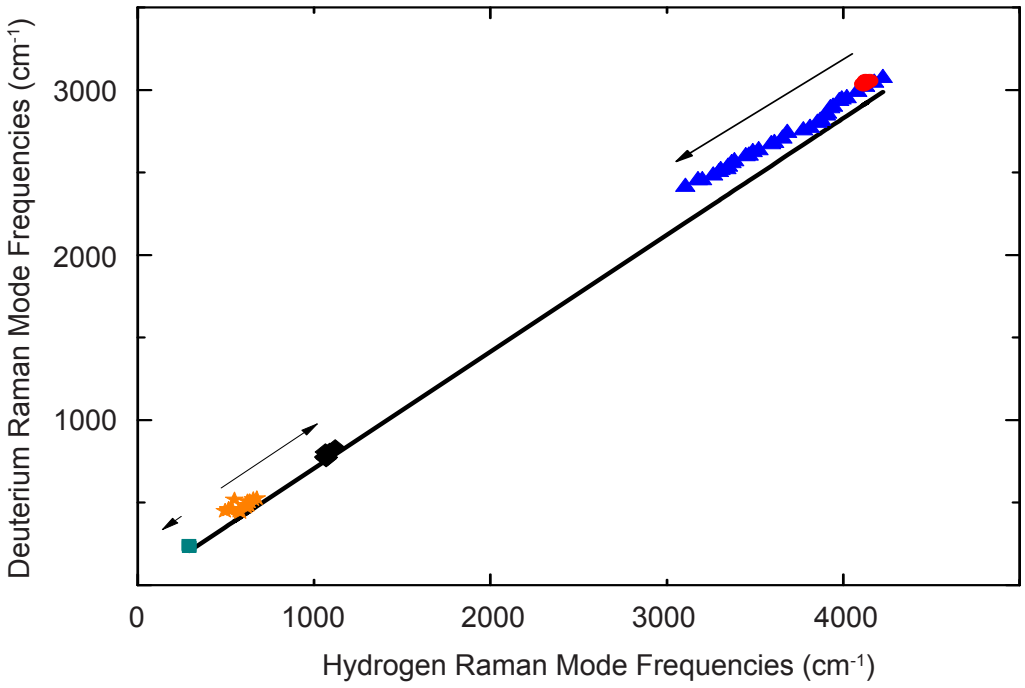

Figure 5.10: The frequencies of the observed modes in hydrogen versus the corresponding frequencies of the deuterium modes from 70 to 275 GPa. The blue filled triangles are the ν_1 mode, the red filled circles are the ν_1 modes. The filled squares and stars are the low energy phonon modes. The arrows indicate the change in frequency of the given excitation when pressure is increased. The straight solid line has the slope of $1/\sqrt{2}$

.

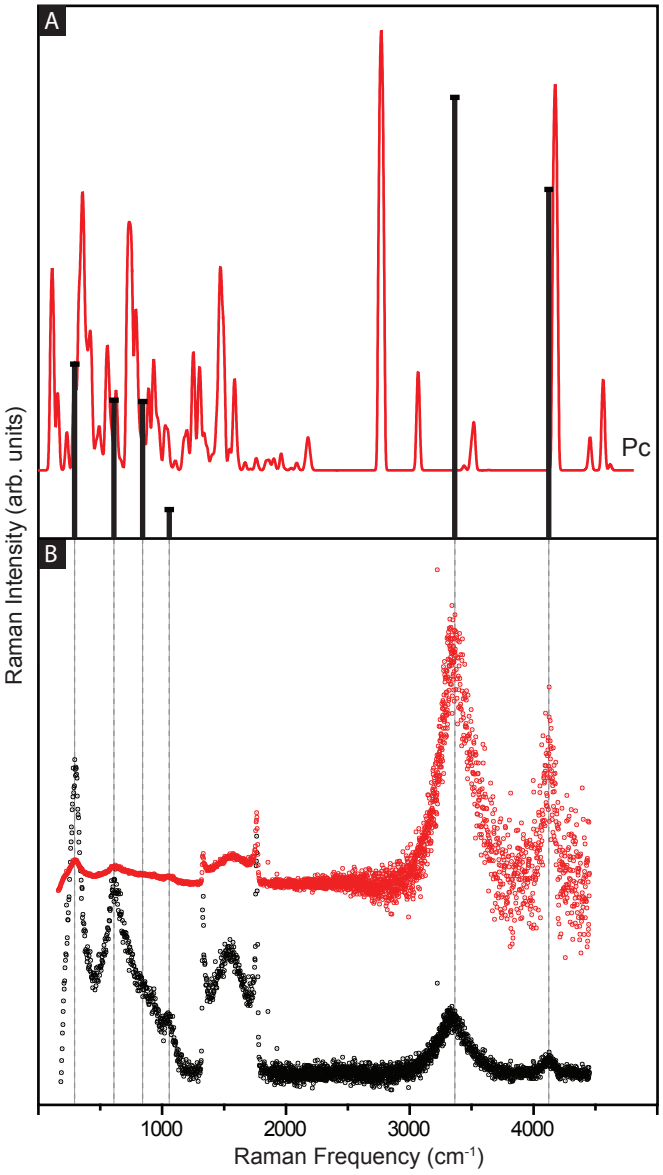

Figure 5.11: Comparison of the experimentally observed and theoretically calculated [Pickard 12] Raman intensities and spectral positions of the hydrogen bands at 250 GPa. (A) Experimental raw spectra observed in phase IV (in black); spectra corrected for decreasing sensitivity of the detector are shown above (in red). The broad peaks between 1333 cm^{-1} and 1800 $cm^{-}1$ are due to the first order Raman from diamond. (B) Experimental renormalized spectra plotted as Gaussian distributions for phase IV (vertical black lines); theoretically calculated spectra for Pc. The intensities for renormalized and theoretically calculated spectra are plotted on a logarithmic scale to clearly compare the weaker low frequency modes.

GPa and 300 K, which is in good agreement with the results presented in this thesis. Fig. 5.11 shows a comparison between the calculated spectral positions and intensities of the *Pc* structure with the renormalized Raman spectra from experimental observations. An interesting feature is that, after renormalizing, the Raman spectra is heavily dominated by the vibron modes. Although the calculated modes for *Pc* are not a perfect fit, they are in much better agreement with the experimental data, compared to the calculated modes for the *Pbcn* structure.

Ultimately, x-ray diffraction studies are needed to unambiguously determine the structure of phase IV, however such experiments remain exceedingly difficult with the current capabilities. It has even been suggested that, due to the extremely large atomic motions, phase IV may not have a well defined crystal structure, which could be a reason for the disagreement between predicted phase IV structures. However, what is promising is that theoretical studies all agree on the presence of two distinct structural units, a "molecular" and a "graphene-like" layer, which repeat periodically in the A-B-A-B sequence. Only the symmetry of the graphene-like layer is a matter of debate. With impending infra-red studies, no doubt the number of potential candidate structures for phase IV will be further reduced, awaiting definitive confirmation from x-ray studies. It is interesting that the hexagonal configuration of molecules in the graphene-like layer is similar to predictions, suggesting that intermolecular complexes could form before the transition to the atomic phase [Labet 12].

5.4.2 Evidence for further high pressure phases

A recent study by Eremets and Troyan [Eremets 11] compressed hydrogen to 300 GPa and provided evidence for the transition to phase IV at 220 GPa. Both the transition pressure and appearance of low frequency Raman modes are in good agreement with phase IV presented in this work. Despite these observations, the authors attributed the transition at 220 GPa to the purely molecular *Cmca-12* structure and claimed the sample to be both opaque and electrically conductive. They reported a further transformation to a metallic monatomic fluid at 270 GPa, inferred from the disappearance of the Raman signal. However, analysis of the presented Raman data in [Eremets 11] suggests that in all runs the signal was

lost, due to factors other than molecular dissociation of H_2 (D_2).

The agreement in the observed frequencies of the vibrational band vs. pressure is good for H_2 up to 260 GPa, whilst there is some discrepancy for the D_2 shifts, most likely due to the different pressure scale used (see next section). Unlike in Ref. [Eremets 11], 6 Raman modes are observed up to the highest pressures reached. Contrary to the claims of the signal disappearance, the intensities with pressure for the lowest lattice mode at $\sim$300 cm^{-1} and both vibrational bands are observed to increase with pressure. Furthermore, the presented Raman data in [Eremets 11] for D_2 are inconsistent with their data for H_2, despite the claim that both isotopes behave similarly. [Eremets 11] did not observe the low frequency modes for D_2, explaining it by the isotope effect and/or pressure difference. It is known that the frequencies of H_2 and D_2 rotons and phonons are scaled by factor of 2 and $\sqrt{2}$ respectively [Silvera 80]. The low energy frequencies for D_2 scale to the corresponding H_2 frequencies as $\sqrt{2}$, indicating that these excitations are phonons (lattice modes); this unequivocally proves that $H_2(D_2)$ is in a *solid state* up to 318 GPa.

The disappearance of the Raman signal in [Eremets 11] could be explained by the partial collapse of the sample chamber and increased background from the diamond. In many of our experimental runs, we have observed partial collapse of the sample chamber, Fig. 5.12. The cause of such collapsing behaviour originates from the preparation of our experiments where we have used either infra-red laser, spark erosion or focussed ion beam gasket drilling. Depending on the laser profile of the infra-red laser used, the sample chambers may be drilled asymmetrically, resulting in partial drilling of the gasket material at the sample chamber edges. As the sample is typically loaded into the diamond anvil cell as a compressed gas, when further compressed, the chamber often collapses in diameter by up to a factor of 2. If the sample is asymmetrically drilled, then the gasket material will flow under the sample and continue to do so up to pressures exceeding 200 GPa (see Fig. 5.12).

Fig 4 shows representative Raman spectra of H_2 and D_2 on the transparent part of the sample (upper spectra and A in photomicrograph) and the partially collapsed gasket part of the sample (lower spectra and B in photomicrograph). It was observed that there is still a Raman signal from $H_2(D_2)$ on the partially

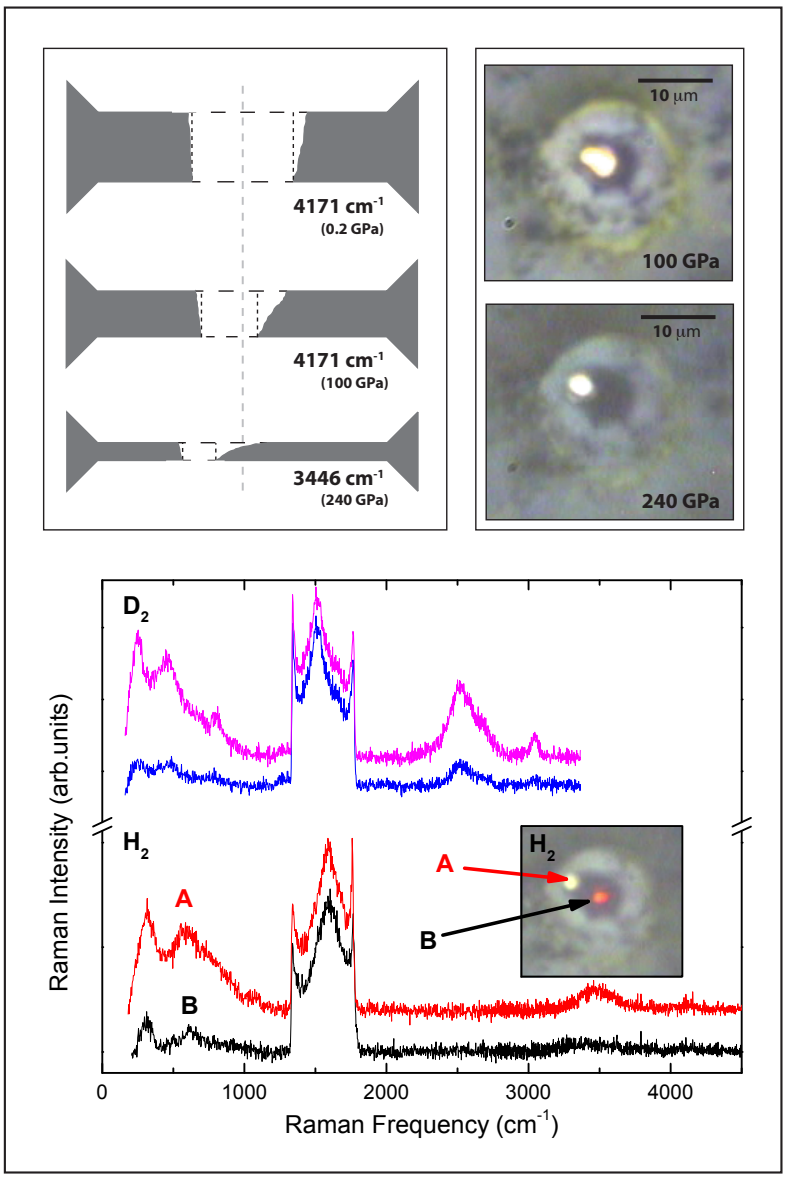

Figure 5.12: Upper: Illustrations and photomicrographs showing how the sample chamber was observed to partially collapse. Hydrogen vibron frequencies and pressure estimates (calculated using Ref. [Akahama 10b] are indicated at each stage of deformation. Lower: Raman spectra of H_2 (bottom) and D_2 (top) at diamond edge frequencies of 1765 cm^{-1} and 1770 cm^{-1} respectively. The upper spectrum in each isotope shows measurements on the transparent part of the sample. The lower (weaker) spectrum shows measurements on the partially collapsed sample chamber, as illustrated in the photomicrograph inset. The inset shows a photomicrograph in both transmitted and reflected light, whilst the probing laser reflects on the partially collapsed gasket segment of the sample.

collapsed gasket, indicating that there must be a thin layer of hydrogen lying on the hydride formed from the gasket material. The signal is weaker due to probing only a small depth of hydrogen, compared with the transparent part of the sample. Such an effect could explain the apparent loss of Raman activity above 270 GPa at the reported 'metallic' transition in [Eremets 11]. Eremets and Troyan also claim high reflectivity of the sample, based on visual observations which are not supported by the measurements and are inconsistent with the presented extremely low values of measured conductivity (one can estimate $\sigma \sim 0.2\ \Omega^{-1}m^{-1}$ from the data provided in [Eremets 11]). This observation can also be explained by the partial collapse of the gasket, as the increased reflectivity would be from the non-transparent layer of metallic gasket material, rather than the layer of H_2 (Fig. 5.12 inset shows the reflection of the laser on the partially collapsed gasket). Contrary to the claims of high reflectivity in [Eremets 11], the sample(s) in this work were still transparent in the visible and infra-red region below ∼1.9 eV. The analysis of the data presented here, demonstrates that $H_2(D_2)$ is a wide band-gap solid semiconductor at 300 K and up to 318 GPa.

Recent theoretical studies have predicted that hydrogen may transform back into a molecular phase at higher pressures [Liu 12, Pickard 12]. Pickard *et. al.* predicted the transformation into a molecular metallic *Cmca-12* phase at pressures above 275 GPa, while Liu *et. al.* predicted a transformation to a *Cmca-4* structure. These predictions of a new metallic phase seem to be in agreement with the claims of metallization above 260 GPa by [Eremets 11]. However, as discussed above, our optical spectroscopy results above 260 GPa are in strong disagreement with these claims. In addition, the theoretically proposed molecular metallic phases (*Cmca-12* and *Cmca-4*) are Raman active, which would also be at variance with the claimed disappearance of Raman modes in [Eremets 11]. Up to pressures of 310 GPa, there are no major changes in the Raman spectra that would indicate a complete change in structure to either *Cmca-12* and *Cmca-4* phases.

Although there is no evidence of the transformation back into a molecular state, there is evidence of slight modulations of the phase IV structure at higher pressure. Above 275 GPa, there is a slight change in the optical properties, such as the appearance of the 4^{th} low energy mode, the change of slopes of the ν_1 frequency and the value of the D_2/H_2 band gaps with pressure. The transition

indicated in Fig. 5.13 may be interpreted as the presence of a new solid structure (phase IV'). However, with very similar Raman spectra, phase IV' must be closely related to phase IV structurally.

5.4.3 Use of the H_2 and D_2 vibron as a pressure gauge

Room temperature studies of hydrogen to above 300 GPa have been reported previously [Narayana 98], but the results remain controversial, due there being no positive diagnostics confirming the presence of hydrogen in the sample chamber at such conditions. Instead, Narayana *et. al.* provided only diagnostics of the gasket material as evidence the gasket (and therefore assumed the softer sample) was above 300 GPa. It is obvious now that pressure metrology in such early experiments is problematic. The majority of researchers in the field have currently adopted the diamond Raman edge as a pressure calibrant. However, the use of the diamond Raman edge as a pressure calibrant is dependent on the physical (pressure, temperature and sample type) and geometrical conditions at which it was calibrated. As more experimental groups are to claim to have compressed hydrogen at room temperature in the multi-megabar regime, it is important to evaluate both the way pressure is determined, and the way in which pressure is used, to compare the stability ranges of phase transitions.

Fig. 5.14 shows a plot of H_2 and D_2 vibron frequencies versus diamond Raman edge frequencies for 10 separate experimental runs. In each run, there is lack of consistency with the frequency of the diamond Raman edge and the frequency of the vibron. In the most extreme case, there is a separation of 10 cm^{-1} in H_2 and 22 cm^{-1} between the diamond Raman edge frequencies at a given vibron frequency. This variation in diamond Raman edge frequency could correspond to changes in pressure of 8 GPa to 18 GPa respectively, thus the diamond edge is ultimately unreliable in claiming stability pressures of reported phases. Furthermore, the insets of Fig. 5.14 provide a comparison between this study and that of Eremets and Troyan [Eremets 11], showing a clear disagreement between pressure and corresponding vibron frequency.

Importantly, what is observed in this study is the consistency in the frequencies of the vibron at which the Raman characteristics of phases III and phase IV

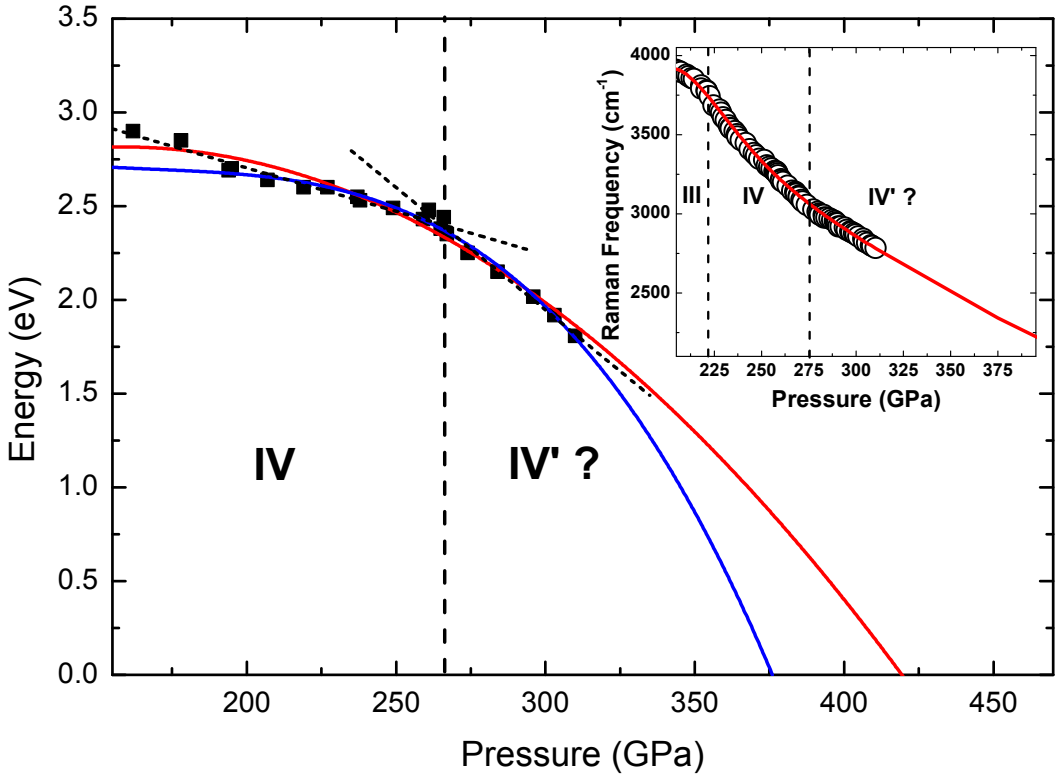

Figure 5.13: Hydrogen and deuterium combined band-gap points (filled squares) as a function of pressure at 300 K. Dotted (black) straight lines are linear fits to the measured data points in phase IV and phase IV'. Quadratic [upper (red) curve] and cubic [lower (blue) curve] polynomial fits extrapolated to higher pressures are shown as solid lines. Inset: Frequency of the ν_1 mode of hydrogen as a function of pressure. Open circles are measured ν_1 vibron frequencies versus pressure. The solid (red) line shows the nearly linear (from 275 to 400 GPa) extrapolation of the ν_1 frequency up to above 375 GPa-the minimal pressure needed to close the optical band gap. Dashed vertical lines indicate the proposed phase transition between phase IV and phase IV'.

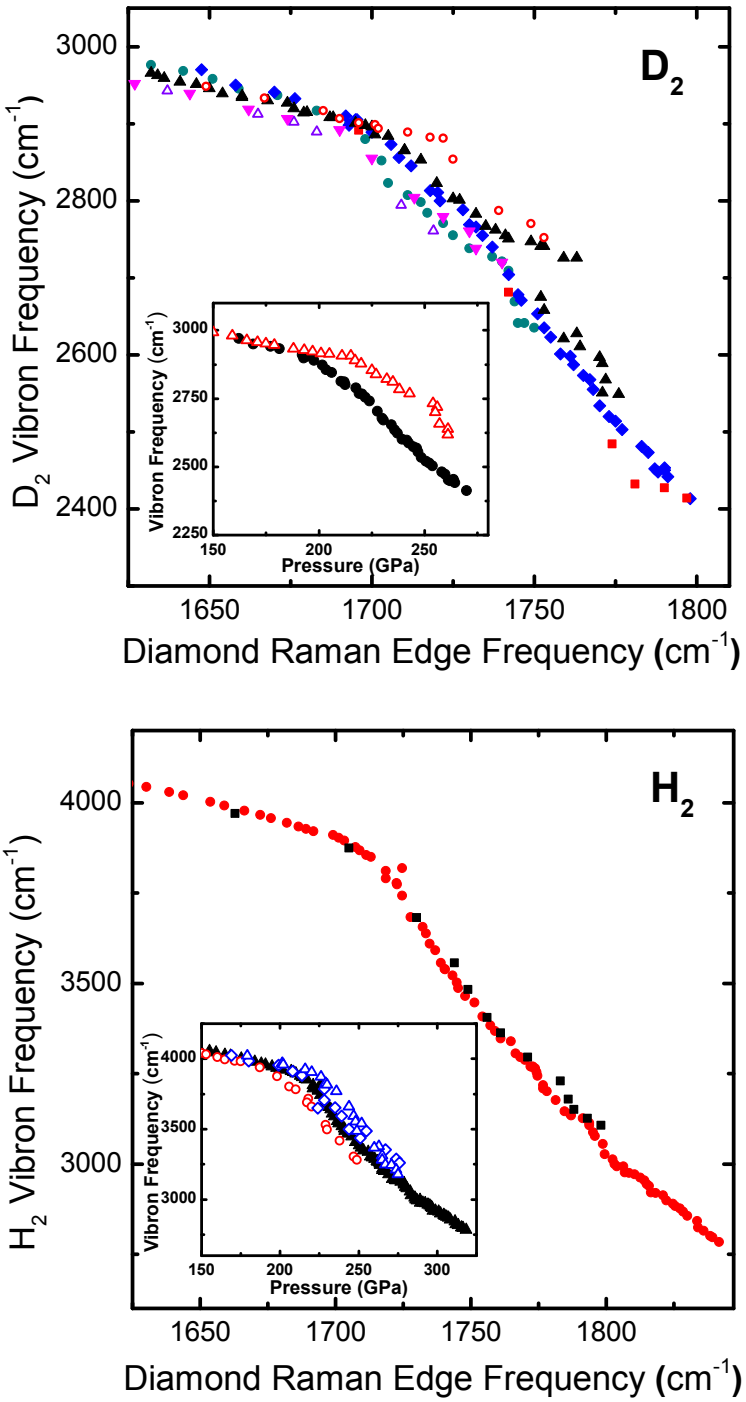

Figure 5.14: H_2 and D_2 vibron frequency versus diamond Raman edge frequency for 10 separate experimental runs. Insets: Vibron frequency versus pressure comparison between this study and [Eremets 11]. Solid symbols represent this study with pressure calibrated using [Akahama 10b] and open symbols are from [Eremets 11].

appear. Phase III is observed at vibron frequencies of 3850 cm^{-1} and 2895 cm^{-1} for H_2 and D_2 respectively. Phase IV is observed at 3780 cm $^{-1}$ for H_2, while for D_2 an overlap of vibrons from Phases III and IV are observed at 2740 cm^{-1} and 2675 cm^{-1} respectively. Ultimately, for external studies to confirm the existence of the new phases recently reported, vibron frequencies within the stability range of the phase must be reported.

To conclude, estimations of the minimum pressure for metallization from extrapolations of band gap measurements give a pressure of 375 GPa as the minimum pressure for complete band gap closure. Extrapolating the H_2 vibron frequency versus pressure, gives a value of 2350 $\pm$ 50 cm^{-1}, which can be considered the minimum vibron frequency value at which hydrogen will become conductive under complete band gap closure.

Chapter 6

Exploring the stability of phase IV in the *P-T* space

6.1 Introduction

The experimental discovery of phase IV of hydrogen (deuterium) is exemplary of how studies of hydrogen at multi-megabar pressures is constitutive to the understanding of the pressure induced complexity in simple systems at extreme compressions [Howie 12a]. At 300 K, hydrogen transforms to phase IV at pressures above 220 GPa exhibiting quite unique and unusual Raman spectra features, which strongly suggests that the structure consists of graphene-like 6-member rings, made up of the elongated H_2 dimers and unbound H_2 molecules. Compared to the three other molecular phases (I, II and III) [Goncharov 11], little is known about the stability field of phase IV. Experiments aimed at determining the stability fields of $H_2(D_2)$ are highly desirable and of fundamental interest, because they are expected to provide a clear picture of the hydrogen phase diagram and therefore reveal new aspects relevant to theoretical modelling and interpretation.

In a second set of experiments, phases III and IV of H_2 and D_2 have been mapped out up to 300 GPa and between 200 and 300 K. Samples were initially compressed at 300 K. At the desired pressure, the cell was mounted in a custom-built continuous-flow cryostat (see Chapter 3) and Raman measurements were

performed on cooling/warming scans between 200 and 300 K. Both 514 nm Ar^+ and 647 nm Kr^+ ion excitation wavelengths were used for Raman measurements up to pressures of 200 GPa. Above 200 GPa, only the 647 nm excitation line was used to minimise the pressure-induced background fluorescence from the diamond anvils. Raman spectra were collected with 3 s exposure time with a laser power of 40 mW. The pressure of the samples below 90 GPa were initially measured with the frequency of the $H_2(D_2)$ main fundamental vibrational mode (ν_1), which was pre-calibrated to the ruby standard in a separate loading. Above 90 GPa, pressure was measured with the frequency of the T_{2g} Raman band of the stressed diamond edge and calibrated, using the scale reported in [Akahama 10b].

6.2 Low Temperature Studies

In the first set of cooling experiments, H_2 was compressed to within the stability field of phase IV at room temperature then cooled to 190 K. Figure 6.1 shows selected Raman spectra of the cooling cycle at 242 GPa. As temperature is decreased below 264 K at 242 GPa (251 K at 262 GPa), the intensities of the low frequency modes associated with phase IV decrease significantly and the ν_2 vibrational mode disappears. Within a cooling interval of 10 K, another intense low frequency Raman band emerges (Fig. 6.1). The appearance of this Raman band is in very good agreement with that observed in the literature for phase III [Goncharov 01]. Together, with the ν_1 vibron observed to harden and becoming narrower with temperature, these changes strongly indicate that there is a transformation from phase IV to phase III. The transition is reversible upon heating, and exhibits no hysteresis; the low frequency modes associated with phase IV and the ν_2 vibrational mode reappear and the ν_1 mode significantly broadens and softens.

In the second set of cooling experiments, D_2 was observed to undergo the same transition upon cooling as was observed with H_2, albeit at different P-T conditions. Selected Raman spectra of D_2 at 245 GPa and 256 GPa, and at various temperatures are shown in Fig. 6.2. At room temperature (phase IV) both ν_1 and ν_2 vibrational modes are clearly visible, having very different widths. Upon cooling at 245 GPa, the ν_1 mode of D_2 shows splitting, with a

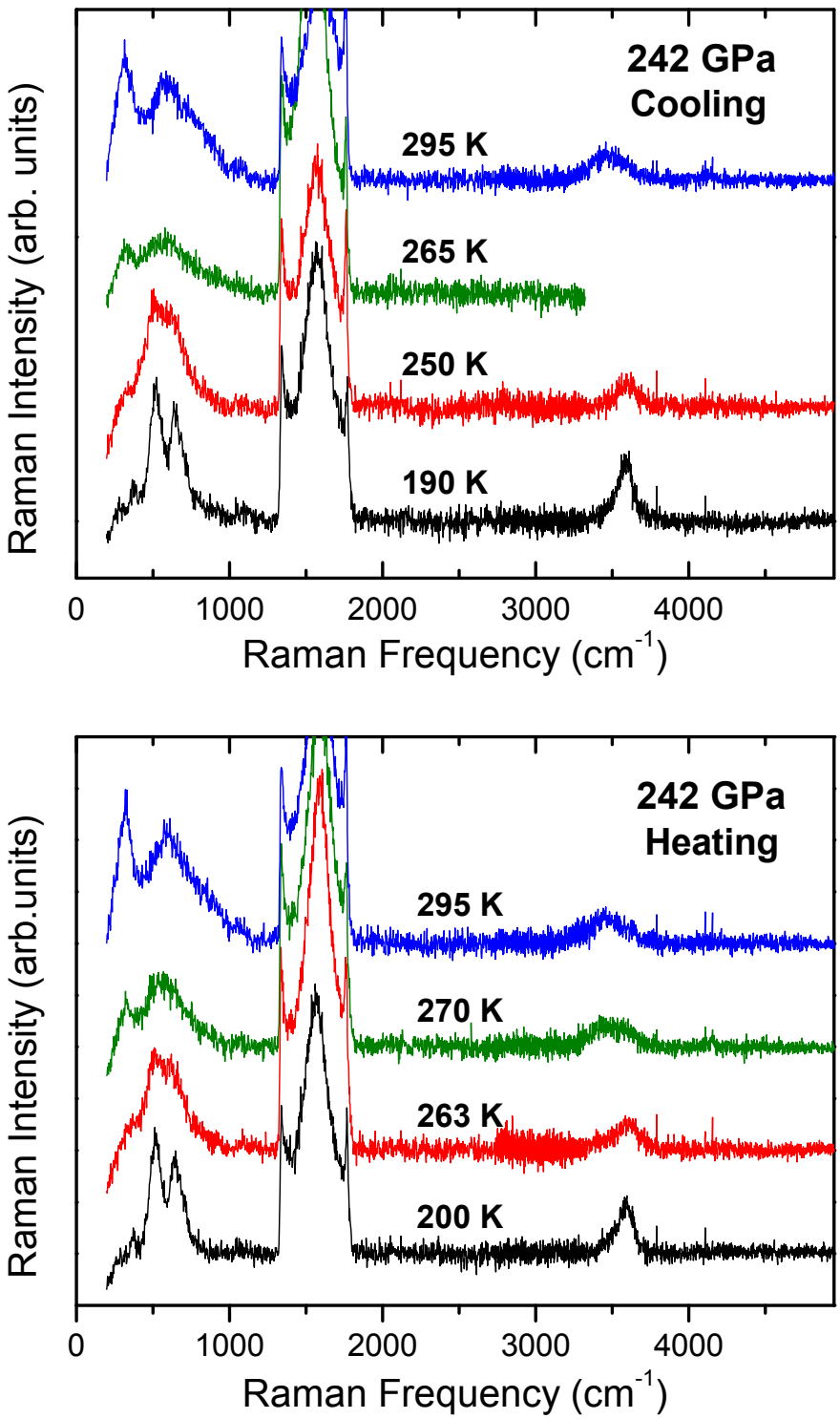

Figure 6.1: Representative Raman spectra of deuterium upon cooling (top) and warming (bottom) showing phase IV-III transformations at 242 GPa.

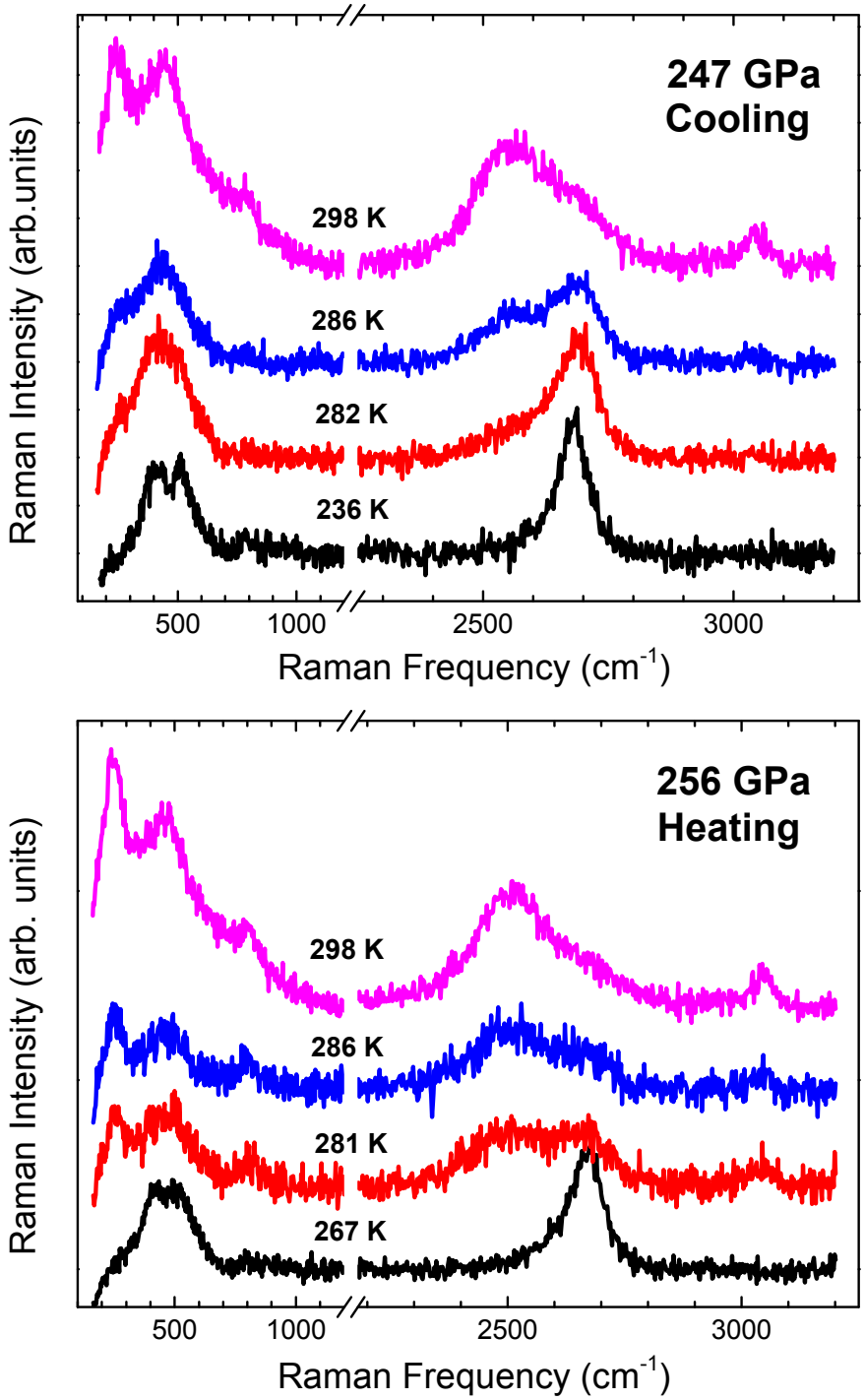

Figure 6.2: Representative Raman spectra of deuterium upon cooling (top) and warming (bottom) showing phase IV-III transformations at 247 and 256 GPa.

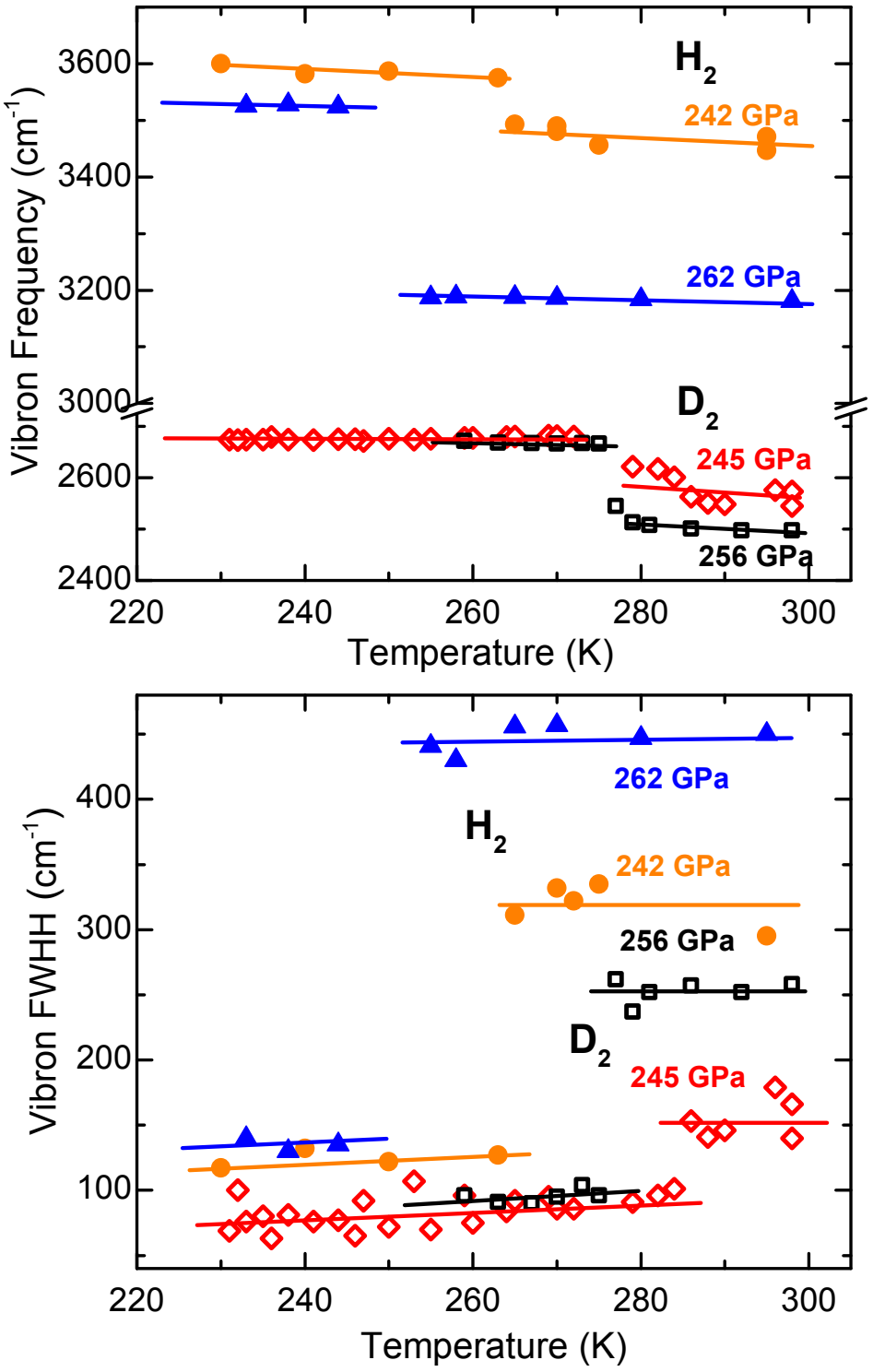

Figure 6.3: Top: Frequency discontinuities of the ν_1 modes of H_2 (filled triangles, 262 GPa; filled circles, 242 GPa) and D_2 (open squares, 256 GPa; open diamonds, 247 GPa) across the III-to-IV transformations. Bottom: FWHH of the ν_1 vibrons of H_2 (filled triangles, 262 GPa; filled circles, 242 GPa) and and D_2 (open squares, 256 GPa; open diamonds, 247 GPa) plotted versus temperature. Note the similar values of FWHH for both isotopes in phase III.

higher frequency band emerging from phase III and the lower band from the remaining phase IV (see Fig. 6.2). Upon cooling, the intensities of all Raman modes associated with phase IV decreases, while new peaks appear and grow. By 285 K, the transition to phase III is complete, the ν_2 mode disappears and the ν_1 hardens significantly. The temperature scans at the higher pressure of 256 GPa show identical changes in the Raman spectra, although at different transition temperatures. To the knowledge of the author, there are no published Raman spectra of low frequency modes in phase III of deuterium to compare our data with. However, the overall spectrum appearances [Goncharov 01] and $\sqrt{2}$ scaling of the corresponding modes frequencies between H_2 and D_2 [Silvera 80] unequivocally demonstrate that the phase at low temperatures is phase III. The phase III to phase IV transformations in both isotopes are very well defined, happen within a 10 K interval and are reversible without any hysteresis both in pressure and temperature, which is expected from the light materials with high ZPE.

The spectral positions of the fundamental vibrational modes of both isotopes shift considerably during the phase transition and the value of the shift increases with increasing pressure and decreasing temperature (Fig. 6.3). For example, when phase IV is reached at 300 K (at 220 (230) GPa for H_2 (D_2)), there is no discontinuity of the vibron mode frequency but only slight change of the frequency versus pressure slope. However, as pressure increased above 220 (230) GPa, and temperature lowered, the vibron modes frequencies undergo discontinuous hardening upon entering phase III from phase IV (see Figs. 6.3 and 6.4).

The most interesting observation is the discontinuity of the FWHH of the ν_1 mode at the III-to-IV transition, which reflects fundamental changes during the transformation and demonstrates quite unusual characteristics of phase IV. Fig. 6.3 shows the FWHH of ν_1 vibron of $D_2(H_2)$ versus T at different pressures. In phase III, the FWHH of the ν_1 is marginally larger for hydrogen; between 290 and 250 GPa the ν_1 width is from 150 to 100 cm^{-1}, while for D_2, it is from 100 to 75 cm^{-1}. However, in the same pressure range (290 to 250 GPa), the behaviour changes quite drastically upon warming. By raising temperature by an interval of 10 K, thus entering phase IV, the H_2-ν_1 broadens to $\sim$450 (350) cm^{-1}, while the D_2-ν_1 reaches $\sim$250 (150) cm^{-1}. The most plausible explanation for the increased FWHH of ν_1 in phase IV, is the intermolecular proton exchange and

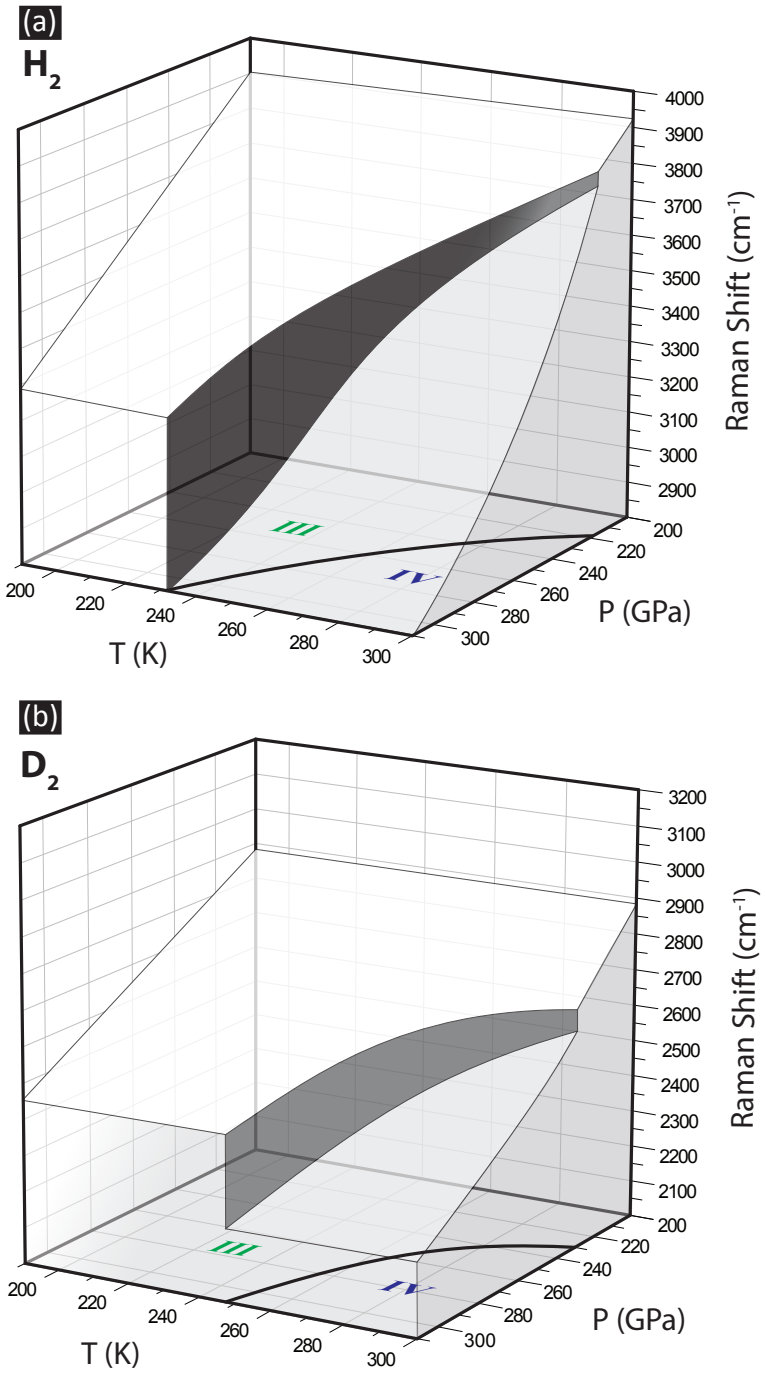

Figure 6.4: Generalized P-T-ν_1 diagrams for (a) D_2 and (b) H_2 showing the difference in the vibron frequency landscapes.

reduced life-time of molecules. The expanded intra-molecular bond-length and association of these elongated molecules in the 6-member rings [Pickard 12] would facilitate such intermolecular proton tunnelling in one phase (IV), compared to another (III) at nearly identical P-T conditions; in particular this effect will be enhanced in lighter hydrogen, as reflected by its much wider FWHH. The effect of the increased FWHH of the vibrational mode is already present in phase III [Akahama 10a, Goncharov 07], but phase III has only one type of molecule with characteristic life-time and bond-length, with the FWHH being from 75 to 150 cm^{-1} for both isotopes in a wide P-T range. The observations of the FWHH behaviour across the III-IV transformation illustrate the importance of temperature effects and that phase IV is a thermally driven partially disordered phase, contributing to the evidence for the proposed mixed atomic and molecular state of dense H_2 and D_2.

By combining the P-T scans of the ν_1 mode frequencies, the 3-D phase diagrams of both species can be constructed (Fig. 6.4). The overall appearances of the phase diagrams are markedly similar but there are several subtle differences. The phase III-to-IV transition pressures are shifted to slightly higher values for D_2. As a result, the III-IV phase line of D_2 lies above the one for H_2. Our measurements for H_2 yield the III-IV line gradient of -1.6 K/GPa, while the slope is twice as shallow for D_2, as seen in Fig. 6.4. Another difference during the III-IV transformation between the isotopes is the very different values of the vibron frequency discontinuities. With increasing pressure, the discontinuity of the III$\leftrightarrow$IV transition is increasing (see Figs 6.3 and 6.4), reaching much larger values for hydrogen, e.g. $\sim$500 cm^{-1} for H_2 at 315 GPa and 250 cm^{-1} for D_2 at 300 GPa. These are the largest discontinuities observed between the different phases; for comparison the largest value of the frequency softening of the ν_1 mode upon entering phase III from II is only around 100 cm^{-1} for *both* H_2 and D_2 [Hemley 88, Goncharov 95].

6.3 Discussion

Recent DFT calculations have proposed the $C2/c$ structure as a possible candidate for phase III and the re-entrance back into a molecular phase V ($Cmca$-

12 above 280 [Pickard 12] or *Cmca*-4 above 250 GPa [Liu 12]), which appears to have metallic properties in both studies. Fig. 6.5 shows a comparison between the low temperature, experimentally observed, phase III and the theoretically calculated Raman intensities and spectral positions of the hydrogen bands of the $C2/c$ structure (phase III) and *Cmca*-12) (phase V) at 250 GPa. Although the experimentally observed spectral position and intensity of the ν_1 vibron is in good agreement with the theoretically calculated ν_1 position and intensity, the low frequency Raman spectra are in utmost disagreement with both $C2/c$ and *Cmca*-12 structures, casting doubt on their candidacy for phase III.

The predictions of a new metallic phase V are in agreement with the recent claims of metallization of $H_2(D_2)$ at above 260 GPa [Eremets 11]. However, the results presented in this work for phase IV are in strong disagreement with Ref. [Eremets 11] (see Chapter 5.4.2). The P-T phase diagram of H_2 is displayed in Fig. 6.6, showing the theoretically proposed phase III-IV-V transition lines [Pickard 12, Liu 12]. Although the calculated phase III-IV boundaries are in good agreement with experiment, the phase IV-V boundary clearly passes within the stability range of phase IV. As the theoretically proposed molecular metallic phases are Raman active, there would be significant changes in the Raman spectra at the transition. Changes would be both in the low frequency Raman bands and with the possible disappearance of ν_2: this is at a variance with the reproducibly experimentally observed persistence of the Raman bands associated with phase IV above 220 GPa at room temperature.

The claim of a metallic phase V also contradicts experiments conducted at identical compressions in the low temperature regime [Loubeyre 02, Akahama 10a, Zha 12], whereby phase III is observed to persist up to 360 GPa below 100 K. In a recent infra-red study, H_2 was compressed to 360 GPa and infra-red measurements conducted over a broad P-T range [Zha 12]. Phase IV was not observed and the study concluded that the observations of a pronounced IR vibron, together with no discontinuities in frequency as a function of pressure and temperature, indicated that phase III persists over the broad P-T covered in the study. Plotting the P-T conditions based on the IR spectra presented in [Zha 12] on the phase diagram of hydrogen (Fig. 6.6), it becomes apparent that the P-T conditions reached in the IR study were never within the stability regime of phase IV. IR studies would be greatly beneficial in order to gain further insight into both the

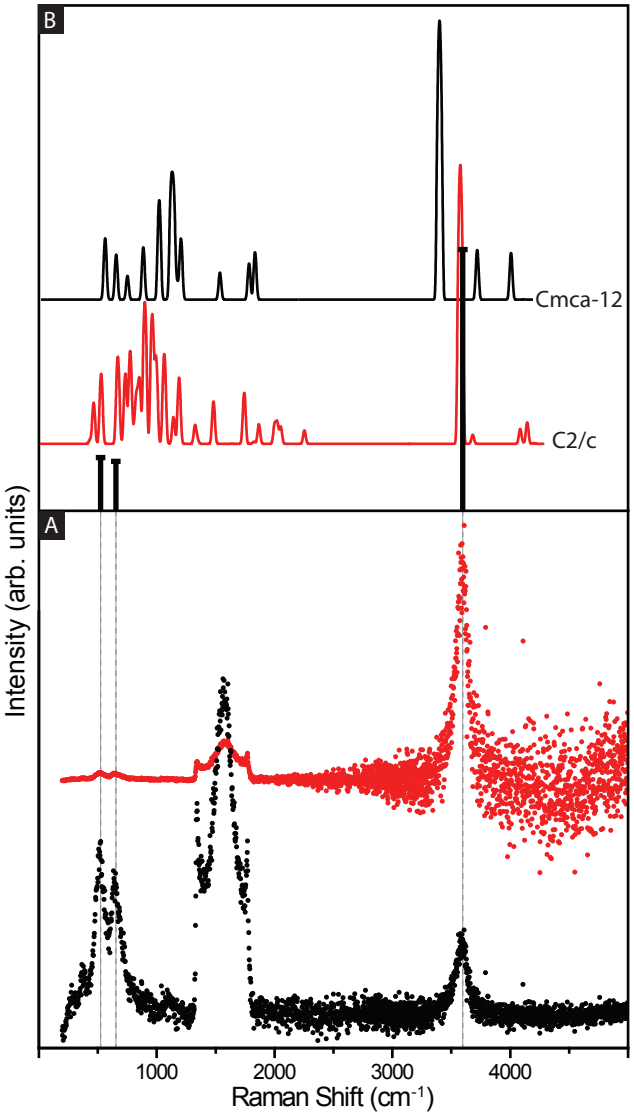

Figure 6.5: Comparison of the experimentally observed and theoretically calculated [Pickard 12] Raman intensities and spectral positions of the hydrogen bands at 250 GPa. (A) Experimental raw spectra observed in phase III (in black); spectra corrected for decreasing sensitivity of the detector are shown above (in red). The broad peaks between 1333 cm^{-1} and 1800 cm^{-1} are due to the first order Raman from diamond. (B) Experimental renormalized spectra plotted as Gaussian distributions for phase III (vertical black lines); theoretically calculated spectra for Cmca-12 (blue) and C2/c (red). The intensities for renormalized and theoretically calculated spectra are plotted on a logarithmic scale to clearly compare the weaker low frequency modes.

structure and properties of phase IV.

In order to better understand the connection between phase IV, the melting curve, and predicted atomic liquid states [Gregoryanz 03, Tamblyn 10, Morales 10], further investigations are clearly needed. The phase I-III-IV triple points are tentatively placed at 210 GPa and 325 K for H_2 and 205 GPa and 330 K for D_2, however the slope of the phase I-IV boundary needs to be established. This boundary is of particular interest, because it has important consequences for the behaviour of the melting curve. Independently of the phase IV slope boundary, it is very likely that the melting curve will change its slope at some P-T condition, because phases I and IV are very dissimilar. Depending on whether the slope has a positive or negative gradient, one could expect that the predicted ground liquid state [Babaev 04] could be realized at higher pressures or may be not realized at all, as in case of lithium [Guillaume 11]. It is interesting to note that the intersection of the molecular to atomic liquid states boundary predicted theoretically [Tamblyn 10, Morales 10] and the extrapolation of the melting curve [Gregoryanz 03] is in close proximity to the stability field of phase IV. This is a clear indication of the connection between changes in both liquid and solid states in this interesting and unusual material.

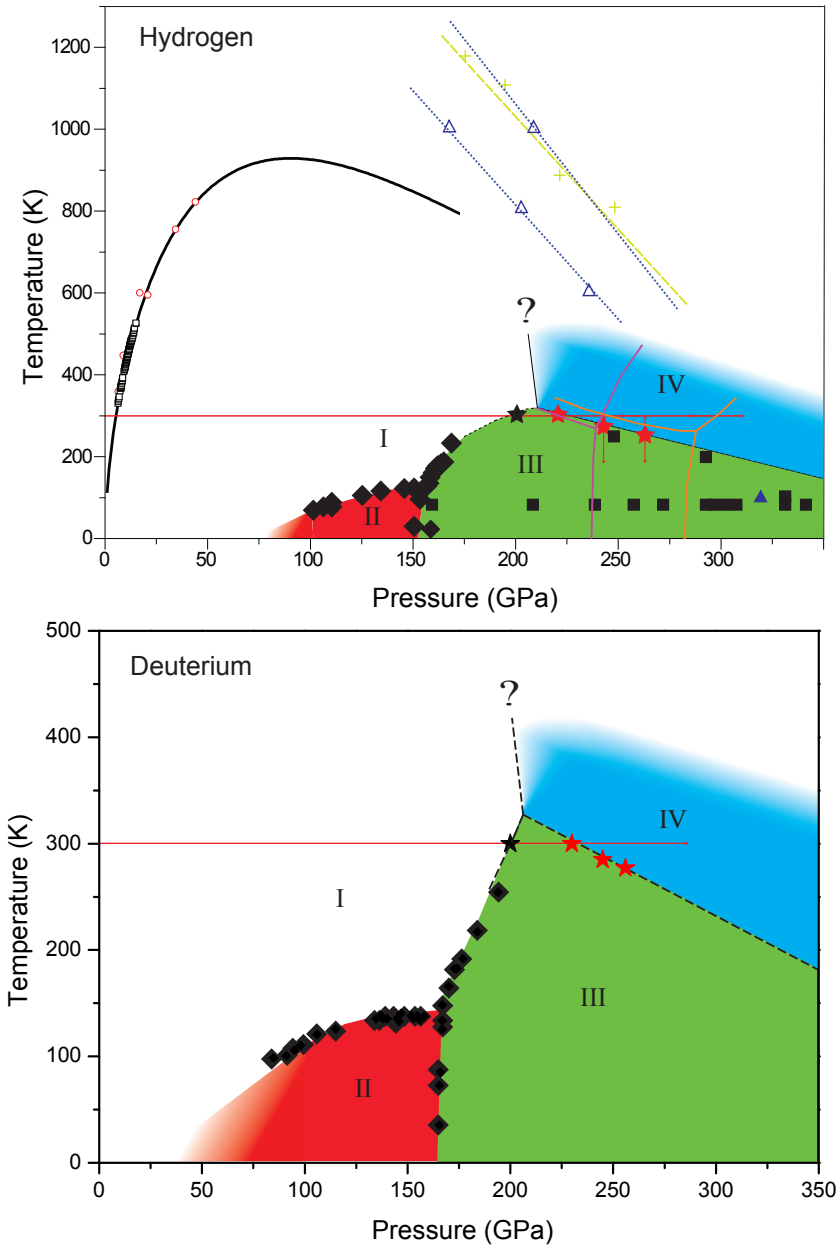

Figure 6.6: Proposed phase diagram of H_2 (top) and D_2 (bottom). The melting curve (thick solid line) of H_2 is a Ketchin fit from [Gregoryanz 03] and the symbols along it are from [Datchi 00, Gregoryanz 03]. The black diamonds separating the phases I, II and III of H_2 and D_2 are from [Goncharov 11]. The thin red solid lines show the P-T paths taken in this study and the stars along them show phase I to III and III to IV transformations. The dashed lines are proposed boundaries between I-III, III-IV and I-IV phases. The solid purple and orange lines show the theoretically predicted phase III-IV-V transition lines [Pickard 12, Liu 12]. The calculated transition lines between molecular and atomic liquid H_2 are shown with dashed lines and crosses [Tamblyn 10] and triangles [Morales 10].

Chapter 7

Conclusion

The aim of this thesis was to study hydrogen and deuterium at pressure and temperature conditions previously unattainable. In surpassing these conditions, a new phase of hydrogen, phase IV, has been observed; the first solid phase to be discovered in the past 25 years.

The first set of experimental results used Raman and visible transmission spectroscopy to investigate dense hydrogen (deuterium) up to 318 (275) GPa at 300 K. Above 190 (185) GPa, there is a transition from phase I to phase III which is the first solid-to-solid phase transition to be observed in hydrogen and deuterium at room temperature. This is succeeded at 220 GPa by a reversible transformation to a new phase, IV. This phase is characterized by the simultaneous appearance of the second vibrational fundamental mode and new low-frequency phonon excitations, and a dramatic softening and broadening of the first vibrational fundamental mode. The optical transmission spectra of phase IV show an overall increase of absorption and a closing band gap which reaches 1.8 eV at 315 GPa. The extrapolation of the band gap yields 375 GPa as the minimum transition pressure to the metallic state of hydrogen (deuterium).

Analysis of the Raman spectra suggests that phase IV is a mixture of graphene-like layers, consisting of elongated dimers, and unbound molecules. The discovery of phase IV has stimulated many theoretical studies in predicting candidate structures. All predicted candidates are structurally similar but differing slightly in symmetry [Pickard 12, Liu 12]. Furthermore, features of the Raman spectra,

together with MD simulations, indicate that the phase IV structure exhibits remarkable fluxional characteristics that are related to its quantum nature [Goncharov 13].

Experiments aimed at determining the stability fields of hydrogen and deuterium are highly desirable and of fundamental interest, because they are expected to provide a clear picture of the phase diagram and, therefore, reveal new aspects relevant to the theoretical modelling and interpretation. In a series of low-temperature experiments, phases III and IV were mapped out up to 270 GPa, imposing constraints on the P-T phase diagram. The low temperature stability of phase IV was investigated, revealing differences in the stability fields between the isotopes and similarities in the electronic structure. The spectral features of the phase IV-III transition and differences in appearances of the isotopes Raman spectra strongly indicate the presence of proton tunnelling in phase IV.

Although the discovery of phase IV is of fundamental importance in the understanding of hydrogen and deuterium, key questions still remain about the higher pressure behaviour. Theoretical predictions propose that phase IV may transform to a metallic molecular phase [Pickard 12, Liu 12] and could compete with monatomic phases at similar compressions [McMahon 11, Labet 12]. Although no further phase transformations were observed in experiments, minute changes in the optical spectra above 275 GPa might suggest the presence of a new solid modification of hydrogen (deuterium), closely related structurally to phase IV.

With the continuous improvement of static compression techniques, experimental studies may soon be within range of routinely reaching pressures above 300 GPa [Dubrovinsky 12]. Accessing such a pressure regime will succeed in both verifying theoretical predictions and unifying experiments. Such studies will no doubt allude to the existence of the predicted ground state fluid atomic metallic hydrogen [Babaev 04]. There is still so much more to learn and understand about the complexity of element number one.

Appendix A

The variation of the polarizability of a molecule with respect to direction can be defined in the form of a tensor, due to the polarizability of a molecule varying for different directions in space:

$$\alpha_{ij} = \begin{bmatrix} \alpha_{xx} & \alpha_{xy} & \alpha_{xz} \\ \alpha_{xx} & \alpha_{xy} & \alpha_{xz} \\ \alpha_{xx} & \alpha_{xy} & \alpha_{xz} \end{bmatrix}$$

If the molecule itself vibrates with a certain frequency, then the components of the polarization can be represented in the following approximation:

$$\alpha_{ij} = (\alpha_{ij})_0 + (\frac{d\alpha_{ij}}{dQ})_0 Q \tag{7.1}$$

where $(\alpha_{ij})_0$ is the value of α_{ij} at the nuclei equilibrium positions and $(\frac{d\alpha_{ij}}{dQ})$ is the change of polarization tensor α_{ij}, describing the displacement of the atoms in the molecule during vibration about their equilibrium positions. The normal mode, Q, varies as the following function:

$$Q = Acos(\omega_M t) \tag{7.2}$$

where A is the amplitude of the normal vibration of angular frequency ω_M. Substituting Eqn. (7.1) and Eqn. (7.2) into Eqn. (3.6), one finds a more refined equation for the induced dipole moment:

$$\mu_{ind} = \alpha_0 \boldsymbol{E_0} cos(2\pi\nu_0 t) + \frac{1}{2}(\frac{d\alpha_{ij}}{dQ})_0 A \boldsymbol{E_0}[cos(2\pi(\nu_0 - \nu_M)t) - cos(2\pi(\nu_0 + \nu_M)t) \tag{7.3}$$

Bibliography

[Akahama 06] Yuichi Akahama & Haruki Kawamura. *Pressure calibration of diamond anvil Raman gauge to 310 GPa*. Journal of Applied Physics, vol. 100, no. 4, page 043516, 2006.

[Akahama 10a] Y Akahama, H Kawamura, N Hirao, Y Ohishi & K Takemura. *Raman scattering and x-ray diffraction experiments for phase III of solid hydrogen*. Journal of Physics: Conference Series, vol. 215, no. 1, page 012056, 2010.

[Akahama 10b] Yuichi Akahama & Haruki Kawamura. *Pressure calibration of diamond anvil Raman gauge to 410 GPa*. Journal of Physics: Conference Series, vol. 215, no. 1, page 012195, 2010.

[Akahama 10c] Yuichi Akahama, Manabu Nishimura, Haruki Kawamura, Naohisa Hirao, Yasuo Ohishi & Kenichi Takemura. *Evidence from x-ray diffraction of orientational ordering in phase III of solid hydrogen at pressures up to 183 GPa*. Phys. Rev. B, vol. 82, page 060101, Aug 2010.

[Anderson 71] A. Anderson, editeur. The raman effect. Marcel Dekker, Inc., New York, 1971.

[Antonov 02] V.E Antonov. *Phase transformations, crystal and magnetic structures of high-pressure hydrides of d-metals*. Journal of Alloys and Compounds, vol. 330–332, no. 0, pages 110 – 116, 2002.

[Ashcroft 68] N. W. Ashcroft. *Metallic Hydrogen: A High-Temperature Superconductor?* Phys. Rev. Lett., vol. 21, pages 1748–1749, Dec 1968.

[Babaev 04] Egor Babaev, Asle Sudbo & N. W. Ashcroft. *A superconductor to superfluid phase transition in liquid metallic hydrogen*. Nature, vol. 431, no. 7009, pages 666–668, 10 2004.

[Baer 07] Bruce J. Baer, William J. Evans & Choong-Shik Yoo. *Coherent Anti-Stokes Raman Spectroscopy of Highly Compressed Solid Deuterium at 300 K: Evidence for a New Phase and Implications for the Band Gap*. Phys. Rev. Lett., vol. 98, page 235503, Jun 2007.

[Baer 08] Bruce J. Baer, Melanie E. Chang & William J. Evans. *Raman shift of stressed diamond anvils: Pressure calibration and culet geometry dependence.* Journal of Applied Physics, vol. 104, no. 3, page 034504, 2008.

[Baer 09] Bruce J. Baer, William J. Evans & Choong-Shik Yoo. *Erratum: Coherent Anti-Stokes Raman Spectroscopy of Highly Compressed Solid Deuterium at 300 K: Evidence for a New Phase and Implications for the Band Gap [Phys. Rev. Lett. 98, 235503 (2007)].* Phys. Rev. Lett., vol. 102, page 209901, May 2009.

[Banwell 94] C.N. Banwell & E.M. McCash. Fundamentals of molecular spectroscopy. McGraw-Hill International (UK) Limited, 1994.

[Bell 84] P. M. Bell, H. K. Mao & K. Goettel. *Ultrahigh Pressure: Beyond 2 Megabars and the Ruby Fluorescence Scale.* Science, vol. 226, no. 4674, pages 542–544, 1984.

[Cui 95] Lijing Cui, Nancy H. Chen & Isaac F. Silvera. *Excitations, order parameters, and phase diagram of solid deuterium at megabar pressures.* Phys. Rev. B, vol. 51, pages 14987–14997, Jun 1995.

[Datchi 00] Frédéric Datchi, Paul Loubeyre & René LeToullec. *Extended and accurate determination of the melting curves of argon, helium, ice* (H_2O), *and hydrogen* (H_2). Phys. Rev. B, vol. 61, pages 6535–6546, Mar 2000.

[Deemyad 08] Shanti Deemyad & Isaac F. Silvera. *Melting Line of Hydrogen at High Pressures.* Phys. Rev. Lett., vol. 100, page 155701, Apr 2008.

[Degtyareva 09] Olga Degtyareva, John E. Proctor, Christophe L. Guillaume, Eugene Gregoryanz & Michael Hanfland. *Formation of transition metal hydrides at high pressures.* Solid State Communications, vol. 149, no. 39–40, pages 1583 – 1586, 2009.

[Dubrovinsky 12] Leonid Dubrovinsky, Natalia Dubrovinskaia, Vitali B Prakapenka & Artem M Abakumov. *Implementation of micro-ball nanodiamond anvils for high-pressure studies above 6[thinsp]Mbar.* Nat Commun, vol. 3, page 1163, 10 2012.

[Eggert 99] Jon H. Eggert, Eran Karmon, Russell J. Hemley, Ho-kwang Mao & Alexander F. Goncharov. *Pressure-enhanced ortho-para conversion in solid hydrogen up to 58 GPa.* Proceedings of the National Academy of Sciences, vol. 96, no. 22, pages 12269–12272, 1999.

[Eremets 08] M. I. Eremets, I. A. Trojan, S. A. Medvedev, J. S. Tse & Y. Yao. *Superconductivity in Hydrogen Dominant Materials: Silane.* Science, vol. 319, no. 5869, pages 1506–1509, 2008.

[Eremets 09] Mikhail I. Eremets & Ivan A. Trojan. *Evidence of Maximum in the Melting Curve of Hydrogen at Megabar Pressures.* JETP Letters, vol. 89, pages 174–179, 2009.

[Eremets 11] M. I. Eremets & I. A. Troyan. *Conductive dense hydrogen.* Nat Mater, vol. 10, no. 12, pages 927–931, 12 2011.

[Freeman 74] S. Freeman. Applications of laser raman spectroscopy. John Wiley Sons Ltd. New York, 1974.

[Gierak 09] Jacques Gierak. *Focused ion beam technology and ultimate applications.* Semiconductor Science and Technology, vol. 24, no. 4, page 043001, 2009.

[Goncharenko 05] Igor Goncharenko & Paul Loubeyre. *Neutron and X-ray diffraction study of the broken symmetry phase transition in solid deuterium.* Nature, vol. 435, no. 7046, pages 1206–1209, 06 2005.

[Goncharov 95] Alexander F. Goncharov, I. I. Mazin, Jon H. Eggert, Russell J. Hemley & Ho-kwang Mao. *Invariant Points and Phase Transitions in Deuterium at Megabar Pressures.* Phys. Rev. Lett., vol. 75, pages 2514–2517, Sep 1995.

[Goncharov 96] Alexander F. Goncharov, Jon H. Eggert, I. I. Mazin, Russell J. Hemley & Ho-kwang Mao. *Raman excitations and orientational ordering in deuterium at high pressure.* Phys. Rev. B, vol. 54, pages R15590–R15593, Dec 1996.

[Goncharov 98] Alexander F. Goncharov, Russell J. Hemley, Ho-kwang Mao & Jinfu Shu. *New High-Pressure Excitations in Parahydrogen.* Phys. Rev. Lett., vol. 80, pages 101–104, Jan 1998.

[Goncharov 99] Alexander F. Goncharov, Viktor V. Struzhkin, Ho-kwang Mao & Russell J. Hemley. *Raman Spectroscopy of Dense* H_2O *and the Transition to Symmetric Hydrogen Bonds.* Phys. Rev. Lett., vol. 83, pages 1998–2001, Sep 1999.

[Goncharov 00] Alexander F. Goncharov. *New Techniques for optical spectroscopy at ultra high pressures.* In Science and Technology of High Pressure: Proceedings of AIRAPT-17. Universities Press, Hyderabad, India, 2000, 2000.

[Goncharov 01] Alexander F. Goncharov, Eugene Gregoryanz, Russell J. Hemley & Ho-kwang Mao. *Spectroscopic studies of the vibrational and electronic properties of solid hydrogen to 285 GPa.* Proceedings of the National Academy of Sciences, vol. 98, no. 25, pages 14234–14237, 2001.

[Goncharov 03] Alexander F. Goncharov & Viktor V. Struzhkin. *Raman spectroscopy of metals, high-temperature superconductors and related materials under high pressure.* Journal of Raman Spectroscopy, vol. 34, no. 7-8, pages 532–548, 2003.

[Goncharov 07] Alexander F. Goncharov & Jonathan Crowhurst. *Proton delocalization under extreme conditions of high pressure and temperature.* Phase Transitions, vol. 80, no. 10-12, pages 1051–1072, 2007.

[Goncharov 09] Alexander Goncharov, Russell J. Hemley & E. Gregoryanz. *Comment on "Melting Line of Hydrogen at High Pressures".* Phys. Rev. Lett., vol. 102, page 149601, Apr 2009.

[Goncharov 11] Alexander F. Goncharov, Russell J. Hemley & Ho kwang Mao. *Vibron frequencies of solid H2 and D2 to 200 GPa and implications for the P–T phase diagram.* The Journal of Chemical Physics, vol. 134, no. 17, page 174501, 2011.

[Goncharov 13] Alexander F. Goncharov, John S. Tse, Hui Wang, Jianjun Yang, Viktor V. Struzhkin, Ross T. Howie & Eugene Gregoryanz. *Bonding, structures, and band gap closure of hydrogen at high pressures.* Phys. Rev. B, vol. 87, page 024101, Jan 2013.

[Gregoryanz 03] Eugene Gregoryanz, Alexander F. Goncharov, Kiyoto Matsuishi, Ho-kwang Mao & Russell J. Hemley. *Raman Spectroscopy of Hot Dense Hydrogen.* Phys. Rev. Lett., vol. 90, page 175701, Apr 2003.

[Gregoryanz 05] Eugene Gregoryanz, Olga Degtyareva, Maddury Somayazulu, Russell J. Hemley & Ho-kwang Mao. *Melting of Dense Sodium.* Phys. Rev. Lett., vol. 94, page 185502, May 2005.

[Gregoryanz 08] Eugene Gregoryanz, Lars F. Lundegaard, Malcolm I. McMahon, Christophe Guillaume, Richard J. Nelmes & Mohamed Mezouar. *Structural Diversity of Sodium.* Science, vol. 320, no. 5879, pages 1054–1057, 2008.

[Guillaume 11] Christophe L. Guillaume, Eugene Gregoryanz, Olga Degtyareva, Malcolm I. McMahon, Michael Hanfland, Shaun Evans, Malcolm Guthrie, Stanislav V. Sinogeikin & H-K. Mao. *Cold melting and solid structures of dense lithium.* Nat Phys, vol. 7, no. 3, pages 211–214, 03 2011.

[Hanfland 85] M. Hanfland & K. Syassen. *A Raman study of diamond anvils under stress.* Journal of Applied Physics, vol. 57, no. 8, pages 2752–2756, 1985.

[Hanfland 93] Michael Hanfland, Russell J. Hemley & Ho-kwang Mao. *Novel infrared vibron absorption in solid hydrogen at megabar pressures.* Phys. Rev. Lett., vol. 70, pages 3760–3763, Jun 1993.

[Hanfland 11] Michael Hanfland, John E. Proctor, Christophe L. Guillaume, Olga Degtyareva & Eugene Gregoryanz. *High-Pressure Synthesis, Amorphization, and Decomposition of Silane.* Phys. Rev. Lett., vol. 106, page 095503, Mar 2011.

[Hayes 78] W. Hayes & R. Loudon. Scattering of light by crystals. John Wiley Sons, Ltd., New York, 1978.

[Hazen 87] R. M. Hazen, H. K. Mao, L. W. Finger & R. J. Hemley. *Single-crystal x-ray diffraction of n-H_2 at high pressure.* Phys. Rev. B, vol. 36, pages 3944–3947, Sep 1987.

[Hemley 88] R. J. Hemley & H. K. Mao. *Phase Transition in Solid Molecular Hydrogen at Ultrahigh Pressures.* Phys. Rev. Lett., vol. 61, pages 857–860, Aug 1988.

[Herzberg 60] G. Herzberg. Molecular spectra and molecular structure. D. Van Nostrand Company, New York, 1960.

[Howie 12a] Ross T. Howie, Christophe L. Guillaume, Thomas Scheler, Alexander F. Goncharov & Eugene Gregoryanz. *Mixed Molecular and Atomic Phase of Dense Hydrogen.* Phys. Rev. Lett., vol. 108, page 125501, Mar 2012.

[Howie 12b] Ross T. Howie, Olga Narygina, Christophe L. Guillaume, Shaun Evans & Eugene Gregoryanz. *High-pressure synthesis of lithium hydride.* Phys. Rev. B, vol. 86, page 064108, Aug 2012.

[Ibach 90] H. Ibach & H. Luth. Solid-state physics. Springer-Verlag, Berlin, 1990.

[Iqbal 84] Z. Iqbal & F. Owens. Vibrational spectroscopy of phase transitions. Academic Press, Inc, Orlando, 1984.

[Jayaraman 83] A. Jayaraman. *Diamond anvil cell and high-pressure physical investigations.* Rev. Mod. Phys., vol. 55, pages 65–108, Jan 1983.

[Johnson 00] Kurt A. Johnson & N. W. Ashcroft. *Structure and bandgap closure in dense hydrogen.* Nature, vol. 403, no. 6770, pages 632–635, 02 2000.

[Kawai 75] N. Kawai, M. Togay & O. Mishima. *Experimental Metallization of Hydrogen.* Proc. of the Japan Academy, vol. 51, pages 630–633, 1975.

[Kitamura 00] Hikaru Kitamura, Shinji Tsuneyuki, Tadashi Ogitsu & Takashi Miyake. *Quantum distribution of protons in solid molecular hydrogen at megabar pressures.* Nature, vol. 404, no. 6775, pages 259–262, 03 2000.

[Kohanoff 97] Jorge Kohanoff, Sandro Scandolo, Guido L. Chiarotti & Erio Tosatti. *Solid Molecular Hydrogen: The Broken Symmetry Phase.* Phys. Rev. Lett., vol. 78, pages 2783–2786, Apr 1997.

[Kranendonk 83] J. Van Kranendonk. Solid hydrogen. Plenum, New York, 1983.

[Labet 12] Vanessa Labet, Roald Hoffmann & N. W. Ashcroft. *A fresh look at dense hydrogen under pressure. IV. Two structural models on the road from paired to monatomic hydrogen, via a possible non-crystalline phase.* The Journal of Chemical Physics, vol. 136, no. 7, page 074504, 2012.

[Landsberg 58] Landsberg. Selected works. Izdatel'stvo AN SSSR, Moscow, 1958.

[Lazicki 09] A. Lazicki, A. F. Goncharov, V. V. Struzhkin, R. E. Cohen, Z. Liu, E. Gregoryanz, C. Guillaume, H.-K. Mao & Russell J. Hemley. *Anomalous optical and electronic properties of dense sodium.* Proceedings of the National Academy of Sciences, vol. 106, no. 16, pages 6525–6528, 2009.

[Liu 12] Hanyu Liu, Li Zhu, Wenwen Cui & Yanming Ma. *Room-temperature structures of solid hydrogen at high pressures.* The Journal of Chemical Physics, vol. 137, no. 7, page 074501, 2012.

[Lorenzana 89] Hector E. Lorenzana, Isaac F. Silvera & Kenneth A. Goettel. *Evidence for a structural phase transition in solid hydrogen at megabar pressures.* Phys. Rev. Lett., vol. 63, pages 2080–2083, Nov 1989.

[Lorenzana 90] Hector E. Lorenzana, Isaac F. Silvera & Kenneth A. Goettel. *Orientational phase transitions in hydrogen at megabar pressures.* Phys. Rev. Lett., vol. 64, pages 1939–1942, Apr 1990.

[Loubeyre 02] Paul Loubeyre, Florent Occelli & Rene LeToullec. *Optical studies of solid hydrogen to 320 GPa and evidence for black hydrogen.* Nature, vol. 416, no. 6881, pages 613–617, 04 2002.

[Lundegaard 09] L. F. Lundegaard, E. Gregoryanz, M. I. McMahon, C. Guillaume, I. Loa & R. J. Nelmes. *Single-crystal studies of incommensurate Na to 1.5 Mbar.* Phys. Rev. B, vol. 79, page 064105, Feb 2009.

[Ma 09] Yanming Ma, Mikhail Eremets, Artem R. Oganov, Yu Xie, Ivan Trojan, Sergey Medvedev, Andriy O. Lyakhov, Mario Valle & Vitali Prakapenka. *Transparent dense sodium.* Nature, vol. 458, no. 7235, pages 182–185, 03 2009.

[Mandelstam 47] L. Mandelstam. Selected works. Izdatel'stvo AN SSSR, Moscow, 1947.

[Mao 76] H. K. Mao & P. M. Bell. *High-Pressure Physics: The 1-Megabar Mark on the Ruby R1 Static Pressure Scale.* Science, vol. 191, no. 4229, pages 851–852, 1976.

[Mao 78] H. K. Mao, P. M. Bell, J. W. Shaner & D. J. Steinberg. *Specific volume measurements of Cu, Mo, Pd, and Ag and calibration of the ruby R[sub 1] fluorescence pressure gauge from 0.06 to 1 Mbar.* Journal of Applied Physics, vol. 49, no. 6, pages 3276–3283, 1978.

[Mao 94] Ho-kwang Mao & Russell J. Hemley. *Ultrahigh-pressure transitions in solid hydrogen.* Rev. Mod. Phys., vol. 66, pages 671–692, Apr 1994.

[Marques 11] Miriam Marques, Mario Santoro, Christophe L. Guillaume, Federico A. Gorelli, Julia Contreras-Garcia, Ross T. Howie, Alexander F. Goncharov & Eugene Gregoryanz. *Optical and electronic properties of dense sodium.* Phys. Rev. B, vol. 83, page 184106, May 2011.

[Mazin 97] I. I. Mazin, Russell J. Hemley, A. F. Goncharov, Michael Hanfland & Ho-kwang Mao. *Quantum and Classical Orientational Ordering in Solid Hydrogen.* Phys. Rev. Lett., vol. 78, pages 1066–1069, Feb 1997.

[McMahon 11] Jeffrey M. McMahon & David M. Ceperley. *Ground-State Structures of Atomic Metallic Hydrogen.* Phys. Rev. Lett., vol. 106, page 165302, Apr 2011.

[Mills 65] R. L. Mills & A. F. Schuch. *Crystal Structure of Normal Hydrogen at Low Temperatures.* Phys. Rev. Lett., vol. 15, pages 722–724, Nov 1965.

[Mills 80] R. L. Mills, D. H. Liebenberg, J. C. Bronson & L. C. Schmidt. *Procedure for loading diamond cells with high-pressure gas.* Review of Scientific Instruments, vol. 51, no. 7, pages 891–895, 1980.

[Morales 10] Miguel A. Morales, Carlo Pierleoni, Eric Schwegler & D. M. Ceperley. *Evidence for a first-order liquid-liquid transition in high-pressure hydrogen from ab initio simulations.* Proceedings of the National Academy of Sciences, vol. 107, no. 29, pages 12799–12803, 2010.

[Nagao 99] Kazutaka Nagao, Tomoki Takezawa & Hitose Nagara. *Ab initio calculation of optical-mode frequencies in compressed solid hydrogen.* Phys. Rev. B, vol. 59, pages 13741–13753, Jun 1999.

[Narayana 98] Chandrabhas Narayana, Huan Luo, Jon Orloff & Arthur L. Ruoff. *Solid hydrogen at 342 GPa: no evidence for an alkali metal.* Nature, vol. 393, no. 6680, pages 46–49, 05 1998.

[Nellis 99] W. J. Nellis, S. T. Weir & A. C. Mitchell. *Minimum metallic conductivity of fluid hydrogen at 140 GPa (1.4 Mbar).* Phys. Rev. B, vol. 59, pages 3434–3449, Feb 1999.

[Occelli 03] Florent Occelli, Paul Loubeyre & Rene LeToullec. *Properties of diamond under hydrostatic pressures up to 140 GPa.* Nat Mater, vol. 2, no. 3, pages 151–154, 03 2003.

[Orloff 00] Jon Orloff, Chandrabhas Narayana & Arthur L. Ruoff. *Use of focused ion beams for making tiny sample holes in gaskets for diamond anvil cells.* Review of Scientific Instruments, vol. 71, no. 1, pages 216–219, 2000.

[Pickard 06] Chris J. Pickard & R. J. Needs. *High-Pressure Phases of Silane.* Phys. Rev. Lett., vol. 97, page 045504, Jul 2006.

[Pickard 07] Chris J. Pickard & Richard J. Needs. *Structure of phase III of solid hydrogen.* Nat Phys, vol. 3, no. 7, pages 473–476, 07 2007.

[Pickard 09] C. J. Pickard & R. J. Needs. *Structures at high pressure from random searching.* physica status solidi (b), vol. 246, no. 3, pages 536–540, 2009.

[Pickard 11] Chris J Pickard & R J Needs. *Ab initio random structure searching.* Journal of Physics: Condensed Matter, vol. 23, no. 5, page 053201, 2011.

[Pickard 12] Chris J. Pickard, Miguel Martinez-Canales & Richard J. Needs. *Density functional theory study of phase IV of solid hydrogen.* Phys. Rev. B, vol. 85, page 214114, Jun 2012.

[Piermarini 75] G. J. Piermarini, S. Block, J. D. Barnett & R. A. Forman. *Calibration of the pressure dependence of the R[sub 1] ruby fluorescence line to 195 kbar.* Journal of Applied Physics, vol. 46, no. 6, pages 2774–2780, 1975.

[Raman 28a] C.V. Raman & Krishnan K.S. *A new type of secondary radiation.* Nature, no. 121, page 501, 1928.

[Raman 28b] C.V. Raman & Krishnan K.S. *The Optical Analogue of the Compton Effect.* Nature, vol. 121, page 711, 1928.

[Reyntjens 01] Steve Reyntjens & Robert Puers. *A review of focused ion beam applications in microsystem technology.* Journal of Micromechanics and Microengineering, vol. 11, no. 4, page 287, 2001.

[Scheler 11a] Thomas Scheler, Olga Degtyareva & Eugene Gregoryanz. *On the effects of high temperature and high pressure on the hydrogen solubility in rhenium.* The Journal of Chemical Physics, vol. 135, no. 21, page 214501, 2011.

[Scheler 11b] Thomas Scheler, Olga Degtyareva, Miriam Marqués, Christophe L. Guillaume, John E. Proctor, Shaun Evans & Eugene Gregoryanz. *Synthesis and properties of platinum hydride.* Phys. Rev. B, vol. 83, page 214106, Jun 2011.

[Scheler 13] Thomas Scheler, Feng Peng, Christophe L. Guillaume, Ross T. Howie, Yanming Ma & Eugene Gregoryanz. *Structure and Mechanical Study of Tungsten Hydride.* submittted, 2013.

[Sherwood 72] P. Sherwood. Vibrational spectroscopy of solids. Cambridge University Press, London, 1972.

[Silvera 80] Isaac F. Silvera. *The solid molecular hydrogens in the condensed phase: Fundamentals and static properties.* Rev. Mod. Phys., vol. 52, pages 393–452, Apr 1980.

[Silvera 81] Isaac F. Silvera & Rinke J. Wijngaarden. *New Low-Temperature Phase of Molecular Deuterium at Ultrahigh Pressure.* Phys. Rev. Lett., vol. 47, pages 39–42, Jul 1981.

[Silvera 10] Isaac F Silvera & John W Cole. *Metallic hydrogen: The most powerful rocket fuel yet to exist.* Journal of Physics: Conference Series, vol. 215, no. 1, page 012194, 2010.

[Smekal 23] A. Smekal. *Zur Quantentheorie der Dispersion.* Naturwiss., vol. 11, page 873, 1923.

[Stadele 00] Martin Stadele & Richard M. Martin. *Metallization of Molecular Hydrogen: Predictions from Exact-Exchange Calculations.* Phys. Rev. Lett., vol. 84, pages 6070–6073, Jun 2000.

[Subramanian 11] Natarajan Subramanian, Alexander F. Goncharov, Viktor V. Struzhkin, Maddury Somayazulu & Russell J. Hemley. *Bonding changes in hot fluid hydrogen at megabar pressures.* Proceedings of the National Academy of Sciences, vol. 108, no. 15, pages 6014–6019, 2011.

[Surh 97] Michael P. Surh, K. J. Runge, T. W. Barbee, E. L. Pollock & C. Mailhiot. *Ab initio calculations for solid molecular hydrogen.* Phys. Rev. B, vol. 55, pages 11330–11341, May 1997.

[Tamblyn 10] Isaac Tamblyn & Stanimir A. Bonev. *Structure and Phase Boundaries of Compressed Liquid Hydrogen.* Phys. Rev. Lett., vol. 104, page 065702, Feb 2010.

[Upadhyaya 94] J. C. Upadhyaya, D. K. Sharma, D. Prakash & S. C. Upadhyaya. *Three-particle forces in the lattice dynamics of some hexagonal close-packed metals.* Canadian Journal of Physics, vol. 72, no. 1-2, pages 61–72, 1994.

[Vereshchagin 75] L.F. Vereshchagin, E.N. Yakovlev & Y.A. Timofeev. *Possibility of Transition of Hydrogen into the Metallic State*. JETP Lett., vol. 21, pages 85–86, 1975.

[Volkert 01] C A Volkert & A M Minor. *A review of focused ion beam technology and its applications in microsystem technology*. Jour. Micromechanics and Microengineering, vol. 11, page 287, 2001.

[Weir 96] S. T. Weir, A. C. Mitchell & W. J. Nellis. *Metallization of Fluid Molecular Hydrogen at 140 GPa (1.4 Mbar)*. Phys. Rev. Lett., vol. 76, pages 1860–1863, Mar 1996.

[Wigner 35] E. Wigner & H. B. Huntington. *On the Possibility of a Metallic Modification of Hydrogen*. The Journal of Chemical Physics, vol. 3, no. 12, pages 764–770, 1935.

[Xu 86] J. A. Xu, H. K. Mao & P. M. Bell. *High-Pressure Ruby and Diamond Fluorescence: Observations at 0.21 to 0.55 Terapascal*. Science, vol. 232, no. 4756, pages 1404–1406, 1986.

[Zha 12] Chang-Sheng Zha, Zhenxian Liu & Russell J. Hemley. *Synchrotron Infrared Measurements of Dense Hydrogen to 360 GPa*. Phys. Rev. Lett., vol. 108, page 146402, Apr 2012.

[Zhang 07] L J Zhang, Y L Niu, T Cui, Y Li, Y M Ma, Z He & G T Zou. *The broken-symmetry phase of solid hydrogen: evidence from infrared and Raman active vibrons*. Journal of Physics: Condensed Matter, vol. 19, no. 42, page 425237, 2007.

[Zurek 09] Eva Zurek, Roald Hoffmann, N. W. Ashcroft, Artem R. Oganov & Andriy O. Lyakhov. *A little bit of lithium does a lot for hydrogen*. Proceedings of the National Academy of Sciences, vol. 106, no. 42, pages 17640–17643, 2009.

Publications

T. Scheler; M. Marques; Z. Konopkova; C.L. Guillaume; R.T. Howie; E. Gregoryanz. High pressure Synthesis of Iridium-Trihydride. *submitted*.

T. Scheler; F. Peng; C.L. Guillaume; R.T. Howie; Y. Ma; E. Gregoryanz. Structure and Mechanical Study of Tungsten Hydride. *submitted*.

A.F. Goncharov; R.T. Howie; E. Gregoryanz. Hydrogen at Extreme Pressures. *Fizika Nizkikh Temperatur*, 39, 5 (2013).

A.F. Goncharov; J.S. Tse; H. Wang; J. Yang; V.V. Struzhkin; R.T. Howie; E. Gregoryanz. Bonding, structures, and band gap closure of hydrogen at high pressures. *Phys. Rev. B*, 87, 024101 (2013).

R.T. Howie, C.L. Guillaume, T. Scheler, E. Gregoryanz. Proton tunnelling in phase IV of hydrogen and deuterium. *Phys. Rev. B*, 86, 214104 (2012).

R.T. Howie, O. Narygina, C.L. Guillaume, S. Evans, E. Gregoryanz. High-pressure synthesis of lithium hydride. *Phys. Rev. B*, 86, 064108 (2012).

R.T. Howie, C.L. Guillaume, T. Scheler, A.F. Goncharov, E. Gregoryanz. Mixed Molecular and Atomic Phase of Dense Hydrogen. *Phys. Rev. Lett.*, 108, 125501 (2012).

M. Marques, S. Santoro, C.L. Guillaume, F.A. Gorelli, J. Contreras-Garcia, R.T. Howie, A.F. Goncharov, E. Gregoryanz. Optical and electronic properties of dense sodium. *Phys. Rev. B*, 83, 184106 (2011).

High-pressure synthesis and characterization of iridium-trihydride

Thomas Scheler[1], Miriam Marqués[2], Zuzana Konôpková[3],
Christophe L. Guillaume[1], Ross T. Howie[1] and Eugene Gregoryanz[1,*]
[1] *Centre for Science at Extreme Conditions, School of Physics and Astronomy, The University of Edinburgh, Edinburgh, EH9 3JZ, UK,*
[2] *MALTA Team and Dpto. Química Física y Analítica. Universidad de Oviedo, E-33006 Oviedo, Spain,*
[3] *DESY Photon Science, Notkestr. 85, 22 607 Hamburg, Germany*

We have performed *in-situ* synchrotron x-ray diffraction studies of the iridium-hydrogen system up to 125 GPa. At 55 GPa, a phase transition in the metal lattice from the *fcc*- to a distorted simple cubic phase is observed. The new phase is characterized by a drastically increased volume per metal atom, indicating the formation of a metal hydride, and substantially decreased bulk modulus of 190 GPa (383 GPa for pure Ir). *Ab-initio* calculations show, that the hydrogen atoms occupy the face-centered positions in the metal matrix, making this the first known *non-interstitial* noble metal hydride and, with a stoichiometry of IrH_3, the one with the highest volumetric hydrogen content. Computations also reveal that several energetically competing phases exist, which can all be seen as having distorted simple cubic lattices. Slow kinetics during decomposition at pressures as low as 6 GPa suggest that this material is metastable at ambient pressure and low temperatures.

PACS numbers:

High pressure as a general route to material synthesis [1–3] has been used in the past to obtain hydride phases of most transition metals under thermodynamic equilibrium conditions [4, 5]. However, in particular for the noble metals, the required pressures can be substantial (with the sole exception of palladium [6]). So far, the highest reported pressures for hydride synthesis are 25 GPa for tungsten [7, 8] and 27 GPa for platinum hydride [9]. Most known *d*-metal hydrides exhibit a closed-packed metal host lattice with hydrogen atoms occupying the octahedral or tetrahedral interstitial sites, the former being by far the most common modification [5]. Thus, these hydrides usually exhibit a hydrogen:metal (H:M) ratio close to 1, with few exceptions where higher ratios are achieved (*e.g.* rhodium-dihydride [10]). No hydride phases are known for the noble metals silver, gold [11], osmium and iridium. Interstitial hydrogen alloys are interesting due their potentially important physical properties, such as modified crystalline structures and mechanical properties [12], altered microstructure [8] (nanocrystallinity), hydrogen mediated superconductivity [13, 14] or potential hydrogen storage capabilities [10, 15, 16]. Furthermore, according to theoretical predictions, hydrogen confined in a host matrix might undergo the elusive transition to a metallic groundstate at considerably lower pressures than pure hydrogen [17, 18]. Recent studies [19] estimate the metallization pressure for pure hydrogen to be above 375 GPa, still out of reach of current static compression techniques. The formation of a hydride phase is readily observed in x-ray diffraction (XRD) measurements as an expansion of the unit-cell (see *e.g.* in rhenium [12]), or a structural phase transition with increased volume per metal atom compared to the parent metal (*e.g.* *bcc*-to-*hcp* in tungsten [7, 8, 20] or *fcc*-to-*hcp* in platinum [9]). It has been found that, due to contributing its electron to the valence band of the surrounding metal, the presence of one hydrogen atom expands the host lattice by 2-3 Å^3 (depending on the material, see Ref. [4, 5]). From the formation of the nitrides of iridium and osmium [21] at conditions identical to those at which platinum nitride forms [22], it could be argued that an equivalent behaviour might be observed for hydrogen. However, although platinum hydride readily forms at 27 GPa, no hydride phases of iridium or osmium are known.

We have performed x-ray diffraction (XRD) studies on iridium in a hydrogen medium at pressures up to 125 GPa in the diamond anvil cell (DAC) (see Ref. [23] for details). At 55 GPa an additional phase appears in XRD patterns of iridium. The new phase can easily be indexed in the $Pm\bar{3}m$ space group (simple cubic, see Figure 1) and exhibits a significantly larger volume per atom than pure iridium at the same pressure. This indicates the formation of a compound material, *i.e.* a metal hydride (as opposed to a phase transition in pure iridium). At 65 GPa, the volume difference amounts to $\sim$ 6.6 Å^3 per metal atom, substantially more than usually observed for interstitial metal hydrides (*e.g.* 2.1 Å^3 for platinum hydride [9]). Direct comparison with other metal hydrides suggests a H:M ratio of 3 (assuming full stoichiometry). However, such comparisons are not directly valid since estimating the hydrogen content by comparing unit-cell volumes is based on *empirical* findings in *interstitial* hydrides. The simple cubic lattice does not exhibit comparable interstitial sites. At room temperature, the formation of the new phase progresses very slowly at first and accelerates exponentially over time during the first 50 hours after crossing synthesis conditions (see inset Figure 1). The transition was

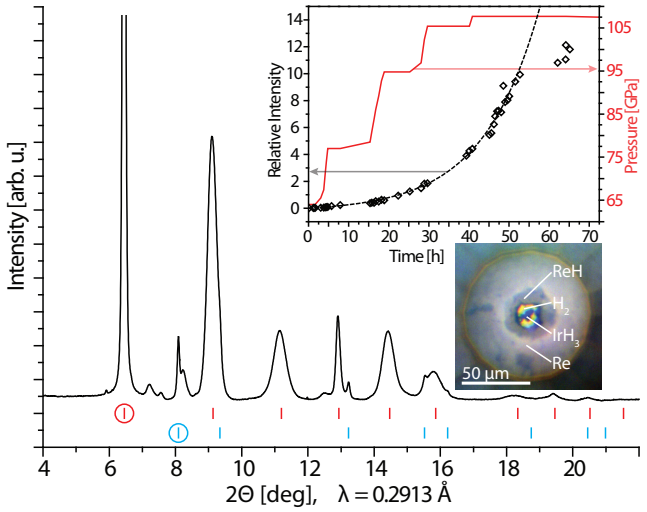

FIG. 1: Integrated x-ray diffraction pattern at 120 GPa, indexed with simple cubic iridium hydride ($a = 2.591$ Å, upper red tick marks) and *fcc* iridium ($a = 3.577$ Å, lower blue tick marks). Other visible reflections stem from rhenium hydride formed at the gasket rim. The inset shows the development over time of the relative scattering intensity (left scale) of the IrH_3 (001)-peak compared to the Ir (111)-peak (circled reflections in the diffraction pattern). The dashed line indicates an exponential guide to the eye to the data up to t=50h. The solid red line denotes the applied pressure (right scale). The optical micrograph shows the gasket and sample at 100 GPa. The extension of the rhenium hydride zone in the gasket is clearly visible.

measured through the relative scattering intensities between Bragg peaks belonging to the hydride phase and parent material measured in the same diffraction pattern. Interestingly, the progress is independent of pressure. During this period, pressure was increased to 110 GPa with no deviation from exponential growth detectable. However, after 50 h, the formation process slows down. Even after two weeks at 110 GPa, pure Ir is still present in the sample volume. We therefore employed low-power single-sided laser heating to accelerate the formation process. Indeed, within a few minutes, the parent material had completely vanished and only the hydride phase remained. Due to the low laser power applied (<6 W), temperature measurement was not possible but could only be estimated to be below 1000 K. In a subsequent experiment, we repeated the laser heating process at 55 GPa and achieved almost complete transformation of the sample within ca. 30 min.

On decompression we found the hydride phase of iridium to be visible to pressures as low as 6 GPa, with onset of decomposition visible between 15 and 20 GPa (indicated by a decrease in scattering intensity). Thus, we were able to establish the equation of state of this phase in the pressure range between 6 and 125 GPa. The data was fitted to a Vinet-type equation of state yielding a zero-pressure volume $V_0 = 23.33$Å^3 and a surprisingly low zero-pressure bulk modulus B_0 =190(3) GPa ($B_0' = 5.62(11)$) (see Fig. 2). A similar change in mechanical properties is only known for chemically produced hexagonal copper hydride where the bulk modulus drops from 142 GPa to 70 GPa, a phenomenon attributed to the hydrogen-metal bond which is partly covalent and ionic [24, 25]. However, copper hydride still exhibits a closed-packed structure. No other hydride is known to exhibit a simple cubic host lattice which makes it difficult to establish the correct crystal structure by comparison, *i.e.* determine the position of the hydrogen atoms which are almost invisible to x-rays. We therefore employed *ab-initio* computational methods to address crystal structure, thermodynamic properties and stability of this material. Assuming the $Pm\bar{3}m$ space group (Ir atoms located on the 1*a* sites), there are three potential stoichiometries IrH_n, $n = 1 - 3$. Taking the experimentally observed volume at 81 GPa (V = 18.59 Å^3), placing a single hydrogen atom on the 1*b* site yielded a calculated pressure of -0.5 GPa while three hydrogen atoms on the 3*d* sites lead to a pressure of 324.6 GPa. Therefore, these two configurations can be ruled out as possible candidates. A derived layered structure with only two of the three available 3*c* sites occupied (IrH_2, $P4/mmm$, Ir(1*a*), H(2*e*)) would correspond to a somewhat plausible pressure of 49.8 GPa. However, it is well known that calculations employing the PBE functional slightly overestimate the pressure and better agreement (98.5 GPa) is found for the IrH_3 structure with hydrogens occupying the 3*c* sites (for more details see Ref. [23]).

It can therefore be concluded that the hydrogen atoms most probably occupy the center of the faces in the simple cubic metal lattice, making this phase iridium trihydride. The calculated parameters for the equation of state are, V_0=23.739 Å^3, B_0=238.3 GPa, B_0'=4.36. The difference to the calculated volume of pure iridium at 65 GPa is 7 Å^3, in good agreement with experimental data. The calculated volume is 1.75 % larger than the experimental value, which is typical for GGA-based DFT calculations. However, the bulk modulus is unexpectedy larger than the one found in fitting an equation of state to our experimental data. The inclusion of the spin-orbit coupling (SOC) yields a slightly smaller bulk modulus (232.28 GPa), but associated to a bigger equilibrium volume (23.858 Å^3). This implies an almost negligible influence on the equation of state. Moreover, including Hubbard interaction to account for the correlated 5*d* states or going one step further on Jacob's ladder by using a rev-TPSS meta-GGA functional [28] leads to an even larger bulk modulus, 239.13 GPa and 249.90 GPa, respectively (see Figure 2). When constraining $B' = 4$ in fitting the equation of state to our experimental data, a bulk modulus of $B_0 = 231$ GPa is found. However,

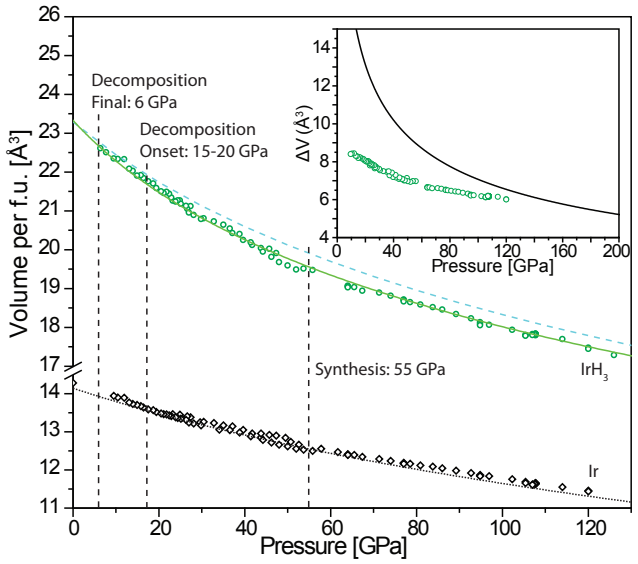

FIG. 2: (Colour online) Measured pressure-volume data of iridium (black diamonds) and iridium hydride (green circles). The dotted black line is a literature equation of state of iridium (V_0 = 14.145 Å^3, B_0 =383 GPa, B_0' = 3.1, see Refs. [21, 26]). The solid green line is a Vinet fit to our data (V_0 = 23.33 Å^3, B_0 =190(3) GPa, B_0' = 5.62(11)), the dashed blue line the calculated equation of state of IrH_3 using a rev-TPSS approach for the $Pm\bar{3}m$ structure (V_0=23.291 Å^3, B_0=249.9 GPa, B_0'=4.32). Inset shows the volume difference between IrH_3 and Ir in comparison to the equation of state for free hydrogen (solid line, showing volume for 3 hydrogen atoms, adapted from Ref. [27]).

the quality of fit deteriorates drastically, rendering this value significantly less plausible. Thus, to test if the lower experimental bulk modulus arises from a not-fully stoichiometric phase, we also calculated the equation of state of $IrH_{2.875}$, modelled by creating a single hydrogen vacancy on a 2x2x2 supercell of the simple cubic phase. However, its compressibility turned out to be very close to that of the fully stoichiometric IrH_3 phase (B_0=240 GPa). Although we can not exclude a deviation from ideal stoichiometry at higher pressures, it does not seem physically reasonable. Even if site vacancies exist in the synthesized material, taking into account the overestimation of the volume linked to the use of the PBE functional, the H:M ratio would still be very close to 3.

Interestingly, the $Pm\bar{3}m$ structure does not emerge as dynamically stable, with phonon softening in all the high-symmetry points at low pressures and in M and X at high pressures (see Figs. 1 and 2 in [23]). Freezing-in the atomic distortions involved in these soft modes leads to several structures with lower enthalphies (see Fig. 3a). For instance, the unstable M_3^- mode that consists of the closing and elongation of two of the C_2 axis of the Ir-Ir_6 octahedra yields to a $P4/nmm$ structure involving a doubling of the simple cubic unit-cell. It exhibits imaginary phonons at Γ (see Fig. 3 in [23]), related to a lowering of the symmetry to the $P\bar{4}2_1m$ space group, where two thirds of the hydrogen atoms deviate from the center of the cube faces. It corresponds, in fact, to the condensation of the M_3^- and M_2^+ modes. Moreover, the simultaneous condensation of the M_3^-,M_2^+ and X_5^- modes leads to a $P2_12_12_1$ structure without imaginary frequencies (see Fig. 4 in [23]).

From structural searches (see Ref. [23] for details), two competitive structures ($Pna2_1$ and C_c) appear as thermodynamically stable below 68 GPa at 0 K. These structures are also distortions of the simple cubic lattice with decreased distortion amplitude when increasing pressure. It can be noted that the observed diffraction peaks exhibit varying degrees of broadening which is not explained by a strain- or size-effect. However, the broadening can be explained by overlapping doublets or triplet peaks of these distorted-simple cubic structures, in which the positions of the iridium atoms deviate slightly from their ideal positions in a simple cubic cell (see Table 1 in Ref. [23]). In fact, the $Pna2_1$ structure is dynamically stable at 125 GPa and a Le Bail fit yields good agreement with experimental data (see Figs. 5 and 6 in Ref. [23]). However, this structure can not be confirmed as a unique solution given the variety of structures energetically competitive and very similar to the simple cubic structure at that pressure and susceptible to be stabilized by local stress, thermal and anharmonic effects. Particularly, entropic and anharmonic contributions might help to reduce the distortion amplitudes and, ultimately, stabilize less distorted structures than those computationally predicted at 0 K. It can be still concluded that the present structure is most probably no perfectly simple cubic but rather slightly distorted.

At pressures above 68 GPa, a different phase with $Pnma$ space group emerges as energetically favourable at 0 K and dynamically stable (see Fig. 7 in Ref. [23]). This structure, which still exhibits a H:M ratio of 3, is not a simple distortion of the simple cubic lattice (see Table 1 in Ref. [23]). Although the metallic atoms are hexaconnected as in the (distorted)-simple cubic structures, the motif of iridium octahedra with hydrogens located close to the center of the edges transforms to one of triangular prisms with interstitial hydrogens and short distances in between (At 125 GPa, the shortest H-H distance is 1.46 Å, being 1.85 Å for the simple cubic structure). We do not see any experimental evidence for this phase in our data up to 125 GPa. It can be assumed that, similarly to other hydride phases, the formation is hindered by an energy barrier, which also accounts for the large hysteresis between synthesis and decomposition in the cubic phase. It has been suggested

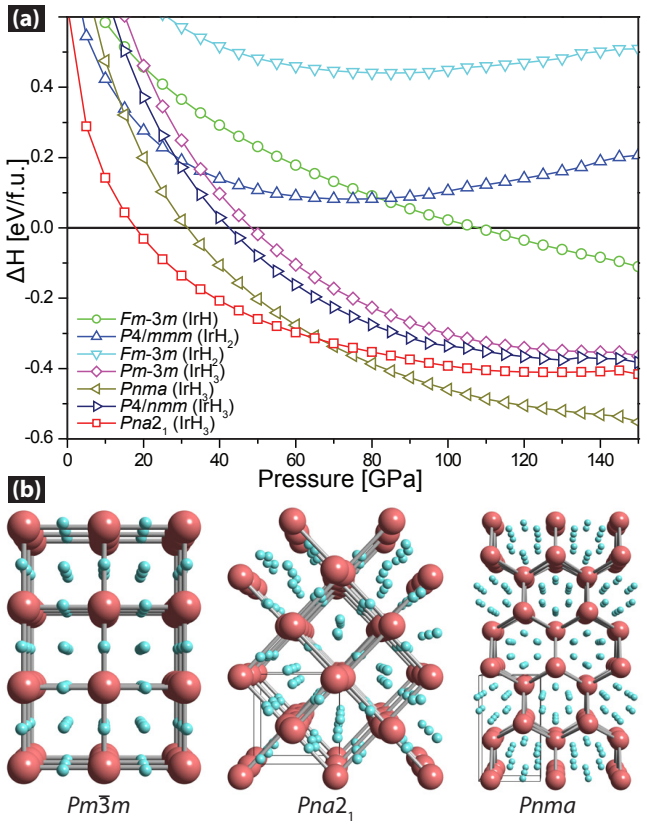

FIG. 3: (Colour online) (a) Calculated enthalpies of formation as a function of pressure for proposed iridium hydride structures. The enthalpy of the constituent elements at the corresponding pressure is taken as the reference enthalpy. $\Delta H = H(\mathrm{IrH}_n) - H(\mathrm{Ir}) - nH(0.5\mathrm{H}_2)$. (b) Atomic framework in the $Pm\bar{3}m$-structure (left), $Pna2_1$-structure (middle) and $Pnma$-structure (right). Details of the positioning for $Pna2_1$ and $Pnma$ can be found in Table 1 in [23]. Larger red spheres denote iridium atoms, smaller blue spheres hydrogen atoms.

that a higher observed synthesis pressure compared to the calculated equilibrium pressure is due to the additional energy required to dissociate the hydrogen molecule and macroscopically expand the metal sample (which requires energies comparable to the yield strength of the metal) [29]. Therefore, it could well be possible that the distorted cubic phase transforms into this phase at pressures above 125 GPa. Taking into account that experiments are performed at room temperature, it is also plausible that the observable structure remains trapped in any of the local minima of the flat energy surface in the vicinity of the simple cubic structure.

It is interesting to compare the differences between iridium hydride and other transition metal hydrides: In most known *d*-metal hydrides, synthesized at high pressures, the hydrogen atoms occupy the octahedral or tetrahedral interstitial sites in the closed-packed metal host lattices. On these sites, hydrogen appears to be mostly incompressible and the mechanical behaviour of the hydride is almost identical to that of the parent material. In iridium hydride however, the presence of the hydrogen atoms has profound impact on the material's mechanical properties, decreasing the bulk modulus significantly. It is sometimes observed that the formation process in other hydrides is slow but can usually be accelerated by increasing pressure (*e.g* in tungsten or rhenium), which is not observed here. Decomposition usually happens rapidly (instantaneously within the time scale of the experiment, *i.e.* usually <5 min.) as soon as pressure falls below equilibrium conditions. Again, this is not observed in IrH_3 where decomposition happens slowly. Since formation is accelerated at higher temperatures, it can be assumed that the material might be "frozen" at lower temperatures and decomposition prevented, rendering it (meta-)stable at ambient pressure (similar to copper hydride). The calculated elastic constants for the simple cubic structure ($Pm\bar{3}m$) at zero pressure (C_{11}= 460.63 GPa, C_{12}= 127.54 GPa, C_{44}= 24.31 GPa) of IrH_3 obey the Born stability criteria for the mechanical stability and inform on its metastability. It is also interesting to note the high Zener anisotropy ($2C_{44}/(C_{11}$-$C_{12})$=0.15) of this material and, especially, its low shear modulus (59.07 GPa, under the Voigt-Reuss-Hill approximation [30]), in contrast to the high value (210 GPa) for pure *fcc* iridium. Thus, one can conclude that the hydrogenation process turns a brittle into a ductile material. The observation of the high hydrogen content in conjunction with a severely increased compressibility lends itself to the debate whether the confined hydrogen might be compressed to densities surpassing the proposed metallization density. However, a direct comparison between the equations of state for iridium and iridium hydride shows that the volume difference approaches a constant value in the high-pressure limit corresponding to pure hydrogen at ∼250 GPa, well below predicted metallization pressures (see also inset Figure 2).

In conclusion, we have synthesized a novel metal hydride from the elements with very high hydrogen content and unusual crystalline structure (distorted simple cubic metal host lattice) that is seen up to the highest pressures reached in this study (125 GPa). The formation of the lowest-enthalpy phase above 68 GPa (*Pnma* spacegroup) is not observed and might be hindered by an energy barrier. The transition into the hydride phase as well as its decomposition are characterized by slow kinetics which suggests that the material might be metastable at ambient pressure and low temperatures. The results presented in this work have important implications for the synthesis of new materials at high pressures and the study of metal hydrides in general, and we hope that our findings will encourage further experimental and theoretical work.

Acknowledgments:

The authors would like to thank M. Hanfland (ID09a, ESRF) and A. Kleppe (I15, DLS) for technical support. This work is supported by a research grant from EPSRC. TS acknowledges financial support from CM-DTC. MM acknoledges the MALTA-Consolider program and MINECO for financial support. The allocation of beamtime by ESRF, Diamond Light Source and PETRA-III is greatly acknowledged.

*Corresponding author: e.gregoryanz@ed.ac.uk

[1] P.F. McMillan, Nature Materials, **1**, 19 (2002).
[2] V.L. Solozhenko & E. Gregoryanz, Materials Today **8**, issue 11, 44-51 (2005).
[3] V.V. Brazhkin, High Pressure Research, **27**, 333 (2007).
[4] V.E. Antonov, J. of Alloys and Compounds **330**, 110 (2002).
[5] Y. Fukai *The Metal-Hydrogen System.* (Springer Verlag, Berlin 2005).
[6] B.B. Baranowski, Platinum Metals Rev., **16**, 10 (1972).
[7] H. Kawamura, T. Moriwaki, Y. Akahama & K. Takemura, in *Proc. of Joint 20th AIRAPT - 43rd EHPRG International Conference on High Pressure Science and Technology*, Karlsruhe (2005)
[8] T. Scheler, F. Peng, C.L. Guillaume, R.T. Howie, Y. Ma, E. Gregoryanz, (to be published)
[9] T. Scheler, O. Degtyareva, M. Marqués, C.L. Guillaume, J.E. Proctor, S. Evans, & E. Gregoryanz, Phys. Rev. B, **83**, 214106 (2011)
[10] B. Li, Y. Ding, D.Y. Kim, R. Ahuja, G. Zou, H.-K. Mao, Proc. Natl. Acad. Sci. U.S.A., **108**, 18618 (2011)
[11] The synthesis of gold hydride was reported in 1982 (V.E. Antonov, Doklady Akademii Nauk SSSR, **266**, 376 (1982)), but has not been confirmed since then. We studied gold under hydrogen atmopshere at pressures up to 120 GPa and did not observe any signs of hydride formation (C. Donnerer, T. Scheler & E. Gregoryanz, accepted for publication in J. Chem. Phys.).
[12] T. Scheler, O. Degtyareva & E. Gregoryanz, J. Chem. Phys., **135**, 214501 (2011).
[13] H. Hemmes, A. Driessen, R. Griessen & M. Gupta, Phys. Rev. B, **39**, 4110 (1989)
[14] I.O. Bashkin, V.E. Antonov & E.G. Ponyatovsky in *Studies of High Temperature Superconductors, Vol. 45: Cuprates and Some Unconventional Systems*, Vol. 1, pp. 171-241 (Nova Science Publishers, New York 2003)
[15] B. Sakintuna, F. Lamari-Darkrim, F. & M. Hirscher, International Journal of Hydrogen Energy, **32**, 1121 (2007)
[16] I.P. Jain, C. Lal & A. Jain, International Journal of Hydrogen Energy, **35**, 5133 (2010)
[17] N.W. Ashcroft, Phys. Rev. Lett., **92**, 187002 (2004)
[18] E. Babaev, A. Sudbø, N.W. Ashcroft, Phys. Rev. Lett., **95**, 105301 (2005)
[19] R.T. Howie, C.L. Guillaume, T. Scheler, A.F. Goncharov & E. Gregoryanz, Phys. Rev. Lett., **108**, 125501 (2012); R.T. Howie, T. Scheler, C.L. Guillaume & E. Gregoryanz, Phys. Rev. B, **86**, 214104 (2012)
[20] P. Zaleski-Ejgierd, V. Labet, T.A. Strobel, R. Hoffmann & N.W. Ashcroft, J. Phys. Condens. Matter, **24**, 155701 (2012)
[21] A. Young, C. Sanloup, E. Gregoryanz, S. Scandolo, R. Hemley & H.-K. Mao, Phys. Rev. Lett., **96**, 155501 (2006)
[22] E. Gregoryanz, C. Sanloup, M. Somayazulu, J. Badro, G. Fiquet, H.-K. Mao & R.J. Hemley, Nature Materials, **3**, 294 (2004)
[23] See supplementary material at (...) for further details
[24] M. Tkacz & R. Burtovyy, J. alloys and compounds, **404**, 368 (2004)
[25] J. Filipek, Advanced Science, **19**, 1 (2007)
[26] H. Cynn, J.E. Klepsis, C.-S. Yoo & D.A. Young, Phys. Rev. Lett., **88**, 135701 (2002)
[27] P. Loubeyre, R. Letoullec, D. Hausermann, M. Hanfland, R.J. Hemley, H.-K. Mao & L.W. Finger, Nature, **383**, 702 (1996)
[28] J. Sun, M. Marsman, G.I. Csonka, A. Ruzsinsky, P. Hao, Y.-S. Kim, G. Kresse & J.P. Perdew, Phys. Rev. B **84**, 035117 (2011).
[29] V.E. Antonov, I. Latynin & M. Tkacz, Journal of Physics: Condensed Matter, **16**, 8387 (2004).
[30] R. Hill, Proc. Phys. Soc. Lond. **65**, 349 (1952).

Nanocrystalline Tungsten Hydrides at High Pressures

Thomas Scheler[1], Feng Peng[2], Christophe L. Guillaume[1], Ross T. Howie[1], Yanming Ma[2], Eugene Gregoryanz[1*]
[1] *SUPA, School of Physics and Astronomy and Centre for Science at Extreme Conditions, The University of Edinburgh, Edinburgh, EH9 3JZ, UK*
[2] *State Key Lab of Superhard Materials, Jilin University, 130012 Changchun, P.R. China*

A combined experimental and theoretical study has been carried out on the synthesis and characterization of tungsten hydride at high pressures. We confirm the synthesis of tungsten monohydride at above 25 GPa and 300 K. At higher pressures, hydrogen content is found to increase and *ab-initio* calculations reveal the formation of tungsten dihydride in a mixed composition of $(1-y)$WH + (y)WH$_2$ with $y \sim \frac{1}{3}$. Synchrotron x-ray diffraction and transmission electron microscopy (TEM) measurements demonstrate the formation of a nano-crystalline microstructure upon hydrogenation. TEM micrographs show elongated grains with diameters of ∼20 nm, a structure similar to nanocrystalline diamond.

PACS numbers:

The application of extreme conditions, namely high pressures and temperatures, offers a very general route for synthesizing novel materials and manipulating their physical properties. In the past this led to several important discoveries, including nanopolycrystalline diamond (NPD) [1], cubic boron nitride (c-BN) [2] and the highly incompressible nitrides of osmium, iridium and platinum [3, 4]. Most recently, nanotwinned c-BN was found to be ultrahard, even exceeding the hardness of diamond [5]. In the past few years, hydrogen compounds and alloys have attracted the renewed attention of researchers due to their potential applications in a hydrogen economy [6–8] and implications for the behaviour of free hydrogen, such as its elusive metallic state [9, 10]. Here, high-pressure synthesis has also been successfully applied to synthesize novel hydrides, *e.g.* platinum hydride [11, 12], ϵ_2-rhenium hydride [13], a polymeric phase of silicon tetrahydride at pressures exceeding 1 Mbar [14] and tungsten hydride [15, 16]. With the exemption of SiH_4, the aforementioned materials are interstitial metal hydrides in which the hydrogen atoms occupy octahedral or tetrahedral sites in the closed-packed metal host lattice. Most of the known hydride phases of the *d*-metals between the Cr-group and Cu-group elements are of this type [17]. Furthermore, none of the metals in this group readily reacts with hydrogen at ambient conditions and high pressures are necessary to form a hydride under equilibrium conditions [17]. The conditions for the formation of stoichiometric hydrides range from less than 1 GPa (*e.g.* NiH at 0.6 GPa, [18]) to 27 GPa in platinum [11], so far the highest synthesis pressure observed in this group.

In this paper, we present a combined x-ray diffraction, electron microscopy and computational study of tungsten hydride at high pressures. We studied the formation, decomposition and mechanical properties of tungsten hydride synthesized from the elements in a diamond anvil cell up to 115 GPa by x-ray diffraction as well as the microstructure of recovered dehydrogenated tungsten by transmission electron microscopy. The hydrogenation process was found to create a nanocrystalline microstructure. Theoretical *ab-initio* calculations in conjunction with measurement of the equation of state suggest that between 25 and ∼ 50 GPa, tungsten dihydride is formed and coexists with the monohydride at higher pressures in a mixed composition of $(1-y)$WH + (y)WH$_2$, saturating at $y \sim \frac{1}{3}$ above 50 GPa. Details on the experimental and computational methods are given in the supplementary material (Ref. [19]).

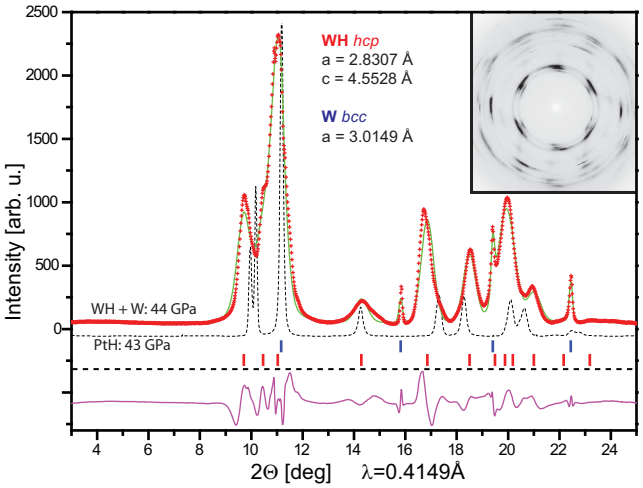

FIG. 1: (Color online) Powder x-ray diffraction spectrum of tungsten hydride at 44 GPa. The green line denotes the result from a LeBail fit. Tick marks indicate peak positions for cubic W (upper, blue) and hexagonal WH (lower, red). The diffraction spectrum of platinum hydride at 43 GPa is added for comparison [11] (grey dashed line). Note the difference in peak width. PtH forms under similar conditions as WH and also exhibits the *hcp*-structure.

Tungsten is a widely used material in both industry

and science. In high-pressure applications it is particularly valued as a pressure calibrant and gasket material [20]. In the past, it was widely accepted that tungsten does not react with hydrogen, even at very high pressures, and therefore was frequently used as a sealing material in high-pressure experiments. However, it was reported a few years ago that binary tungsten hydride is formed when compressing pure tungsten to above 25 GPa at room temperature in a dense hydrogen medium [15]. In a recent theoretical study of this material, several potentially metastable phases of varying hydrogen content were found [16], although only tungsten monohydride was observed experimentally. The monohydride is characterized by a hexagonally closed-packed arrangement of the tungsten atoms (spacegroup $P6_3/mmc$) with hydrogen atoms occupying the octahedral interstitial sites. This is equivalent to the NiAs-type structure, which is known for many other hydrides in the *d*-metals as well and is also the one adopted by the hydrides of the same group, MoH [21] and CrH [22].

In our experimental runs, we observe a reaction between tungsten and hydrogen at 25 GPa with the appearance of new diffraction peaks in addition to *bcc*-tungsten. The new phase can be indexed in the $P6_3/mmc$ spacegroup with an expanded volume per tungsten atom in the unit-cell. So far, our observations are identical with earlier reports on tungsten hydride. The synthesis conditions of WH are reminiscent of *hcp* platinum hydride [11] (PtH), which forms at pressures above 27 GPa and room temperature. However, in contrast to PtH, the hydride formation in tungsten progresses very slowly over time and the diffraction pattern of WH exhibits broadened Bragg peaks (see Figure 1). In one of our experimental runs, we reached pressures of ∼45 GPa within hours of surpassing synthesis conditions. At this time, the sample has not been completely converted to tungsten hydride and the sharp Bragg peaks of *bcc*-tungsten are still clearly visible (see Figure 1). For comparison we include the diffraction pattern of platinum hydride at similar pressures. It is evident that the diffraction peaks of tungsten hydride are considerably broadened compared to both its parent metal and another hydride synthesized under nearly identical conditions. While increasing pressure seems to accelerate the transformation process, with time the whole sample fully transforms into the hydride also at constant pressures. In one of the experimental runs the sample was left at a pressure of 38 GPa for one month. Afterwards, the whole sample was hydrogenated and no sign of *bcc*-tungsten was detected. Laser heating has also been shown to accelerate the transition into the hydride phase [16]. On decompression, tungsten hydride was found to be stable to pressures far below synthesis conditions. We observed the decomposition reproducibly at pressures between 8 and 9 GPa. The slow progression of the hydrogenation process, its acceleration upon heating and the large hysteresis effect in decomposition suggest the presence of a kinetic energy barrier hindering the formation at lower pressures and faster hydrogenation. We found that dehydrogenated tungsten still exhibits broadened Bragg peaks compared to its original state.

We recovered such dehydrogenated tungsten samples from the diamond anvil cells and used focused ion beam techniques to prepare transmission electron microscopy (TEM) samples. TEM brightfield and darkfield imaging revealed elongated crystallites with shortest dimensions of below 20 nm (see Figure 2(a-c)). The observed structure is similar to that of NPD which also exhibits elongated crystallites with diameters of 10-20 nm and lengths of up to a few 100 nm [1]. This new form of artificial diamond was reported to be harder than natural single crystalline diamond [1]. Electron diffraction measurements on dehydrogenated tungsten further show that the crystallites are not randomly oriented but follow a preferred orientation (Figure 2(d)) which explains the texture in the x-ray diffraction patterns. In a control experiment we prepared TEM samples from untreated tungsten. Both, TEM micrographs and electron diffraction patterns (Figure 2(e)) indicate perfect single crystallinity.

This microstructure can be related to the observed broadening of the diffraction peaks. Peak broadening in x-ray diffraction patterns during high-pressure experiments can be attributed to three different effects: i) instrument broadening, ii) strain broadening and iii) size broadening. While instrument broadening can be neglected when using modern third generation synchrotron radiation sources, both strain and size broadening contribute to the peak shape. The simple Scherrer formula $L = \frac{K\lambda}{\beta cos(\Theta)}$ (see *e.g.* Ref. [14]) connects the peak width to the crystallite size, ignoring however any strain contribution. Here, L is the grain size, λ the x-ray wavelength, β the peak width and Θ the scattering angle of the reflection. K is the empirical Scherrer constant and usually 1. When comparing the values in Table 1 for tungsten hydride with the results of the TEM measurements on recovered dehydrogenated tungsten, it is evident that strain plays a significant role at rising pressures (indicated by the decreasing calculated grain size). However, when extrapolating the data in Table 1 to zero pressure, a grain size comparable to what is found in the TEM images can be derived. It should be emphasized here, that the calculated values at high pressures do not correspond to actual grain sizes. From the emergence of the broad diffraction peaks upon synthesis we conclude that it is, in fact, the hydrogenation process that leads to the formation of a nanomaterial.

We offer the following explanation for the formation

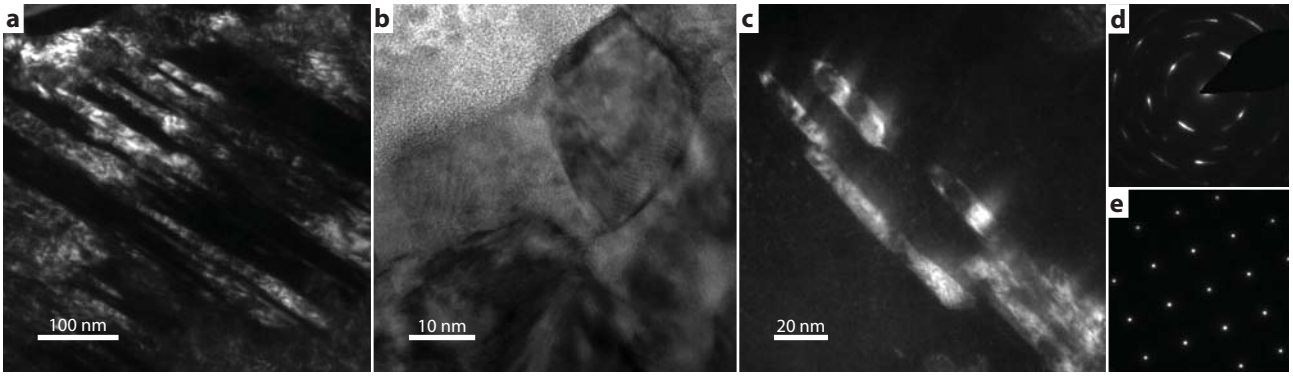

FIG. 2: Transmission electron micrographs of recovered nanocrystalline tungsten. a) Darkfield image showing an array of elongated crystallites. b) Brightfield image of crystallites near the surface with preferred orientation perpendicular to the TEM-section. c) Darkfield image of small grains inside the sample. d) Electron diffraction pattern of nanocrystalline tungsten. e) Electron diffraction pattern of a control sample.

TABLE I: Calculated grain size from the widths of the Bragg peaks in tungsten hydride at various pressures using the Scherrer approximation.

P [GPa]	HKL	Position [deg]	FWHM [deg]	est. grain size [nm]
9.7	(010)	9.368	0.21	11.5
9.7	(110)	16.251	0.229	11
15.8	(010)	9.439	0.344	7
15.8	(110)	16.301	0.276	9
37.5	(010)	9.512	0.398	6
37.5	(110)	16.432	0.26	9.5
49.7	(010)	9.57	0.41	6
49.7	(110)	16.52	0.304	8
73.7	(010)	9.715	0.428	5.5
73.7	(110)	16.785	0.377	6.5
115	(010)	9.998	0.476	5
115	(110)	17.198	0.454	5.5

mechanism of a nanostructured material during the hydrogenation process: The unusually slow progression of hydride formation (hindered by a large energy barrier), accompanied by a structural phase transition, and the volume expansion during hydrogenation, creates significant stress between the hydrogenated and non-hydrogenated parts of the tungsten sample. Starting from the sample surface, hydrogenation slowly progresses into the material with only a very small volume near the hydride boundary undergoing the transition at any given time. With the release of local boundary strain, this leads to the formation of nanometer sized crystallites. The long dimension of the crystal grains found in our TEM studies is probably oriented along the hydride boundary during synthesis. The decomposition pressure usually lies close to the thermodynamic equilibrium of the system while the formation pressure lies higher due to the dissociation barrier encountered by the hydrogen molecule at the metal surface. Thus, once pressure is lowered below the equilibrium conditions, rapid dehydrogenation occurs leaving the microstructure intact. As a consequence, the dehydrogenated tungsten exhibits the same microstructure as its binary hydride. It can be expected, that annealing at high temperatures would lead to a realignment of the nanometer sized grains and the formation of larger crystallites. Indeed, Zaleski-Ejgierd *et al.* seem to have observed this exact effect when laser heating tungsten hydride to above 1000 K [16]. Room temperature however does not appear to have immediate or short term effect on the crystallite size. One of the samples studied by transmission electron microscopy was residing at ambient conditions for several months before TEM-sample preparation, while a different sample was recovered from high pressure only a few days prior to TEM measurements. There were no detectable differences in the microstructure between the two specimens.

Decreasing the grain size in materials down to a few tens of nanometers often entails significantly altered material properties, and it is known that, as the grain size decreases, the influence of interface and confinement effects on the properties of a material increases [23, 24]. As a result, a nanostructured material might exhibit increased resistance to plastic deformation [25] or different chemical stabilities compared to macroscopic systems [26]. In the case of metal hydrides, the grain size has profound impact on (de)hydrogenation processes, the overall hydrogen content and the volume expansion of the metallic host lattice [26] due to interface stress between the grains. It was found for example in ball milled nanoparticles of vanadium hydride that the hydrogen content depends on the particle size [27]. These possible nanometric effects make it difficult to compare tungsten hydride to other transition metal hydrides, *e.g.* in terms of volume expansion as a measure for hydrogen content [17] or when comparing experimental with computational results.

We attempted to fit a Vinet-type equation of state to our x-ray diffraction data resulting in a zero-pressure bulk modulus of near 500 GPa (depending on parametrization). Such extremely low compressibility could be attributed to a size-effect of the nanocrystalline microstructure. However, the quality of fit was not convincing, showing deviations at lower and very high pressures. The construction of the equation of state obviously assumes constant stoichiometry throughout the probed pressure range, which unfortunately cannot be guaranteed for metal hydrides. In fact, the volume difference between hydride phase and parent metal is directly used to infer the hydrogen content, assuming no change in compressibility between hydride and metal (see *e.g.* Refs. [11, 13, 17]).

We therefore performed *ab-initio* calculations to understand hydrogen content and the experimental equation of states. Structure predictions through CALYPSO methodology [28–30] were performed by fixing the W atomic positions in the *hcp* lattice, taken from the known experimental XRD pattern. We performed structural searches within various stoichiometric compositions WH_n (n = 0.5, 1.0, 1.5, 2) with simulation cell sizes of 1-4 formula units (f.u.) at 30 and 60 GPa, respectively. We did not probe higher hydrogen contents since the resulting volumes are too large to fit our experimental data. Our calculations gave convex hulls on the formation enthalpy of various WH_n with respect to elemental W and solid H_2 as shown in Fig. 3 (Details can be found in Ref. [19]). As expected, at zero pressure all W-H systems exhibit positive formation enthalpy and cannot form. At 20 and 40 GPa, the monohydride WH is the most stable compound and also the only stoichiometry which can be synthesized, which agrees well with the observed appearance of the hexagonal hydride phase in this pressure range. Interestingly, at a pressure of 60 GPa and above, WH_2 becomes stable against decomposition into WH + $\frac{1}{2}H_2$. Our results are in good agreement with those presented in Ref. [16]. However, below 120 GPa, the proposed formation of $P4/nmm$-structured WH_4 or other phases with even higher hydrogen contents can be excluded based on our experimental observations. At pressures above ~220 GPa, when hydrogen enters phase IV which is characterized by a mixed atomic and molecular state of hydrogen [31], the formation of higher stoichiometries is possible due the absence of the dissociation barrier.

From our calculations, WH stabilizes in the $P6_3/mmc$ spacegroup and WH_2 in the $Pnma$ spacegroup above 50 GPa. For WH, tungsten atoms form a hexagonal closed-packed host matrix with hydrogen atoms occupying the octahedral interstitial sites. In the $Pnma$ structure of WH_2, the metal atoms are arranged in a slightly distorted hexagonal lattice. In addition to the octahedral sites in the WH-phase, hydrogen atoms also occupy half of the available tetrahedral sites. A transition between these two phases therefore does not require a major rearrangement of the metal host lattice and thus, WH_2 can form in addition to WH at higher pressures. Figure 4 shows the calculated equation of state for WH, WH_2 and a mixed composition phase of $(1-y)$WH + $(y)WH_2$ ($y = \frac{1}{3}$), together with our experimental data for comparison. We found that below 25 GPa, the experimental EoS can be satisfactorily

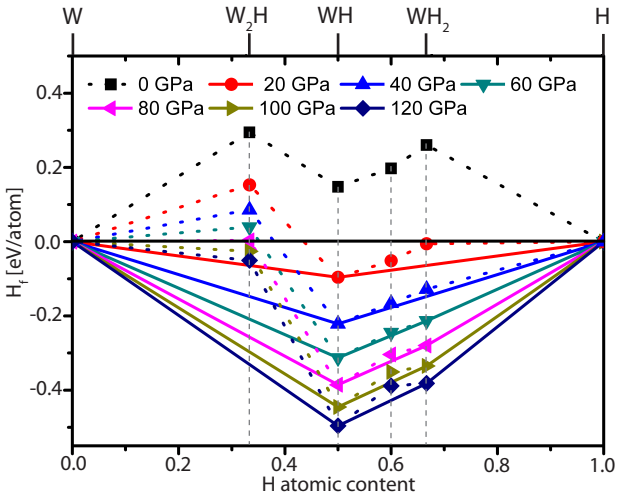

FIG. 3: (Color online) The relative enthalpies of formation per atom with respect to elemental W and molecular H_2 for different WH_n compositions. The convex hulls are shown by solid lines. Dotted lines through the neighboring points residing above the convex hull are guides for the eye.

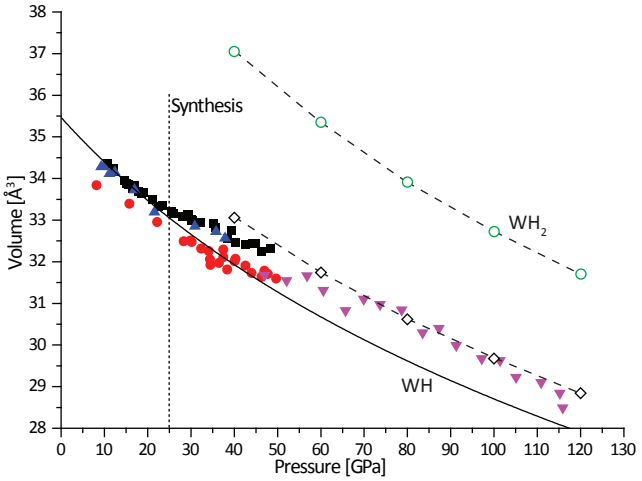

FIG. 4: (Color online) Pressure-Volume diagram of tungsten hydride. The solid line indicates the calculated equations of state for WH, the open circles the EoS for WH_2. Open diamonds denote calculated pV data for a fractional mixture of $\frac{2}{3}$ WH and $\frac{1}{3}$ WH_2. The dashed lines are guides to the eye. Solid symbols are experimental unit-cell volumes fitted with a hexagonal cell.

explained by pure tungsten monohydride. However, at pressures between 25 and 50 GPa, the experimental volume deviates from the EoS of pure WH, suggesting an additional uptake of hydrogen. Above 50 GPa, the observed pressure-volume data show a behaviour which is not explained by either pure WH or pure WH_2. Instead, a mixed-phase model of WH + WH_2 where all octahedral sites and a fraction of the available tetrahedral sites are occupied, can explain the observed behaviour. This leads to the conclusion that the reaction WH + $\frac{1}{2}H_2 \rightarrow WH_2$ is initiated and driven by pressure but appears to be halted at pressures above 50 GPa reaching a composition of $(1-y)$WH + $(y)WH_2$ ($y = \frac{1}{3}$). In other words, once all octahedral sites are filled and sufficient pressure is applied, hydrogen atoms start to occupy a fraction of the tetrahedral sites. Whether the metallic lattice transforms into the distorted *Pnma* structure or remains perfectly hexagonally oriented is experimentally difficult to address because of the very broad diffraction peaks which allow indexing in either configuration. At the highest pressures reached in this study (120 GPa), the reaction is still not complete and tetrahedral occupation seems to saturate at $\sim$17% ($= y/2$). Even with time (some of our samples resided in this pressure region for several weeks), no higher hydrogen content was reached. In samples that were not fully transformed into the monohydride phase, a slightly smaller volume is measured, indicating a lower hydrogen content, probably due to a deficient filling of the octahedral sites. The nanocrystalline nature of the hydride however might add to uncertainty in hydrogen content and atomic ordering. At the same lattice expansion, a larger hydrogen content might be possible due to surface-effects in the nanocrystalline grains.

The results presented here are of immediate interest to the field of high-pressure research. The change in microstructure as well as increased hydrogen uptake could have potentially significant consequences since tungsten is often employed as a sealing material in experiments involving pure hydrogen. Due to the higher synthesis pressure of the hydride phase and slower formation kinetics, tungsten gaskets show improved stability at pressures above 1 Mbar compared to rhenium. We hope that the findings presented here will encourage further experimental and theoretical studies on the influence of microstructure and also kinetic effects on the formation and properties of metal hydrides.

Acknowledgments

The authors would like to thank A. Kleppe from I15 at Diamond Light Source, M. Hanfland from ID09a at the European Synchrotron Radiation Facility and M. Ward from the Leeds Electron Microscopy and Spectroscopy Centre for technical support. The authors further thank O. Degtyareva for useful discussions and T. Strobel for providing unpublished data. This work is supported by a research grant from EPSRC. TS acknowledges financial support from CM-DTC. FP and YM are supported by the National Natural Science Foundation of China under Grant No. 11025418. The allocation of beamtime and access to instruments by ESRF, DLS and LEMAS/LENNF is greatly acknowledged.

Corresponding author: e.gregoryanz@ed.ac.uk

[1] T. Irifune, A. Kurio, S. Sakamoto, T. Inoue, H. Sumiya, *Nature* **421**, 599-601 (2003).
[2] R.H. Wentorf, *J. Chem. Phys.*, **34**, 809-812 (1961).
[3] E. Gregoryanz, C. Sanloup, M. Somayazulu, J. Badro, G. Fiquet, H.-K. Mao and R.J. Hemley, *Nature Mater.*, **3**, 294-297 (2004).
[4] A.F. Young, C. Sanloup, E. Gregoryanz, S. Scandolo, R.J. Hemley and H.-K. Mao, *Phys. Rev. Lett.*, **96**, 155501 (2006).
[5] Y. Tian, B. Xu, D. Yu, Y. Ma, Y. Wang, Y. Jiang, W. Hu, C. Tang, Y. Gao, K. Luo, Z. Zhao, L.-M. Wang, B. Wen, J. He and Z.Liu, *Nature* **493**, 385 (2013).
[6] A. Züttel, *Die Naturwissenschaften*, **91**, 157 (2004)
[7] B. Sakintuna *et al.*, *International Journal of Hydrogen Energy*, **32**, 1121 (2007)
[8] V. Yartys *et al.*, in T. Veziroglu, S. Zaginaichenko, D. Schur, B. Baranowski, A. Shpak, & V. Skorokhod (Eds.), Hydrogen Materials Science and Chemistry of carbon Nanomaterials (Vol. 172, pp. 75-104) (2004)
[9] N.W. Ashcroft, *Phys. Rev. Lett.*, **92**, 187002 (2004)
[10] E. Babaev *et al.*, *Phys. Rev. Lett.*, **95**, 105301 (2005)
[11] T. Scheler, O. Degtyareva, M. Marqués, C.L. Guillaume, J.E. Proctor, S. Evans and E. Gregoryanz, *Phys. Rev. B*, **83**, 214106 (2011).
[12] O. Degtyareva, J.E. Proctor, C.L. Guillaume, E. Gregoryanz, M. Hanfland, *Solid State Commun.* **149**, 1583-1586 (2009).
[13] T. Scheler, O. Degtyareva, E. Gregoryanz, *J. Chem. Phys.* **135**, 214501 (2011).
[14] M. Hanfland, J.E. Proctor, C.L. Guillaume, O. Degtyareva, E. Gregoryanz, *Phys. Rev. Lett.* **106**, 095503 (2011).
[15] H. Kawamura, T. Moriwaki, Y. Akahama, K. Takemura, *Proc. of Joint 20th AIRAPT - 43rd EHPRG International Conference on High Pressure Science and Technology* Karlsruhe (2005).
[16] P. Zaleski-Ejgierd, V. Labet, T.A. Strobel, R. Hoffmann, N.W. Ashcroft, *J.Phys.: Condens. Matter* **24**, 155701 (2012).
[17] Y. Fukai, *The Metal-Hydrogen System.* (Springer Verlag, Berlin 2005)
[18] S.P. Besedin and A.P. Jephcoat, *Rev. High Pressure Sci. Technol.* **7**, 301 (1998)
[19] See supplementary material at (...)
[20] A. Dewaele, P. Loubeyre, M. Mezouar, *Phys. Rev. B* **70**, 094112 (2004)
[21] B. Baranowski and K. Bojarski, *Roczniki Chemii Ann. Soc. Chim. Polonorum* **46**, 525 (1972).
[22] V. Antonov, A.I. Latynin and M. Tkacz, *J. Phys.: Con-*

dens. Matter **16**, 8387 (2004).
[23] M.D. Uchic, D.M. Dimiduk, J.N. Florando, W.D. Nix, *Science* **305**, 986-989 (2004).
[24] G.C.A.M. Janssen, B.R. Pujada, *Appl. Phys. Lett.* **91**, 121913 (2007).
[25] S. Veprek, A.S. Argon R.F. Zhang, *Philosophical Magazine*, **90**, 4101-4115 (2010).
[26] M. Fichtner, *Nanotechnology* **20**, 204009 (2009).
[27] S.-I. Orimo, F. Kimmerle and G. Majer, *Phys. Rev. B*, **63**, 094307 (2001).
[28] Y. Wang, J. Lv, L. Zhu, Y. Ma, *Phys. Rev. B*, **82**, 094116 (2010).
[29] Y. Wang, J. Lv, L. Zhu, Y. Ma, *Comput. Phys. Commun.*, **183**, 2063 (2012) - CALYPSO code is free for academic use, please register at http://www.calypso.cn
[30] J. Lv, Y. Wang, L. Zhu and Y. Ma, *J. Chem. Phys.*, **137**, 084104 (2012).
[31] R.T. Howie, C.L. Guillaume, T. Scheler, A.F. Goncharov and E. Gregoryanz, *Phys. Rev. Lett.* 108, 125501 (2012).

Low Temperature Physics/Fizika Nizkikh Temperatur, 2013, v. 39, No. 5, pp.

Hydrogen at extreme pressures

(Review Article)

Alexander F. Goncharov

Geophysical Laboratory, Carnegie Institution of Washington, Washington, D.C. 20015, USA
E-mail: agoncharov@ciw.edu

Ross T. Howie and Eugene Gregoryanz

Centre for Science at Extreme Conditions and School of Physic and Astronomy, University of Edinburgh, Mayfield Road, Edinburgh EH9 3JZ, United Kingdom

Received February 25, 2013

Here we review recent experimental and theoretical studies of hydrogen approaching metallization regime. Experimental techniques have made great advances over the last several years making it possible to reach previously unachievable conditions of pressure and temperature and to probe hydrogen at these conditions. Theoretical methods have also greatly improved; exemplified through the prediction of new structural and ordered quantum states. Recently, a new solid phase of hydrogen, phase IV, has been discovered in a high-pressure high-temperature domain. This phase is quite unusual structurally and chemically as it represents an intermediate state between common molecular and monatomic configurations. Moreover, it shows remarkable fluxional characteristics related to its quantum nature, which makes it unique among the solid phases, even of light elements. Moreover, phase IV shows the presence of a band gap and exhibits distinct phonon and libron characteristic of classical solids. The quantum behavior of hydrogen in the limit of very high pressure remains an open question. Prospects of studying hydrogen at more extreme conditions by static and combined static-dynamic methods are also presented.

PACS: 64.30.Jk Equations of state of nonmetals;
67.80.F– Solids of hydrogen and isotopes.

Keywords: hydrogen, extreme pressures, solid phase of hydrogen.

Contents

1. Introduction .....
2. Phase relations .....
3. Melting and fluid behavior .....
4. Phase II .....
5. Phase III .....
6. Phase IV .....
7. Conclusions .....
References .....

1. Introduction

Hydrogen has a special interest for many fields of research as it represents the perfect model object due to its seeming simplicity and abundance in the cosmos [1–4]. One of the objectives of studying hydrogen at extreme pressures is to rationalize the notion of metallic hydrogen as a future energy carrier. There are three major technical drivers in this pursuit: theoretical calculations and dynamic and static compressions. Each has its own pressure — temperature — time-scale domain, which largely do not intersect and this poses a serious difficulty in unifying and comparing results. This issue is now being addressed by improving and modifying these techniques and by creating new combined static-dynamic experimental methods.

With regard to theoretical and dynamic experimental studies, we refer readers to the recent review on mainly the theoretical approach to study hydrogen under extreme conditions [5], which also contains a brief review of experimental works. Study of hydrogen using dynamic compression (see the review papers [1,6,7]) is progressing very rapidly now with a development of laser driven technique compression of statically pre-compressed samples [8,9].

The purpose of this review paper is to critically look at the most recent studies in the search for metallic hydrogen, which have been performed either using diamond anvil cell (DAC) techniques, combined DAC- dynamic ultrafast compressions, or heating experiments.

Static compression of hydrogen to very high pressure is technically very challenging. Hydrogen is very compressible, while the materials commonly used to form the sample chamber around it are not. Generating high-pressure on hydrogen requires larger compression of the gasket material than with less compressible samples due to the limitation of plastic flow. Secondly, hydrogen is very diffusive; it tends to penetrate and rupture any small crack in both the diamond and gasket. In the case of diamond this always results in premature anvil failures. These effects accelerate with temperature: rarely occurring below 100 K, but increasing substantially above 200 K. Owing to this, until 2011, there were no reliable reports on static compression of hydrogen or deuterium above 180 GPa at room temperature [10]. Improved sample loading techniques, which include diamond protective coating, focused electron beam (FIB) gasket drilling, and better optimized anvil geometry have recently allowed achieving static compression of hydrogen well above 300 GPa at 300 K [11].

These technical breakthroughs resulted in extending the achievable pressure range for hydrogen research up to 320 GPa at 300 K [11] and up to 360 GPa at 80 K [12]. New semiconducting (or semimetallic) solid phase hydrogen has been discovered above 220 GPa at 300 K by combined experimental (Raman and optical spectroscopy) and theoretical efforts [11,13]. A conflicting report claiming electrically conducting hydrogen in the fluid state above 260–270 GPa has been earlier published by Eremets and Troyan [14]. Infrared measurements in phase III to 360 GPa [12] also did not report metallic conductivity. However, one should note, that pressure metrology remain a problem as measurements of the diamond Raman edge as pressure calibrant [15] are somewhat uncertain, and, moreover, some experiments relied on higher pressure extrapolations [12]. Here, we will review the recent works and present prospects of new technical advances, which can enable next major breakthroughs.

2. Phase relations

Until recently, only three solid states of hydrogen have been known (Fig. 1). Phase I is a plastic phase of freely rotating molecules forming an hcp lattice whilst phases II and III are partially (or completely) ordered phases, which appear at lower temperatures and/or higher pressures (see Refs. 2, 16, 17 for review). The symmetries and orientation order types of phases II and III have been extensively discussed in the literature based on experimental spectroscopy observations [2,16,17,19,33–37] and theoretical calculations [20,38–45], however the available x-ray diffraction

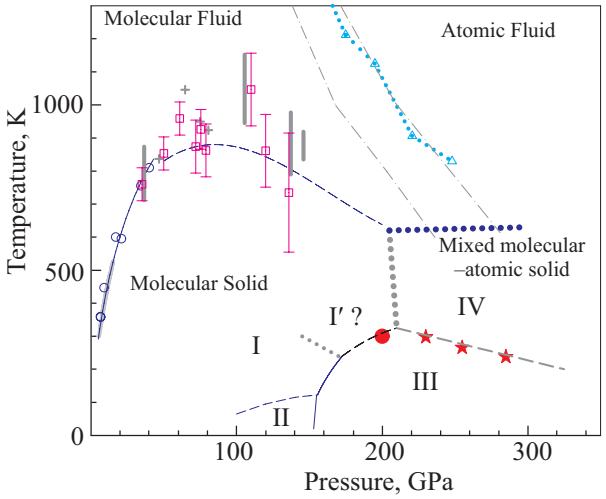

Fig. 1. (Color online) Phase diagram of hydrogen. The I–II and I–III phase line for normal H_2 are from Ref. 18; the I–III phase (solid line) has been corrected as proposed in Ref. 17. The filed circle is room temperature data from Ref. 11; the dashed line is the proposed I–III phase line at high *T*. The dotted gray line shows a schematic location of the I–I' phase line inferred in Refs. 19–23. The melting measurements are from Refs. 24–29: thick gray line (Ref. 24), open circles (Ref. 25), crosses (Ref. 27), vertical gray bars (Ref. 28), open squares (Ref. 26), dashed line (Ref. 29). Stars correspond to the III–IV transition [11] (see also Ref. 30). Open triangles and gray dashed-dotted lines (from DFT and QMC calculations) are theoretical results for a liquid-liquid transition [31,32] associated with the molecular dissociation. Thick dotted gray and blue lines are suggested I–IV and IV–liquid lines, respectively.

data are still not conclusive [46,48]. The important issue of ortho–para distinction, and its effect on both the structure and phase transitions, has also been discussed extensively. However, the available data remain fragmentary due to difficulties in performing experiments on materials with pure ortho–para composition. Nonetheless, the current consensus is that the ortho–para distinction does not affect the transition to phase III, which is suggested to be classically orientationally ordered [18,49]. Due to technical difficulties, the extension of the phase line between phases I and III to room temperature could not have been reached until recently. It has been proposed [23] based on the crystal symmetry arguments that this line should have a termination at a critical point with finite *P*–*T* conditions, and phase I', with the same symmetry as phase III, merges with phase I in the triple point, giving rise to the I–I' phase line (Fig. 1). However, suggestions about the existence of phase I' based on these symmetry considerations, theoretical calculations [20] or experimental observations of subtle changes in vibrational frequencies [21] have yet to be confirmed (see Ref. 17 for more information). Instead, recently it has been found that the I–III phase line does extend to room temperature,

and perhaps even beyond, where it meets a new phase line with solid phase IV (Fig. 1). At room temperature the transition sequence is I–III–IV, and the corresponding transitions occur at 200 and 230 GPa (in H_2) [11].

3. Melting and fluid behavior

Determination of the melting line of hydrogen, especially in the limit of high pressures, remains one of the most challenging experimental tasks. Theoretical two-phase simulations up to 200 GPa suggest that there is a decline in the melting line above 90 GPa related to softening of the intermolecular interactions, which occur at a faster rate in the liquid than in the solid as a function of pressure [29]. First principles calculations performed on this and other works also suggest the presence of another high-temperature boundary above the melt line related to the molecular dissociation. This transformation is often called the plasma line but can be also considered as a first-order liquid-liquid transition [32,50–53]. Extrapolations of the melt line and the liquid–liquid phase transition [29] determined in theoretical calculations suggest the presence of a triple point at 300 GPa and 400 K. Above this pressure, the solid is expected to melt into a metallic liquid.

Two major experimental techniques have been used to detect melting: visual observations, which include detection of the laser speckle pattern [24,27,28], and Raman spectroscopy measurements [25,26]. Generally, the results of visual observations should be considered quite reliable at relatively low pressures as the optical contrast between solid and fluid is sufficiently large due to the difference in the refractive indices. The results of two available experimental studies [24,54] are in agreement within the *P–T* range of overlap. The study by Datchi *et al*. [24] extended the melting line up 15.2 GPa and 530 K, but experienced difficulties in reaching more extreme conditions because the metallic gasket materials used could not contain the hydrogen sample. These visual observation experiments required substantial time as very slow temperature change is required to stabilize fluid and solid materials in equilibrium. Gregoryanz *et al*. [25] used cubic boron nitride and alumina insets in rhenium gaskets and employed express Raman observations to detect melting. At melting, they observed a small Raman vibron discontinuity up to 44 GPa, but no further discontinuities have been detected above this pressure. They also reported a large increase in the negative temperature shift of the Raman vibron with pressure. Combined melting temperature data to 44 GPa obtained in resistive heating experiments [24,25,54] suggest a possible melting line maximum near 100 GPa and 1000 K in qualitative agreement with the theoretical calculations of Ref. 29.

Experiments on the melting of hydrogen to higher pressures have been performed using laser heating techniques [26–28] including pulsed laser heating. The results of these very challenging experiments remain largely controversial, as there are a number of inconsistent observations. In particular the results of Deemyad, and Silvera [27], which utilized visual observations, are standing alone, as they suggest a very narrow maximum at the melting line, inconsistent with the theoretical predictions and the results of other measurements. Notably, Deemyad and Silvera have reported four pressure points obtained in one single experimental run; they have not been able to provide any experimental evidence of presence of hydrogen in the high-pressure cavity after the initial laser heating experiments. The results of this study were not reproduced in subsequent investigations [26,28], which presents results of multiple loads, and clear Raman evidence of hydrogen present in the sample cavity. Both studies [26,28] suggest that the melt line has a broad maximum near 100 GPa, in a qualitative agreement with the theoretical calculations of Ref. 29. However, the diagnostics of melting in Refs. 26, 28 is somewhat controversial. Eremets and Trojan [28] report changes in the laser speckle pattern and a large reversible drop in resistivity of a Pt foil which probe the sample cavity. These observations may be related to melting but could, in principle, be due to chemical reactions, or other phenomena unrelated to melting. A drop in the resistance of the Pt foil, claimed by Eremets and Trojan to be an indication of melting, was proposed to be due to a shunting by conducting fluid hydrogen. Instead, we suggest that the thermal flux, out of the laser heated Pt foil, increases rapidly through the convection in molten hydrogen, causing the foil to drop the temperature, and hence the electrical resistance. Subramanian *et al*. [26] reported on a large discontinuity of the Raman vibron at melting and attributed this to a change in chemical bonding in fluid hydrogen. However, this observation seemingly contradicts Raman measurements in resistively heated DACs, where a very small, or even no discontinuity was observed [25]. The reason for such discrepancy may be due to difficulties of containing, and hence measuring Raman spectra of fluid hydrogen in resistively heated DACs. Also, or alternatively, very large temperature gradients across the sample can give rise to bimodal Raman spectra observed in the laser heating experiments [26] as the Raman vibron shows a very steep temperature dependence. Summary of the experimental data on hydrogen melting strongly indicate that the available results *do not provide* the definitive prove of maximum in the melting line of hydrogen.

Conventionally, it is assumed that fluid hydrogen is molecular at moderate pressures below the triple point with solid and dissociated fluid >200 GPa, <1000 K. Raman measurements of fluid hydrogen [26,55] however show a continuous change with pressure in intramolecular bonding in the fluid state. Goncharov and Crowhurst [55] also found a large increase in the vibron bandwidth accompanied by a decreased vibron anharmonicity deduced from the spacings between excited vibrational states. Subrama-

nian *et al*. [26] show that the roton modes essentially disappear in the fluid state above 30 GPa. These observations can be understood due to the drastic decrease in lifetime of molecular states in fluid hydrogen with pressure. The lifetime of the molecular states become comparable with the vibrational period, but are shorter than the rotational period, making the latter unobservable.

Until recently, experimental observations of conducting states in dense hydrogen could only be performed in shock wave experiments [56–59] and static DAC experiments on hydrogen exceeding temperatures of 3000 K were inaccessible. Recently, Goncharov *et al*. [60] developed a new optical spectroscopy technique in pulsed laser heated DAC which allow to measure optical spectra in the visible spectral range. The sample is heated by 1–5 μs pulses of electrically modulated Yb fiber laser at 1070 nm. The optical spectra are measured using a supercontinuum generated in a photonic crystal fiber and are recorded as a function of time using a streak camera in a single two-dimensional CCD image along with the radiation spectra to measure the temperature spectroradiometrically. Such technique has opened a window of opportunity to probe hot dense hydrogen at *P–T* conditions thought to be unachievable through static compressions.

4. Phase II

The transition to phase II has been originally described as the one from spherically symmetric rotational states of pure para H_2 or ortho D_2 to a broken symmetry phase in which these symmetric states deform and material transforms an orientationally ordered state [34]. It has been shown that mixed ortho-para materials (for example with a normal composition corresponding to the high-*T* limit [61]) also transform to phase II (which reveals different rotational dynamics [37] and perhaps even a different crystal symmetry) at lower pressures. A very large isotope effect has been observed for the transition to phase II [34,62,63]. The large isotope effect on the transition pressure to BSP phase suggests that the transition is related to ordering of the quantum rotational degrees of freedom [18,49] as the rotational constants $B = h/4\pi^2 cI$, where I is the rotational moment of inertia, governing the rotational energies are very different for H_2 and D_2. On the microscopic level, at the entry to phase II, free molecular rotations are expected to transform to wide-angle librations for some of the rotational coordinates, which can be largely incoherent [39]. The first-principles path-integral molecular dynamic calculations revealed the quantum character of these molecular motions, however, these experience a "quantum localization" (or "quantum confinement") as molecular rotations become hindered in some rotation directions [38]. In contrast, recent *ab initio* path integral molecular dynamics (PIMD) of Li *et al*. [49] do not support the "quantum confinement" and instead suggest that the transition is governed by a competition between anisotropic inter-molecular interactions, and the thermal and quantum nuclear fluctuations.

Raman spectra of phase II reveal a combination of free molecular rotation excitations and libron like vibrations characteristic of the orientationally ordered molecules [35]. Raman and IR spectra of vibron modes have been used to map the II–I phase line. Below approximately 140 GPa, the transition can be traced by observing a small vibron discontinuity [16,18,19,34,37]. Above 140 GPa, the vibron frequency has a strong temperature dependence in phase II prior to the transition to phase I [17,33], suggesting that the orientational ordering develops gradually with pressure within phase II.

The determination of the structure of orientationally ordered hydrogen phases is a very challenging topic. Theoretical structure search is difficult because phase II retains a large amount of orientational disorder. Thus, a single theoretical approach (e.g., density functional theory, DFT) does not work well. Recently, Li *et al*. [49] suggested using PIMD technique for the most stable static molecular configuration to account for quantum nuclear motion at finite temperatures. However, the validity of these results needs to be verified against the experimental observations.

The experimental data are also very limited [46–48,64]. Normally, only 1 or 2 of the strongest reflections originating from 100 and 101 major peaks of hcp phase I of hydrogen could be observed. However, Goncharenko and Loubeyre [47] additionally reported one extra reflection observed in single crystal x-ray and neutron diffraction of D_2. They interpreted this as due to an incommensurate long-range order. In contrast, Raman study [37] rather suggested 3x5 Brillouin zone folding. Moreover, the modulation appears at a lower pressure than that reported for the I–II in Raman measurements [37].

5. Phase III

Phase III has been discovered in Raman observations at 77 K: the Raman vibron revealed an astonishing 100 cm^{-1} discontinuity at 155 GPa, and observations showed a two-phase coexistence in the pressure range of about 20 GPa, which is characteristic of the first-order transition [65]. Subsequent infrared absorption (IR) measurements showed a two order of magnitude increase in the vibron mode activity in phase III [36,66–68]. These observations initiated a number of suggestions about a new chemical bonding type in phase III related to a large intermolecular charge transfer [69]. However, direct reflectivity measurements [68] showed that the dipole moment associated to the IR vibron is very small (0.04e at 210 GPa), so the charge transfer may be of dynamic nature and be restricted within the molecule. However, density functional theory does predict a small structural distortion of the parent hexagonal closed-packed lattice of phase I [39,44].

For a long time vibrational spectroscopy served as the sole source of information on properties of phase III. Raman spectroscopy measurements of phase III revealed a number of observations, which shed light on the structural and dynamical properties of phase III. In addition to the vibron discontinuity, the II–III transition is characterized by a total alteration of the low-frequency spectra: the roton spectra (or their remnants) disappear and a number of new peaks appear at the transition to phase III (Fig. 2). These show a very strong pressure dependence, which identify them as the lattice modes (translational and librational) unlike the rotational modes (rotons) in phases I and II which are very weakly pressure dependent [34,70]. The frequencies of the Raman modes increase strongly with pressure and the modes become sharper (Fig. 2) [35]. Raman and IR spectra of phase III are also strongly temperature dependent. The Raman and IR vibron frequencies increase with temperature continuously in a wide temperature range which was determined in quasi-isobaric experimental scans [17–19]. There is a discontinuity in the vibron frequency at the II–III and I–III transitions , which quickly decreases with pressure and was reported to disappear above 235 K (in D_2) [37] even though two vibron peaks were observed near the transition. This was interpreted as a (tri)critical point, where either the transition becomes second order or terminates, so there is no distinction between phases I and III at higher pressures (and temperatures). The IR intensity was also found to decrease in intensity in the temperature runs [18,33] similar to that of the Raman and IR frequencies. This was described by a Maier–Saupe model [71], which characterizes the orientational ordering of classical rotors and initially was derived for liquid crystals. Within this model, the IR frequency and intensity and Raman frequency of the vibron can be treated as scalar order parameters characterizing the orientational ordering in phase III [18,33]. The conclusion about the nature of orientational ordering in low-temperature phase III is also supported by a relatively weak isotope effect (cf. transition pressures of transitions to phase II for H_2 and D_2), the insensitivity of the transition pressure to the ortho-para concentration [18,35] and the observation of the total disappearance of the roton Raman bands (Fig. 2).

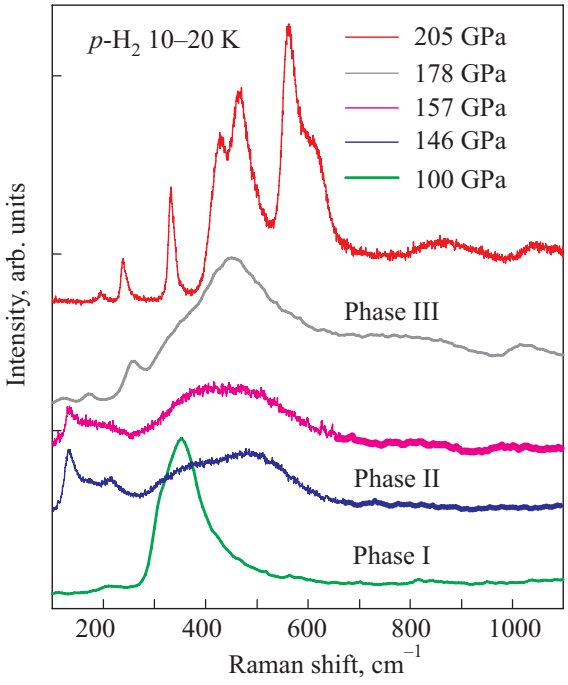

Fig. 2. (Color online) Raman spectra of hydrogen through transitions to phases II and III [35].

As in the case of phase II, the determination of the structure of orientationally ordered phase III of hydrogen is a very challenging topic and the experimental data are very limited [46]. Moreover, only 1 or 2 strongest reflections originated from 100 and 101 major peaks of hcp phase I of hydrogen could be observed. Recently, x-ray diffraction studies have been performed in the *P–T* range of stability of phase III (>155 GPa below 120 K) [46]. The results suggest that an hcp lattice remains a structural basis of phase III.

Theoretical structural search for high-pressure phases of hydrogen has a long history [39–44,72–74]. Here we briefly review the most relevant works for the high-pressure (>100 GPa) range, where the effects of quantum rotations and ortho-para distinctions is substantially diminished. In this regime the (DFT) should be well applicable. However, these results should also be treated carefully as the quantum effect related to large zero point energy make substantial contributions into the free energy.

The results of an extensive theoretical DFT structural search [40,42] suggested a monoclinic $C2/c$ structure as the primary candidate for phase III. A number of structures are very competitive in enthalpy in the pressure range of interest; the results depend on the level of DFT theory, form of pseudopotentials used, and treatment of proton zero point motion [40]. It is interesting that none of these structures agree well with the x-ray diffraction data (Fig. 3), although some level of agreement has been achieved with the Raman and IR data [35,67,75], especially with the presence of a strong IR vibron absorption mode. It is interesting that hybrid DFT calculations [76] find the $P6_3/m$ structure (which would yield the x-ray pattern that nicely agrees with the x-ray experiment) the most stable, although the previous study found that this structure is dynamically unstable above 120 GPa [40]. However, this structure seems inconsistent with the IR observations. For the sake of completeness, we would like to mention that the $Cmc2_1$ structure proposed by Toledano *et al.* [23] based on group theory is somewhat higher in DFT enthalpy, although Raman and IR activity and x-ray diffraction patterns broadly agree with the observations.

It is interesting that in spite of a large number of energetically competing structures determined in theoretical calculations, experimental observations show the stability of only one classically oriented solid phase in a very broad

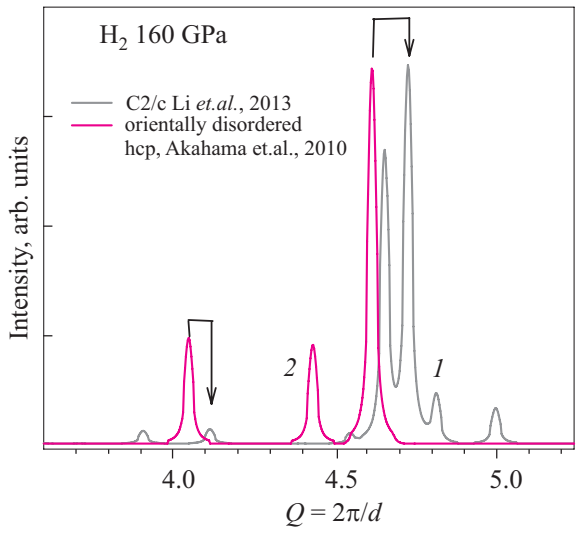

Fig. 3. (Color online) X-ray diffraction of phase III of hydrogen. Gray line (*1*): *C2*/c structure from Ref. 49 and pink line (*2*) is an hcp of molecular centers with the lattice parameters from the experimental study of Akahama *et al*. [46].

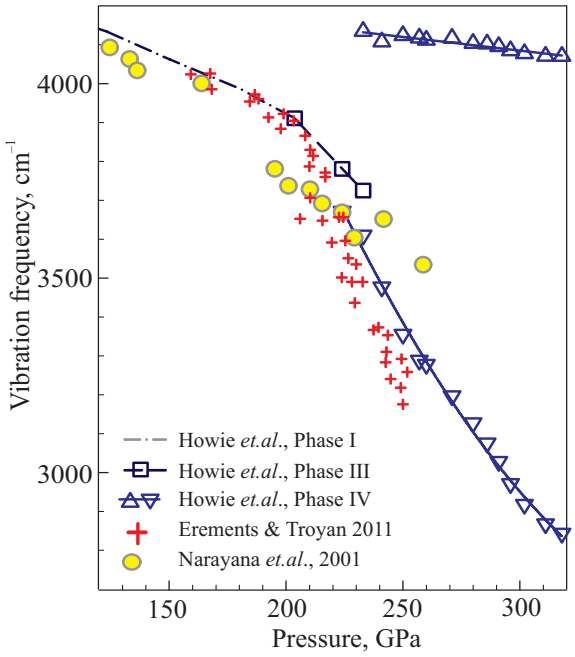

Fig. 4. (Color online) Raman vibron frequencies of hydrogen though the transition to phases III and IV at 300 K [10,11,14,81]

pressure-temperature range [12,77]. The pressure and temperature dependencies of vibron and phonon frequencies suggest that phase III becomes more stable at higher pressures and lower temperatures. A rather strong softening of molecular vibron Raman mode (above 35 GPa) has been interpreted as a "harbinger" of molecular dissociation, but later it was understood (e.g., Ref. 78) that a substantial part of this softening is coming from the increase of the intramolecular coupling [79,80]. The IR vibron, which contains much less contribution of this coupling starts softening only above 120 GPa [79]. However, unlike the situation with the classical soft modes related to the displacive phase transitions, there is no acceleration of the softening with pressure, making predictions of molecular dissociation with pressure rather uncertain [75]. Extrapolation of the optical data suggests that the optical closure in phase II should occur near 450 Gpa [75,77]. The effect of temperature was recognized to be very essential for metallization of hydrogen in static high-pressure conditions [11,14].

6. Phase IV

Until 2011 only the high-pressure room-temperature studies of hydrogen up to 180 Gpa [10] and to the claimed 340 GPa have been reported [81,82]. The latter results are very controversial mainly due to the fact that no positive diagnostics of hydrogen was offered. In Fig. 4 we show the compilation of the recently obtained Raman data on the molecular vibron up to 320 GPa compared to that reported previously by Ruoff [81]. The obvious conclusion is that either the pressure metrology in these early experiments was not reliable or other factors (e.g., lack of hydrogen in the sample chamber) are responsible for apparent discrepancy with the current results. The currently adopted in the field technique is the usage of the diamond Raman edge as a pressure calibrant. The Raman frequency of the diamond edge (e.g., Ref. 15) had been calibrated with respect to other sensors (mostly ruby) and is reliable in situations when the experiments are performed in similar geometrical conditions. However the results of Ruoff [81] obviously stand alone (Fig. 4) making the claim of transparent hydrogen at 342 GPa in the subsequent paper [82], which also does not present any positive diagnostics of hydrogen, highly questionable.

Two independent experiments have recently succeeded in reaching pressures in excess of 300 GPa at 300 K [11,14]. Similar Raman observations have been reported that show remarkable changes in Raman spectra above 200 GPa; firstly: the gradient of the vibron frequency versus pressure slope changes dramatically and a broad low-frequency peaks appear, and secondly: another system of low-frequency high intensity peaks emerge and the vibron splits in two. Eremets and Troyan [14] did not notice the appearance of new low-frequency peaks and interpreted this change as due to a transition to the *Cmca*-12 phase [40]. They also reported a change in optical properties and a total disappearance of Raman signal above 260–270 GPa, which was suggested to be due to transformation to metallic monatomic fluid.

On the contrary, Howie *et al.* [11] observed Raman signal to the highest pressure reached in the experiment — 320 GPa. They noticed the appearance of a second Raman vibron with very different pressure behavior of both the frequency and linewidth. Based on these observations and

theoretical predictions [40], they suggested a *Pbcn* structure for phase IV of hydrogen. This structure matches much better with the experimental observations, as the appearance of two distinct vibron modes and a strong low-frequency libron mode can be naturally explained based on the unique features of phase IV. Indeed, *Pbcn* hydrogen consists of molecular layers of two kinds: weakly bounded hexagonal, and strongly bounded graphene-like [40], which differ by the intramolecular distances that are substantially larger in the graphene-like layer. It is interesting that the hexagonal configuration of molecules in the graphene-like layer is somewhat reminiscent to the prediction of LeSar and Herschbach (Ref. 83, see also Ref. 84), who suggested that termolecular complexes $[(H_2)_3]$ could form before the transition to the atomic phase. This structure has been further examined theoretically in a number of recent publications, which suggest slightly different crystal symmetries [13,85] and fluxional behavior of graphene-like layers [86] related to large atomic tunneling quantum effects, and even suggest quantum liquid behavior for these layers [87]. Experimental and theoretical studies clearly indicate that phase IV is insulating or semimetallic as the optical spectra show the presence of the optical gap [11,30].

7. Conclusions

Key questions still remain about the higher pressure behavior. Predictions propose that phase IV will transform to a metallic molecular phase with *Cmca*-4 structure above 360 GPa [86]. However, monatomic phases [88–90] may compete at these compressions. We believe that experimental static compression studies which will verify these predictions are down the road [91]. Such studies will also address the issue of the predicted ground state fluid atomic metallic hydrogen [92–94]. The central problem is the treatment of the quantum effects at such regimes, which needs to be solved for such fundamentally important system as the element number one.

Acknowledgment

A. F. G. acknowledges support from the NSF, Army Research Office, NAI, and EFRee.

E.G. and R. T. H acknowledge support from the U.K. Engineering and Physical Sciences Research Council and Institute of the Shock Physics, Imperial College.

1. W.J. Nellis, *Rep. Prog. Phys*. **69**, 1479 (2006).
2. A.F. Goncharov and R.J. Hemley, *Chem. Soc. Rev*. **35**, 899 (2006).
3. A.F. Goncharov and J. Crowhurst, *Phase Transitions* **80**, 1051 (2007).
4. E.G. Maksimov and Y.I. Shilov, *Usp. Fiz. Nauk*. **169**, 1223 (1999).
5. J.M. McMahon, M.A. Morales, C. Pierleoni, and D.M. Ceperley, *Rev. Mod. Phys*. **84**, 1607 (2012).
6. R. Jeanloz, P.M. Celliers, G.W. Collins, J.H. Eggert, K.K.M. Lee, R.S. McWilliams, S. Brygoo, and P. Loubeyre, *P. Natl. Acad. Sci. USA* **104**, 9172 (2007).
7. R.F. Trunin, V.D. Urlin, and A.B. Medvedev, *Phys. Usp*. **53**, 577 (2010).
8. D.G. Hicks, T.R. Boehly, P.M. Celliers, J.H. Eggert, S.J. Moon, D.D. Meyerhofer, and G.W. Collins, *Phys. Rev. B* **79**, 014112 (2009).
9. P. Loubeyre, S. Brygoo, J. Eggert, P.M. Celliers, D.K. Spaulding, J.R. Rygg, T.R. Boehly, G.W. Collins, and R. Jeanloz, *Phys. Rev. B* **86**, 144115 (2012).
10. B.J. Baer, M.E. Chang, and W.J. Evans, *J. Appl. Phys*. **104** (3) (2008).
11. R.T. Howie, C.L. Guillaume, T. Scheler, A.F. Goncharov, and E. Gregoryanz, *Phys. Rev. Lett*. **108**, 125501 (2012).
12. C.S. Zha, Z.X. Liu, and R.J. Hemley, *Phys. Rev. Lett*. **108**, 146402 (2012).
13. C.J. Pickard, M. Martinez-Canales, and R.J. Needs, *Phys. Rev. B* **85**, 214114 (2012).
14. M.I. Eremets and I.A. Troyan, *Nat. Mater*. **10**, 927(2011).
15. Y. Akahama and H. Kawamura, *J. Appl. Phys*. **100**, 043516 (2006).
16. H.K. Mao and R.J. Hemley, *Rev. Mod. Phys*. **66**, 671 (1994).
17. A.F. Goncharov, R.J. Hemley, and H.K. Mao, *J. Chem. Phys*. **134**, 174501 (2011).
18. I.I. Mazin, R.J. Hemley, A.F. Goncharov, M. Hanfland, and H.K. Mao, *Phys. Rev. Lett*. **78**, 1066 (1997).
19. A.F. Goncharov, I.I. Mazin, J.H. Eggert, R.J. Hemley, and H.K. Mao, *Phys. Rev. Lett*. **75**, 2514 (1995).
20. M.P. Surh, K.J. Runge, T.W. Barbee, E.L. Pollock, and C. Mailhiot, *Phys. Rev. B* **55**, 11330 (1997).
21. B.J. Baer, W.J. Evans, and C.S. Yoo, *Phys. Rev. Lett*. **98**, 235503 (2007).
22. B.J. Baer, W.J. Evans, and C.S. Yoo, *Phys. Rev. Lett*. **102**, 235503 (2009).
23. P. Toledano, H. Katzke, A.F. Goncharov, and R.J. Hemley, *Phys. Rev. Lett*. **103**, 105301 (2009).
24. F. Datchi, P. Loubeyre, and R. LeToullec, *Phys. Rev. B* **61**, 6535 (2000).
25. E. Gregoryanz, A.F. Goncharov, K. Matsuishi, H. Mao and R.J. Hemley, *Phys. Rev. Lett*. **90**, 175701 (2003).
26. N. Subramanian, A.F. Goncharov, V.V. Struzhkin, M. Somayazulu, and R.J. Hemley, *P. Natl. Acad. Sci. USA* **108**, 6014 (2011).
27. S. Deemyad and I.F. Silvera, *Phys. Rev. Lett*. **100**, 155701 (2008).
28. M.I. Eremets and I.A. Trojan, *Jetp. Lett*. **89**, 174 (2009).
29. S.A. Bonev, E. Schwegler, T. Ogitsu, and G. Galli, *Nature* **431**, 669 (2004).
30. R.T. Howie, T. Scheler, C.L. Guillaume, and E. Gregoryanz, *Phys. Rev. B* **86**, 214104 (2012).
31. I. Tamblyn and S.A. Bonev, *Phys. Rev. Lett.* **104**, 065702 (2010).
32. M.A. Morales, C. Pierleoni, E. Schwegler, and D.M. Ceperley, *P. Natl. Acad. Sci. USA* **107**, 12799 (2010).

33. L.J. Cui, N.H. Chen, and I.F. Silvera, *Phys. Rev. B* **51**, 14987 (1995).
34. I.F. Silvera and R.J. Wijngaarden, *Phys. Rev. Lett*. **47**, 39 (1981).
35. A.F. Goncharov, R.J. Hemley, H.K. Mao, and J.F. Shu, *Phys. Rev. Lett*. **80**, 101 (1998).
36. M. Hanfland, R.J. Hemley, and H.K. Mao, *Phys. Rev. Lett*. **70**, 3760 (1993).
37. A.F. Goncharov, J.H. Eggert, I.I. Mazin, R.J. Hemley, and H.K. Mao, *Phys. Rev. B* **54**, 15590 (1996).
38. H. Kitamura, S. Tsuneyuki, T. Ogitsu, and T. Miyake, *Nature* **404**, 259 (2000).
39. K.A. Johnson and N.W. Ashcroft, *Nature* **403**, 632 (2000).
40. C.J. Pickard and R.J. Needs, *Nat. Phys*. **3**, 473 (2007).
41. J.S. Tse and D.D. Klug, *Nature* **378**, 595 (1995).
42. J.S. Tse, D.D. Klug, Y. Yao, Y. Le Page, and J.R. Rodgers, *Solid State Commun*. **145**, 5 (2008).
43. J. Kohanoff, S. Scandolo, G.L. Chiarotti, and E. Tosatti, *Phys. Rev. Lett*. **78**, 2783 (1997).
44. J. Kohanoff, S. Scandolo, S. de Gironcoli, and E. Tosatti, *Phys. Rev. Lett*. **83**, 4097 (1999).
45. K.J. Runge, M.P. Surh, C. Mailhiot, and E.L. Pollock, *Phys. Rev. Lett*. **69**, 3527 (1992).
46. Y. Akahama, M. Nishimura, H. Kawamura, N. Hirao, Y. Ohishi, and K. Takemura, *Phys. Rev. B* **82**, 060101(R) (2010).
47. I. Goncharenko and P. Loubeyre, *Nature* **435**, 1206 (2005).
48. H. Kawamura, Y. Akahama, S. Umemoto, K. Takemura, Y. Ohishi, and O. Shimomura, *J. Phys.: Condens. Matter* **14**, 10407 (2002).
49. X.-Z. Li, B. Walker, M.I.J. Probert, C.J. Pickard, R.J. Needs, and A. Michaelides, *J. Phys.: Condens. Matter* **25** 085402 (2013).
50. W.R. Magro, D.M. Ceperley, C. Pierleoni, and B. Bernu, *Phys. Rev. Lett*. **76**, 1240 (1996).
51. D. Saumon and G. Chabrier, *Phys. Rev. A* **46**, 2084 (1992).
52. S. Scandolo, *P. Natl. Acad. Sci. USA* **100**, 3051 (2003).
53. B. Boates and S.A. Bonev, *Phys. Rev. Lett*. **102**, 015701 (2009).
54. V. Diatschenko, C.W. Chu, D.H. Liebenberg, D.A. Young, M. Ross, and R.L. Mills, *Phys. Rev. B* **32**, 381 (1985).
55. A.F. Goncharov and J.C. Crowhurst, *Phys. Rev. Lett*. **96**, 055504 (2006).
56. S.T. Weir, A.C. Mitchell, and W.J. Nellis, *Phys. Rev. Lett*. **76**, 1860 (1996).
57. W.J. Nellis, S.T. Weir, and A.C. Mitchell, *Phys. Rev. B* **59**, 3434 (1999).
58. P. Loubeyre, P.M. Celliers, D.G. Hicks, E. Henry, A. Dewaele, J. Pasley, J. Eggert, M. Koenig, F. Occelli, K.M. Lee, R. Jeanloz, D. Neely, A. Benuzzi-Mounaix, D. Bradley, M. Bastea, S. Moon, and G.W. Collins, *High Pressure Res.* **24**, 25 (2004).
59. P.M. Celliers, G.W. Collins, L.B. Da Silva, D.M. Gold, R. Cauble, R.J. Wallace, M.E. Foord, and B.A. Hammel, *Phys. Rev. Lett*. **84**, 5564 (2000).
60. A.F. Goncharov, D.A. Dalton, R.S. McWilliams, and M.F. Mahmood, *Mater. Res. Soc. Symp. Proc*. 1405 DOI:10.1557/opl.2012.1560 (2012).
61. I.F. Silvera, *Rev. Mod. Phys*. **52**, 393 (1980).
62. H.E. Lorenzana, I.F. Silvera, and K.A. Goettel, *Phys. Rev. Lett*. **64**, 1939 (1990).
63. F. Moshary, N.H. Chen, and I.F. Silvera, *Phys. Rev. Lett*. **71**, 3814 (1993).
64. H. Kawamura, Y. Akahama, S. Umemoto, K. Takemura, Y. Ohishi, and O. Shimomura, *Solid State Commun*. **119**, 29 (2001).
65. R.J. Hemley and H.K. Mao, *Phys. Rev. Lett*. **61**, 857 (1988).
66. L.J. Cui, N.H. Chen, and I.F. Silvera, *Phys. Rev. Lett*. **74**, 4011 (1995).
67. N.H. Chen, E. Sterer, and I.F. Silvera, *Phys. Rev. Lett*. **76**, 1663 (1996).
68. R.J. Hemley, I.I. Mazin, A.F. Goncharov, and H.K. Mao, *Europhys. Lett*. **37**, 403 (1997).
69. R.J. Hemley, Z.G. Soos, M. Hanfland, and H.K. Mao, *Nature* **369**, 384 (1994).
70. A.F. Goncharov, M.A. Strzhemechny, H.K. Mao, and R.J. Hemley, *Phys. Rev. B* **63**, 064304 (2001).
71. M. Plischke and B. Bergersen, in: *Equilibrium Statistical Physics Prentice Hall*, Englewood Cliffs, NJ (1989), p. 74.
72. C.J. Pickard and R.J. Needs, *Phys. Rev. Lett*. **102** (2009).
73. E. Kaxiras and J. Broughton, *Europhys. Lett*. **17**, 151 (1992).
74. E. Kaxiras, J. Broughton,and R.J. Hemley, *Phys. Rev. Lett*. **67**, 1138 (1991).
75. A.F. Goncharov, E. Gregoryanz, R.J. Hemley, and H.K. Mao, *P. Natl. Acad. Sci. USA* **98**, 14234 (2001).
76. S. Azadi and T.D. Kuhne, *Pis'ma v ZhETF* **95**, 509 (2012).
77. P. Loubeyre, F. Occelli, and R. LeToullec, *Nature* **416**, 613 (2002).
78. N.W. Ashcroft, *Phys. Rev. B* **41**, 10963 (1990).
79. M. Hanfland, R.J. Hemley, H.K. Mao, and G.P. Williams, *Phys. Rev. Lett*. **69**, 1129 (1992).
80. F. Moshary, N.H. Chen, and I.F. Silvera, *Phys. Rev. B* **48**, 12613 (1993).
81. A.L. Ruoff, in: *High Pressure Science and Technology*, W. Trzeciakowski (ed.) World Scientific, Singapore (1996).
82. C. Narayana, H. Luo, J. Orloff, and A.L. Ruoff, *Nature* **393**, 46 (1998).
83. R. Lesar and D.R. Herschbach, *J. Phys. Chem*. **85**, 3787 (1981).
84. V. Labet, R. Hoffmann, and N.W. Ashcroft, *J. Chem. Phys*. **136**, 074502 (2012).
85. H.Y. Liu, L. Zhu, W.W. Cui, and Y.M. Ma, *J. Chem. Phys*. **137**, 074501 (2012).
86. A.F. Goncharov, J.S. Tse, H. Wang, J.H. Yang, V.V. Struzhkin, R.T. Howie, and E. Gregoryanz, *Phys. Rev. B* **87**, 024101 (2013).
87. H. Liu and Y. Ma, *Phys. Rev. Lett*. **110**, 025903 (2013).
88. J.M. McMahon and D.M. Ceperley, *Phys. Rev. Lett.* **106**, 165302 (2011).
89. V. Labet, R. Hoffmann, and N.W. Ashcroft, *J. Chem. Phys*. **136**, 074504 (2012).

90. H.Y. Liu, H. Wang, and Y.M. Ma, *J. Phys. Chem. C* **116**, 9221 (2012).
91. L. Dubrovinsky, N. Dubrovinskaia, V.B. Prakapenka, and A.M. Abakumov, *Nat. Commun*. **3**, 1163 (2012).
92. E. Babaev, A. Sudbo, and N.W. Ashcroft, *Nature* **431**, 666 (2004).
93. E. Babaev, A. Sudbo, and N.W. Ashcroft, *Phys. Rev. Lett*. **95**, 105301 (2005).
94. J. Chen, X.-Z. Li, Q. Zhang, M.I.J. Probert, C.J. Pickard, R.J. Needs, A. Michaelides, and E. Wang, *arXiv:1212.4554v1 [cond-mat.mtrl-sci]* (2012).

Bonding, structures, and band gap closure of hydrogen at high pressures

Alexander F. Goncharov,[1] John S. Tse,[2,3] Hui Wang,[2,3] Jianjun Yang,[2] Viktor V. Struzhkin,[1]
Ross T. Howie,[4] and Eugene Gregoryanz[4]

[1]*Geophysical Laboratory, Carnegie Institution of Washington, 5251 Broad Branch Road, Washington, D.C. 20015, USA*
[2]*Department of Physics and Engineering Physics, University of Saskatchewan, Saskatoon, SK Canada S7N 5E2*
[3]*State Key Lab of Superhard Materials, Jilin University, 130012, Changchun, P. R. China*
[4]*Centre for Science at Extreme Conditions and School of Physic and Astronomy, University of Edinburgh, Edinburgh, EH9 3JZ, United Kingdom*

(Received 27 August 2012; published 2 January 2013)

We have studied dense hydrogen and deuterium experimentally up to 320 GPa and using *ab initio* molecular dynamic (MD) simulations up to 370 GPa between 250 and 300 K. Raman and optical absorption spectra show significant anharmonic and quantum effects in mixed atomic and molecular dense phase-IV of hydrogen. In agreement with these observations, *ab initio* MD simulations near 300 K show extremely large atomic motions, which include molecular rotations, hopping, and even pair fluctuations, suggesting that phase IV may not have a well-defined crystalline structure. The structurally diverse layers (molecular and graphenelike) are strongly coupled, thus opening an indirect band gap; moreover, at 300 GPa, we find fast synchronized intralayer structural fluctuations. At 370 GPa, the mixed structure collapses to form a metallic molecular *Cmca*-4 phase, which exhibits a new interstitial valence charge bonding scheme.

DOI: 10.1103/PhysRevB.87.024101 PACS number(s): 62.50.−p, 61.50.Ks, 67.80.F−, 71.30.+h

Hydrogen at high densities is remarkably rich in phenomena as revealed through both dynamic[1] and static[2–5] experiments and theoretical calculations.[6–9] Phases I and II have distinct quantum properties related to molecular rotations and possess species with different parity of the rotational states (ortho-para distinction).[10] In contrast, phase III was proposed to be orientationally ordered in a classical sense,[4,6] similar to molecular phases of heavier diatomic molecules, e.g., nitrogen. Surprisingly, the structure of a recently discovered phase IV has been found to consist of two very distinct structural units, as manifested by the presence of the Raman intramolecular vibrations (vibrons) with frequencies substantially different from each other and from other known phases of hydrogen.[5,8,11]

Based on the structural search of the lowest enthalpy phases, which included zero-point motion and full vibrational contributions, a number of candidate structures were proposed for phase IV.[8,11,12] The theoretical studies all agree on the presence of two distinct structural units: a "molecular" (Br_2-like) and "graphenelike" (G) layers, which repeat periodically in the A-B-A-B sequence. However, the symmetry of the graphenelike layer, which consists of elongated weakly bonded H_2 molecules, is a matter of debate. It has been pointed out[11,12] that the originally proposed *Pbcn* structure,[8] which contains three kinds of hexagonal rings, is dynamically unstable as the lowest-frequency libron $(H_2)_3$ ring mode has an imaginary frequency. Two other very similar structures [Pc (Ref. 11) and Cc (Ref. 12)] have further been proposed as they have slightly lower enthalpy and show no imaginary frequencies.

Raman measurements of phase IV show a dramatic softening of the G-layer vibron mode with pressure[5] in a qualitative agreement with theoretical calculations[11] which reported that weakly bonded H_2 molecules elongate with pressure, thus revealing a tendency of the G layers to transform to truly graphene layers with symmetric hydrogen bonds. Thus, one can expect that phase IV would transform to the *Ibam* structure[11] at 350 GPa. However, the *Cmca*-4 structure[7,8] was found to be energetically favorable above 225 GPa,[11,13] while metadynamics simulations[12] showed the transition to the same structure at 275 GPa. Both the *Cmca*-4 and competing with it energetically *Cmca*-12 phases are metallic[7,8,11,14] and their occurrence in the calculations has been invoked to explain the experimental observations of atomic metallic fluid hydrogen in Ref. 15. However, the findings of Ref. 15 are found to disagree with the optical data of Ref. 5.

In this paper, by combining the experimental data of Ref. 5 with *ab initio* molecular dynamical (MD) theoretical calculations, we demonstrate fluxional characteristics of phase IV, which makes the description of the instantaneous structure of phase IV difficult in terms of the conventional space groups. This is demonstrated by experimental observations of significant quantum effects in molecular vibrations and librations in the G layer, which are consistent with frequent molecular rotations and intermolecular atomic fluctuations. These findings are supported by MD calculations, which show very large atomic motions and intralayer H_2 re-arrangements at 250–300 K. MD simulations also demonstrate the transformation to the *Cmca*-4 structure at 370 GPa, where the structural diversity of the Br_2-like and G layers vanishes and large atomic motions cease.

Constant pressure–constant temperature (N,P,T) ensemble classical molecular dynamics calculations were performed with the pseudopotential (PS) plane-wave method. The quality of the PS has been checked against all electron calculations to guarantee the results are valid within the pressure range studied here. A $1 \times 1 \times 2$ *Pbcn* (Ref. 8) supercell with 48 atoms was used as the initial structure. We have performed MD calculations for phase IV of hydrogen at 250–370 GPa at 250–300 K. Thermodynamic equilibrium was usually achieved in the first 6 ps. The length of the simulation varied from 20 ps at 250 and 370 GPa to 87 ps at 300 GPa. The maximum deviation throughout the duration of the MD calculations is less than 0.4 meV/atom in the internal energy and the pressure was

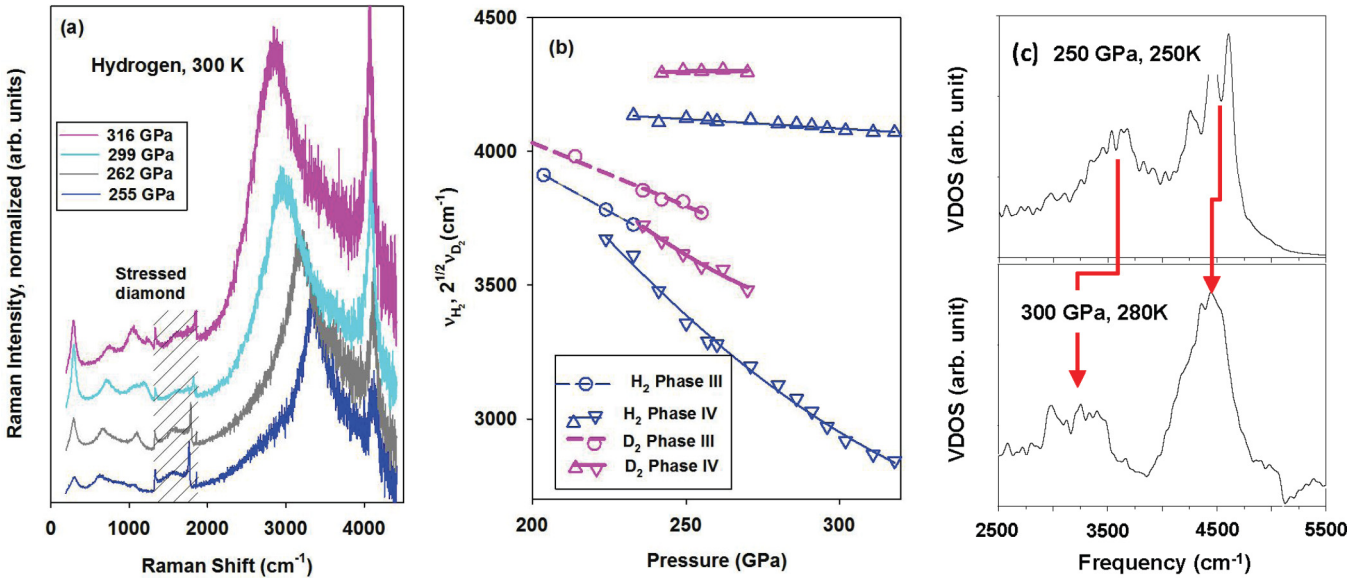

FIG. 1. (Color online) Vibrational properties of H_2 and D_2 at 300 K up to 320 GPa. (a) Intensity normalized Raman spectra with pressure; the hatched area corresponds to Raman signal of stressed diamonds; (b) experimental Raman frequencies of the soft vibron modes in H_2 and D_2 with pressure; the frequencies of D_2 are multiplied by $\sqrt{2}$; discontinuities of the vibron frequencies at 230 GPa are due to the III-IV transition; there is a 10–15 GPa pressure range of phase coexistence; (c) vibrational spectra deduced from MD simulations. The vertical red lines show the behavior of two major Raman vibrons.

within 2% of the target. The results of the simulations should be at least qualitatively correct since the ratio of the mean atomic distance $(V/N)^{1/3}$ and the thermal de Broglie wavelength is larger than 1 for the studied density range.[16] Quantum effect normally enhances delocalization of the hydrogen spatial distribution. Since the classical simulations were performed at relatively high temperature (ca. 300 K), it is expected that the quantum zero-point motions will not fundamentally alter the hopping and molecular rearrangement processes.[6] *GW* calculations were performed with the code VASP,[17] employing the projector augmented wave (PAW) potential.[18] The band structure was constructed from interpolation of *GW* corrected Monkhorst-pact *k*-point set using Wannier functions.[19]

The detailed experimental procedures are described in Ref. 5. We have carried out an intensity calibration performed using a light source with a known spectral distribution to the Raman spectra measured [Fig. 1(a)] and applied a coupled oscillator model[20] to the intensity corrected Raman spectra. An interesting feature of the normalized Raman spectra is that they are dominated by the vibron modes. The model calculations show that the observed pressure-induced relative change in intensity of some of the Raman modes with frequencies below 1300 cm^{-1} (300, 800, and 1050 cm^{-1} bands at 240 GPa) can be explained by their vibrational coupling with the lower-frequency vibron mode from the *G* layer, which softens with pressure abruptly (soft vibron mode). However, the 500- and 700 cm^{-1} bands do not show any measurable intensity variation with pressure (Fig. 2). We interpret this diverse mode behavior as due to their different vector of the normal modes of vibrations (Fig. 3). The latter two modes correspond to the molecular translation and rotations in the Br_2-like layers, while the former ones, which show a substantial variation in intensity with pressure, correspond to similar motions in the *G* layers. The 300 cm^{-1} band is a unique *G*-layer mode corresponding to the librational motion of the hydrogen rings consisting of three H_2 dimers. Our mode assignment is based on theoretical calculations for *Pc* (Ref. 11) and *Pbcn* (Ref. 8) (Fig. 3) structures of hydrogen.

The vibron frequencies show a distinct isotope effect for the vibron [Fig. 1(b)] and the lowest-frequency libron mode (300 cm^{-1}), while the other modes show very small isotope dependencies (Figs. 4 and 5). The isotope effect on the vibron and libron modes increases with pressure. For the vibron modes, the isotope effect is substantially larger for the soft mode. The linewidth of the soft vibron mode increases very steeply at 230–250 GPa and then remains almost pressure independent up to 320 GPa [Fig. 4(b)].

A very large isotope effect and broadening (compared to other hydrogen phases) of the soft vibron mode from the *G* layers is evidence for the dramatically increased anharmonicity of this mode. Using the Morse formalism for an underlying effective potential[21] we determined the pressure-dependent parameters of this potential using the experimental data for H_2 and D_2 [Fig. 1(b)]. We find that at 320 GPa, the potential well becomes very shallow due to the lowering of the barrier between the potential wells; it can accommodate only two vibrational levels for hydrogen (Fig. 6). The proximity of the first excited level to the barrier top splits this level as the tunneling between the wells becomes very frequent.[24] This provides a qualitative explanation for the anharmonic broadening effects [Fig. 4(b)]. We would like to stress that these effects have truly quantum characteristics, as much smaller peak broadening is observed for D_2 and there is a very large isotopic frequency difference for both the soft vibron and roton mode in the *G* layer (Figs. 4 and 5). The vibrational properties of H_2 deduced from MD simulations [Fig. 1(c)] show substantial softening and broadening of the

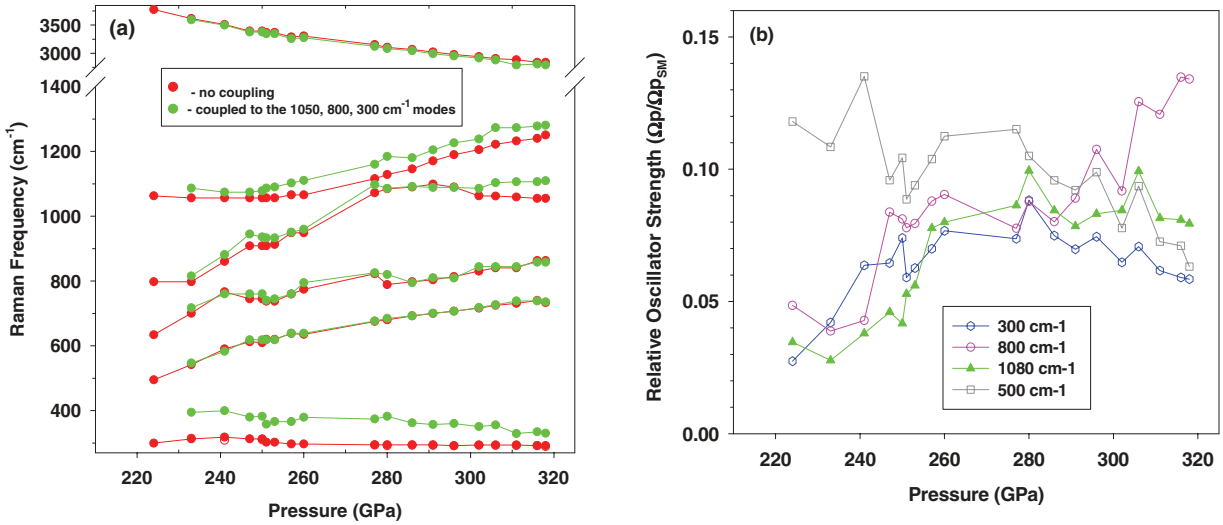

FIG. 2. (Color online) The results of the Raman modes analysis performed using a coupled oscillator model (Ref. 20). Panel (a) shows the positions of the experimentally measured Raman bands as a function of pressure determined by applying this model to the intensity corrected Raman spectra. The positions of the bare frequencies are given in two cases: (i) the 300, 800, and 1050 cm^{-1} modes are coupled to the soft mode and the intensities of these modes are fully due to the coupling (green circles); (ii) there is no coupling (red circles), the positions of the bands and their intensities correspond to the measured ones. These cases correspond to two extremes; we expect that the reality is somewhere in-between. Panel (b) shows the relative intensities of the four most intense low-frequency Raman bands with respect to that of the soft vibron mode. This illustrates the diverse behavior of the modes with respect to the vibrational coupling, which is expected to increase with pressure as the soft vibron mode and other modes become closer in frequencies.

G-layer vibron at 3100–3600 cm^{-1} between 250 and 300 GPa, which is in qualitative agreement with the experiment.

Figure 7 summarizes the results of the analysis of the MD trajectories for two dissimilar planes. At 250 GPa, the Br_2-like layers consist of a hexagonal lattice of "clouds" (Fig. 7, leftmost columns). These correspond to almost free rotation of H_2 molecules about the center of their bonds and maintaining the intramolecular bond lengths characteristic of "free" molecules (0.72 Å). In comparison, the G layers can be represented as an almost equally populated honeycomb lattice, and one does not see any difference in dimensions or shape of the constituting hexagons, which are expected for the *Pbcn* (Ref. 8) and *Pc* (Ref. 11) structures. Further inspection includes the color of dots (tracing the atoms) as the change in color would correspond to collaborative "hopping" of the H_2 molecules in the Br_2 layers and H atoms in the G layers from one site to the other. At 250 GPa, this hopping is relatively infrequent for the Br_2 layers, while it seems more frequent for the G layers with an average of ca. 1 jump every 4 ps. At 300 GPa (Fig. 7, central columns), the time average difference in distribution of the H atoms between Br_2 and G layers apparently disappears; both show a honeycomb structure superimposed by the increased "clouds" due to molecular rotations. Closer analysis of the MD trajectories shows that this occurs due to synchronized intralayer atomic fluctuations, which change the molecularlike Br_2 layers to the more atomiclike G layers and vice versa. Further details of the analysis will be published elsewhere. Based on extraordinary large atomic fluctuations observed in the MD runs at 250 and 300 GPa, we conclude that the structural presentation of phase IV in terms of an ideal crystal lattice *may not* be valid. The averaged over time crystal structure can be represented by the *Ibam* phase[8] with eight atoms in the primitive unit cell.

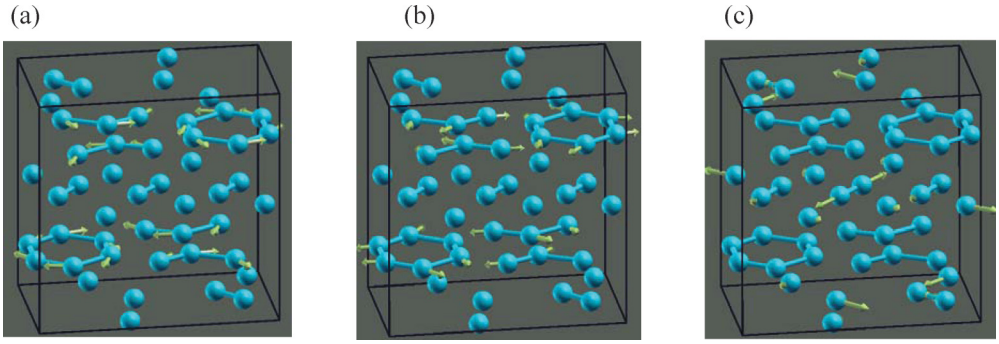

FIG. 3. (Color online) The atomic motions for the most prominent Raman modes of *Pbcn* hydrogen as the result of the DFT calculations: (a) low-frequency libron mode; (b) soft vibron mode of the graphenelike layer; (c) vibron mode of the Br_2- like layer.

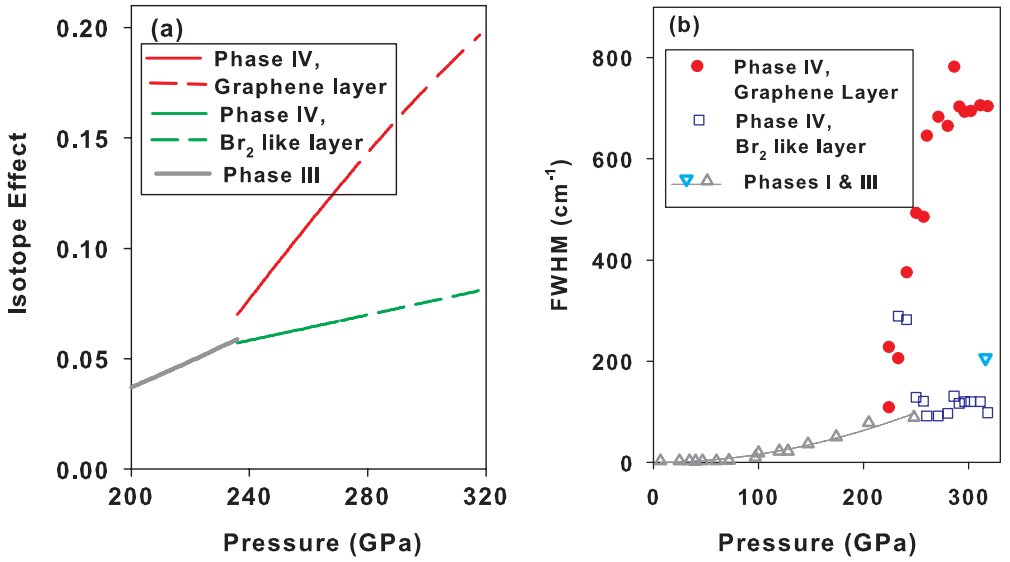

FIG. 4. (Color online) (a) The Raman isotope effect on the vibron frequency determined as $\alpha = \log_{10}(\sqrt{2}\nu_{D_2}/\nu_{H_2})/\log_{10}(2)$; the dashed lines correspond to linear extrapolations of the D_2 data to higher pressures; (b) vibron linewidths of H_2 as a function of pressure. Data for phases I and III are from Refs. 22 and 23 (gray triangles and cyan triangle, respectively).

Simulations at 370 GPa and 300 K (Fig. 7, rightmost columns) show a transition to another phase, which is very different from phase IV structurally and chemically (cf. *Ibam*). The amplitudes of the atomic motions are much smaller for this structure and all the crystallographic layers become structurally equivalent. This phase is metallic and it has *Cmca*-4 symmetry, which has been previously proposed.[7,8] The structure consists of crystallographically equivalent molecules with the bond length of 0.776 Å. The frequencies of the vibron in the *Cmca*-4 phase merge to a single set of modes at 3100 cm^{-1} (Fig. 8). As will be discussed later, this is a consequence of weaker H-H bonds due to electron transfer from the bonding to the interstitial region.

Now, we switch to the electronic properties. Optical absorption spectra [Fig. 9(a)] near the absorption edge demonstrate that the expression $\alpha \propto (h\upsilon)^2$ holds. This suggests that the

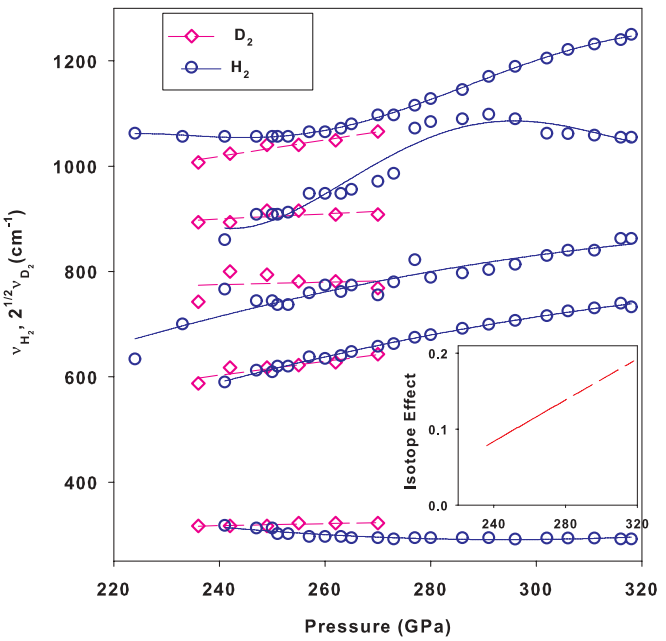

FIG. 5. (Color online) Raman frequencies of the lattice and librational modes of H_2 and D_2 with pressure; the Raman frequencies of D_2 are multiplied by $\sqrt{2}$. Inset: the Raman isotope effect on the lowest-frequency libron frequency determined as $\alpha = \log_{10}(\sqrt{2}\nu_{D_2}/\nu_{H_2})/\log_{10}(2)$; the dashed lines correspond to linear extrapolations of the D_2 data to higher pressures.

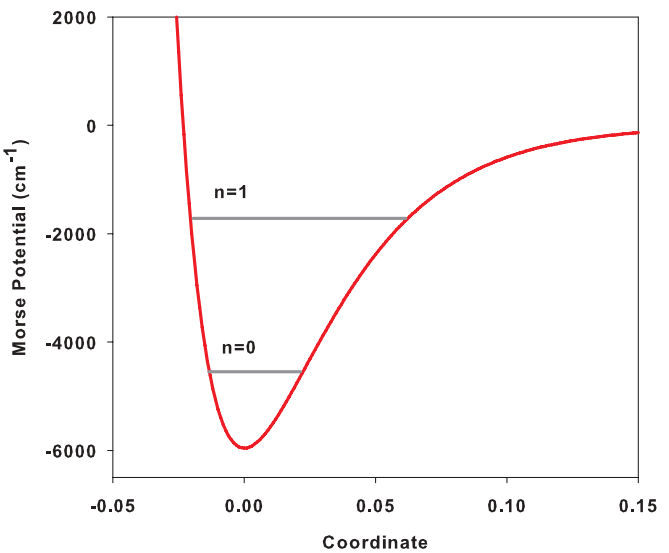

FIG. 6. (Color online) Effective intramolecular potential for dense hydrogen at 320 GPa determined from the Raman data for the soft vibron mode of H_2 and D_2 [Fig. 1(b)] (Ref. 21). The data for D_2 are extrapolated using the best second-order polynomial fit shown in Fig. 1(b). The potential is approximated by the Morse function and is plotted as a function of a dimensionless linear coordinate (Ref. 21). Horizontal lines represent the vibrational levels. Only two lowest-energy vibrational levels correspond to the bound states at 320 GPa (solid lines).

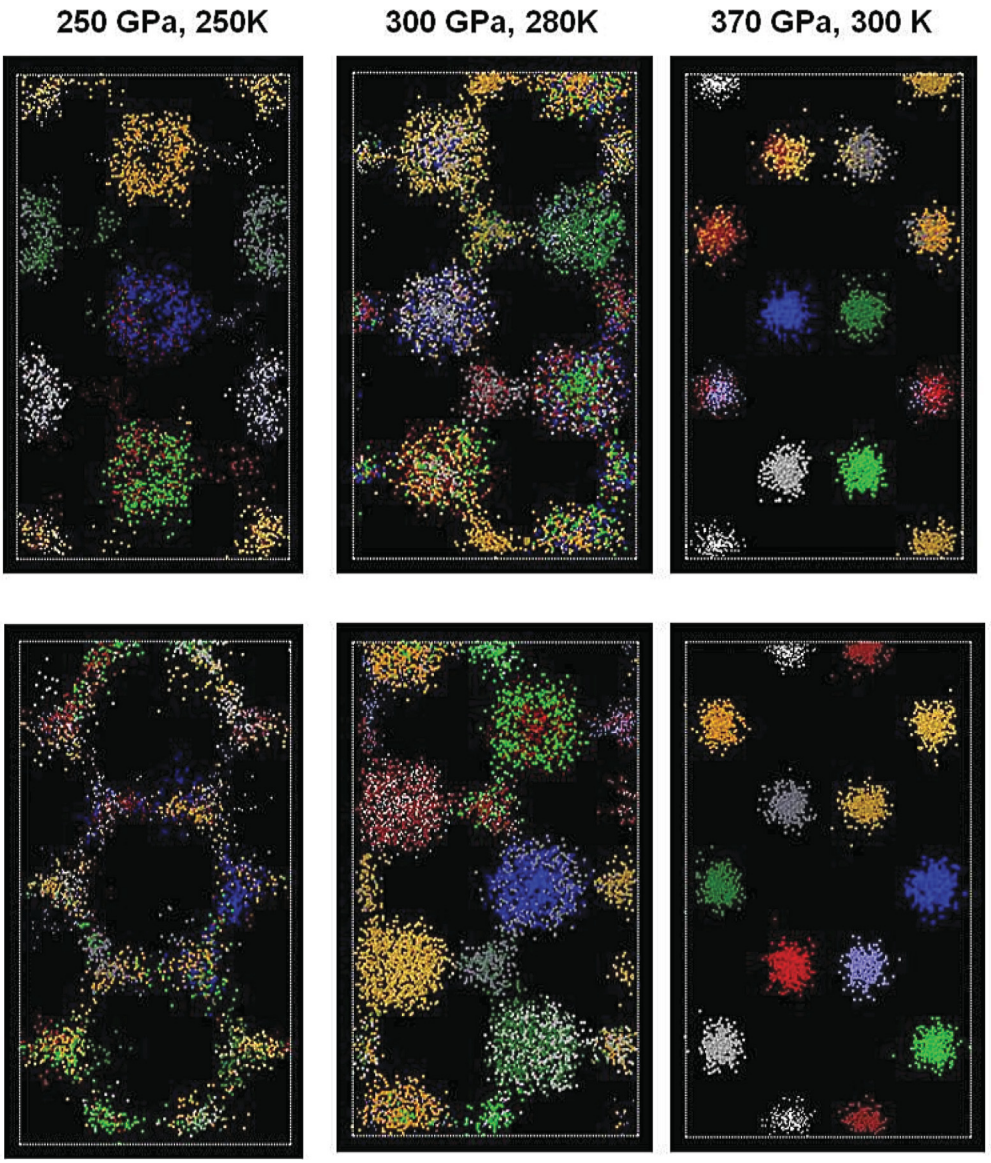

FIG. 7. (Color online) Molecular dynamics trajectories of three runs. The top row corresponds to the Br_2-like layer, while the bottom row to the *G* layer. Different colors correspond to different atoms.

absorption edge is determined by indirect optical transitions. This is in agreement with theoretical calculations, which clearly demonstrate that the band gap is indirect as the extrema of the conduction and valence bands are not in the Γ point (Fig. 10). Also, the experimental and theoretical (*GW*) pressure dependencies of the indirect band gap agree very well [Fig. 9(b)].

Theoretical calculations of the band gap using the hybrid density functional theory (DFT techniques)[25] agree well with our data (Fig. 9), while those determined by standard DFT methods[11] show much lower band gaps (not shown). Also, our theoretical calculations do predict the band-gap closure at approximately the same pressure, at which the transition to the *Cmca* phase occurs in MD simulations. This may be purely coincidental as we have performed calculations for a limited number of pressure points. Moreover, the calculated band gaps are for the static *Pbcn* structures, while we believe that the structure of phase IV is fluxional. More investigations should be performed to find out whether this good agreement of the experimental and theoretical *GW* and hybrid DFT band gaps is meaningful. The experimental spectra also show additional lower-energy absorption [Fig. 9(a)], which we attribute to disorder-induced processes similar to the Urbach absorption in disordered semiconductors. Similar effects have been observed previously in a disordered high-pressure phase of nitrogen.[27] Notably, the experimentally determined band gap of phase IV appears to be lower than that for phase III.

To investigate the nature of the chemical interactions on the electronic structure, calculations were performed on independent Br_2-like and *G* layers in the *Pbcn* structure and compared with the full crystal (Fig. 11). It is surprising that both the Br_2 and *G* layers are metallic! However, the interactions of these two distinct layers led to an opening of the band gap in the *Pbcn* structure. This finding can be explained by a charge transfer from the graphene layer to the Br_2 layer in the full structure. The valence band width was increased by

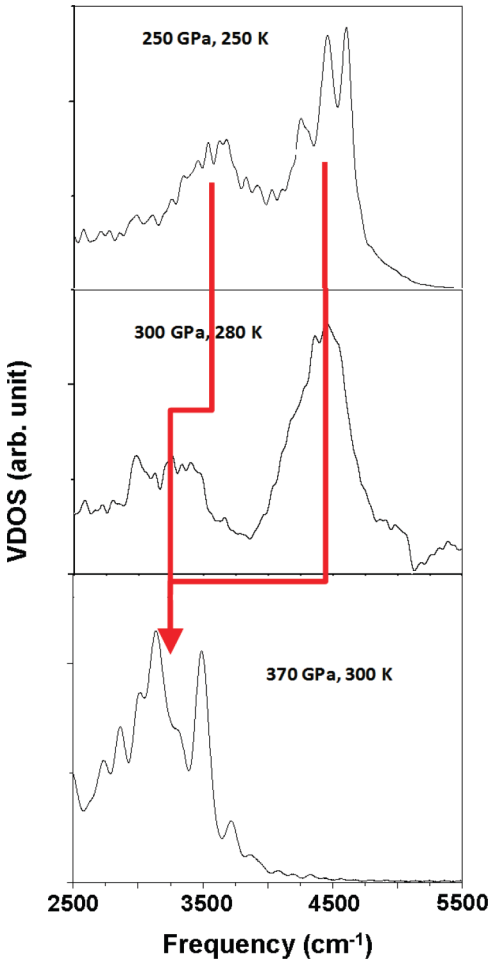

FIG. 8. (Color online) The vibrational spectra deduced from MD simulations (the lines are guides to the eye showing the evolution of the H_2 vibrons with increasing pressure).

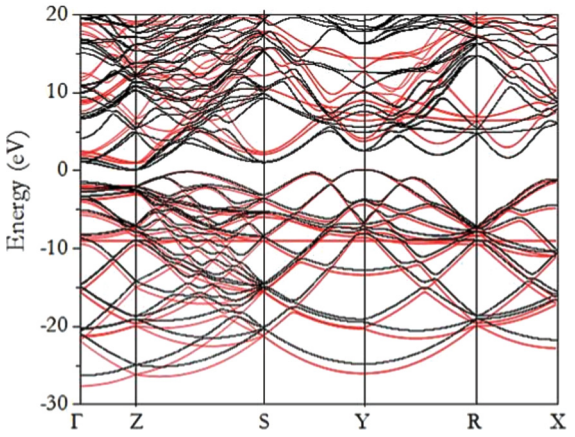

FIG. 10. (Color online) Electronic band structure of *Pbcn* H_2 at 300 GPa. Black and red lines are the results for GGA and *GW* methods, respectively.

almost 5 eV as a result of the interaction of the Br_2 and *G* layers. This is accompanied by the opening of a small energy gap between the valence and conduction bands at 250 and 300 GPa.

The electronic structures of both high-pressure high-temperature phases of hydrogen, phase IV, and *Cmca*-4 are unusual for simple molecular solids. Plots of the difference in total charge density of the *Pbcn* structure from the constituent hydrogen atoms are shown in Fig. 12. Notably, the electron density is depleted in the atomic regions near the interstitial sites of the graphene layer. Therefore, there is a charge transfer from the *G* layers to the Br_2 layer resulting in insulating behavior, which helps to stabilize the novel structure. Bader analysis of the electron density topology of the structure at 250 and 300 GPa (Fig. 13) shows that the electrons in the graphene layer are not delocalized, and bond critical points between pairs of H atoms can be clearly defined. Thus, phase IV of

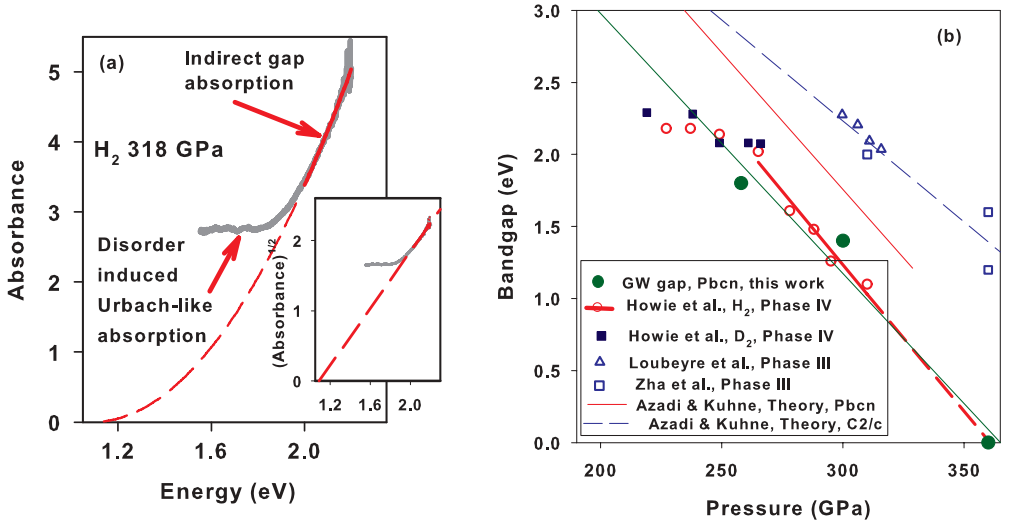

FIG. 9. (Color online) Band gap of phase IV of H_2. (a) Experimental optical absorption spectra at 318 GPa. The inset shows that the square root of absorbance is linear with energy near the absorption edge, which is characteristic of indirect gap absorption. (b) Experimental and theoretical band gaps for phases III and IV of H_2 and D_2. The data presented correspond to the following references: Howie *et al.* (Ref. 5) reanalyzed here assuming that the band gap is indirect, *resulting in lower values than in the original paper*, Azadi & Kuhne (Ref. 25), Loubeyre *et al.* (Ref. 23), and Zha *et al.* (Ref. 26).

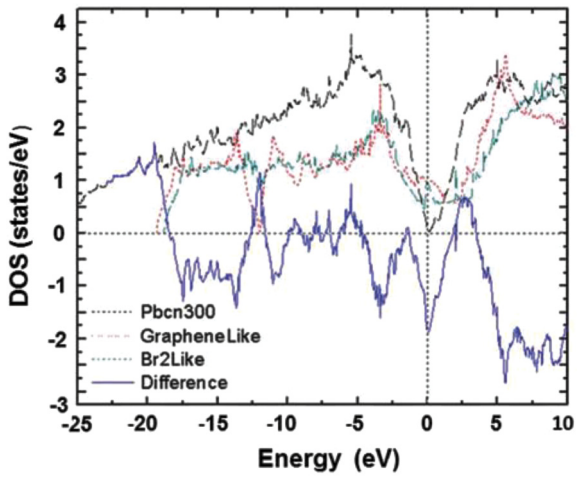

FIG. 11. (Color online) Full and partial density of electronic states of *Pbcn* hydrogen at 300 GPa.

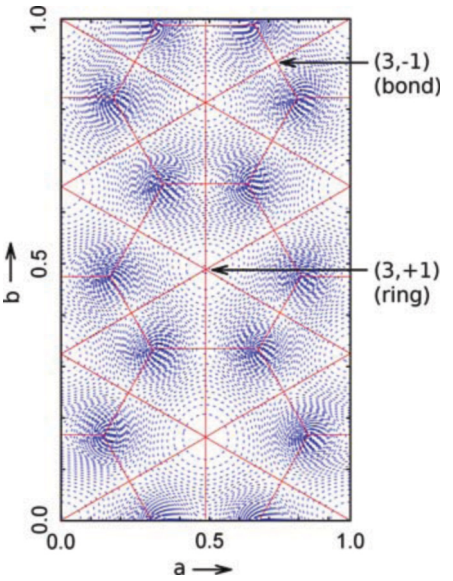

FIG. 13. (Color online) The Bader analysis (Ref. 28) of the *G* layers of *Pbcn* hydrogen at 250 GPa. The *ab* plane is shown. The (3, −1) bond critical points are at 0.236, 0.079, 0.250; 0.730, 0.757, 0.251; 0.500, 0.343; 0.250; 0.000, 0.486, 0.250; 0.243, 0.414, 0.249; 0.00, 0.172, 0.250. The electrons in the graphene layer are not delocalized. The bond critical points between a pair of H atoms can be clearly defined. The H_2 remain molecular in nature.

H_2 remains molecular in nature. However, these molecules must be extremely short-lived judging from the results of MD simulation (Fig. 7), showing the extreme mobility of atoms in the *G* layers. Moreover, at 300 GPa we even see the interlayer structural fluctuations (Fig. 7), which are very fast (<10 fs).

Finally, we analyze chemical bonding in the *Cmca*-4 structure, which becomes energetically more favorable than *Pbcn* above 320 GPa in our calculations; our MD simulations show that it forms at 370 GPa spontaneously. Electron density topological analysis[28] reveals that the structure of *Cmca*-4 is truly molecular but the electronic structure is metallic. The electronic density is partially pushed out of the intramolecular space to interstitials Fig. 12(b), thus resulting in decreased vibron frequency [Fig. 1(c)] with the rather short closest interatomic distance of 0.776 Å. The hypothetic high-pressure structure of H_2 (*Cmca*-4) demonstrates the presence of interstitial space "pockets" with an increased electronic density. Such phenomena have been previously reported under pressure in other light elements, for example, in Li,[29] but this is the first indication of that kind of behavior in hydrogen. Similar to the light alkalis, the interatomic potentials in hydrogen evolve with density to become very flat prior to this change in chemical bonding scheme (Fig. 6). Light elements in this regime tend to show structural diversity,[29–31] low-frequency vibrational modes,[22,32] and low melting temperatures.[30,31] This is the consequence of proton zero-point energy becoming the important energy scale because of a decline of the intramolecular bonding (e.g., Refs. 22 and 31).

In conclusion, combined experimental and theoretical studies on the high-pressure phases of hydrogen at

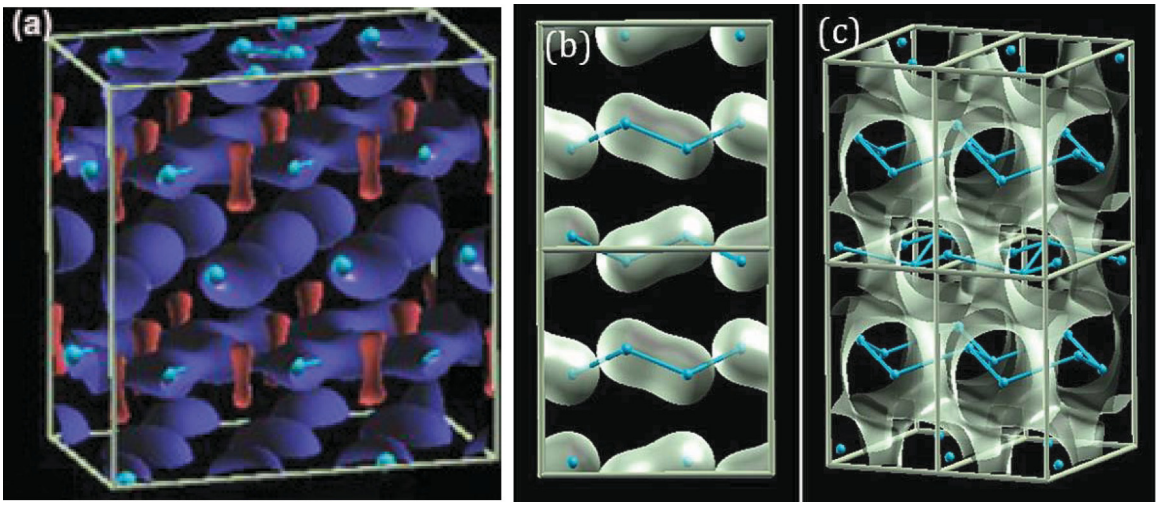

FIG. 12. (Color online) Electron topology of high-pressure phases of H_2. (a) Total electron density difference for *Pbcn* from the constituent hydrogen ($\Delta\rho = -0.176$ e/Å^3). (b), (c) Electron density isosurfaces for the values of 1.0 e/Å^3 and 0.5 e/Å^3, respectively, for the *Cmca*-4 structure.

250–300 K reveal a number of new phenomena, which were not expected previously (e.g., Refs. 8,11, and 33). The optical and vibrational spectroscopy experiments on phase IV up to 320 GPa show strong anharmonic effects, consistent with large atomic motions and strong proton tunneling phenomena. The MD simulations document the strong atomic motion for phase IV (which makes the averaged in time structure to be *Ibam*), and in addition demonstrate a spontaneous transition to the *Cmca*-4 structure. Electronic band-structure calculations performed on *Pbcn* hydrogen, used as a structural proxy for phase IV, demonstrate the intermolecular charge transfer that opens an indirect band gap in good accord with the experimental observations. Both studied high-pressure phases of hydrogen show the electronic density anomalies, which reduce the intramolecular bond order index. Further experiments to higher pressures are needed to verify the predicted phase changes reported here.

A.F.G. acknowledges support from the NSF, Army Research Office, NAI, and EFRee. V.V.S. acknowledges support of the DOE Grant No. DE-FG02-02ER45955. R.H and E.G. acknowledge support from the U. K. Engineering and Physical Sciences Research Council and Institute of the Shock Physics, Imperial College. We thank C. J. Pickard for important comments on the results concerning the charge density, and for sending us the results of phonon calculations for the *Pc* structure of phase IV of H_2.

[1]S. Weir, A. Mitchell, and W. Nellis, Phys. Rev. Lett. **76**, 1860 (1996).
[2]I. F. Silvera and R. J. Wijngaarden, Phys. Rev. Lett. **47**, 39 (1981).
[3]H. K. Mao and R. J. Hemley, Rev. Mod. Phys. **66**, 671 (1994).
[4]I. I. Mazin, R. J. Hemley, A. F. Goncharov, M. Hanfland, and H. K. Mao, Phys. Rev. Lett. **78**, 1066 (1997).
[5]R. T. Howie, C. L. Guillaume, T. Scheler, A. F. Goncharov, and E. Gregoryanz, Phys. Rev. Lett. **108**, 125501 (2012).
[6]H. Kitamura, S. Tsuneyuki, T. Ogitsu, and T. Miyake, Nature (London) **404**, 259 (2000).
[7]K. A. Johnson and N. W. Ashcroft, Nature (London) **403**, 632 (2000).
[8]C. J. Pickard and R. J. Needs, Nat. Phys. **3**, 473 (2007).
[9]E. Babaev, A. Sudbo, and N. W. Ashcroft, Nature (London) **431**, 666 (2004).
[10]I. F. Silvera, Rev. Mod. Phys. **52**, 393 (1980).
[11]C. J. Pickard, M. Martinez-Canales, and R. J. Needs, Phys. Rev. B **85**, 214114 (2012).
[12]H. Liu, L. Zhu, W. Cui, and Y. Ma, J. Chem. Phys. **137**, 074501 (2012).
[13]C. J. Pickard, M. Martinez-Canales, and R. J. Needs, Phys. Rev. B **86**, 059902(E) (2012).
[14]S. Lebegue *et al.*, Proc. Natl. Acad. Sci. USA **109**, 9766 (2012).
[15]M. I. Eremets and I. A. Troyan, Nat. Mater. **10**, 927 (2011).
[16]Z. J. Yan, Eur. J. Phys. **21**, 625 (2000).
[17]G. Kresse and J. Furthmuller, Phys. Rev. B **54**, 11169 (1996).
[18]G. Kresse and D. Joubert, Phys. Rev. B **59**, 1758 (1999).
[19]D. R. Hamann and D. Vanderbilt, Phys. Rev. B **79**, 045109 (2009).
[20]A. F. Goncharov, V. V. Struzhkin, H. K. Mao, and R. J. Hemley, Phys. Rev. Lett. **83**, 1998 (1999).
[21]N. W. Ashcroft, Phys. Rev. B **41**, 10963 (1990).
[22]A. F. Goncharov and J. Crowhurst, Phase Transitions **80**, 105 (2007).
[23]P. Loubeyre, F. Occelli, and R. LeToullec, Nature (London) **416**, 613 (2002).
[24]K. S. Schweizer and F. H. Stillinger, J. Chem. Phys. **80**, 1230 (1984).
[25]S. Azadi and T. D. Kuhne, Pis'ma Zh. Tekh. Fiz. **95**, 509 (2012) [JETP Letters **95**, 449 (2012)].
[26]C. S. Zha, Z. X. Liu, and R. J. Hemley, Phys. Rev. Lett. **108**, 146402 (2012).
[27]A. F. Goncharov, E. Gregoryanz, H. K. Mao, Z. X. Liu, and R. J. Hemley, Phys. Rev. Lett. **85**, 1262 (2000).
[28]R. F. Bader, *Atoms in Molecules-A Quantum Theory* (Oxford University Press, Oxford, 1990).
[29]M. Marqués, M. I. McMahon, E. Gregoryanz, M. Hanfland, C. L. Guillaume, C. J. Pickard, G. J. Ackland, and R. J. Nelmes, Phys. Rev. Lett. **106**, 095502 (2011).
[30]E. Gregoryanz, L. F. Lundegaard, M. I. McMahon, C. Guillaume, R. J. Nelmes, and M. Mezouar, Science **320**, 1054 (2008).
[31]C. L. Guillaume, E. Gregoryanz, O. Degtyareva, M. I. McMahon, M. Hanfland, S. Evans, M. Guthrie, S. V. Sinogeikin, and H.-K. Mao, Nat. Phys. **7**, 201 (2011).
[32]F. A. Gorelli, S. F. Elatresh, C. L. Guillaume, M. Marqués, G. J. Ackland, M. Santoro, S. A. Bonev, and E. Gregoryanz, Phys. Rev. Lett. **108**, 055501 (2012).
[33]V. Labet, R. Hoffmann, and N. W. Ashcroft, J. Chem. Phys. **136**, 074502 (2012).

Proton tunneling in phase IV of hydrogen and deuterium

Ross T. Howie, Thomas Scheler, Christophe L. Guillaume, and Eugene Gregoryanz*
Centre for Science at Extreme Conditions and School of Physics and Astronomy, University of Edinburgh, Edinburgh EH9 3JZ, United Kingdom
(Received 6 August 2012; published 10 December 2012)

Using *in situ* optical spectroscopy we have investigated the temperature stability of the mixed atomic and molecular phases IV of dense deuterium and hydrogen. Through a series of low-temperature experiments at high pressures, we observe phase III-to-IV transformation, imposing constraints on the *P*-*T* phase diagrams. The spectral features of the phase IV-III transition and differences in appearances of the isotopes Raman spectra strongly indicate the presence of proton tunneling in phase IV. No differences between isotopes were observed in absorption spectroscopic studies, resulting in identical values for the band gap. The extrapolation of the combined band gap yields 375 GPa as the minimum transition pressure to the metallic state of hydrogen (deuterium). The minute changes in optical spectra above 275 GPa *might* suggest the presence of a new solid modification of hydrogen (deuterium), closely related structurally to phase IV.

DOI: 10.1103/PhysRevB.86.214104 PACS number(s): 62.50.−p, 61.50.Ks, 78.40.Ri

The recent experimental discovery of phase IV of hydrogen and deuterium is exemplary of how studies of hydrogen at multimegabar pressures is constitutive to the understanding of the pressure-induced complexity in simple systems at extreme compressions.[1] Raman studies have shown that, at 300 K, hydrogen transforms to a new phase (phase IV) at pressures above 220 GPa. Quite unique and unusual features of the Raman spectra, e.g., the appearance of the second fundamental vibrational mode, were interpreted as phase IV, consisting of graphene-like six-member rings made up of elongated H_2 dimers, which experience large pairing fluctuations, and unbound H_2 molecules. This unusual structure, having *Pbcn* symmetry and 48 atoms per unit cell, was earlier proposed by density functional theory (DFT) as a possible candidate for phase III at 0 K.[2] The newly found experimental ability to compress hydrogen at room temperature above 180 GPa in the diamond anvil cell has resulted in major revision of the hydrogen phase diagram.[1] However, the new findings did not answer many questions and both experimental[3] and theoretical[4,5] studies produced somewhat contradictory results, posing many more uncertainties about the possible states of dense hydrogen. For example, in one experimental study at 300 K, H_2 phase IV was probably observed (which is not supported by the data presented on deuterium) however the authors did not suggest a mixed atomic-molecular state, instead claiming pressure-induced molecular dissociation and metallization above 260 GPa.[3] On the other hand, theoretical studies[4,5] predict the transformation of phases III and IV into molecular phase V at pressures above 250 GPa, which is at variance with many experimental observations.[1,6–8]

Our previous study focused on the behavior of hydrogen and deuterium at 300 K and[1] reported some preliminary results on H_2 phase IV at low temperatures. Compared to the three other molecular phases (I, II and III),[9] little is known about the low-temperature stability field of H_2 phase IV[1] and nothing is known about the stability field of deuterium phase IV. As hydrogen and deuterium have the highest relative isotopic mass difference among elements, the effects of zero point energy (ZPE) might play an important role. Based on the fact that phase IV exists at relatively "high" temperatures and the transition line separating it from phase III has a negative slope with respect to the pressure axis, we surmised[1] that the transition to the mixed state (phase IV) is entropy driven. This suggestion is supported by the significant differences in the Raman spectra of phase III vs phase IV, which is indicative of very dissimilar structures of these phases. Since the structure of phase III is not known and the proposed structural model for phase IV needs confirmation, it is impossible to make a quantitative comparison of entropies and ZPEs of both phases. Therefore, experiments aimed at determining the stability fields of hydrogen (deuterium) are highly desirable and of fundamental interest, because they are expected to provide a clear picture of the hydrogen (deuterium) phase diagram and therefore reveal new aspects relevant to the theoretical modeling and interpretation.

In this study, we mapped out phases III and IV of deuterium (hydrogen) up to 300 GPa and between 200 and 300 K. We investigate the low-temperature stability of deuterium (hydrogen) phase IV, revealing the differences in the stability fields of the isotopes and similarities in the electronic structures. We show that the phase III-to-IV transformation is accompanied by a large discontinuity of the fundamental vibrational mode frequency, the largest discontinuity observed between different phases of hydrogen (deuterium). We also demonstrate that the full width at half-maximum (FWHM) of the vibrational fundamental reaches $\sim$450 cm^{-1} for H_2 and $\sim$250 cm^{-1} for D_2 in phase IV while staying below $\sim$150 cm^{-1} for both isotopes at pressures above 250 GPa in phase III. The large difference between the peak widths of the main vibrational modes of the two isotopes in phase IV indicates substantial proton tunneling in hydrogen, probably due to the higher ZPE of the lighter species.

High-purity normal D_2 (H_2) was loaded at 0.2 GPa into a long piston-cylinder diamond anvil cell and compressed at room temperature. At the desired pressure, the cell was mounted in a custom-built continuous-flow cryostat and Raman measurements were performed on cooling/warming scans between 200 and 300 K. We have used both 514-nm Ar^+ ion and 647-nm Kr^+ ion laser excitation wavelengths for optical measurements. Pressure was determined from the shift of the T_2g Raman band of the stressed diamond using

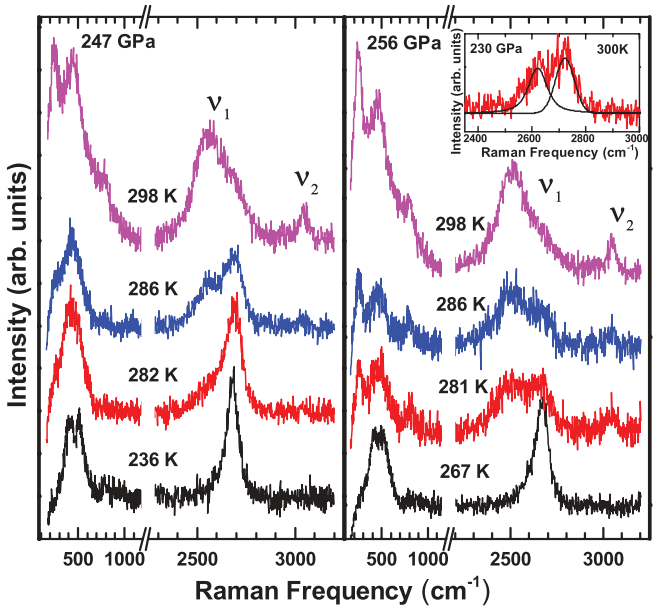

FIG. 1. (Color online) Representative Raman spectra of deuterium upon cooling (left) and warming (right) showing phase IV-III transformations at 247 and 256 GPa. Inset: Coexistence of the ν_1 modes at 300 K and 230 GPa in phases III (higher frequency mode) and IV (lower frequency mode)

the relation proposed in Ref. 10. For a full description of the experimental procedures see Refs. 1 and 11–14.

Selected Raman spectra of deuterium at 247 and 256 GPa and at various temperatures are shown in Fig. 1. At room temperature (phase IV) both ν_1 and ν_2 vibrational modes are clearly visible, having very different widths. Upon cooling at 247 GPa the ν_1 mode of D_2 shows splitting, with a higher frequency band emerging from phase III and the lower band from the remaining phase IV (Fig. 1). Upon cooling the intensities of all Raman modes associated with phase IV decrease, while new peaks appear and grow (Fig. 1). By 285 K, the transition to phase III is complete, the ν_2 mode disappears, and the ν_1 hardens significantly. To our knowledge, there are no published Raman spectra of low-frequency modes in phase III of deuterium to compare our data with. However, the overall spectrum appearances[1,15] and $\sqrt{2}$ scaling of the corresponding modes frequencies between hydrogen and deuterium[1,16] unequivocally demonstrate that the phase at low temperatures is phase III. The temperature scans at higher pressures (e.g., the 256 GPa run in Fig. 1) show identical changes in the Raman spectra, although at different transition temperatures. We find that the III ↔ IV transformation in both isotopes is very well defined, happens within a 10 K range, and is reversible without any hysteresis in either pressure or temperature, which is expected from light materials with high ZPEs. The spectral positions of the fundamental vibrational modes of both isotopes shift considerably during the phase transition and the value of the shift increases with increasing pressure and decreasing temperature [Fig. 2(a)]. For example, when phase IV is reached for deuterium at 300 K and 230 GPa the discontinuity between the vibron modes in two phases is around 60 cm^{-1} (see inset in Fig. 1) but as the pressure is increased above 230 GPa and the temperature lowered, the vibron mode frequencies undergo more pronounced hardening upon entering phase III from phase IV, reaching discontinuity values of above 200 cm^{-1} [Fig. 2(a); see also below and Fig. 3].

The most interesting observation is the discontinuity of the FWHM of the ν_1 mode at the III ↔ IV transition, which reflects fundamental changes during the phase transformation

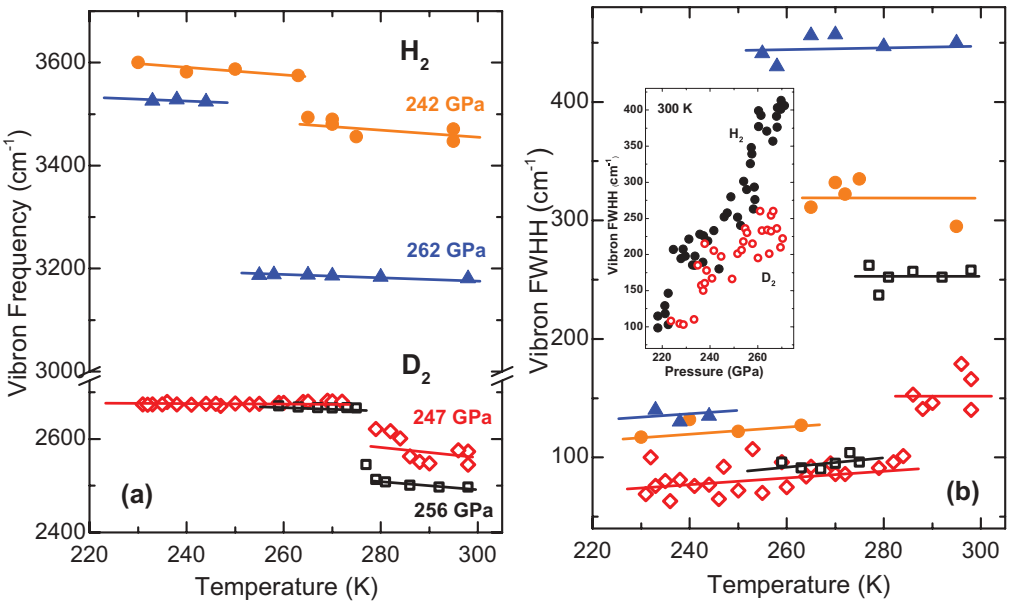

FIG. 2. (Color online) (a) Frequency discontinuities of the ν_1 modes of H_2 (filled triangles, 262 GPa; filled circles, 242 GPa) and D_2 (open squares, 256 GPa; open diamonds, 247 GPa) across the III-to-IV transformations. (b) FWHM of the ν_1 vibrons of H_2 (filled triangles, 262 GPa; filled circles, 242 GPa) and D_2 (open squares, 256 GPa; open diamonds, 247 GPa) plotted versus temperature. Note the quite similar values of FWHM for both isotopes in phase III. Lines in (a) and (b) are guides for the eye only. Inset: FWHM of the H_2 (filled circles) and D_2 (open circles) ν_1 vibron versus pressure at 300 K.

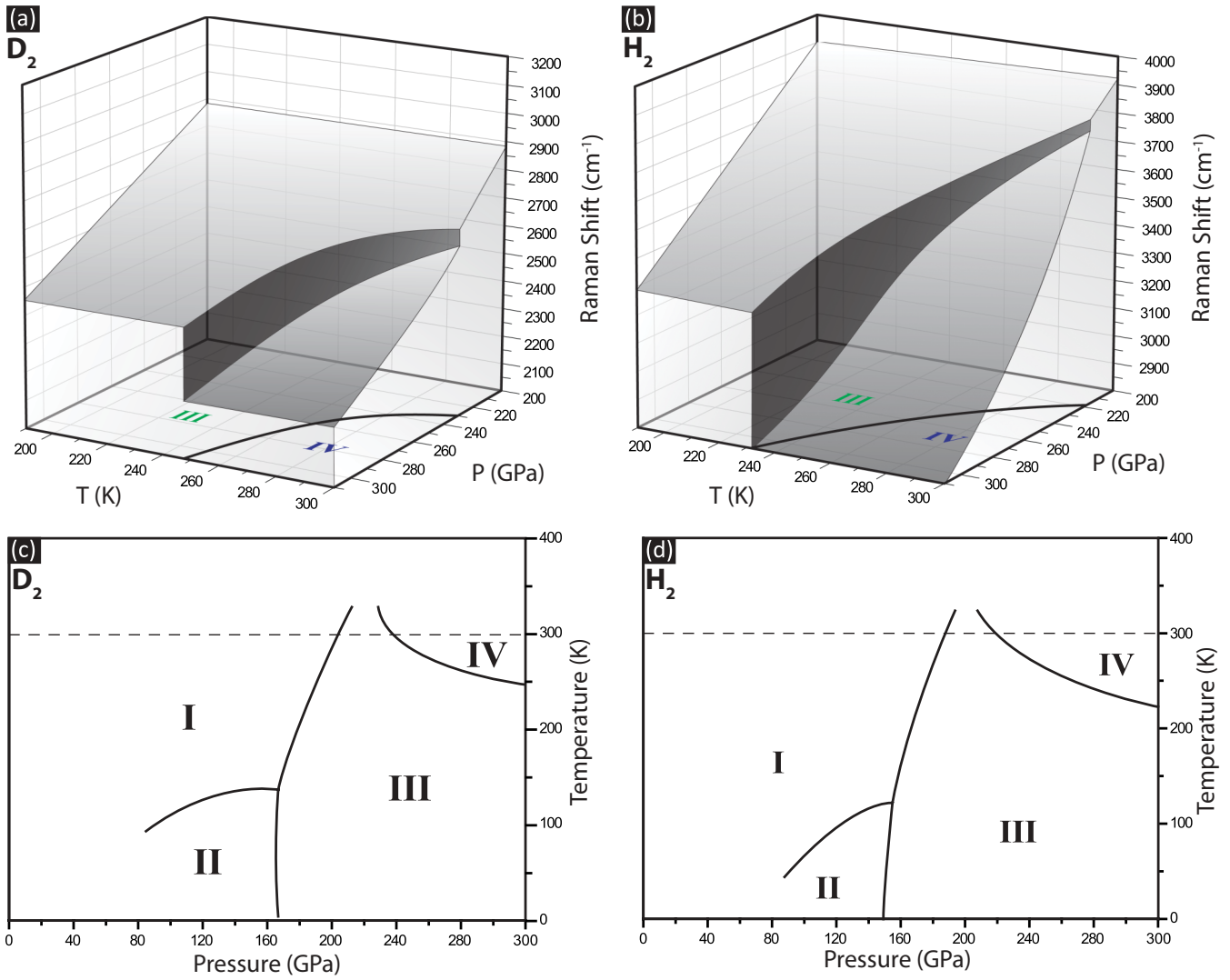

FIG. 3. (Color online) Generalized P-T- ν_1 diagrams for (a) D_2 and (b) H_2 showing the difference in the vibron frequency landscapes. P-T phase diagrams for (c) D_2 and (d) H_2. The lines separating the phases I, II and III at temperatures below 200 K are from Ref. 9.

and demonstrates the quite unusual character of phase IV. Figure 2(b) shows the FWHM of the ν_1 vibron of D_2 (H_2) versus temperature at different pressures. In phase III, the FWHM of ν_1 is marginally larger for hydrogen—between 290 and 250 GPa the width of ν_1 varies from 150 to 100 cm^{-1}—while for D_2 it is from 100 to 75 cm^{-1} [Fig. 2(b)]. However, in the same pressure range (290 to 250 GPa), the picture changes quite drastically upon warming by 10 K and entrance into phase IV: at 290 GPa ν_1 for H_2 broadens to ~450 cm^{-1} (350 cm^{-1} at 250 GPa), while ν_1 for D_2 reaches ~250 cm^{-1} at 290 GPa (150 cm^{-1} at 250 GPa). The most plausible explanation for the increased FWHM of ν_1 in phase IV is the intermolecular proton exchange and reduced lifetime of molecules. The expanded intramolecular bond length and association of these elongated molecules in six-member rings[1,2] would facilitate such intermolecular proton tunneling in one phase (IV) compared to another (III) under nearly identical P-T conditions; particularly, this effect will be enhanced in lighter hydrogen as reflected by its much larger FWHM. It is important to note that some other factors such as larger anharmonicity or enhanced electron-photon coupling could also be responsible for the observed mode broadening. The ultimate explanation of the described effects should come from theoretical studies. In fact, a very recent *ab initio* variable-cell molecular dynamics simulations[17] study observed "intralayer proton transfer" increasing with pressure and temperature in phase IV, in broad agreement with the present work.

The effect of the increased FWHM of the vibrational mode is already present in phase III,[1,7,18] but phase III has only one type of molecule with characteristic lifetime and bond length, with the FWHM being from 75 to 150 cm^{-1} for both isotopes in a wide P-T range [Fig. 2(b)]. In phase IV, the $Pbcn$ structure was shown to be dynamically unstable,[4] but several $Pbcn$-like structural models with P_c-48 (which still has imaginary phonons),[4] P_c-96,[4] and C_c[5] (both dynamically stable) symmetries having six-member rings were proposed. X-ray diffraction studies are needed to unambiguously determine the structure of phase IV but such experiments are exceedingly difficult at the moment. Our observations of the

FWHM behavior across the III-IV transformation illustrate the importance of temperature effects and that phase IV is a thermally driven partially disordered phase, thus adding additional weight to the proposed mixed atomic and molecular state of dense hydrogen (deuterium).[1,2]

By combining the *P-T* scans of the ν_1 mode frequencies we constructed three-dimensional *P-T-*ν diagrams of both species [Figs. 3(a) and 3(b)]. The overall appearance of the phase diagrams is markedly similar but there are several subtle differences. The III-to-IV transition pressures are shifted to slightly higher values for D_2. As a result, the III-IV phase line of D_2 lies above the one for H_2 [Figs. 3(c) and 3(d)]. Our measurements for H_2 yield a III-IV line gradient of -1.6 K/;GPa, while the slope is twice as shallow for D_2 as shown in Fig. 3. Another difference between the isotopes during the III-IV transformation is the very different values of the vibron frequency discontinuities. With increasing pressure the discontinuity upon the III $\leftrightarrow$ IV transition increases (see Figs. 2 and 3), reaching much larger values for hydrogen, e.g., $\sim$500 cm^{-1} for H_2 at 315 GPa and 250 cm^{-1} for D_2 at 300 GPa. These are the largest discontinuities observed between the different phases; for comparison the largest value of the frequency softening of the ν_1 mode upon entering phase III from phase II is only around 100 cm^{-1} for *both* H_2 and D_2.[19,20]

ZPE and thermal effects must play a crucial role in the formation of phase IV under the *P-T* conditions described here. The competition between ZPE and entropy would shape the appearance of the phase diagrams [Figs. 3(c) and 3(d)] and create differences in the slopes. Recent DFT studies proposed more energetically stable then *Pbcn* candidate structures for the phase IV with P_c[4] or C_c[5] symmetries. These calculations suggest that hydrogen would transform to phase IV above 220 GPa and $\sim$300 K and that this phase would be separated from the phase III by phase line having negative (with respect to pressure axis) slope, in good agreement with our current and previous results.[1] The calculated Raman spectral positions and intensities of the *Pc* structure[4] are in much better agreement with our experimental observations than *Pbcn*, although they are still not a perfect fit (Fig. 4). The DFT calculations also proposed a $C2/c$ structure as a possible candidate for phase III

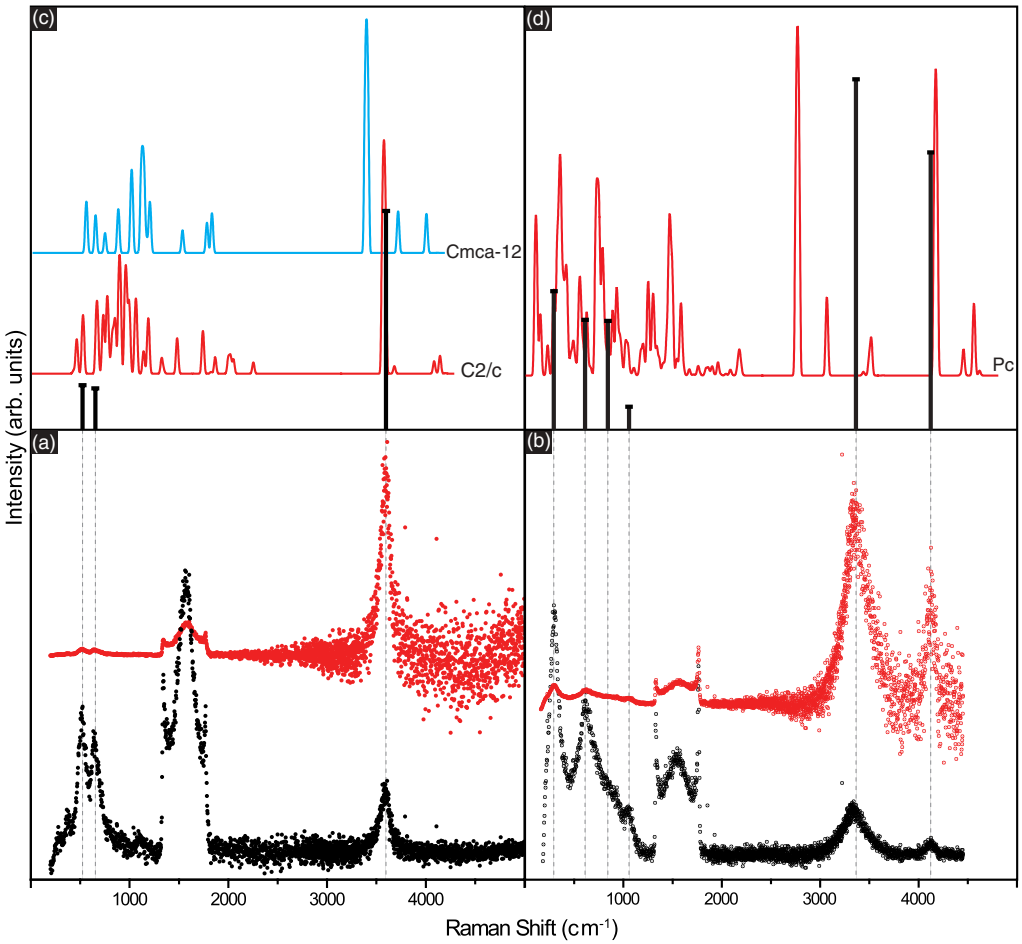

FIG. 4. (Color online) Comparison of experimentally observed and theoretically calculated[2] Raman intensities and spectral positions of the hydrogen bands at 250 GPa. (a, b) Experimental raw spectra observed in phases III (a) and IV (b) are shown below (in black); spectra corrected for decreasing sensitivity of the detector are shown above (in red). The broad peaks between 1333 and $\sim$1800 cm^{-1} are due to the first-order Raman from diamond. (c, d) Experimental renormalized spectra plotted as Gaussian distributions for phases III (c) and IV (d) [vertical (black) lines]; theoretically calculated spectra for (c) $C2/c$ (red) and *Cmca*-12 (blue) and (d) P_c (red). Note that the intensities for renormalized and theoretically calculated spectra are given on a logarithmic scale to show much weaker low-frequency modes and additional vibrational bands besides ν_1 and ν_2.

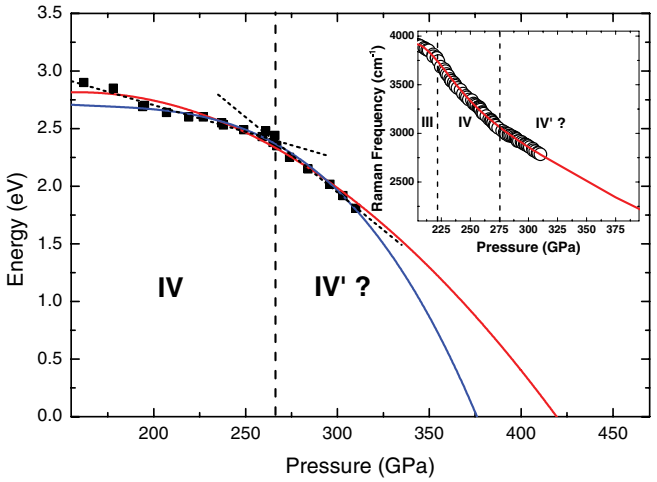

FIG. 5. (Color online) Hydrogen and deuterium combined band-gap points (filled squares) as a function of the pressure at 300 K. Dotted (black) straight lines are linear fits to the measured data points in phases IV and IV′. Quadratic [upper (red) curve] and cubic [lower (blue) curve] polynomial fits extrapolated to higher pressures are shown as solid lines. Inset: Frequency of the ν_1 mode of hydrogen as a function of pressure. Open circles are measured ν_1 vibron frequencies versus pressure. The solid (red) line shows the nearly linear (from 275 to 400 GPa) extrapolation of the ν_1 frequency up to above 375 GPa—the minimal pressure needed to close the optical band gap. Dashed vertical lines indicate the proposed phase transition between phase IV and phase IV′.

(a comparison between observed and calculated Raman spectra in phase III is shown in Fig. 4) and, more importantly, the re-entrance back into a molecular phase V (*Cmca*-12 above 280[4] or *Cmca*-4 above 250 GPa[5]) which appears to have metallic properties in both studies. These predictions of a new metallic phase seem to be in agreement with the recent claims of metallization of $H_2(D_2)$ at above 260 GPa.[3] However, our optical spectroscopy results above 260 GPa are in strong disagreement with Ref. 3, where the *total* disappearance of the Raman signal, increased reflectivity, and a closed band gap were reported. We observed an *increase* in Raman signal intensities with pressure (in our studies higher pressures than in Ref. 3 were reached for both isotopes, as evidenced by the lower vibron frequencies) and an optical band gap of ∼2 eV persisting above 300 GPa. This metallization claim contradicts several experiments conducted at identical compressions[6,7] including a quite recent infrared study of phase III of H_2 at low temperatures and up to 360 GPa.[8] The theoretically proposed molecular metallic phases (*Cmca*-12 and *Cmca*-4) are Raman active (see Fig. 4), which would also be at variance with the claimed disappearance of Raman modes in Ref. 3. Therefore we attribute the experimental findings in Ref. 3 to the changes in the sample chamber geometry and partial sample loss rather than to the claimed "metallic liquid atomic state."

However, the slight changes in optical properties at 275 GPa, such as the appearance of the fourth low-energy mode (see Fig. 2 in Ref. 1), the change in slopes of the ν_1 frequency, and the value of the D_2/H_2 band gaps with pressure (Fig. 5), *might* indicate the presence of a new solid structure (phase IV') of dense H_2 (D_2). The very similar Raman spectra suggest that if phase IV′ exists, it is structurally very closely related to phase IV. Phase IV′ appears to be semiconducting in our measurements but one can estimate the pressures needed to close the band gap and reach the metallic state. We have combined D_2 and H_2 band-gap points and used different polynomials to fit and extrapolate our data (Fig. 5). The pressures at which the band gap is fully closed vary widely depending on the power of the polynomial but the lowest value is approximately 375 GPa (Fig. 5). It is instructive to estimate the frequency of the Raman ν_1 mode at this pressure. Indeed, the frequency and increasing intensity of the ν_1 mode are very sensitive to compression (inset in Fig. 5). Therefore the frequency should be considered as an absolute pressure gauge in the experiments with H_2 (D_2) and could be used for direct result comparison in both experimental and theoretical studies. The extrapolation of hydrogen frequency versus pressure is almost linear (Fig. 5) and yields 2350 ± 50 cm^{-1} at 375 GPa. We note that this value is about 55% of the vibron frequency under ambient conditions and is much lower than any frequencies ever reported in experiments.

In summary, we have mapped out the transformation between phase III and phase IV of H_2 (D_2), demonstrating increased proton tunneling in phase IV. We estimate that the H_2 (D_2) will metallize above 375 GPa, a pressure which is in good agreement with several previous experimental measurements.[6,7]

The authors are grateful to Chris Pickard, Graeme Ackland, and Stanimir Bonev for very useful discussions and Yanming Ma for providing unpublished data. This work was supported by research grants from the U.K. Engineering and Physical Sciences Research Council and the Institute of Shock Physics, Imperial College.

*e.gregoryanz@ed.ac.uk

[1] R. T. Howie, C. L. Guillaume, T. Scheler, A. F. Goncharov, and E. Gregoryanz, Phys. Rev. Lett. **108**, 125501 (2012).
[2] C. Pickard and R. Needs, Nat. Phys. **3**, 473 (2007).
[3] M. Eremets and I. Troyan, Nat. Mater. **10**, 927 (2011).
[4] C. J. Pickard, M. Martinez-Canales, and R. J. Needs, Phys. Rev. B **85**, 214114 (2012); **86**, 059902(E) (2012).
[5] H. Liu, H. Wang, Y. Ma *et al.*, J. Chem. Phys. **137**, 074501 (2012).
[6] P. Loubeyre, F. Occelli, and R. LeToullec, Nature **416**, 613 (2002).
[7] Y. Akahama, H. Kawamura, N. Hirao, Y. Ohishi, and K. Takemura, J. Phys.: Conf. Ser. **215**, 012056 (2010).
[8] C. S. Zha, Z. Liu, and R. J. Hemley, Phys. Rev. Lett. **108**, 146402 (2012).
[9] A. Goncharov, R. Hemley, and H. K. Mao, J. Chem. Phys. **134**, 174501 (2011).
[10] Y. Akahamaa and H. Kawamura, J. Appl. Phys. **100**, 043516 (2006).
[11] J. E. Proctor, E. Gregoryanz, K. S. Novoselov, M. Lotya, J. N. Coleman, and M. P. Halsall, Phys. Rev. B **80**, 073408 (2009).

[12]M. Marquès, M. Santoro, C. L. Guillaume, F. A. Gorelli, J. Contreras-Garcia, R. T. Howie, A. F. Goncharov, and E. Gregoryanz, Phys. Rev. B **83**, 184106 (2011).
[13]C. L. Guillaume *et al.*, Nat. Phys. **7**, 207 (2011).
[14]F. A. Gorelli, S. F. Elatresh, C. L. Guillaume, M. Marques, G. J. Ackland, M. Santoro, S. A. Bonev, and E. Gregoryanz, Phys. Rev. Lett. **108**, 055501 (2012).
[15]A. Goncharov, E. Gregoryanz, R. Hemley, and H. Mao, Proc. Natl. Acad. Sci. USA **98**, 14234 (2001).
[16]I. Silvera, Rev. Mod. Phys. **52**, 393 (1980).
[17]H. Liu and Y. Ma, arXiv:1210.0280.
[18]A. Goncharov and J. Crowhurst, Phase Trans. **80**, 1051 (2007).
[19]R. J. Hemley and H. K. Mao, Phys. Rev. Lett. **61**, 857 (1988).
[20]A. F. Goncharov, I. I. Mazin, J. H. Eggert, R. J. Hemley, and H. K. Mao, Phys. Rev. Lett. **75**, 2514 (1995).

High-pressure synthesis of lithium hydride

Ross T. Howie,[1] Olga Narygina,[1] Christophe L. Guillaume,[1] Shaun Evans,[2] and Eugene Gregoryanz[1]
[1]*School of Physics and Astronomy and Centre for Science at Extreme Conditions, University of Edinburgh, Edinburgh EH9 3JZ, United Kingdom*
[2]*European Synchrotron Radiation Facility, BP 220, Grenoble, France*
(Received 1 January 2012; published 16 August 2012)

By compressing elemental lithium and hydrogen in a diamond anvil cell, we have synthesized lithium hydride (LiH) at pressures as low as 50 MPa at room temperature. Combined Raman spectroscopy and synchrotron x-ray diffraction measurements reveal that, once synthesized, LiH remains stable at 300 K up to 160 GPa in the presence of molecular hydrogen. The mixture of lithium hydride and molecular hydrogen and application of pressure alone *cannot* form a higher H_2 content hydride (LiH_x, $x > 1$) as was suggested from the theoretical *ab initio* calculations and therefore, cannot be considered as a route to low-pressure hydrogen rich material metallization.

DOI: 10.1103/PhysRevB.86.064108 PACS number(s): 62.50.−p

Lithium hydride, LiH, is the most elementary ionic compound in terms of electronic structure, having only four electrons per unit cell, and has the highest hydrogen content, in mass percentage, of any saline hydride. Its volumetric and gravimetric hydrogen contents are also very competitive among other hydrides, electing LiH a prospective candidate for hydrogen storage.[1] Hydrogen is a propitious alternative energy source that could be the primary facilitator in the transition from fossil fuels to clean sources of energy. There is, however, a challenge to produce a material capable of both reacting with hydrogen to form a stable state and release a significant quantity on demand, at minimum energy expense. LiH is an industrially versatile compound with applications in hydrogen generators, in the manufacturing of ceramics, and in both the shielding and cooling of nuclear reactors. Because of its high reactivity, LiH is an excellent desiccant and chemical reducing agent, as well as the precursor for the synthesis of binary intermetallic hydrides such as lithium aluminium hydride, another potential candidate for hydrogen storage.[2]

There are various industrial methods in producing pure LiH, all of which involve the hydrogenation of the constituent materials, often in the presence of a catalyst, at elevated temperatures.[3,4] At ambient pressure, hydrogen is absorbed into molten lithium at temperatures ranging between 700 and 1000 K; the melting point of lithium at ambient pressure is 453.7 K while LiH itself melts at 961 K.[5] The synthesis temperatures of NaH and KH also occur above the melting temperature of pure Na and K, motivating investigations into alternative, energy economical, synthesis routes. Surprisingly no synthesis method has been reported involving *cold* (room temperature) synthesis of LiH from its pure constituents. Pressure can have a profound effect on chemical reactivity, inducing changes in atomic and electronic structure. Two different elements that do not react at ambient conditions can form novel compounds if statically compressed, even without additional heating. Pressure alone was sufficient enough to form novel compounds such as PtH, silicon dihydride or rhenium hydride,[6–9] showing that the kinetics of the solid-state reactions could be greatly influenced by the application of high densities. LiH does not decompose into pure elements until heated to above its melting point (>1000 K) at atmospheric pressure, however it easily reacts with water to the corresponding hydroxide liberating hydrogen from water.[10] The decomposition of LiH at high pressures and temperatures has yet to be investigated, which would have direct consequences for the viability of LiH as a hydrogen storage material.

LiH, which crystallizes in the rock-salt structure, is the only known stable point in the Li/H_2 mixture phase diagram, other than the elements at ambient conditions. Recently, there has been much interest in the chemical compression of hydrogen from a fundamental solid state physics perspective. Through theoretical calculations, it has been shown that *a little bit of lithium* could have the profound effect of lowering the metallization pressure of hydrogen through the formation of a higher hydrogen content hydride.[11] Metallic LiH_2, LiH_6, and LiH_8 were predicted to become more stable than the $LiH + H_2$ mixture at pressures above 100 GPa,[11] well within experimental capabilities. Further yet, another theoretical study using *ab initio* random structure searching[12] reported that at a lower pressure of 100 GPa, the lithium-hydrogen compound with much higher hydrogen content (LiH_{16}) is stable against decomposition into LiH_8 and H_2.

Utilizing x-ray diffraction and Raman spectroscopy measurements, we report the synthesis of LiH from the pure constituents at pressures as low as 500 bar, to our knowledge the lowest pressure at which metallic hydride was synthesized at room temperature. In assessment of LiH as a candidate for a hydrogen storage material, we investigate possible high temperature and pressure decomposition. Furthermore we show that at 300 K and in the presence of molecular hydrogen, LiH is a stable compound up to 160 GPa, which *does not* form any of the predicted higher hydrogen content hydrides.

We have conducted two types of experiments: synthesis of LiH from its constituencies and studies of LiH in H_2 up to 160 GPa. To synthesize LiH we have loaded Li (99.9% purity) together with precompressed hydrogen in the Re gasket of a diamond anvil cell with 600 and 300 μm flat and 80 μm diameter bevelled diamonds. Due to the high reactivity of lithium in the presence of oxygen and moisture, all loadings were performed in a glove box under an atmosphere of dry argon. The cell was then gas loaded with hydrogen (99.9% purity) at pressures varying from 50 MPa to 0.2 GPa. We conducted experiments with various Li to H_2 volume ratios ranging from 1:10 to 1:1. We also conducted several

experiments loading industrially produced LiH (99.4% purity) by itself together with H_2. Pressure was determined from ruby luminescence, the equation of state of LiH, Li, or from the frequency dependence of the ν_1 vibron mode of hydrogen. Powder x-ray diffraction data for all experiments were collected at beamline ID09 at the ESRF, Grenoble. A focused monochromatic beam was used, with a wavelength between 0.4117 and 0.4130 Å, and the data were recorded on a MAR image plate. Raman spectra were recorded using a custom-constructed Raman microprobe system described in Ref. 13 with both 514.5 and 647.1 nm excitations at room and low temperature.

The pressure in the first cell with Li + H_2 after loading was measured to be 0.32 GPa. X-ray diffraction pattern collected at this pressure contained signatures from the *fcc* phase of LiH [Fig. 1(a)]. Lattice parameter of the LiH *fcc* structure is in agreement with the known values from high-pressure

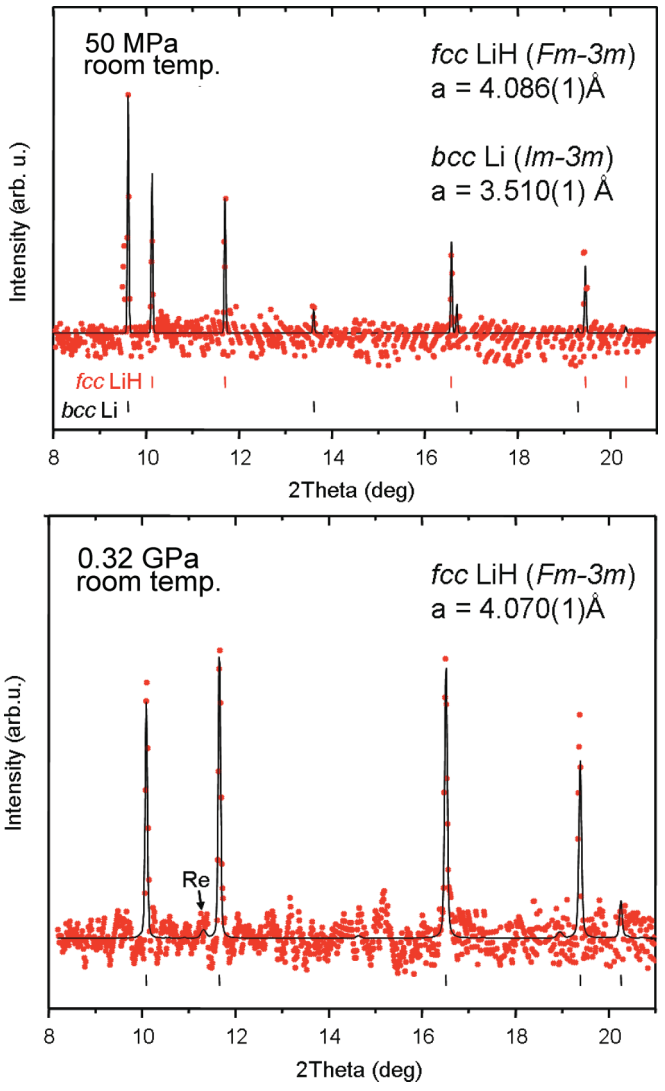

FIG. 1. (Color online) Representative XRD profile collected from Li + H_2 phase assembly at 0.05 GPa (top) and 0.32 GPa (bottom) at room temperature (crosses) and its LeBail fit (solid line); the background baseline has been subtracted. Positions of diffraction peaks of *bcc*-Li and *fcc*-LiH are shown by tick marks below; XRD reflections from rhenium gasket are also marked.

study of LiH.[14] In some of our experimental runs we observed the persistence of a signal from pure Li in our x-ray data which we attributed to the large volume ratio of Li to H_2 (1:2) together with the reaction rate. With such a volume ratio, the lithium is often "bridged" between the two diamonds resulting in only a small surface area exposed to the hydrogen. Once lithium hydride is formed on the surface, the rate of absorption is reduced, resulting in a slower rate of reaction (several days to completely transform). Since all known synthesis methods include high temperatures and catalysts we decided to investigate the minimal pressure required to synthesize LiH at room temperature. We loaded pure lithium at a hydrogen pressure of 50 MPa with a Li to H_2 volume ratio of 1:10. No bridging of the sample was observed resulting in the entire surface area of Li exposed to H_2. Immediately after loading x-ray diffraction confirmed the synthesis of lithium hydride [Fig. 1(b)]. Within a reaction period of 48 hours the entire sample became transparent, an indication that the bulk sample transformed to LiH. To our knowledge, this is the lowest pressure synthesis of any metal hydride at pressures above ambient at 300 K, when the whole sample completely transformed. The pressures 50 MPa could be easily generated in large volumes, and therefore our finding could provide the pathway for synthesis of this industrially important material in large quantities without application of temperature.

LiH exhibits no first-order Raman activity due to the crystal having inverse symmetry about host-lattice ion. However, unusually strong second-order spectra are observed in the region of 500–1500 cm^{-1}, involving combinations of phonons throughout the Brillouin zone.[15,16] In all our loadings, both the second-order LiH Raman band and hydrogen fundamental molecular modes were observed, confirming the presence of both LiH and the fluid H_2 [Figs. 2(a) and 2(b)]. The intensities of the Raman spectra arising from the hydrogen intramolecular

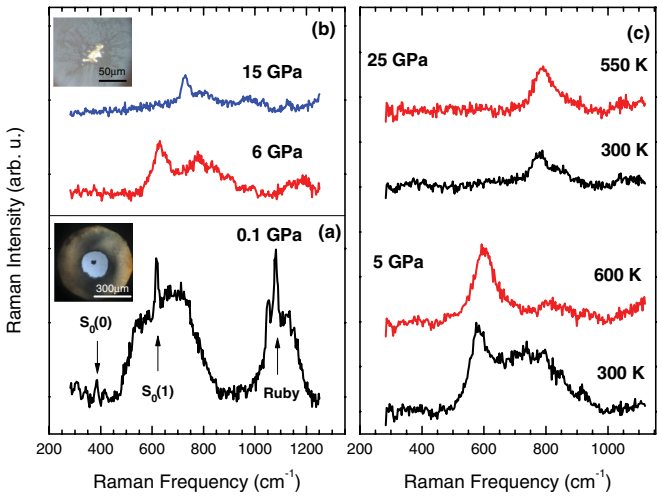

FIG. 2. (Color online) (a) Representative second-order Raman spectra of synthesised LiH + H_2. Arrows indicate peaks corresponding to rotational modes from pure hydrogen and ruby fluorescence used as a pressure gauge. Inset: photomicrograph of sample at 0.05 GPa. (b) Raman spectra of recovered synthesized LiH at various pressures. Inset: photomicrograph of recovered transparent LiH sample from (a). (c) High temperature Raman measurements of the recovered synthesized LiH.

rotations (rotons) are far greater than the second-order Raman bands from LiH. In the fluid the hydrogen rotons are sharp and highly intense, however in the solid, the rotons broaden obscuring the LiH Raman signal, restricting Raman measurements of LiH in this pressure regime. As LiH is stable to atmospheric conditions, we resolved this problem by releasing the excess hydrogen in an inert environment and recovering some of our synthesized LiH samples. Figure 2 shows Raman spectra of the recovered synthesized LiH to 25 GPa.

In an attempt to decompose the synthesized LiH, we heated our samples to temperatures of 600 and 550 K at pressures of 5 and 25 GPa respectively [Fig. 2(c)]. We did not observe through heating the appearance of the hydrogen vibrational fundamental mode ν_1, which would be a clear indication of decomposition. It appears that LiH is a very stable compound to which the application of temperature and pressure within the scale of the industrial capabilities is not enough to promote decomposition. According to a computational study, temperatures in excess of 1600 K may be required for decomposition at 25 GPa.[17] In order for LiH to be a viable candidate for a hydrogen storage material, other reaction mechanisms to decompose LiH must be invented.

Through single crystal x-ray diffraction, the LiH rock-salt phase has been shown to be stable at ambient temperature up to 200 GPa.[14,18] However, does a hydrogen media have any affect on the stability of LiH at such high pressures? The results of the present study represent an attempt to experimentally observe the new chemistry recently predicted for hydrogen in the presence of Li. The presence of elemental lithium in a hydrogen medium has been suggested to reduce the pressure required to attain the long sought metallization of hydrogen. We have studied the synthesized LiH sample embedded in H_2 to pressures as high as 160 GPa to investigate the predicted formation of LiH_2, LiH_6, and LiH_8.[11,12] All predicted lithium polyhydride structures contain hydrogen molecules which, as with any structural change, will be observable in x-ray diffraction. However, such light elements as lithium and hydrogen both have very weak x-ray scattering cross sections making x-ray diffraction on $LiH + H_2$ mixtures very challenging to study at high pressures in the diamond anvil cell. A very useful, subtle characteristic of all predicted structures is that they all contain stretched hydrogen molecules. The vibrational intramolecular Raman-active mode ν_1 is extremely sensitive to any structural changes. It is predicted that LiH_6 will have Raman active optical phonons with the highest mode at frequencies of 2920 cm^{-1} at 100 GPa, which would be a significant deviation from the pure hydrogen vibrational mode (4170 cm^{-1}). As LiH_6 is predicted to be metallic, it is expected that the sample would become optically opaque in transmitted light as a result of band-gap closure.

Our x-ray diffraction study up to 65 GPa shows that the mixture of synthesized (or industrially produced) LiH and H_2 do not react and behave according to their known equation of states.[14,18,19] Figure 3 shows the evolution of observed d spacings for Li, LiH, and H_2 as observed by x-ray diffraction in the present work, demonstrating a perfect agreement with the known values.[14,20,22,23] In the runs with pure Li as starting

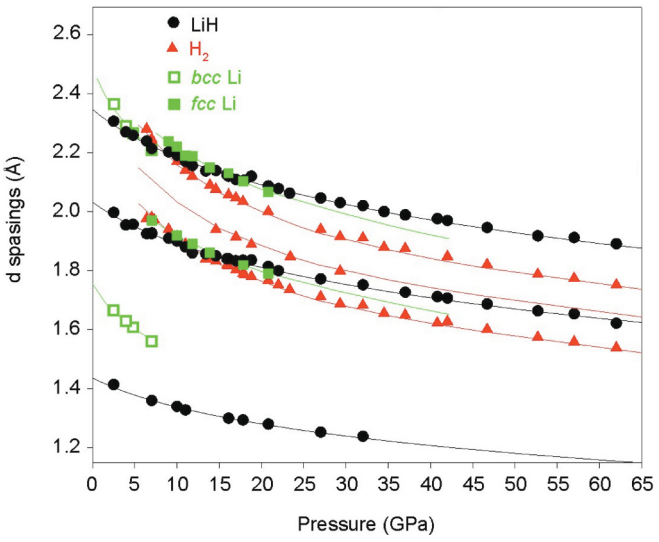

FIG. 3. (Color online) d spacings of observed phases as a function of pressure (open and solid symbols) plotted against previously reported compression data of Li (Refs. 20 and 21), LiH (Refs. 14 and 18), and H_2 (Refs. 22 and 23).

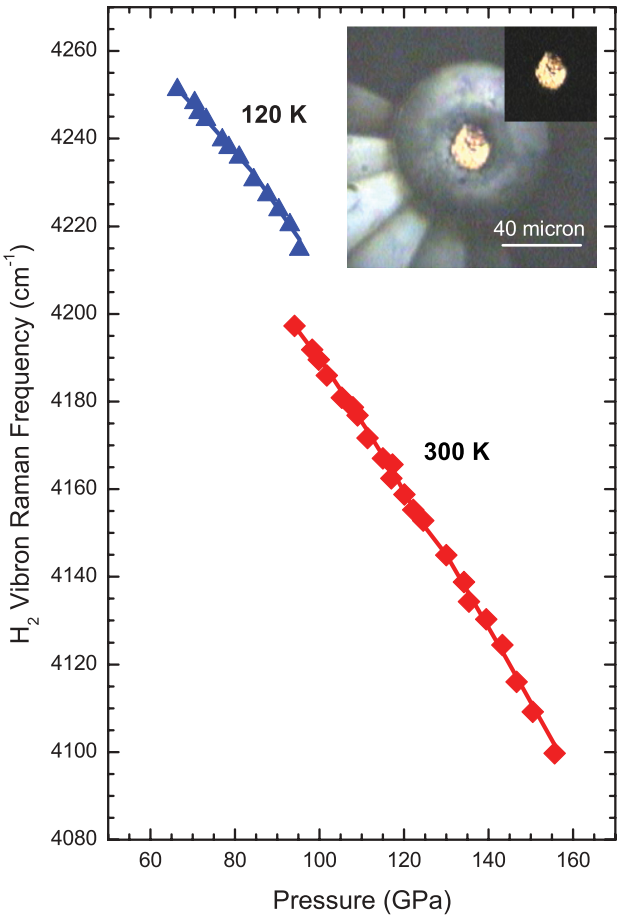

FIG. 4. (Color online) Pressure evolution of the frequency of the H_2 vibron with pressure. Symbols and lines represent measurements on the LiH part and hydrogen part of the sample, respectively. Triangles and line (blue) show measurements at 120 K while diamonds and line (red) represent measurements at room temperature. The inset shows the synthesized LiH sample in hydrogen media at a pressure of 155 GPa.

material we were able to follow Li *d* spacings up to 25–35 GPa (see Fig. 3). Above these pressures we did not observe Li either due to its melting[24] or to due complete transformation to LiH. At pressures above 65 GPa we utilized Raman spectroscopy and visual observations which would be very sensitive to any chemical changes. The initial reaction to be studied was between pure lithium and hydrogen, thus upon loading we compressed the sample from 0.2 GPa to 20 GPa in a period of seconds in an attempt to avoid complete transformation to LiH. It is well known from our previous studies[24] that prolonged lithium exposure at high pressure causes premature anvil failure to diamonds and that the application of low temperatures can, to an extent, prevent such an occurrence. As such, at pressures above 60 GPa, we cooled our samples to 120 K as a preventative measure. However, above 95 GPa, through visible observations, it was clear that all lithium had reacted to form lithium hydride and cooling was no longer required. Up to the maximum pressure reached (160 GPa), only ν_1 vibron of H_2 has been observed in our Raman spectra (see Fig. 4), and its frequency corresponded very well to the know value of pure H_2 at 120 and 300 K; no additional Raman lines or change of color were detected that would be indicative of the predicted LiH_x compound.[11] One might argue that the appearance of the predicted hydrogen rich compound in the experiment is hindered by the kinetics. The synthesis of silicon dihydride at above 120 GPa took several months to complete,[7] but it is possible that if high temperature were involved it could happen within minutes, e.g., formation of PtN_2 at high *P*-*T*.[25] There might be a kinetic barrier, which would allow LiH to persist on compression to much higher pressures than the predicted 110–120 GPa. Possible heating of the $LiH + H_2$ mixtures in the diamond anvil cell at pressures about 120 GPa could accelerate the chemical reaction. However, currently the heating of the transparent material in hydrogen media at above 100 GPa is not a trivial task. Alternatively, our recent experiments at room temperature on pure hydrogen to above 300 GPa showed the clear change of color and closing band gap which reached 1.8 eV at 310 GPa. That demonstrates the possibility of static compression of hydrogen at *hot* temperatures which perhaps is the simpler and more direct approach to achieve the long-sought metallic state of hydrogen.[26]

In conclusion, the synthesis of LiH from the elemental metals at pressures as low as 500 bar at room temperature is undoubtedly a result that will stimulate further experimental studies especially aimed at bringing this process to the large industrial scales. The reported high pressure synthesis of LiH represents an energetically efficient and clean way of producing this compound that has a high industrial demand. Contrary to theoretical predictions, no further reaction takes place between LiH and H_2 to form higher hydrogen content metallic hydrides to the maximum pressure of 160 GPa at 300 K.

This work is supported by a research grant from the UK Engineering and Physical Sciences Research Council and facilities made available by the European Synchrotron Radiation Facility.

[1] L. George and S. K. Saxena, Int. J. Hydrogen. Energ. **35**, 5454 (2010).
[2] S. Orimo, Y. Nakamori, J. R. Eliseo, A. Züttel, and C. M. Jensen, Chem. Rev. **107**, 4111 (2007).
[3] J. Synder, U.S. Patent Office 3, 387, 949 (1968); R. Lemieux, *ibid*. 4, 007, 257 (1977); B. Bogdanovic, *ibid*. 4, 396, 589 (1983); J. Y. Dumousseau, *ibid*. 4, 605, 547 (1986).
[4] S. Liao, W. Kong, H. Z. Liu, J. K. Li, and Y. Xu, Acta Chimica Sinica **3**, 201 (1985).
[5] C. Messer, E. Damon, P. Maybury, J. Mellor, and R. Seales, J. Phys. Chem. **62**, 220 (1958)
[6] O. Degtyareva, J. E. Proctor, C. L. Guillaume, E. Gregoryanz, and M. Hanfland, Solid State Commun. **149**, 1583 (2009).
[7] M. Hanfland, J. E. Proctor, C. L. Guillaume, O. Degtyareva, and E. Gregoryanz, Phys. Rev. Lett. **106**, 095503 (2011).
[8] T. Scheler, O. Degtyareva, M. Marquśs, C. L. Guillaume, J. E. Proctor, S. Evans, and E. Gregoryanz, Phys. Rev. B **83**, 214106 (2011).
[9] T. Scheler, O. Degtyareva, and E. Gregoryanz, J. Chem. Phys. **135**, 214501 (2011).
[10] A. Züttel, Naturwissenschaften **91**, 157 (2004).
[11] E. Zurek, R. Hoffmann, N. W. Ashcroft, O. R. Oganov, and A. O. Lyakhov, Natl. Acad. Sci. USA Phys. **106**, 17640 (2009).
[12] C. Pickard and R. Needs, J. Phys.: Condens. Matter. **23**, 053201 (2011).
[13] J. E. Proctor, E. Gregoryanz, K. S. Novoselov, M. Lotya, J. N. Coleman, and M. P. Halsall, Phys. Rev. B **80**, 073408 (2009); M. Marqués, M. Santoro, C. L. Guillaume, F. A. Gorelli, J. Contreras-García, R. T. Howie, A. F. Goncharov, and E. Gregoryanz, *ibid*. **83**, 184106 (2011).
[14] P. Loubeyre, R. Le Toullec, M. Hanfland, L. Ulivi, F. Datchi, and D. Hausermann, Phys. Rev. B **57**, 10403 (1998).
[15] A. C. Ho, R. C. Hanson, and A. Chizmeshya, Phys. Rev. B **55**, 14818 (1997).
[16] A. Anderson and F. Luty, Phys. Rev. B **28**, 3415 (1983).
[17] T. Ogitsu, E. Schwegler, F. Gygi, and G. Galli, Phys. Rev. Lett. **91**, 175502 (2003).
[18] P. Loubeyre and F. Occelli, ESRF Report, HS2866 (2005).
[19] A. Lazicki, P. Loubeyre, F. Occelli, R. J. Hemley, and M. Mezouar, Phys. Rev. B **85**, 054103 (2012).
[20] M. Hanfland, K. Syassen, N. E. Christensen, and D. L. Novikov, Nature (London) **408**, 174 (2000).
[21] M. Hanfland, I. Loa, K. Syassen, U. Schwarz, and K. Takemura, Solid State Commun. **112**, 123 (1999).
[22] P. Loubeyre, R. LeToullec, D. Hausermann, M. Hanfland, R. J. Hemley, H. K. Mao, and L. W. Finger, Nature (London) **383**, 702 (1996).
[23] R. J. Hemley, H. K. Mao, L. W. Finger, A. P. Jephcoat, R. M. Hazen, and C. S. Zha, Phys. Rev. B **42**, 6458 (1990).
[24] C. L. Guillaume, E. Gregoryanz, O. Degtyareva, M. I. McMahon, M. Hanfland, S. Evans, M. Guthrie, S. V. Sinogeikin, and H. K. Mao, Nat. Phys. **7**, 211 (2011).
[25] E. Gregoryanz, C. Sanloup, M. Somayazulu, J. Badro, G. Fiquet, H. K. Mao, and R. J. Hemley, Nat. Mater. **3**, 294 (2004).
[26] R. T. Howie, C. L. Guillaume, T. Scheler, A. F. Goncharov, and E. Gregoryanz, Phys. Rev. Lett. **108**, 125501 (2012).

Mixed Molecular and Atomic Phase of Dense Hydrogen

Ross T. Howie,[1] Christophe L. Guillaume,[1] Thomas Scheler,[1] Alexander F. Goncharov,[2] and Eugene Gregoryanz[1,*]

[1]*Centre for Science at Extreme Conditions and School of Physic and Astronomy, University of Edinburgh, Edinburgh, EH9 3JZ, United Kingdom*

[2]*Geophysical Laboratory, CIW, 5251 Broad Branch Road, Washington, D.C. 20015, USA*

(Received 1 November 2011; published 19 March 2012)

We used Raman and visible transmission spectroscopy to investigate dense hydrogen (deuterium) up to 315 (275) GPa at 300 K. At around 200 GPa, we observe the phase transformation, which we attribute to phase III, previously observed only at low temperatures. This is succeeded at 220 GPa by a reversible transformation to a new phase, IV, characterized by the simultaneous appearance of the second vibrational fundamental and new low-frequency phonon excitations and a dramatic softening and broadening of the first vibrational fundamental mode. The optical transmission spectra of phase IV show an overall increase of absorption and a closing band gap which reaches 1.8 eV at 315 GPa. Analysis of the Raman spectra suggests that phase IV is a mixture of graphenelike layers, consisting of elongated H_2 dimers experiencing large pairing fluctuations, and unbound H_2 molecules.

DOI: 10.1103/PhysRevLett.108.125501 PACS numbers: 62.50.−p, 61.50.Ks, 78.30.Na, 78.40.Ri

The behavior of hydrogen at very high pressures is still poorly understood due to the limitations imposed on conventional experimental techniques. Currently, three solid phases of hydrogen and deuterium (labeled I, II, and III) are known (see Fig. 1) [1,2]. Phase I has a hexagonal closed-packed structure with freely rotating molecules. Phase II (the broken symmetry phase), which possesses some degree of orientational order and may differ from the lattice symmetry of phase I, exists at temperatures below 135 K and up to ~160 GPa [3,4]. Phase III is separated from phase II by an almost vertical phase line from 0 to 125 K at ~155 (165 for D_2) GPa [5,6], and the transition between the two is characterized by a large discontinuity (~ 100 cm^{-1}) in the vibron frequency. Phases I, II, and III coexist at a triple point at 125 K and 155 GPa (135 K and 165 GPa for D_2), above which a phase line with positive slope separates phases I and III. The I-III transition exhibits a similar discontinuity in vibron frequency which rapidly decreases with increasing temperature, disappearing at 250 K [7]. At 77 K and pressures in excess of 275 GPa, a change of color [8,9] and band gap of the order of 2 eV has been reported with an estimation that the band gap would close at pressures of 420–450 GPa [8–10]. Because of the difficulties associated with the containment of hydrogen at high pressures and elevated temperatures (> 250 K), the highest pressure reached at 300 K prior to this study is approximately 180 GPa [11]. Therefore, experimental high-pressure 300 K studies of hydrogen are of fundamental interest, as they may reveal new facts relevant to the I-III and other possible phase transformations or even shed light on the behavior of the melting curve at high pressures [12–14] and predicted unusual liquid state [15]. Vibrational spectroscopy is crucial for making direct measurements on the state of bonding of the material at high pressures and temperatures. In addition to information on bonding, these spectroscopic techniques have been the sole means for identifying phase transitions in H_2 at above 150 GPa, because vibrational excitations are extremely sensitive to changes in crystal structure, including melting [5,6,12]. The combined experimental evidence, from the shock-wave study on hot dense liquid hydrogen [16] and from static studies [12,14] on solid and liquid hydrogen states, indicates that the application of "*high*"

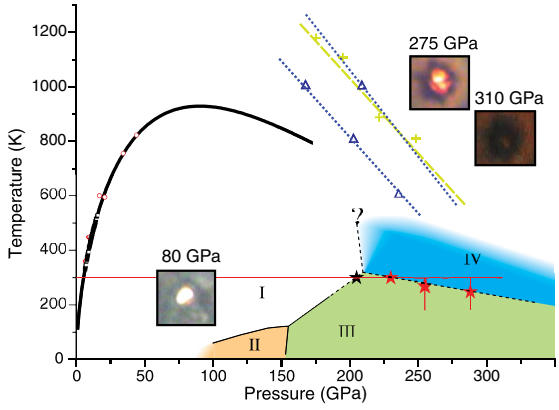

FIG. 1 (color online). Proposed phase diagram of H_2. The melting curve (thick solid line) is a Ketchin fit from Ref. [12], and the symbols along it are from Refs. [12,27]. The solid lines separating the phases I, II, and III are from Ref. [28]. The thin solid lines show the *P-T* paths taken in this study, and the stars along them show phase I to III and III to IV transformations. The dashed lines are proposed boundaries between I–III, III–IV, and I–IV phases. The calculated transition lines between molecular and atomic liquid are shown with dashed lines and crosses [24] and triangles [25]. The microphotographs show the appearance of deuterium in phase I and hydrogen in phase IV.

temperatures might facilitate the dissociation of the hydrogen molecule and therefore promote transformation to an atomic and metallic state at lower pressures. In this Letter, using high-pressure Raman and visible transmission spectroscopy, we show that at high temperatures ($T = 300$ K) and above 220 GPa hydrogen adopts an unusual structure containing 6-atom rings corresponding to a "predissociated" semimetallic state separated by a layer of free-like (unbound) molecules.

We have conducted several experiments at room and low temperatures on H_2 (and D_2) with the highest pressures reached 315 (275) GPa (see Ref. [17] for the details). With increasing pressure, the low energy (< 1000 cm^{-1}) bands of H_2 (D_2) broaden and decrease in intensity [Figs. 2(a) and 2(b)]. However, when pressures above ~190 GPa were reached, we observed the appearance of a new, relatively intense broad Raman band at 500 cm^{-1} (Fig. 2). The emergence of this band is accompanied by the drastic change of the slope of the main vibrational mode ν_1 from -5 to -12.7 cm^{-1}/GPa (Fig. 3). The full width at half maximum (FWHM) of the ν_1 mode also reflects changes at the transition; from the solidification point at 5.5 GPa, the FWHM increases linearly, reaching 100 cm^{-1} by 210 GPa. At this point, the broadening abruptly changes rate, and within an interval of 50–60 GPa (at 260–270 GPa) the FWHM reaches ~460 cm^{-1} (Fig. 3). Our observations of the low energy broad band are similar to a band at 450 cm^{-1} observed in H_2-III at 178 GPa and 18 K [6]). The change in slope of the ν_1 and the increase of FWHM are in good agreement with similar observations made in phase III at low temperatures (18 K for librons and 250 K for vibrons) [6,9]. The 190 GPa–300 K P-T point, where we observe an apparent phase transition, could fit on the phase I-III boundary of existing low temperature data if extrapolated to 300 K and above 190 GPa (Fig. 1).

As pressure is increased above 220 GPa and the ν_1 mode reaches a frequency of ~3800 cm^{-1}, the transition to a new phase (referred here as IV) starts. The transformation is evidenced by the profound changes in vibrational and low (< 1200 cm^{-1}) energy spectra. At above 220 GPa, the low-frequency broad band is superseded by three new sharp Raman modes. A new vibrational mode ($\nu_2 \sim 4150$ cm^{-1}) appears at 235 GPa (Fig. 2). At the same pressure, the ν_1 frequency reduces below the values expected for the vibron of phase III at 77 K (Fig. 3). This observation suggests that phase IV has a modified bonding character compared to phase III (see below). The ν_1 mode frequency softens very rapidly with pressure at a much higher rate than the vibron of phase III. At 315 GPa, the frequency of the ν_1 mode is 2750 cm^{-1} (35% reduction of frequency compared to ~4260 cm^{-1} at 40 GPa where the

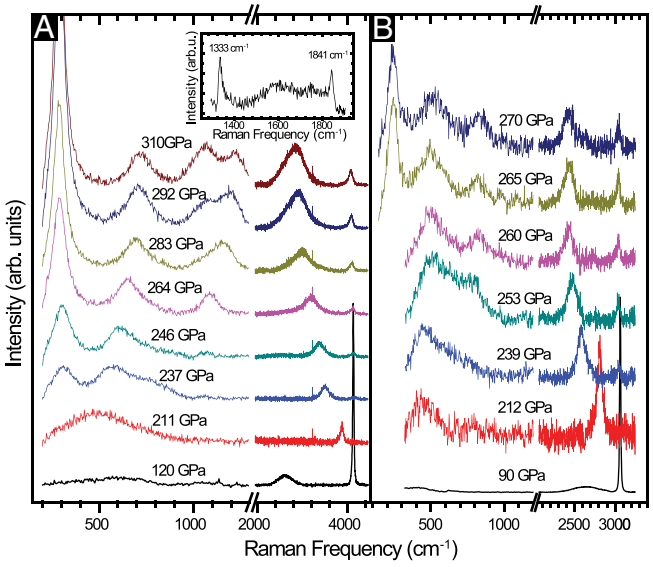

FIG. 2 (color online). Representative Raman spectra of H_2 (a) and D_2 (b) at different pressures (shifted vertically for clarity). The weak broad peaks at ~2400 cm^{-1} on spectra at 120 GPa for H_2 and 90 GPa for D_2 are due to the 2nd-order Raman from diamond. The inset in (a) shows the stressed diamond peak at 315 GPa.

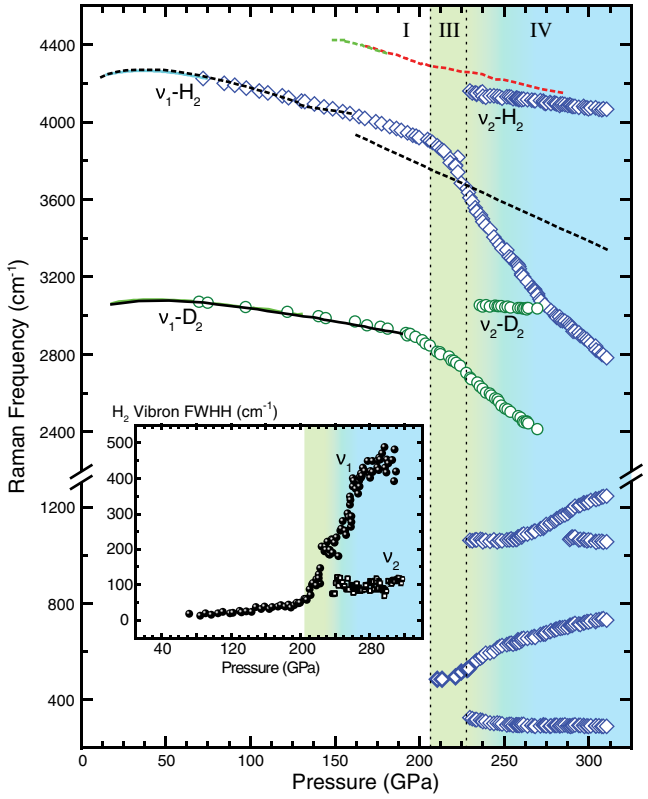

FIG. 3 (color online). H_2 and D_2 phonons frequency shifts as a function of pressure. Open squares are the ν_1, ν_2, and low energy modes of hydrogen; open circles are ν_1 and ν_2 modes of deuterium. The dashed lines are infrared and Raman measurements at low temperatures from Refs. [6,8,20]. The solid line is the ν_1 mode of deuterium at 300 K from Ref. [11]. Inset: Hydrogen ν_1 (solid circles) and ν_2 (open squares) modes FWHM as a function of pressure.

ν_1 mode goes through the maximum of its frequency), which is much lower than that in phase III at 77 K and 320 GPa ($\nu_1 \sim 3400$ cm^{-1} [8]). The FWHM of the ν_2 mode lies on the linear extrapolation of the vibron mode of phase I (Fig. 3) and is clearly driven by the normal pressure-induced broadening unlike the ν_1 mode, indicating two very different local atomic environments involved in these modes (see below). In the high-pressure regime, the frequency of the ν_1 versus pressure shows a slope change (slope changes from -12.7 to -7 cm^{-1}/GPa), and a 1050 cm^{-1} band branches off to give rise to another weakly softening band above 280 GPa (Figs. 2 and 3), which rapidly increases in intensity. The relative intensity of the lowest-frequency band at 295 cm^{-1} significantly increases, while the mode shows small softening with pressure (Fig. 2). This complex behavior suggests that the ν_1 mode couples to other modes of the same symmetry (e.g., Ref. [18]) with the gain of intensity for the 295 and 1050 cm^{-1} modes. The strong coupling between the modes also forces a small upturn of the ν_1 vibron frequency with pressure above 275 GPa (Fig. 3).

The structures of high-pressure phases of hydrogen are unknown, which makes the definitive interpretation of the observed phenomena difficult. We use the structure(s) recently proposed by the *ab initio* theoretical calculations for phase III of hydrogen [19] to analyze our findings. With the inclusion of the zero-point energy, the calculations suggest 3 structures ($C2/c$, *Cmca*-12, and *Pbcn*) as the most plausible candidates for phase III. In $C2/c$ and *Cmca*-12 structures, all H_2 molecules have approximately the same bond length (within 1%) but would have the second Raman vibrational mode due to the Brillouin zone *doubling* with respect to phase I. This is in some agreement with the experimentally observed infrared [10,20] and ν_2 Raman [6] modes. The extremely weak Raman ν_2 vibron was observed in phase III and was assigned to a folded mode from the Brillouin zone boundary; the frequency of this mode is quite close to that of the strong IR mode (Fig. 3), as they both correspond to the vibrational states near the top of the vibrational band [21]. Both IR and Raman (at $\sim$175 GPa) are relatively close in frequency (~ 4400 cm^{-1}) to the unbound state [21]. On the other hand, the proposed for H_2-III *Pbcn* structure could explain all features of the Raman spectra of phase IV reported here. This structure is highly unusual; it consists of unbound molecules sandwiched between the honeycomb graphenelike layers made of 6-atom rings, which have different size lengths (from 0.85 to 1.04 Å; see Fig. S2 in [17] and Ref. [19]), yielding both molecular and atomic hydrogen at the same time. The density-functional theory calculations give the positions of Raman active modes [19] for the *Pbcn* structure; we observe 6 out of 16 predicted fully symmetric modes (A_g) which are expected to be the most intense. The spectral positions of all observed modes agree well with the theoretical calculations (see Fig. S3 in [17]). Using empirical formula relating the frequencies (ν) and the bond lengths (r), $\nu r^3 = \text{const}$ [22], we *qualitatively* assign the observed vibron frequencies in the *Pbcn* structure. The 0.72 Å length, which is very close to the bond length of an unbound molecule, could be easily assigned to the ν_2 mode ($\nu_2 \sim 4150$ cm^{-1}), and the ν_1 2800 cm^{-1} mode could be assigned to the 0.82 Å bond length. At this point we note that 1.04 and 1.03 Å bond lengths *could* correspond to a calculated (see Fig. S3) and observed doublet at 1050 and 1200 cm^{-1}. We have not observed the band at $\sim$1800 cm^{-1}, corresponding to the 0.95 Å length, but this band most probably is hidden behind the stressed diamond signal, covering the area from 1333 to 1850 cm^{-1} at 315 GPa (inset in Fig. 2). Two other modes observed here below 700 cm^{-1} (Fig. 3) correspond to the out-of-plane translational and librational modes.

The increased vibron mode softening, its broadening, and the presence of the intense ν_2 mode in phase IV can be understood by the difference in local molecular association. Phase IV provides a unique continuous route for molecular dissociation (retaining unbound molecules), similar to that which has been previously observed in ice VII through the hydrogen bond symmetrization [18]. In the vicinity of the symmetrization transition, the lattice becomes highly anharmonic, causing a pronounced softening and broadening of the O-H stretch mode [18] very similar to the observations in this study. We speculate that the pressure-dependent changes of the soft mode, mode coupling, and optical absorption are related to the predicted continuous structural transformation of the *Pbcn* structure into the higher symmetry *Ibam* [19] configuration with formation of the perfect graphenelike hydrogen layers with *equal* distances between atoms in a 6-member ring. Because of the larger zero-point energy, the higher mobility of the proton compared to the deuteron is expected, leading to the enhanced proton tunneling in the regime approaching symmetrization as was observed in water [23]. In this case, the hydrogen vibron would show larger softening of the ν_1 mode relative to deuterium as demonstrated in the divergence from the $\sqrt{2}$ ratio between H_2 and D_2 ν_1 modes (see Fig. S2 in Ref. [17]) as the lighter hydrogen tunnels more easily. This also could explain the presence of the regime of an increased optical absorption above $\sim$280 GPa (see Fig. 4). Above 268 GPa, a strong band-gap feature appears in the spectra and shifts in red with pressure. The overall absorption increases with pressure in this regime; the sample becomes dark in appearance (Fig. 1 and Ref. [17]). Although the band-gap shift with pressure is comparable to that for phase III (Fig. 4), the overall significant increase in absorption suggests that above 278 GPa hydrogen may become semimetallic. This is in excellent agreement with the theoretical prediction that *Pbcn* structure will metallize at above 300 GPa [19].

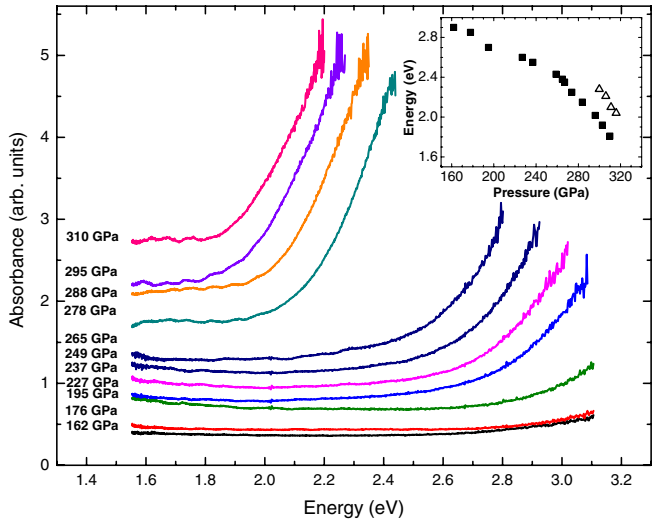

FIG. 4 (color online). Optical absorption spectra of H_2 in a visible spectral range at 300 K and different pressures. The reference transmission spectrum was measured at 75 GPa. Inset: Estimated band gap as a function of pressure at 300 K (solid squares) and at 77 K from Ref. [8] (open triangles).

We have observed reversible phase IV to III transformations between 230 and 285 GPa upon cooling or warming (see Fig. S5 in [17]). These results allow us to constrain the phase diagram of hydrogen at very high pressures. Our observations suggest that phase IV supersedes phase III at high temperatures and will most likely become metallic. The transition line between phases III and IV has a negative slope, and it is relatively shallow in P-T coordinates. This substantiates that the transition is entropy driven, which is supported by the described above difference in structure and related to it proton tunneling in phase IV. Theory [19], together with this experimental study, confirms that a unique mixed molecular and atomic state provides a route to solid metallic hydrogen at high temperatures. In order to better understand the connection between the described here phase IV, the melting curve, and predicted atomic liquid states [24,25], further investigations are clearly needed. We tentatively place the second triple point at 210 GPa and 320 K, but the slope of the I–IV boundary needs to be established. This boundary is of particular interest, because it has important consequences for the behavior of the melting curve. Independently of the I–IV slope boundary, it is very likely that the melting curve will change its slope at some P-T condition, because the phases I and IV are very dissimilar. Depending on the sign of this slope, one could expect that the predicted ground liquid state [15] could be realized at higher pressures or may be not realized at all as in case with Li [26]. Since phase IV could have strong quantum tunneling of protons within two-dimensional layers, it could possess some features of quantum proton fluid. It is interesting to note that the intersection of the molecular to atomic liquid states boundary predicted theoretically [24,25] and the extrapolation of the melting curve is in close proximity to the stability field of phase IV discovered in this work (Fig. 1). This is a clear indication of the connection between changes in both liquid and solid states in this interesting and unusual material.

The authors are grateful to Chris Pickard for providing unpublished data, very useful discussions, and remarks. This work is supported by research grants from the U.K. Engineering and Physical Sciences Research Council and Institute of the Shock Physics, Imperial College. T. S. acknowledges financial support by the EPSRC CM-DTC. A. F. G. acknowledges support from the NSF, Army Research Office, NAI, and EFRee.

*Corresponding author.
e.gregoryanz@ed.ac.uk

[1] H. Mao and R. Hemley, Rev. Mod. Phys. **66**, 671 (1994).
[2] N. Ashcroft, in *Proceedings of the International School of Physics "Enrico Fermi,"* edited by R. Hemley *et al.* (IOS, Amsterdam, 2002), Vol. CXLVII, pp. 151–194, and references therein.
[3] H. Lorenzana, I. Silvera, and K. Goettel, Phys. Rev. Lett. **64**, 1939 (1990).
[4] I. Goncharenko and P. Loubeyre, Nature (London) **435**, 1206 (2005).
[5] R. J. Hemley and H. Mao, Phys. Rev. Lett. **61**, 857 (1988).
[6] A. F. Goncharov, R. J. Hemley, H. K. Mao, and J. Shu, Phys. Rev. Lett. **80**, 101 (1998).
[7] A. Goncharov, I. Mazin, J. Eggert, R. J. Hemley, and H. K. Mao, Phys. Rev. Lett. **75**, 2514 (1995).
[8] P. Loubeyre, F. Occelli, and R. LeToullec, Nature (London) **416**, 613 (2002).
[9] Y. Akahama, H. Kawamura, N. Hirao, Y. Ohishi, and K. Takemura, J. Phys. Conf. Ser. **215**, 012056 (2010).
[10] A. Goncharov, E. Gregoryanz, R. Hemley, and H. Mao, Proc. Natl. Acad. Sci. U.S.A. **98**, 14 234 (2001).
[11] B. Baer, W. Evans, and C. Yoo, Phys. Rev. Lett. **98**, 235503 (2007).
[12] E. Gregoryanz, A. F. Goncharov, K. Matsuishi, H. K. Mao, and R. J. Hemley, Phys. Rev. Lett. **90**, 175701 (2003).
[13] S. Bonev, E. Schwegler, T. Ogitsu, and G. Galli, Nature (London) **431**, 669 (2004).
[14] N. Subramanian, A. F. Goncharov, V. V. Struzhkin, M. Somayazulu, and R. J. Hemley, Proc. Natl. Acad. Sci. U.S.A. **108**, 6014 (2011).
[15] E. Babaev, A. Sudbo, and N. Ashcroft, Nature (London) **431**, 666 (2004).
[16] W. Nellis, S. Weir, and A. Mitchell, Phys. Rev. Lett. **76**, 1860 (1996).
[17] See Supplemental Material at http://link.aps.org/supplemental/10.1103/PhysRevLett.108.125501 for the additional details.
[18] A. Goncharov, V. V. Struzhkin, H. K. Mao, and R. J. Hemley, Phys. Rev. Lett. **83**, 1998 (1999).
[19] C. J. Pickard and R. J. Needs, Nature Phys. 3, 473 (2007); C. Pickard (private communications).

[20] M. Hanfland, R. Hemley, and H. Mao, Phys. Rev. Lett. **70**, 3760 (1993).

[21] J. van Kranendonk and G. Karl, Rev. Mod. Phys. **40**, 531 (1968).

[22] G. Herzberg, in *Molecular Spectra and Molecular Structure I: Diatomic Molecules* (Krieger, Malabar, FL, 1989), p. 457; see also W. Sherman, J. Phys. C **13**, 4601 (1980).

[23] J. Pruzan, E. Wolanin, M. Gauthier, J. C. Chervin, B. Canny, D. Hausermann, and M. Hanfland, J. Phys. Chem. B **101**, 6230 (1997).

[24] I. Tamblyn and S. Bonev, Phys. Rev. Lett. **104**, 065702 (2010).

[25] M. Morales, C. Pierleonib, E. Schweglerd, and D. M. Ceperley, Proc. Natl. Acad. Sci. U.S.A. **107**, 12 799 (2010).

[26] C. L. Guillaume, E. Gregoryanz, O. Degtyareva, M. I. McMahon, M. Hanfland, S. Evans, M. Guthrie, S. V. Sinogeikin, and H-K. Mao, Nature Phys. **7**, 211 (2011).

[27] F. Datchi, P. Loubeyre, and R. LeToullec, Phys. Rev. B **61**, 6535 (2000).

[28] A. F. Goncharov, R. J. Hemley, and H. Mao, J. Chem. Phys. **134**, 174501 (2011).

Optical and electronic properties of dense sodium

Miriam Marqués,[1] Mario Santoro,[2,3] Christophe L. Guillaume,[1] Federico A. Gorelli,[2,3] Julia Contreras-García,[4] Ross T. Howie,[1] Alexander F. Goncharov,[5] and Eugene Gregoryanz[1]

[1]*Centre for Science at Extreme Conditions and School of Physics and Astronomy, University of Edinburgh, Edinburgh EH9 3JZ, United Kingdom*

[2]*European Laboratory for Non-Linear Spectroscopy, University of Florence, I-50121 Florence, Italy*

[3]*IPCF-CNR, UOS Roma, Piazzale Aldo Moro 5, 00185 Roma, Italy*

[4]*Department of Chemistry, Duke University, Durham, North Carolina 27708, USA*

[5]*Geophysical Laboratory, Carnegie Institution of Washington, Washington DC 20005 USA*

(Received 13 January 2011; revised manuscript received 5 March 2011; published 17 May 2011)

High-resolution Raman spectroscopy of dense sodium reveals additonal low-energy lattice excitations in the three high-pressure phases $cI16$, $oP8$, and $tI19$ from 108 to 178 GPa. The Raman-active lattice modes indicate profound changes of the chemical bonding in Na upon its transformation to an insulating state ($hP4$ phase) at pressures above 178(2) GPa. The calculated values of the valence electron localization maxima versus pressure provide insights into the experimentally observed solid-solid phase transitions and anomalous melting behavior of sodium.

DOI: 10.1103/PhysRevB.83.184106 PACS number(s): 62.50.−p, 61.50.Ks, 63.20.−e, 71.15.−m

I. INTRODUCTION

The profound changes in elements induced by extreme conditions are fundamental to a broad range of problems in physics. The group-I alkali metals have been the testing grounds for simple systems, which have been predicted to adopt low-symmetry structures upon compression.[1,2] The proposed instability of cubic phases of Li under compression and the prediction that the low-symmetry phases will take over at higher pressures[2] were later confirmed experimentally for both Li and Na.[3–7] The appearance of open and incommensurate structures has been explained in terms of Peierls distortions,[2,8] $s \rightarrow p$ and $s \rightarrow d$ electronic transitions,[3] Fermi surface–Brillouin zone interactions,[9,10] and more recently in terms of a combined effect of Couloumb repulsion, Pauli exclusion, and orbital orthogonality that results in an increase of valence electrons in interstitial regions.[11] Theory also suggested that as the density rises both Li and Na will become increasingly less metallic, approaching a semiconducting phase; several candidate structures have been proposed at very high pressures, including $oC8$ and $hP4$.[12,13] Indeed, the experimental studies[5,14] reported the existence of Raman activity, color change, and reflectivity decrease in Na, signaling profound electronic modifications. The optical reflectivity measurements and electronic structure calculations demonstrated that Na transforms from a high-reflecting free-electron metal at ambient conditions to the nearly insulating $oP8$ phase with significantly reduced reflectivity at $P > 118$ GPa and suggested that compression of the $oP8$ phase beyond its range of stability would result in a metal-insulator transition at a fivefold reduction in volume.[15] The direct resistivity measurements indicated that Li exhibits a zero-gap-semiconductor behavior above 78 GPa,[16] while optical spectroscopy and x-ray diffraction showed that at around 200 GPa Na turns into a wide-gap insulator having the $hP4$ structure.[17] In addition to the high-density low-symmetry structures predicted by theory, some quite unexpected phenomena have been observed in light alkali metals, such as pressure-induced superconductivity[18] and anomalously low melting temperatures at high compression.[6,19] Even though the physical mechanisms responsible for the decreasing melting temperatures over a wide pressure range for Na and Li have been extensively studied,[20–25] there is no general agreement and the phenomenon still requires a better understanding.

Although Raman spectroscopy of metals at high pressures is used as a probing tool,[26,27] it is not widely applied due to several factors, such as very weak scattering and a strong background from the sample environment. The appearance of low-symmetry structures in Na may give rise to Raman activity, enabling the study of vibrational dynamics and chemical bonding. In this paper we report Raman measurements on Na from 100 to 200 GPa in a wide temperature range. In the lower-pressure phases ($cI16$, $oP8$, and $tI19$) we observe additional Raman peaks below 200 cm^{-1}, while the highest-pressure phase ($hP4$) has only one intense band at $\sim$350 cm^{-1}, indicating profound changes in the electronic structure and therefore a change of bonding. Using *ab initio* calculations we show that the changes of the interstitial electron localization patterns in the solid above 60 GPa are responsible for the previously observed unusual melting behavior and for the rich polymorphism of dense sodium.

II. EXPERIMENTAL AND THEORETICAL DETAILS

We have conducted experiments on three separate Na samples, two of which were used in the structural and infrared measurements reported in Refs. 5, 14, 15, reaching maximum pressures of 130 to 200 GPa and temperatures ranging from 140 to 550 K. A number of pressure-heating-cooling cycles were made on each sample, enabling us to establish reproducible behavior. For the Raman spectroscopy we have used a triple-grating monochromator (trivista555, Acton-Roper), coupled to a CCD detector (Princeton Instruments), with the first two stages operating in subtractive mode. For the low temperature Raman measurements we have used the Raman set-up and the cryostat described in Refs. 28 and 29. In order to ensure that the detected signals are indeed Raman scattering emanating from the sample, we performed our measurements

using the 647.1 and 752.5 nm lines of a Kr^+ ion laser and the 514.5 nm line of an Ar^+ ion laser as the excitation sources, and collected anti-Stokes components of the Raman signal. With the exception of the insulating $hP4$ phase synchrotron x-ray diffraction was used to identify the structural modifications of the sample. The pressure was measured from the Ta equation of state[30] and correlated with the optically measured stressed diamond edge.[31] For further information on sample preparation and loading, see Refs. 4–6.

First-principles total energy calculations were performed within the density-functional theory formalism with a plane-wave pseudopotential approach, as implemented in the Vienna *ab initio* simulation package.[32] We used the Perdew-Burke-Ernzerhof generalized gradient exchange-correlation functional[33] and the projector augmented wave all-electron description of the electron–ion-core interaction.[34] Due to the extremely large compressions involved, we treat the $2s$, $2p$, and $3s$ electrons as valence electrons. Brillouin zone integrals were approximated using the method of Monkhorst and Pack[35] and the energies converged with respect to k-point density ($21 \times 21 \times 21$, $13 \times 17 \times 11$, and $16 \times 16 \times 16\,k$ meshes for the $cI16$, $oP8$, and $hP4$ structures, respectively) and the plane wave cutoff (850 eV). Phonon frequencies were calculated within density-functional perturbation theory as implemented in the QUANTUM-ESPRESSO package.[36] The total energies required in the calculation of the phonons were obtained using the same Perdew-Burke-Ernzerhof parametrization of the exchange correlation potential.[33] The ion-electron interaction was described by an ultrasoft (Vanderbilt[37]) pseudopotential with $2s$ and $2p$ as valence states. Brillouin zone integrations were performed using the same grids as in the VASP calculations. The topological analysis of the electron localization function (ELF) was performed with the CRITIC code.[38] To this end, the VASP optimized structures were recalculated with the CRYSTAL98 code[39] in order to obtain all-electron wave functions. Additionally, we have used the ELK code.[40]

III. RESULTS AND DISCUSSION

Up to 100 GPa Na exists in the Raman-inactive bcc and fcc structures. Above 100 GPa sodium adopts the $cI16$ structure with eight atoms in the primitive cell and five active Raman modes. Our calculated Raman frequencies for $cI16$ range from ~70 to ~490 cm^{-1} at 115(1) GPa. Figure 1 shows the observed Raman spectrum (Stokes and anti-Stokes) of the $cI16$ phase consisting of an unresolved doublet at 70 cm^{-1}. We assign the lower-frequency peak to the A_1 mode, which is due to the change associated with symmetric atomic stretching movements. The Raman activity changes when Na enters into the $oP8$ phase at pressures above 118(1) GPa.[5] At this point significant redistribution of the electronic charges takes place in the solid (see below) with additional higher-frequency ($\omega > 100$ cm^{-1}) modes appearing. Group theory analysis for the $oP8$ phase yields 12 Raman-active modes, out of which which we are able to observe eight. The inset of Fig. 1 shows the Raman spectra of the $oP8$ phase measured upon increasing temperature. At 127 GPa the Raman signal disappears at about 350 K, indicative of the melting and confirming the low melting temperature previously observed in x-ray diffraction experiments.[19] Above 127(1) GPa Na transforms to the

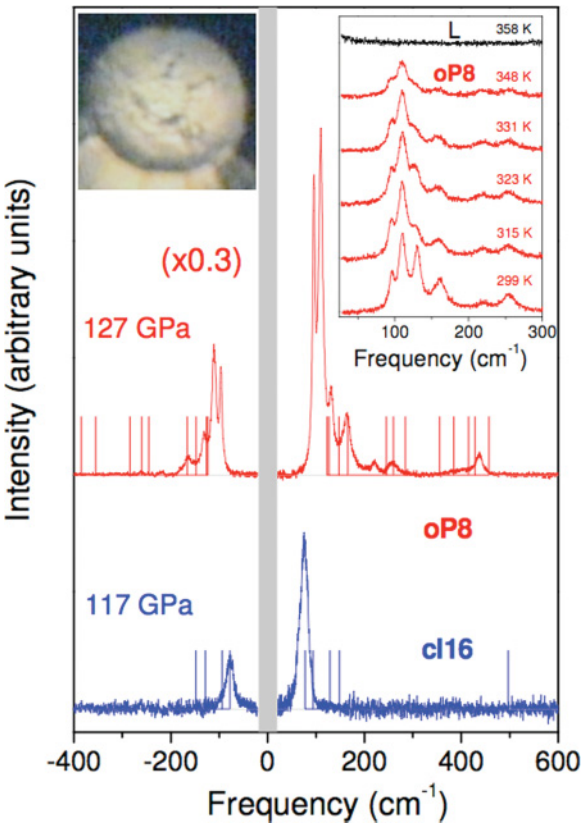

FIG. 1. (Color online) Representative Raman spectra of the $cI16$ and $oP8$ phases. The vertical bars indicate the calculated frequencies. Inset (right): Raman spectra of the $oP8$ phase at 127 GPa taken at different temperatures. The disappearance of the spectra corresponds to the melting at around the minima of the melting curves. Smooth polynomial lines have been fitted to the broad luminescence background emanating from diamonds and to the wings of the Rayleigh line, and then subtracted from the spectra in both panels. The spectra have been vertically scaled for clarity. Inset (left): microphotograph of the sample in the $oP8$ phase.

incommensurate $tI19$ phase with a pronounced reduction of the reflectivity (see Fig. 2 and Refs. 14, 15). The Raman activity in the $tI19$ phase is determined by the host structure ($tI16$) which has eight allowed Raman modes while the guest has one atom per unit cell and has no Raman activity. We have observed all eight modes, which consist of a quite intense triplet, below 200 cm^{-1}, and five weaker peaks of higher frequency (see Fig. 2). The calculations performed on the approximate structures of $tI18(20)$ show further increase of the pseudogap opening with respect to the $oP8$ phase, with the valence charge density accumulating along the guest chains.[15] At pressures of 178(3) GPa the $tI19$ phase abruptly changes to a completely transparent insulating phase with very intense Raman signal (Fig. 2). The evolution of the optimized structural parameters of the $oP8$ phase with pressure indicates that this phase will transform to the hexagonal structure ($hP4$) at around 240 GPa in good agreement with Refs. 15 and 17.

We calculated the electron localization function for the $cI16$, $oP8$, and $hP4$ phases of Na (see Figs. 3 and 4 for the ELF isosurfaces and contour plots, respectively). Topological analysis of the ELF can reveal the bonding and

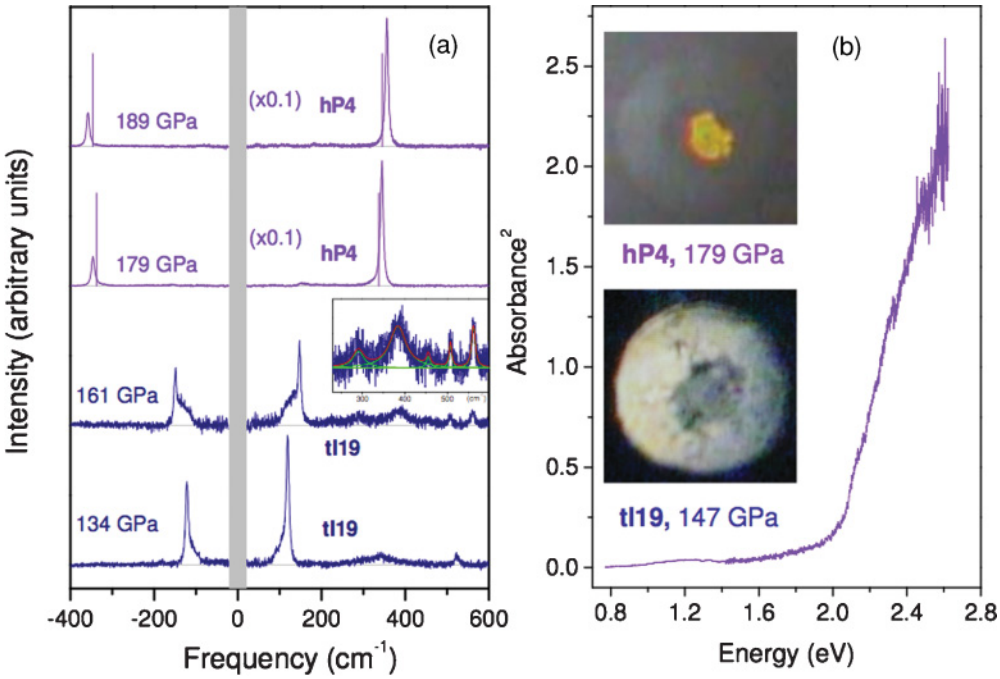

FIG. 2. (Color online) Left panel: representative Raman spectra of the $tI19$ and $hP4$ phases. The vertical bars indicate the calculated frequencies for the $hP4$ phase. Inset: magnified high-energy weak peaks in the $tI19$ phase. Right panel: sample microphotograph (top inset) and its optical absorption spectrum (absorbance to the second power) in the $hP4$ phase. Bottom inset: Sample microphotograph in the $tI19$ phase. The photographs were taken under transmitted and reflected light and show the same sample as in Fig. 1.

localization pattern from first principles. Two stationary points are analyzed: attractors (ELF maxima) and bips (first-order saddle points). In general, the ELF value approaches 1 in regions of space where electron pairing occurs (e.g., atomic shells, bonds, and lone pairs), and 0 in the limit between those surfaces, where there is a high probability of finding electrons from different pairs. The value 0.5 corresponds to the homogeneous electron gas (HEG). Hence, the ELF profile in the valence region of simple metals is nearly flat and usually close to 0.5,[41] as would be expected for the bcc phase of Na. Indeed, our calculations in the bcc phase at ambient pressure show a very homogeneous electron distribution consisting of valence ELF attractors on tetrahedral 12d sites with ELF value around 0.6 and joined through bips with a similar ELF value. This profile is maintained until the bcc-fcc phase transition at 65 GPa. The fcc phase presents two different ELF attractors on octahedral and tetrahedral sites. Their corresponding ELF values are, respectively, higher and lower than the HEG value of 0.5 and monotonically increase/decrease with pressure. This is in agreement with the pressure-induced electron density increase on octahedral interstices at the expense of the tetrahedral sites proposed in Ref. 11. This trend is maintained in the $cI16$ phase, with two differentiated ELF attractor regions of high and low ELF value around the tetrahedral 12a and 12b sites, respectively. Interestingly, the $cI16$ phase is a distorted $2 \times 2 \times 2$ superstructure of the bcc structure, and

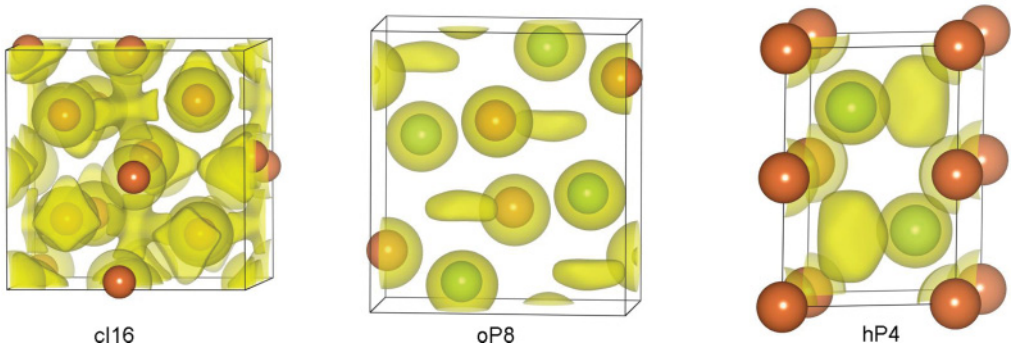

FIG. 3. (Color online) ELF isosurfaces (light grey; yellow online) for the $cI16$, $oP8$, and $hP4$ structures. The ELF values are fixed at 0.25, 0.5, and 0.7, respectively. The atomic positions are shown by spheres of different tonalities (dark and medium grey; red, green oline) representing nonequivalent atomic sites. The dark (red online) spheres correspond to the equivalent Na atoms of the $cI16$ structure, one 4c site of the $oP8$ structure, and the 2a site of the $hP4$ structure. The medium dark (green online) spheres correspond to the other 4c site of the $oP8$ structure and the 2c site of the $hP4$ structure.

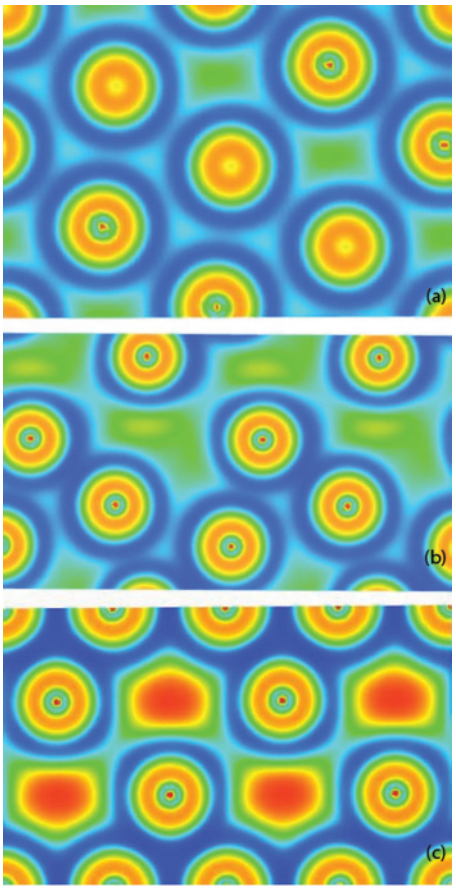

FIG. 4. (Color online) ELF contour plots for the (a) (110) plane of $cI16$, (b) (040) plane of $oP8$, and the (c) (110) plane of $hP4$, respectively. The ELF values range from 0 (dark grey; blue online) to 1 (light grey; red online).

the ideal bcc structure in the experimental pressure range of $cI16$ would have identical ELF attractors on tetrahedral sites with a low ELF value of 0.38. As compression into $oP8$ takes place, the polarizability screening of the free electron present at lower pressures does not hold (compare $cI16$ and $oP8$ in Fig. 3) and intense modes appear in the Raman spectrum (Fig. 1). In the $oP8$ phase only one attractor type on $4c$ sites is present, having values close to the unity. Although the localization of interstitial electrons in $oP8$ is deprived of the most characteristic HEG features, some of the metallic properties are still preserved. The localization of electrons leads to the widening of the pseudogap but the exchange between valence electrons still takes place, as can be seen from the connection between different valence regions (see Fig. 4).[42] Moreover, the value of the ELF at the bips connecting the different localized regions becomes smaller with increasing pressure, eventually leading to an insulating structure. The small range of stability of this phase (from ∼118 to ∼125 GPa) and its transformation to the incommensurate $tI19$ phase preclude this possibility (see also Ref. 15), shifting the metal-to-insulator transformation to much higher pressures. In the insulating phase, $hP4$ [see Fig. 3(c)], the valence electrons localize even more strongly in the interstitial voids, forming well-defined entities with very low ELF values at the bips connecting them, highlighting their

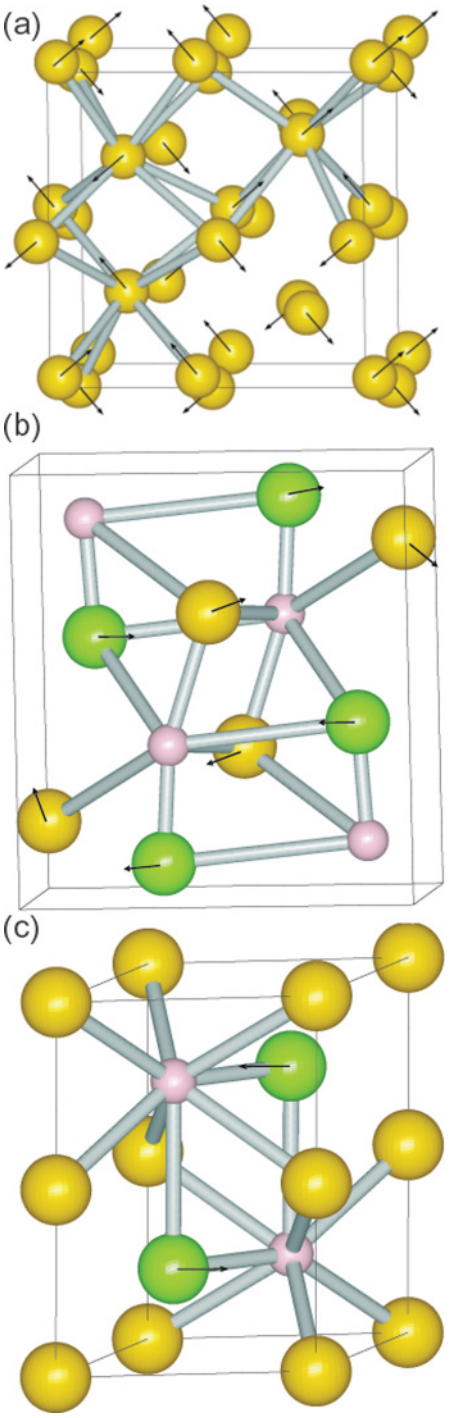

FIG. 5. (Color online) Atomic movements showing observed Raman modes in $cI16$, $oP8$, and $hP4$ phases. (a) $cI16$, A_1 mode; (b) $oP8$, A_g mode; (c) $hP4$, E_{2g} mode. The light grey (yellow online) spheres correspond to the equivalent Na atoms of the $cI16$ structure, one $4c$ site of the $oP8$ structure, and the $2a$ site of the $hP4$ structure. The dark grey (green online) spheres correspond to the other $4c$ site of the $oP8$ structure and the $2c$ site of the $hP4$ structure. The smaller spheres (pink online) represent the ELF valence attractor maxima.

orthogonality. Curiously, a semiconducting $hP4$ phase has also been reported for K transforming to the $oP8$ phase with pressure.[43] Moreover, these electrons can also be characterized as real electron pairs, as can be seen from the high ELF

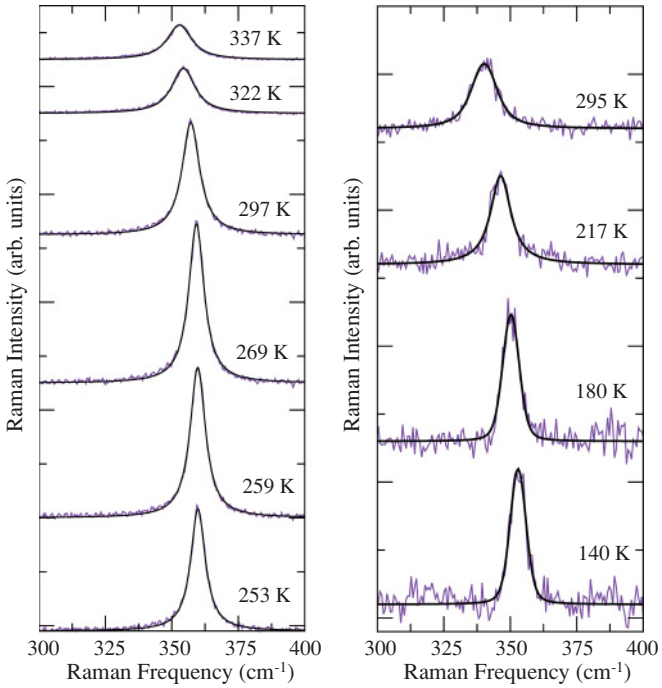

FIG. 6. (Color online) Representative Raman spectra of the $hP4$ phases at 200 GPa (left panel) and 180 GPa (right panel) at different temperatures. The spectra have been vertically scaled for clarity.

value at the center of the interstices (0.9) (see Figs. 3 and 4). The band gap is fully open in this phase and reaches values of $E_g = 2.1$ eV as measured by optical transmission spectroscopy (Fig. 2, right panel). Interestingly, if we consider the attractors as pseudoanions without core,[43] the most intense Raman-active modes can be associated with movements of the sodium atoms with respect to the valence attractors (see Fig. 5). The experimentally observed Raman mode has E_{2g} symmetry. Its intensity is clearly influenced by the change caused by the atomic movements toward the maxima of the newly formed electron pairs (see Fig. 5). Thus, this observation provides experimental proof of the pseudoanionic ELF attractors.

We also tried to measure the Na melting temperatures above 130 GPa in this study. However, heating of Na-$tI19$ at 140 GPa up to 550 K did not melt the sample. One can try to estimate the melting temperatures from the Raman spectroscopy. We measured the temperature dependence of the E_{2g} mode of the $hP4$ phase at 180 and 200 GPa (see Fig. 6). This mode correlates with a transverse acoustic phonon; thus, its frequency shift provides information about the C_{44} elastic constant which represents the slope of this branch at the center of the Brillouin zone. The relation can be derived with a three-body force model for a hexagonal solid with a nonideal c/a ratio.[44] In order to estimate C_{44} we have used the following

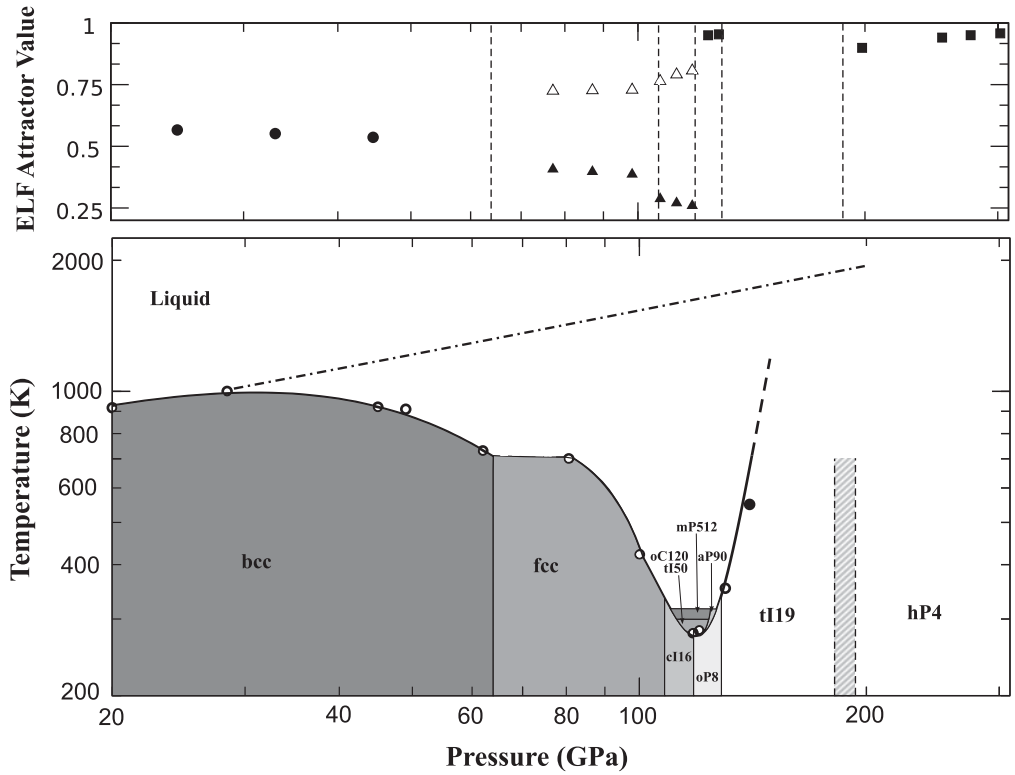

FIG. 7. Lower panel: Proposed phase diagram of Na. The lower-pressure region, shown in open circles, is adapted from the Refs. 5 and 19; the solid circle is measurement in this study; the dot-dashed line shows the extrapolation of the melting curve from 30 GPa with the Simon-Glatzel empirical law (Ref. 45); the dashed line extrapolating the melting curve above 140 GPa is a guide to the eye only; the vertical dashed lines show the region of $tI19$ and $hP4$ coexistence. Upper panel: ELF attractor values as functions of pressure in different solid phases. The solid circles show the ELF attractor values in the bcc phase, empty and solid triangles show the ELF attractor values at nonequivalent interstitial sites (octahedral and tetrahedral sites, respectively, in fcc structure and tetrahedral 12a and 12b sites, respectively, in $cI16$). Solid squares show the ELF attractor values in the $oP8$ and $hP4$ phases.

formula:[44]

$$C_{44} = 2\pi^2 M\left(\frac{\sqrt{3}c}{6a^2}\right)\nu^2,$$

where M is the atomic mass, and a, c, and ν are the measured lattice constants and Raman frequency, respectively. The values of C_{44} in the 180 to 200 GPa pressure range as estimated from the frequencies of the E_{2g} mode (120 GPa) and from first-principles calculations (129 GPa) are in very good agreement. The main shear modulus of the hexagonal medium is $G = 2C_{44} + C_{66}$. The calculations for C_{66} give a value of about 40 GPa, showing that the shear modulus of Na-$hP4$ is mostly driven by C_{44}. The measured temperature dependence of the E_{2g} mode between 180 and 200 GPa (see Fig. 6) is $\sim$0.1 cm^{-1}/K. This estimate suggests that quite high temperatures (upper bound of $T > 3500$ K) are needed to substantially decrease G and to melt Na-$hP4$.

In Fig. 7 we show the ELF attractor values as functions of pressure, together with the phase diagram of Na. Remarkably, there is a clear correlation between the pressure evolution of ELF attractors and solid-solid phase transitions, which suggests that the changes in the interstitial electron distribution are indeed the driving force for these phase transitions. Also, the pressure dependence of ELF attractors tightly correlates with the melting line. At the same pressures ($P > 30$ GPa), when the melting temperatures have passed their maximum and started to decrease, the ELF attractor value is slowly decreasing. When Na enters the pressure domain of the fcc phase, there is a splitting into two attractors with high and low ELFs, as described above. The ELF value at the lower ELF attractor monotonically decreases upon increasing pressure. This trend is maintained in the $cI16$ phase and up to the $cI16$-$oP8$ phase transition point ($\sim$118 GPa), which correlates with the negative slope in the melting line that reaches a minimum in the $cI16$ phase. At the $cI16$-$oP8$ phase transition the ELF attractor value abruptly changes, reaching the typical high values of ionic bonding, and, correspondingly, the melting line starts to steeply increase with pressure. The ELF attractor value is an efficient route to parametrize valence electron localization, which in turn is the source of binding energy and of all effects connected to binding energy, such as phase stabilization, bulk moduli, shear moduli, and, ultimately, melting temperatures. The existence in the fcc and $cI16$ phases of attractors with very low ELF value, which also decreases upon increasing pressure, is likely to indicate weaker binding. And, as a consequence of less strongly bonded atoms, a lower temperature is required to melt the solid. At above 118 GPa ($oP8$), the low ELF attractors disappear, and the high ELF value of the only attractor indicates a change to a strong pseudoionic bonding, which leads to high melting temperatures. Our estimates of the melting temperatures combined with the experimental points indicate that temperatures in excess of 3500 K are needed to melt sodium at around 200 GPa. The extrapolation of the melting curve above 30 GPa using empirical laws which do not have a negative component of the melting curve[45] suggests (see Fig. 7) that the melting curve of Na not only would completely recover the high temperatures after passing through the deep minimum at 118 GPa but might reach much higher values than the simple extrapolation suggests.

ACKNOWLEDGMENTS

We acknowledge financial support from the UK Engineering and Physical Sciences Research Council; the EU Contract No. FP7 G.A. No 228334 laserlabeurope; the Ente Cassa di Risparmio di Firenze, supporting research at LENS under the grant "Firenze Hydrolab"; the Spanish MALTA Consolider Project; and DOE/NNSA (CDAC), Army Research Office, and NSF Grant No. EAR-1015239.

[1] A. K. McMahan, Phys. Rev. B **29**, 5982 (1984).
[2] J. B. Neaton and N. Ashcroft, Nature (London) **400**, 141 (1999).
[3] M. Hanfland *et al.*, Nature (London) **408**, 174 (2000).
[4] M. I. McMahon *et al.*, Proc. Natl. Acad. Sci. USA **104**, 17297 (2007).
[5] E. Gregoryanz *et al.*, Science **320**, 1054 (2008).
[6] C. L. Guillaume *et al.*, Nature Phys. **7**, 211 (2011).
[7] M. Marqués *et al.*, Phys. Rev. Lett. **106**, 095502 (2011).
[8] D. W. Zhou *et al.*, J. Phys.: Condens. Matter **21**, 025508 (2009).
[9] G. J. Ackland and I. R. Macleod, New J. Phys. **6**, 138 (2004).
[10] V. F. Degtyareva, Phys. Usp. **49**, 369 (2006).
[11] B. Rousseau and N. W. Ashcroft, Phys. Rev. Lett. **101**, 046407 (2008).
[12] J. B. Neaton and N. W. Ashcroft, Phys. Rev. Lett. **86**, 2830 (2001).
[13] N. E. Christensen and D. L. Novikov, Solid State Commun. **119**, 477 (2001).
[14] L. F. Lundegaard *et al.*, Phys. Rev. B **79**, 064105 (2009).
[15] A. Lazicki *et al.*, Proc. Natl. Acad. Sci. USA **106**, 6525 (2009).
[16] K. Shimizu and T. Matsuoka, Nature (London) **458**, 186 (2009).
[17] Y. Ma *et al.*, Nature (London) **458**, 182 (2009).
[18] K. Shimizu *et al.*, Nature (London) **419**, 597 (2002); V. Struzhkin *et al.*, Science **298**, 1213 (2002).
[19] E. Gregoryanz *et al.*, Phys. Rev. Lett. **94**, 185502 (2005).
[20] E. R. Hernández and J. Íñiguez, Phys. Rev. Lett. **98**, 055501 (2007).
[21] J. Y. Raty *et al.*, Nature (London) **449**, 448 (2007).
[22] L. Koĉi, R. Ahuja, L. Vitos, and U. Pinsook, Phys. Rev. B **77**, 132101 (2008).
[23] M. Martinez-Canales and A. Bergara, J. Phys. Chem. Solids **69**, 2151 (2008).
[24] I. Tamblyn, J.Y. Raty, and S. A. Bonev, Phys. Rev. Lett. **101**, 075703 (2008).
[25] E. Hernández, A. Rodriguez-Prieto, A. Bergara, and D. Alfe, Phys. Rev. Lett. **104**, 185701 (2010).
[26] H. Olijnyk, Phys. Rev. Lett. **68**, 2232 (1992).
[27] A. F. Goncharov and V. V Struzhkin, J. Raman Spectrosc. **34**, 532 (2003).
[28] J. Proctor *et al.*, Phys. Rev. B **80**, 073408 (2009).
[29] M. Hanfland *et al.*, Phys. Rev. Lett. **106**, 095503 (2011).
[30] M. Hanfland, K. Syassen, and J. Kahler, J. Appl. Phys. **91**, 4143 (2002).
[31] Y. Akahama and H. Kawamura, J. Appl. Phys. **96**, 3748 (2004).
[32] G. Kresse and J. Furthmuller, Phys. Rev. B **54**, 11169 (1996).

[33]J. P. Perdew, K. Burke, and M. Ernzerhof, Phys. Rev. Lett. **77**, 3865 (1996).
[34]G. Kresse and D. Joubert, Phys. Rev. B **59**, 1758 (1999).
[35]H. J. Monkhorst and J. D. Pack, Phys. Rev. B **13**, 5188 (1976).
[36]Computer code QUANTUM-ESPRESSO, [http://www.quantum-espresso.org].
[37]D. Vanderbilt, Phys. Rev. B **41**, 7892 (1990).
[38]J. Contreras-García *et al.*, J. Chem. Theory Comput. **5**, 164 (2009).
[39]V. R. Saunders *et al.*, computer code CRYSTAL98 (University of Torino, Torino, 1998).
[40][http://elk.sourceforge.net].
[41]B. Silvi and C. Gatti, J. Phys. Chem. A **104**, 947 (2000).
[42]J. Contreras-García and J. M. Recio, Theor. Chem. Acc. **128**, 411 (2011).
[43]M. Marqués *et al.*, Phys. Rev. Lett. **103**, 115501 (2009).
[44]J. C. Upadhyaya *et al.*, Can. J. Phys. **72**, 61 (1994).
[45]E. Gregoryanz *et al.*, Phys. Rev. Lett. **90**, 175701 (2003).